Multiorbital Physics in Optical Lattices

Dirk-Sören Lühmann

Multiorbital Physics in Optical Lattices

D i s s e r t a t i o n

zur Erlangung des Doktorgrades des Department Physik
der Universität Hamburg vorgelegt von

D i r k - S ö r e n   L ü h m a n n

aus Brunsbüttel

Hamburg, 2009

Gutachterin / Gutachter der Dissertation:	Prof. Dr. Daniela Pfannkuche
	Prof. Dr. Stephanie M. Reimann
	Prof. Dr. Michael Fleischhauer
Gutachterin / Gutachter der Disputation:	Prof. Dr. Daniela Pfannkuche
	Prof. Dr. Klaus Sengstock
Datum der Disputation:	10. November 2009
Vorsitzender des Prüfungsausschusses:	PD Dr. Alexander L. Chudnovskiy
Vorsitzender des Promotionsausschusses:	Prof. Dr. Robert Klanner
Dekan der Fakultät für Mathematik, Informatik und Naturwissenschaften:	Prof. Dr. Heinrich Graener

To Sarah

Abstract

In this thesis, ultracold bosonic gases and mixtures of bosons and fermions in optical lattices are studied with special regard to finite-size and orbital effects. In preference for a Hubbard-type single-band Hamiltonian, the influence of higher bands in optical lattices has been widely neglected so far. Here, it is shown that the inclusion of higher orbitals leads to novel physical effects such as a self-trapping behavior and the enhanced localization in attractively interacting mixtures as well as a complex quantum phase evolution in purely bosonic systems. The on-site interaction among the particles causes strongly correlated states, which are investigated using a multiorbital exact diagonalization technique.

In attractively interacting Bose-Fermi mixtures (^{87}Rb - ^{40}K) in three-dimensional optical lattices, the mutual interaction leads to a substantial deformation of the effective potentials and a squeezing of the effective orbitals for both species. Mediated by the strongly altered fermion orbital, the bosons exhibit a self-trapping behavior, where the nonlinear dependence on the width of the fermion orbital overcompensates the boson-boson repulsion. The self-amplified modification of the effective potentials, being enhanced with both increasing bosonic filling and stronger interspecies scattering, has profound influence on the bosonic tunneling and the on-site interaction. Introducing a renormalized Bose-Hubbard model with effective parameters, the critical lattice depth for the bosonic quantum phase transition from a superfluid to a Mott insulator is determined. It predicts a substantial shift of the transition in comparison with a purely bosonic system, which has been observed in recent experiments. It is shown that this renormalized model is in excellent agreement with experiments allowing for tunable interspecies interactions. In general, this demonstrates the fundamental importance of interaction induced orbital changes in attractively interacting quantum gas mixtures in optical lattices.

For bosonic gases in finite optical lattices with few sites, a surprisingly strong similarity to macroscopic systems is found. The localization in finite systems with commensurate filling resembles in many aspects the macroscopic quantum phase transition between a superfluid and a Mott-insulator, including a striking similarity of the momentum distribution and the formation of an energy gap. For noncommensurate filling, a coexistence of localized and delocalized particles is observable in deep lattices in accordance to the equivalence of lattice sites. The formed narrow ground-state band is extremely sensitive to lattice perturbations, such as confining potentials, which cause the localization of all particles in a Bose-glass-like phase. For stronger confinements, the precursor of Mott shells is identified. In deep lattices, an approximate approach, where tunneling can be included on a perturbative level, allows to calculate excitation energies, occupation numbers, and particle fluctuations for large three-dimensional systems with an arbitrary shape of the confinement.

For weakly interacting quantum gases in optical lattices, the band structure is calculated for experimental parameters using the Bogoliubov theory. The band structure is substantially modified by interaction effects in agreement with results of momentum-resolved Bragg spectroscopy

performed for ^{87}Rb atoms in the superfluid phase. In strongly interacting systems, the dynamic structure factor is studied by exact diagonalization addressing the fingerprints of the Mott-insulator phase and of possible phases in Bose-Fermi mixtures.

Multiorbital effects in bosonic lattice systems can experimentally be accessed by preparing a coherent superposition of particle number states in deep potentials, which is achieved by rapidly ramping the optical lattice from shallow to deep. In great contrast to the prediction of the single-band Hubbard model, a multifrequency evolution of the matter wave field is observable as each particle number state evolves in accordance to its exact interaction energy. The inclusion of higher orbitals leads to a Hamiltonian with effective multi-body interactions. The interaction energies are calculated using the multiorbital diagonalization method, which fully includes many-particle correlations and corrections from kinetic and potential energy. Due to the anticonfinement in the experimental realization, it can be assumed that only bound orbitals are occupied allowing for a highly accurate comparison of theory and experiment, which show a compelling agreement. In addition, the comparison even allows to determine the s-wave scattering length for ^{87}Rb atoms. This demonstrates that state-of-the-art experiments permit to access highly correlated states and that multiorbital physics plays an important role in optical lattices.

Zusammenfassung

In der vorliegenden Arbeit werden ultrakalte bosonische Gase und Mischungen von Bosonen und Fermionen in optischen Gittern untersucht. Dabei werden insbesondere endliche Systeme und orbitale Effekte behandelt. Bisher wurde der Einfluss von höheren Bändern in optischen Gittern weitestgehend vernachlässigt und das Hubbard-Modell verwendet, das auf das niedrigste Band beschränkt ist. Hier wird gezeigt, dass die Berücksichtigung höherer Bänder zu neuartigen Effekten führt wie dem Self-Trapping und der verstärkten Lokalisierung in attraktiv wechselwirkenden Mischungen sowie einer komplexen Quantenphasenentwicklung in bosonischen Systemen. Die Wechselwirkung zwischen den Teilchen an einem Gitterplatz führt zu stark korrelierten Zuständen, die mit einem multiorbitalen exakten Diagonalisierungsverfahren untersucht werden.

In attraktiv wechselwirkenden Bose-Fermi-Mischungen (^{87}Rb - ^{40}K) in dreidimensionalen optischen Gittern bewirkt die gegenseitige Wechselwirkung eine große Veränderung der effektiven Potentiale und Orbitale beider Atomsorten. Vermittelt durch das stark deformierte Orbital der Fermionen zeigen die Bosonen ein Self-Trapping-Verhalten. Die Boson-Boson-Abstoßung wird dabei durch die nichtlineare Abhängigkeit von der Breite des fermionischen Orbitals überkompensiert. Die sich selbstverstärkende Verformung der effektiven Potentiale nimmt mit höherer Füllung und stärkerer Boson-Fermion-Streuung zu und hat einen erheblichen Einfluss auf das bosonische Tunneln und die Gitterplatzwechselwirkung. Durch die Beschreibung des Systems mittels eines renormalisierten Hubbard-Modells mit effektiven Parametern kann die kritische Gittertiefe des bosonischen Quantenphasenübergangs zwischen Suprafüssigkeit und Mott-Isolator bestimmt werden. Das Modell sagt eine substanzielle Verschiebung des Übergangs im Vergleich zu einem rein bosonischen System voraus, die auch in Experimenten beobachtet wurde. Der Vergleich mit Experimenten, die es erlauben die Boson-Fermion-Wechselwirkung zu verändern, liefert eine hervorragende Übereinstimmung. Dies verdeutlicht den wichtigen Einfluss von wechselwirkungsinduzierten orbitalen Veränderungen in attraktiv wechselwirkenden Quantengasmischungen in optischen Gittern.

Für bosonische Gase in endlichen optischen Gittern mit wenigen Gitterplätzen wird eine überraschend gute Übereinstimmung mit makroskopischen Systemen aufgezeigt. Die Lokalisierung in endlichen Systemen mit kommensurabler Füllung ähnelt dem makroskopischen Phasenübergang von der suprafüssigen zur Mott-isolierenden Phase in vielerlei Hinsicht. Insbesondere wird eine auffällig große Übereinstimmung der Impulsverteilung und bei der Entstehung der Energielücke gefunden. Bei nichtkommensurablen Füllungen in tiefen Gittern ist eine Koexistenz von lokalisierten und delokalisierten Teilchen beobachtbar. Das sich ausbildende schmale Grundzustandsband reagiert extrem empfindlich auf Störungen im Gitter, die zum Beispiel durch das Einschlusspotential verursacht werden und die Lokalisierung aller Teilchen in einer Bose-Glas-artigen Phase verursachen. Für hohe Einschlusspotentiale wird ein Vorläufer von Mott-Schalen gefunden. In tiefen Gittern erlaubt ein Näherungsverfahren, in dem das Tunneln perturbativ behandelt werden kann, die Anregungsenergien, Besetzungszahlen und Teilchenfluk-

tuationen für große dreidimensionale Systeme mit beliebigem Einschlusspotential zu berechnen.

Für schwach wechselwirkende Quantengase in optischen Gittern wird die Bandstruktur für experimentelle Parameter unter Benutzung der Bogoliubov-Theorie berechnet. Die Bandstruktur wird substanziell durch Wechselwirkungseffekte verändert und zeigt eine gute Übereinstimmung mit den Ergebnissen der impulsaufgelösten Bragg-Spektroskopie von ^{87}Rb-Atomen in der supraflüssigen Phase. In stark wechselwirkenden Systemen wird der dynamische Strukturfaktor mittels exakter Diagonalisierung in Hinblick auf charakteristische Merkmale der Mott-Isolator-Phase und möglichen Phasen in Bose-Fermi-Mischungen untersucht.

Multiorbitale Effekte in bosonischen Gittersystemen können experimentell in tiefen Gittern durch die Präparation einer kohärenten Überlagerung von Teilchenzahlzuständen zugänglich gemacht werden. Dies wird erreicht durch eine schnelle Veränderung der Potentialtiefe von einem flachen zu einem tiefen optischen Gitter. Im Gegensatz zu den Vorhersagen des Hubbard-Modells ist eine Mehrfrequenz-Zeitentwicklung des Materiewellenfelds beobachtbar, da sich die Teilchenzahlzustände entsprechend ihrer exakten Wechselwirkungsenergie entwickeln. Die Berücksichtigung höherer Orbitale führt zu einem Hamilton-Operator mit effektiven Vielkörper-Wechselwirkungen. Mit Hilfe der multiorbitalen Diagonalisierung werden die exakten Wechselwirkungsenergien berechnet, die vollständig die Vielteilchenkorrelationen sowie Korrekturen von kinetischer und potentieller Energie berücksichtigen. In der Realisierung dieses Experiments kann aufgrund des fehlenden Einschlusspotentials angenommen werden, dass nur gebundene Orbitale besetzt sind. Dies erlaubt einen sehr genauen Vergleich von Experiment und Theorie, die hervorragend übereinstimmen. Zusätzlich gestattet der Vergleich die Bestimmung der s-Wellenstreulänge für ^{87}Rb-Atome. Dies zeigt, dass neueste Experimente den Zugang zu hoch korrelierten Zuständen ermöglichen und die multiorbitale Physik in optischen Gittern eine wichtige Rolle spielt.

Publications

[1]   D.-S. Lühmann, K. Bongs, K. Sengstock, and D. Pfannkuche,
        Localization and delocalization of ultracold bosonic atoms in finite optical lattices,
        Physical Review A **77**, 023620 (2008).

[2]   D.-S. Lühmann, K. Bongs, K. Sengstock, and D. Pfannkuche,
        Self-Trapping of Bosons and Fermions in Optical Lattices,
        Physical Review Letters **101**, 050402 (2008).

[3]   T. Best, S. Will, U. Schneider, L. Hackermüller, D. van Oosten, I. Bloch,
        and D.-S. Lühmann,
        Role of Interactions in ^{87}Rb-^{40}K Bose-Fermi Mixtures in a 3D Optical Lattice,
        Physical Review Letters **102**, 030408 (2009).

[4]   D.-S. Lühmann, K. Bongs, and D. Pfannkuche,
        Excitation spectrum of Mott shells in optical lattices,
        Journal of Physics B: Atomic, Molecular & Optical Physics **42**, 145305 (2009).

[5]   P. T. Ernst, S. Götze, J. S. Krauser, K. Pyka, D.-S. Lühmann, D. Pfannkuche,
        and K. Sengstock,
        Probing superfluids in optical lattices by momentum-resolved Bragg spectroscopy,
        Nature Physics **6**, 56 (2010).

[6]   S. Will, T. Best, U. Schneider, L. Hackermüller, D.-S. Lühmann, and I. Bloch,
        *Time-resolved observation of coherent multi-body interactions in quantum phase
        revivals*,
        Nature **465**, 197 (2010).

Contents

1

Introduction

The Bose-Einstein condensation in dilute gases had been one of the long-known paradigms in physics [7, 8] lacking its experimental realization until 1995 [9–11]. Remarkable properties of this phase are the macroscopic occupation of a single quantum mechanical state, the superfluid behavior, and the existence of a coherent matter wave. The interference of two overlapping condensates [12], the quantization of vortices [13–15], and the evidence of the long-range phase coherence [16] characterize this fascinating state of matter. In dilute gases, the interaction of particles can be reduced to an effective single-particle picture, described by a nonlinear Schrödinger equation, the Gross-Pitaevskii equation [17, 18], where elementary excitations can be included using the Bogoliubov theory. By loading quantum degenerate bosonic atoms in optical lattices, which are periodic potentials generated by retroreflected laser beams, the field of strongly correlated physics with ultracold atoms has become accessible. While for shallow potentials a superfluid phase is formed, in deep lattices the strong repulsion of the atoms leads to a Mott-insulator phase, where the atoms localize at individual lattice sites. By varying the depth of the periodic potential, it was demonstrated in 2002 that a quantum phase transition is observable between the superfluid and the Mott-insulator phase [19]. This transition was predicted in the context of liquid helium on porous media [20] and was later rediscovered for ultracold atoms [21]. In addition to the accurately adjustable lattice depth, the scattering of ultracold atoms can be tuned by Feshbach resonances [22, 23]. Both possibilities establish a perfect model system for solid-state physics with adjustable tunneling and interaction strength.

The precise control of the experimental parameters allows to test common theories in condensed matter physics and to identify their boundaries. Furthermore, the progress in this field might contribute to the investigation of open questions in solid-state physics. A step forward in this direction took place with the achievement of quantum degeneracy for fermionic atoms [24] and the realization of bosonic multicomponent spinor gases [25, 26]. In addition, degenerate Bose-Fermi mixtures [27, 28] present a fascinating complex system, where particles with a different quantum statistics encounter each other. In solids, superconductivity and polarons are prominent examples of boson-fermion physics, where electrons interact with phonons, while in optical lattices [29, 30] bosons and fermions are on an equal footing. This allows to study the interplay of tunneling, intra-, and interspecies interaction in detail. This novel system has attracted various theoretical studies using the Bose-Fermi-Hubbard model [31, 32] and several phases have been predicted. In particular, the phase separation between bosons and fermions competing with the supersolid phase [32–34], the charge-density wave [34, 35], and the pairing of bosons and fermions forming phases of composite particles [36, 37] have been investigated.

In this thesis, several aspects of ultracold atoms in optical lattices are studied with emphasis on finite-size and orbital effects addressed with a multiorbital exact diagonalization technique. Following a basic introduction to the field of cold atoms and optical lattices in the subsequent chapter, in chapter 3 the fundamental question is addressed, how similar small systems are in comparison to macroscopic ones. Applications are systems for quantum information processing [38–40], experiments with double wells [41, 42], and few-sites systems dedicated to the manipulation of single atoms [43, 44]. The precursors of the Mott-insulator transition for commensurate systems and the Bose glass for noncommensurate filling are investigated by means of the excitation spectrum, the momentum distribution, and the pair correlation function, which exhibit surprisingly strong similarities to their macroscopic counterparts. This includes also the formation of Mott-shell configurations in small systems as discussed in chapter 4. In the limit of deep lattices, an approach for vanishing tunneling is presented, where particle fluctuations can be included perturbatively, addressing the excitation spectrum for large systems with arbitrary confining potentials. Using exact diagonalization, changes in the on-site energy in dependence on the particle number are discussed, which are caused by an admixture of higher orbitals.

In chapter 5, it is shown that admixtures of higher orbital states in Bose-Fermi mixtures with attractive interspecies scattering lead to substantial modifications of the commonly used single-band Hubbard model. The mutual interaction of the constituents is studied causing a strong squeezing of the effective orbitals. This behavior leads to a nonlinear self-trapping effect, which is discussed in detail. Calculating the effective potentials experienced by the bosonic atoms, an effective Bose-Hubbard model is presented with renormalized parameters for on-site interaction and tunneling. This model predicts a shift of the critical potential depth of the phase transition from a superfluid to a Mott insulator, which has been found in experiments with Bose-Fermi mixtures in optical lattices [3, 29, 30]. Its dependence on both bosonic filling and interspecies scattering length is addressed and an excellent agreement with a recent experiment [3] is found, which allows to tune the interspecies interaction. The chapter demonstrates, in general, the important role of higher Bloch bands in attractively interacting mixtures.

A promising technique to probe the excitations in optical lattices is Bragg spectroscopy [5, 45–47], which is discussed in chapter 6. For the experimental parameters in Ref. [5], the chapter presents a discussion of interaction induced changes of the band structure for the superfluid phase using the mean-field Bogoliubov description [48–55]. For strongly interacting systems, the dynamic structure factor is examined by exact diagonalization [56]. The fingerprints of the Mott-insulator phase and of possible phases in Bose-Fermi mixtures are addressed.

The multiorbital physics of bosonic atoms in optical lattices can be accessed experimentally in collapse and revival experiments [6, 57–60], where the lattice is rapidly ramped from shallow to deep. The particle number statistics at each site is preserved, which leads to an evolution of the particle number states in accordance to their interaction energy. In chapter 7, exact diagonalization is performed to compute the energy of these highly correlated states and the observable frequencies. The excellent agreement with the measured frequencies in Ref. [6] demonstrates the significance of multiorbital physics in optical lattices and the accuracy of the theoretical calculation.

Ultracold atomic gases in optical lattices

This chapter presents an overview of ultracold atomic gases covering both theoretical and experimental concepts which are relevant to this thesis. The field of ultracold atoms has been rapidly evolving since the first achievement of Bose-Einstein condensation in dilute gases in 1995 [9–11]. Since then, the physics of cold atoms has been established as an important subject in physics with its own branches and subbranches. It remains, however, closely related to atomic, molecular, and solid-state physics. In spite of the fast progress, a number of excellent reviews have been published giving a survey of the research carried out in this area. The detailed understanding of the interaction process of atoms with light is crucial for the cooling of atoms and was addressed, e.g., in Refs. [61–63], while the interaction of neutral atoms was reviewed in Refs. [48, 64–66]. In dilute gases, many-particle interaction effects can usually be reduced to an effective single-particle description, leading to the Gross-Pitaevskii equation. The aspects of weakly interacting quantum gases, based on this equation, were reviewed in the articles [64, 67] and more recently in the books [48, 65]. Additional aspects have also been addressed in review articles, e.g., solitons and propagating condensates [68], one-dimensional gases [66, 69], rotating two-dimensional gases [48, 65, 66], spinor gases [65, 70], Fermi gases [71], and the BEC-BCS crossover [66]. The technical aspects of optical lattices were reviewed, e.g., in Refs. [72, 73], whereas the condensed matter aspects, including the transition from a superfluid to a Mott insulator, are discussed in Refs. [74–76].

This thesis deals with the many-particle aspects of ultracold gases in optical lattices, which usually go beyond a Gross-Pitaevskii mean-field description. In the following, I survey the theoretical background as well as important technical and experimental details. The basic principles of the light-atom interaction are discussed in section 2.1.1, the cooling and trapping of atoms in section 2.1.2, and the generation of optical lattices in section 2.1.3. In contrast to harmonic traps, optical lattices exhibit a band structure known from solids, which is addressed in section 2.1.4. After a survey of the scattering properties of ultracold atoms (section 2.2.1) including Feshbach resonances (section 2.2.2), the Hamiltonian of the system is derived (section 2.3.1) and the Hubbard model is introduced (section 2.3.2). Section 2.4 describes the method of exact diagonalization including the basis generation, two-particle matrix elements, and the one-particle density matrix. Observables reflecting one-particle and two-particle correlations are presented in section 2.5 including experimental detection techniques. Finally, the superfluid phase, the Mott-insulator phase, and the transition between these phases are discussed (section 2.6).

2.1   Cold atoms in optical lattices

2.1.1   Light-atom interaction

The interaction of atoms with light is one of the foundations of quantum optics. The detailed understanding was crucial for the achievement of Bose-Einstein condensation in dilute gases [9–11], in particular, for the cooling and trapping of atoms, which is discussed in section 2.1.2. The Nobel foundation appreciated the outstanding research in this field and awarded S. Chu, C. Cohen-Tannoudji, and W. D. Phillips in 1997 with the Nobel prize in physics for the "development of methods to cool and trap atoms with laser light" [77–80]. In section 2.1.3, the possibility to create optical potentials with laser light is addressed. Particularly, optical lattices establish a new branch in quantum optics with a close connection to solid-state physics.

Here, the basis concepts of the interaction of an atom with a light field are discussed [61, 63, 81]. Instead of treating the light field classically as an electromagnetic wave, it is described quantum mechanically with the restriction to a single mode k_L. This is an excellent approximation for a laser field, where in the ideal case only one or very few modes are occupied by photons. This approach is called dressed atom approach, since atom and light field couple and must be described in a joint quantum mechanical state, or Jaynes-Cummings model. This procedure is advantageous, since the Hamilton operator is time independent and the elementary processes, i.e., absorption and emission, can be easily identified. In principle, also spontaneous emission, which emerges from the coupling with empty modes, can be incorporated. In the following, we assume that the spontaneous emission rates are small and thus the empty modes can be neglected.

Without interaction between the atom and the light field, the Hilbert space separates into the subspace of photons, which is spanned by basis states $|N\rangle$ corresponding to N photons in the mode k_L, and the atomic subspace. A two-level atom can be assumed, since, in general, all other states of the atom are off-resonant to the laser field. These two atomic states are labeled $|g\rangle$ for the ground state and $|e\rangle$ for the excited state with a transition frequency $\hbar\omega_A$. Consequently, the basis of the total noninteracting system is given by $\{|g,N\rangle, |e,N\rangle\}_{N=0,1,\dots}$. Denoting the Hamiltonian of the atom and the laser field $\hat{H}_A$ and $\hat{H}_L$, respectively, it follows

$$
\begin{aligned}
(\hat{H}_L + \hat{H}_A)\,|g,N\rangle &= N\hbar\omega_L, \\
(\hat{H}_L + \hat{H}_A)\,|e,N\rangle &= N\hbar\omega_L + \hbar\omega_A.
\end{aligned}
\tag{2.1}
$$

For typical wavelengths of the laser light, we can assume that the classical electric field associated with the light field is spatially uniform on the scale of the atom. The coupling of the atom with light treated in the dipole approximation is given by

$$
\hat{H}_{AL} = -\hat{\mathbf{d}}\mathbf{E}(\mathbf{r}),
\tag{2.2}
$$

where $\mathbf{E}(\mathbf{r})$ is the electric field and $\hat{\mathbf{d}} = -e\mathbf{r}$ the electric dipole moment operator for the atomic electrons [61, 63]. Thus, the Hamiltonian including the light-atom interaction becomes $\hat{H} = \hat{H}_L + \hat{H}_A + \hat{H}_{AL}$. The coupling is strong, if the detuning between atomic and laser light frequency, denoted as
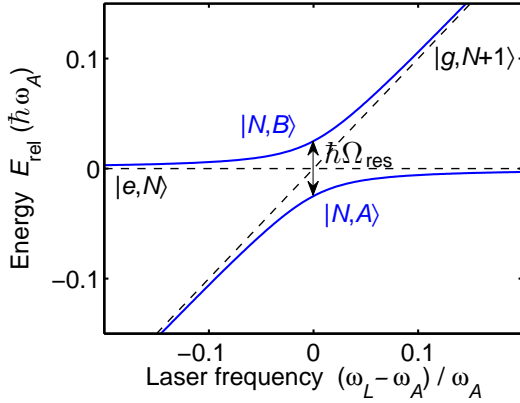
$$
\Delta = \omega_A - \omega_L,
\tag{2.3}
$$

Fig. 2.1: Energy of the dressed atom states $|N, A\rangle = \cos\theta |g, N+1\rangle - \sin\theta |e, N\rangle$ and $|N, B\rangle = \sin\theta |g, N+1\rangle + \cos\theta |e, N\rangle$ as a function of the laser frequency ω_L relative to $N\hbar\omega_L + \hbar\omega_A$, where $\tan(2\theta) = -\Omega_{\mathrm{res}}/\Delta$ and $0 \geq \theta \geq \pi/2$. The asymptotes correspond to the uncoupled states $|g, N+1\rangle$ and $|e, N\rangle$ for $\theta \to 0$ and $\theta \to \pi/2$, respectively.

is small. Near-resonant coupling affects only pairs of states $|g, N+1\rangle$ and $|e, N\rangle$, so that other off-diagonal matrix elements are small. Note that the resonant coupling can be identified with the absorption process $\hat{H}_{AL}|g, N+1\rangle = \frac{1}{2}\hbar\Omega_{\mathrm{res}}|e, N\rangle$ and the process of stimulated emission $\hat{H}_{AL}|e, N\rangle = \frac{1}{2}\hbar\Omega_{\mathrm{res}}|g, N+1\rangle$. The coupling strength is the resonant Rabi frequency Ω_{res}, which is given by

$$\Omega_{\mathrm{res}} = -\langle g|\mathbf{d}|e\rangle\mathbf{E}(\mathbf{r})/\hbar. \tag{2.4}$$

Neglecting off-resonant contributions, the Hamiltonian matrix has a 2×2 block structure. The diagonalization of each block, corresponding to the pair $|g, N+1\rangle$ and $|e, N\rangle$, leads to the eigenvalues

$$E(N) = N\hbar\omega_L + \frac{\hbar}{2}(\omega_A + \omega_L) \pm \frac{\hbar}{2}\Omega, \tag{2.5}$$

where $\hbar\Omega = \hbar\sqrt{\Delta^2 + \Omega_{\mathrm{res}}^2}$ is the energy splitting of each pair of eigenvectors $|N, A\rangle$ and $|N, B\rangle$, the so-called ac Stark shift. The spectrum, which applies to each pair of states, is depicted in Fig. 2.1 in dependence on the laser frequency ω_L. For large detuning from the atomic frequency $\Delta^2 \gg \Omega_{\mathrm{res}}^2$, the coupling is weak and the eigenvectors tend to the unperturbed basis states $|g, N+1\rangle$ and $|e, N\rangle$. In contrast, at resonance $\Delta = 0$ the eigenstates are uniform superpositions of the basis states with an energy splitting $\hbar\Omega_{\mathrm{res}}$.

Since the resonant Rabi frequency Ω_{res} depends on the electric field amplitude, equation (2.5) gives rise to a spatially varying potential for an atom at position $\mathbf{r}$ in the light field. Omitting constant terms, for $|\Delta| \gg \Omega_{\mathrm{res}}$, the expansion of the ac Stark shift (2.5) in a Taylor series to first order in $\Omega_{\mathrm{res}}/\Delta$ gives

$$V(\mathbf{r}) \approx -\frac{\hbar}{2}\frac{\Omega_{\mathrm{res}}^2}{\Delta} = -\frac{1}{2}\alpha(\Delta)|\mathbf{E}(\mathbf{r})|^2, \tag{2.6}$$

where the polarizability is defined by

$$\alpha(\Delta) = \frac{|\langle g|\mathbf{d}\,\mathbf{e_E}|e\rangle|^2}{\hbar\Delta} \tag{2.7}$$

with $\mathbf{e_E}$ being the unit vector in the direction of the electric field. The associated force $\mathbf{F}_{\mathrm{dip}}(\mathbf{r}) = \frac{1}{2}\alpha(\Delta)\nabla|\mathbf{E}(\mathbf{r})|^2$ is called dipole force. For red detuned light ($\omega_L < \omega_A$) the atoms are attracted to the maxima of the electric field, whereas for blue detuned light ($\omega_L > \omega_A$) they are attracted to the minima.

In contrast to expression (2.6), where spontaneous emission processes are neglected, the light field is not fully conservative. The strength of the scattering of an atom with the light field is proportional to Γ^2/Δ^2, where the damping rate Γ of the excited atomic state can be expressed as

$$\Gamma = \frac{\omega_A^3}{3\pi\epsilon_0\hbar c^3} \, |\langle g|\mathbf{d} \, \mathbf{e_E}|e\rangle|^2 \tag{2.8}$$

using a semiclassical approach [63]. A large detuning leads therefore to weak scattering but also to a shallow dipole potential. Thus, the detuning is limited by the maximal laser intensity $I(\mathbf{r})$. Using the damping rate Γ, the dipole potential (2.6) can be written as

$$V_{\text{dip}}(\mathbf{r}) = -\frac{3\pi c^2}{2\omega_A^3} \, \frac{\Gamma}{\Delta} \, \mathbf{I}(\mathbf{r}). \tag{2.9}$$

The possibility to use standing light waves to create periodic potentials is discussed further in section 2.1.3.

2.1.2 Cooling of atoms

While a large detuning of the laser relative to the atomic frequency leads to a conservative dipole force, resonant laser light can be used for a very efficient cooling technique, which is briefly described in the following. Typically, the Bose-Einstein condensation in dilute gases requires densities on the order of 10^{14} cm^{-3} and temperatures below 10^{-5} K [65]. In addition to laser cooling, the atoms must be trapped to increase the atom density and cooled evaporatively. These developments have been reviewed in numerous articles [62, 65, 77–79, 82–85].

The principle of laser cooling is based on the absorption and emission of laser photons [65, 79]. When a two-level atom in its ground state $|g\rangle$ and with momentum $\mathbf{p}_A$ absorbs a photon, the resulting excited atom has a momentum $\mathbf{p}_A + \hbar\mathbf{k}_L$. Subsequently, the atom emits a photon due to spontaneous emission with a decay time $\tau = \Gamma^{-1}$. Of importance is that the momentum of the emitted photon $\hbar\mathbf{k}_s$ has an arbitrary direction, so that averaged over many absorption-emission processes the sum over the recoil momenta cancels. Thus, balancing over many processes results in total momentum transfer to the atom, namely

$$\Delta\bar{\mathbf{p}} = \sum_{i=1}^{N} \hbar\mathbf{k}_L - \sum_{i=1}^{N} \hbar\mathbf{k}_{s,i} \approx N\hbar\mathbf{k}_L. \tag{2.10}$$

The momentum transfer causes an average force, the so-called spontaneous force, which is $\mathbf{F}_s = \frac{\Delta\mathbf{p}}{\Delta t} = \hbar\mathbf{k}_L/t_c$, where t_c is the average time for an absorption-emission cycle.

Typically, the atoms are emitted from a dispenser and counter propagate the laser beam in a so-called Zeeman slower. Laser photons can be absorbed by the atoms only if the Doppler shifted frequency $\omega_{\text{eff}} = \omega_L - \mathbf{k}_L v + O(\mathbf{v}^2)$ equals roughly the atomic transition frequency ω_A. The time for an absorption-emission cycle t_c depends on the saturation of the laser intensity I_L. Using the saturation intensity $I_{\text{sat}} = hc/\lambda^3\tau$, the spontaneous force can be written as [62]

$$\mathbf{F}_S = \frac{\hbar\mathbf{k}_L}{2\tau} \, \frac{I_L}{I_L + [1 + 4\tau^2(\omega_{\text{eff}} - \omega_A)^2] \, I_{\text{sat}}}. \tag{2.11}$$
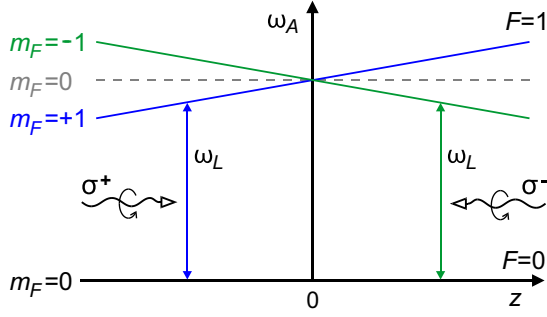
Fig. 2.2: Working principle of a magneto-optical trap. The excited state $|e\rangle$ is split in its hyperfine levels m_F due to a spatially varying magnetic field $\mathbf{B}(\mathbf{r})$.

For infinite laser intensity, the force saturates and becomes $\mathbf{F}_S = \hbar \mathbf{k}_L/2\tau$. This is, however, only valid under the assumption that a closed optical transition exists, which is the reason why Bose-Einstein condensation was firstly achieved for alkali atoms. Due to the Doppler shift only a small fraction of the atoms which have a specific velocity $\mathbf{v}$ can interact with the light beam. In a Zeeman slower an inhomogeneous magnetic field B_z is present causing a tuning of the atomic frequency $\omega_A(B_z)$ due to the Zeeman effect. Thus, passing through the inhomogeneous magnetic field, the spontaneous force slows atoms in all velocity classes by shifting successively all atoms to lower velocities.

Further cooling can be obtained in optical molasses [77, 79, 82, 85], where the precooled atoms are irradiated from six orthogonal spatial directions with red detuned laser light. When counter propagating one of the laser beams, an atom gets in resonance and is slowed due to the spontaneous force. This leads to a further compression in the momentum space, but it does not prevent the atoms from drifting apart in space. To obtain high densities, the atoms are trapped magneto-optically. In the following, let us consider an atom having a ground state with spin $F = 0$ and polarization $m_F = 0$ and a degenerate excited state with $F = 1$ and $m_F = -1, 0, 1$. In a magneto-optical trap, an inhomogeneous magnetic field $\mathbf{B}(\mathbf{r})$ is applied in each spatial direction, which vanishes at the center of the trap. It leads to a spatially varying splitting of the excited state due to $\Delta E(\mathbf{r}) = m_F B(\mathbf{r}) g_F \mu_F$, where μ_F is the magnetic moment and g_F the hyperfine g-factor. In each spatial direction, red detuned σ^+ light is irradiated from the left side, inducing transitions with $\Delta m_F = +1$, and σ^- light from the right side, inducing transitions with $\Delta m_F = -1$ (see Figure 2.2). Due to the magnetic field, atoms on the left hand side from the center with $m_F = +1$ have a lower energy and can interact with the red detuned laser, whereas atoms on the right hand side have a lower energy for $m_F = -1$. Because of the light polarization, the spontaneous force is always directed towards the center of the trap, leading to a compression in space and thus to higher densities.

While the basic principles of the laser cooling are elaborated above, further topics are discussed here only in brief. In particular, it should be noted that the Doppler cooling techniques described above are limited to a lowest temperature $k_B T_{\text{Doppler}} = \hbar/2\tau$, where we find an equilibrium of cooling and heating processes [63, 65, 78]. The Doppler energy $k_B T_{\text{Doppler}}$ is much larger than the recoil energy of a single emission process, which limits the cooling mechanisms fundamentally and is given by

$$E_R = \frac{\hbar^2 k_L^2}{2m}. \tag{2.12}$$

However, the setup of the magneto-optical trap allows an additional cooling below the Doppler limit [65, 78, 82, 85]. For larger detuning, the lasers create a standing wave with a rotating polarization due to the σ^+ and σ^- light. As discussed in the previous section, this leads to a potential, which is in this case shifted by a half period for the different polarizations of the atom. In this potential, the atoms loose kinetic energy when moving from a minimum upwards to a maximum. At the maximum, they decay into the state with the other atomic polarization, which has a minimum in its potential, and so on. This mechanism is called Sisyphus cooling. Furthermore, several cooling techniques have been proposed to cool even below the recoil limit, such as the velocity-selective coherent population trapping [78]. In experiments, the evaporative cooling is often used to obtain low temperatures and high densities simultaneously [84]. For this technique a finite magnetic trap is used to remove selectively high-energetic atoms from the atomic cloud. The atoms rethermalize due to scattering, which is strongly suppressed for a single component fermionic gas that must therefore be cooled sympathetically with a different spin component or a different atomic species. The major drawback of evaporative cooling is the high loss of atoms, which reduces the atom number typically to few percents.

2.1.3 Optical potentials

In section 2.1.1, it is shown that detuned laser light with respect to the atomic frequency establishes an optical potential for atoms. In particular, equation (2.9) states that the strength of the optical potential depends on the detuning and the intensity of the laser field. The intensity profile of a laser is commonly approximated by a Gaussian profile, namely

$$I(x,y,z) = \frac{2P}{\pi W^2(z)} e^{-2(x^2+y^2)/W^2(z)} \tag{2.13}$$

for a laser beam propagating in z direction, where P is the power of the laser [63]. The Gaussian beam waist $W(z) = W_0\sqrt{1 + z^2/z_R^2}$ corresponds to the radius, where the electric field reaches $1/e$ of its maximal value. The minimal beam waist W_0 is typically around $100\ \mu$m. The laser beam has a finite divergence on the scale of the Rayleigh length $z_R = W_0^2\pi/\lambda$, which is usually much larger than the beam waist. Using equation (2.9) and (2.13), the expansion in a Taylor series leads to a dipole trapping potential

$$V(x,y,z) \approx -V_{\mathrm{dip}}^0 \left(1 - \frac{x^2+y^2}{W_0^2/2} - \frac{z^2}{z_R^2}\right), \tag{2.14}$$

for red detuned light, where $V_{\mathrm{dip}}^0 = |V_{\mathrm{dip}}(I = 2P/\pi W_0^2)|$. The trapping frequencies are consequently given by $\omega_x^2 = \omega_y^2 = 4V_{\mathrm{dip}}^0/mW_0^2$ and $\omega_z^2 = 2V_{\mathrm{dip}}^0/mz_R^2$. In particular, optical trapping is desirable when magnetic trapping is not possible, e.g., when the magnetic field is used to address spin degrees of freedom or to manipulate the atomic interactions via Feshbach resonances (see section 2.2.2).

Another application of light potentials are optical lattices, which are created by two counter-propagating laser beams. The interference of the electromagnetic field gives rise to a standing
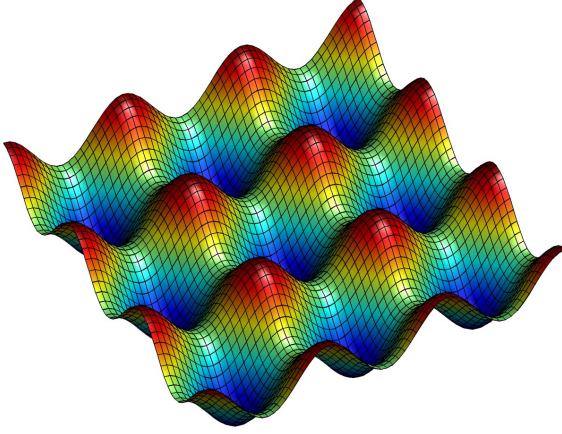
Fig. 2.3: Sinusoidal potential $V_P(x,y) = -V_{0,x} \cos^2(kx) - V_{0,y} \cos^2(ky)$ of a two-dimensional optical lattice.

wave with the periodicity $a = \lambda/2$, where $\lambda = 2\pi/k$ is the wavelength of the laser. Assuming Gaussian beams, it follows immediately for the superposition of the electric fields

$$
\begin{aligned}
\mathbf{E}(\mathbf{r},t) &= E_{0,z}\, \mathbf{e}_x\, e^{-\frac{x^2+y^2}{W^2(z)}} \left(e^{ikz-i\omega t} + e^{-ikz-i\omega t} \right) \\
&= 2E_{0,z}\, \mathbf{e}_x\, e^{-\frac{x^2+y^2}{W^2(z)}} \cos(kz) e^{-i\omega t},
\end{aligned}
\tag{2.15}
$$

where the polarization is in x direction. Neglecting the finite Rayleigh length, the one-dimensional periodic lattice potential is given by

$$
V(x,y,z) = -V_0\, e^{-2(x^2+y^2)/W_0^2} \cos(kz),
\tag{2.16}
$$

where $V_0 = 4V_{\mathrm{dip}}^0$. Note that for red detuned light the sites of the lattice are confined orthogonal to the standing waves due to the finite beam waist.

In two dimensions, a lattice can be generated by two perpendicular pairs of counter-propagating laser beams. For orthogonal polarization of the electric fields no additional interference terms appear, so that a sinusoidal two-dimensional lattice is formed as depicted in Fig. 2.3. Accounting for the confinement in the third direction, one obtains a two-dimensional array of one-dimensional tubes. For sufficiently deep potentials, the tunneling within the lattice plane is negligible, which allows to study strongly correlated one-dimensional atomic gases in the tubes, i.e., the investigation of Luttinger liquids and, in particular, Tonk-Girardeau gases [66, 69].

Using counter propagating laser beams with orthogonal polarizations in three perpendicular directions, a potential

$$
\begin{aligned}
V(\mathbf{r}) = &- V_{0,x} e^{-2\frac{y^2+z^2}{W_0^2}} \cos^2(kx) - V_{0,y} e^{-2\frac{x^2+z^2}{W_0^2}} \cos^2(ky) \\
&- V_{0,z} e^{-2\frac{x^2+y^2}{W_0^2}} \cos^2(kz)
\end{aligned}
\tag{2.17}
$$

is generated, which establishes a three-dimensional optical lattice. Thereby, identical beam waists W_0 are used and the effect due to the Rayleigh length, which is typically much larger than the beam profile, is neglected. Since the potential is not separable in its spatial dimensions, it is preferable to split it into a purely sinusoidal part $V_P(\mathbf{r})$ and a confinement potential $V_C(\mathbf{r})$, i.e.,

$$
V(\mathbf{r}) = V_P(\mathbf{r}) + V_C(\mathbf{r}).
\tag{2.18}
$$

This can be motivated by expanding the exponential functions in equation (2.17) in Taylor series and neglecting the oscillating fraction in the confinement to obtain a harmonic potential. This approach is only valid for large W_0 and leads to a separation of the slowly varying potential from the oscillating one. The purely periodic potential is given by

$$V_P(\mathbf{r}) = -V_{0,x} \cos^2(kx) - V_{0,y} \cos^2(ky) - V_{0,z} \cos^2(kz), \tag{2.19}$$

and the trapping potential is commonly written as

$$V_C(\mathbf{r}) = \frac{1}{2}m(\omega_x^2 x^2 + \omega_y^2 y^2 + \omega_z^2 z^2). \tag{2.20}$$

In many setups, the confinement due to the beam profile is superposed by an additional magnetic or optical dipole trap with frequencies ω_{d,x_i}, so that the total confinement frequency in z direction is $\omega_z^2 = 4(V_{0,x} + V_{0,y})/mW_0^2 + \omega_{d,z}^2$ and respectively for the other directions. In the case of blue detuned laser beams the atoms are trapped in the nodes of the electric field rather than in the antinodes and the finite beam waist leads therefore to an anticonfinement, which can be compensated by additional magnetic or optical trapping.

In theoretical approaches, the confinement V_C is often neglected to derive analytical expressions, to use periodic boundary conditions, or to simplify the problem. In fact, periodic potentials are well studied in the context of solid-state physics. The additional confinement presents a new challenge in the application of theoretical methods, which is addressed, in particular, in chapter 4. Often, however, the confinement is weak enough so that the physics of the purely periodic system is not greatly disturbed.

The discussion above is based on the assumption that the electric fields of the perpendicular laser beams are superposed with orthogonal polarization. By varying the angles and the polarization of the beams, a multitude of lattice structures can be realized. In addition, light fields that are less detuned with respect to the atomic frequencies can establish potentials, which depend on the polarization of the hyperfine levels. Such spin-dependent optical lattices can, e.g., be obtained using counter propagating laser beams with polarizations that enclose a specific angle [38, 72, 86]. In particular, the realization of optical lattices with a double-well unit cell [41] has many applications. If the interwell dynamics can be neglected in such a system, a finite few-particle system emerges resembling double-quantum-dots. The independent tuning of intra- and interwell tunneling yields many possibilities for new experimental techniques [87, 88]. Of course, the concept can be extended to more complicated sub- and superlattice structures [89].

2.1.4 Band structure of optical lattices

In the following, an infinite cubic lattice is considered with a potential of the form (2.19). Since the potential is separable in its spatial coordinates, the solution of the single-particle Schrödinger equation separates in $\phi_x(x)\phi_y(y)\phi_z(z)$. Consequently, it is sufficient to restrict the following discussion to the solution $\phi(z)$ of the one-dimensional Schrödinger equation, which is given by

$$\left(\frac{\hat{p}^2}{2m} - V_0 \cos^2(k_L z) \right) \phi(z) = E\phi(z), \tag{2.21}$$
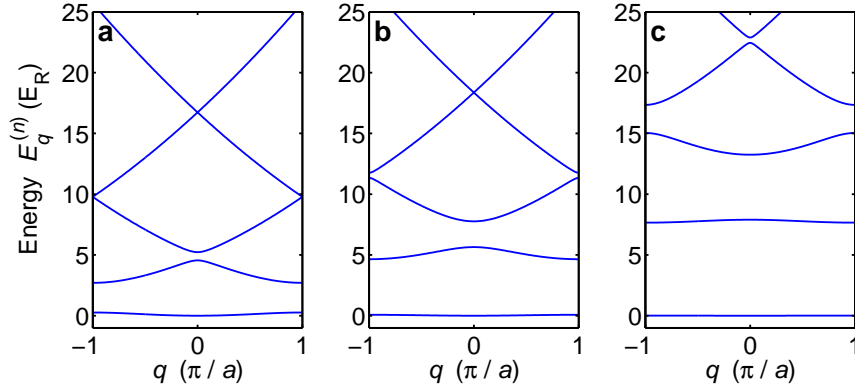
Fig. 2.4: Band energies $E_q^{(n)}$ as a function of the quasimomentum q for (a) $V_0 = 5E_R$, (b) $V_0 = 10E_R$, and (c) $V_0 = 20E_R$.

where $\hat{p} = -i\hbar\frac{\partial}{\partial z}$ and V_0 is positive. Applying Bloch's theorem for periodic potentials, $\phi(z)$ can be written as a Bloch function

$$\phi_q^{(n)}(z) = e^{iqz}u_q^{(n)}(z), \tag{2.22}$$

where n is the band index and q is the quasimomentum. The function $u_q^{(n)}(z)$ is periodic on the interval $[-a/2, a/2]$ with the lattice spacing $a = \pi/k_L$. The reciprocal lattice vector in momentum space is given by $G = 2\pi/a = 2k_L$ and defines the size of the Brillouin zone, which contains the momenta q with $-G/2 \leq q \leq G/2$. Since the $u_q^{(n)}$ are periodic functions, the Bloch functions can be written as Fourier series

$$\phi_q^{(n)}(z) = e^{i\tilde{q}Gz}\sum_k c_k e^{ikGz} \tag{2.23}$$

with the dimensionless quasimomentum $\tilde{q} = q/G$. Further, the periodic potential can be decomposed in

$$V_P(z) = \sum_m \nu_m e^{imGz}. \tag{2.24}$$

By inserting the Fourier series (2.23) and (2.24) in equation (2.21) and by comparison of coefficients, it follows the algebraic equation

$$\frac{\hbar^2 G^2}{2m}(k+\tilde{q})^2 c_k + \sum_m c_{k-m}\nu_m = E_q^{(n)}c_k. \tag{2.25}$$

The term $\hbar^2 G^2/2m$, arising from the kinetic energy operator, equals four times the recoil energy

$$E_R = \frac{\hbar^2 k_L^2}{2m}, \tag{2.26}$$

which was earlier defined in equation (2.12) and consequently provides the natural energy scale for optical lattices. For $V_P(z) = -V_0 \cos^2(k_L z)$, the only nonzero contributions in equation (2.24) are $\nu_0 = -V_0/2$ and $\nu_{\pm 1} = -V_0/4$, so that the single-particle energy $E_q^{(n)}$, corresponding to the quasimomentum q of the nth Bloch band, can be determined by the eigenvalue equation

$$4E_R(k+\tilde{q})^2 c_k - \frac{V_0}{4}c_{k-1} - \frac{V_0}{4}c_{k+1} = E_q^{(n)}c_k, \tag{2.27}$$
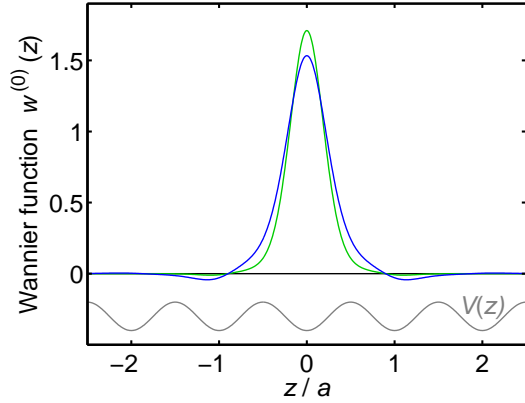
Fig. 2.5: Wannier functions for $V_0 = 5E_R$ (blue) and $V_0 = 10E_R$ (green). The gray line depicts the shape of the lattice potential.

where the constant diagonal term $-V_0/2$ is omitted. Equation (2.27) is solved via diagonalization of a matrix equation with $k = -k_0, ..., k_0$, where, in practice, $k_0 \approx 10$ gives precise results for the lowest bands.

Instead of using delocalized Bloch functions, a Wannier basis [74, 75] is preferred in the context of Hubbard models (section 2.3.2). If the phases of the Bloch functions are properly chosen, the Wannier functions are optimally localized at the lattice sites j and are defined by

$$w^{(n)}(z - z_j) = \frac{1}{\sqrt{N_s}} \sum_q e^{-iqz_j} \phi_q^{(n)}(z),$$
(2.28)

where N_s is the number of lattice sites. In the reverse direction, the Bloch functions can be written in terms of Wannier functions as follows

$$\phi_q^{(n)}(z) = \frac{1}{\sqrt{N_s}} \sum_j e^{iqz_j} w^{(n)}(z - z_j).$$
(2.29)

For infinitely deep lattices the Wannier functions tend to the wave functions of the harmonic oscillator, which is often used as an approximation in analytical calculations.

2.2   Scattering theory of ultracold atoms

2.2.1   Interaction of neutral atoms

The scattering of neutral atoms is, in principle, a complicated many-body problem. In particular, the short-range scattering physics, where the electron shells of the atoms start to overlap, is a subject of nontrivial molecular physics. Fortunately, the long-range behavior can be captured in a rather simple model which is discussed in this section. In addition, for ultracold atoms only scattering states with an angular momentum $l = 0$ (s-wave) for bosons and $l = 1$ (p-wave) for fermions have to be taken into account. Particularly, the s-wave scattering for fermions is strictly forbidden by Pauli's exclusion principle, since two fermions can not be identical in all quantum numbers. For cold atoms in the sub-millikelvin regime, the energy of the relative motion

is usually below the centrifugal barrier of the effective potential for nonzero angular momentum. Therefore, the s-wave scattering dominates for bosons and for fermions p-wave collisions remain as the lowest order. Since usually the p-wave scattering is weak, ultracold fermionic atoms can be treated as noninteracting particles in many approaches. Of course, the situation changes for dipolar atoms, which have been experimentally addressed, e.g., in Refs. [90–94].

The long-range behavior can be described by the lowest-order van-der-Waals potential [64]

$$V_{\text{vdW}}(r) = -C_6/r^6 \qquad \text{for } r > r_c, \tag{2.30}$$

where r is the distance between two scattering atoms. The short-range cut-off is defined by the length r_c, which is on the order of the atom size. The simplest approach is to model the short-range part ($r \leq r_c$) as a hard-core potential, which is of course not very realistic but still captures the basic features. The van-der-Waals length is defined by

$$r_0 = (2m_r C_6/\hbar^2)^{1/4} \tag{2.31}$$

and is the typical extend of the last bound state in the potential, where m_r is the reduced mass. The length r_0 is the distance at which the relative part of the kinetic energy equals the interaction of the two particles. For alkali atoms, the length is on the order of 5 nm [64] being much larger than the atomic scale r_c but much smaller than the average particle distance. At low energies, the scattering can be characterized by the s-wave scattering length a. Using a hard-core potential for $r \leq r_c$, the scattering length can be calculated analytically [95]

$$a = \bar{a}\left[1 - \tan(\Phi - 3\pi/8)\right], \tag{2.32}$$

where $\bar{a} = 0.478 r_0$ and $\Phi = r_0^2/2r_c^2$ is the so-called WKB phase [66]. The scattering length depends on the van-der-Waals length r_0 but also on the WKB phase Φ, which is sensitive to the short-range parameter r_c. The atoms interact attractively for positive values of a and repulsively for negative values. The true interaction potential has one or several bound states in either case, which leads to the possibility of molecule formation. However, this process occurs only via three-body collisions for low energy scattering. The scattering can be expressed in terms of a pseudopotential [65]

$$V(\mathbf{x}) = \frac{4\pi\hbar^2 a}{2m_r} \delta(\mathbf{x}) \frac{\partial}{\partial r} r, \tag{2.33}$$

which depends exclusively on the scattering length (2.32). Assuming regular wave functions at $r = 0$, the pseudopotential simplifies because of the δ function to

$$V(\mathbf{x}) = \frac{4\pi\hbar^2 a}{2m_r} \delta(\mathbf{x}). \tag{2.34}$$

This form of the potential implies that particles interact only at coincident coordinates. Although this approach neglects completely the inner part of the interaction potential, it provides a good description of the long range scattering of ultracold atoms and is valid at typical densities.
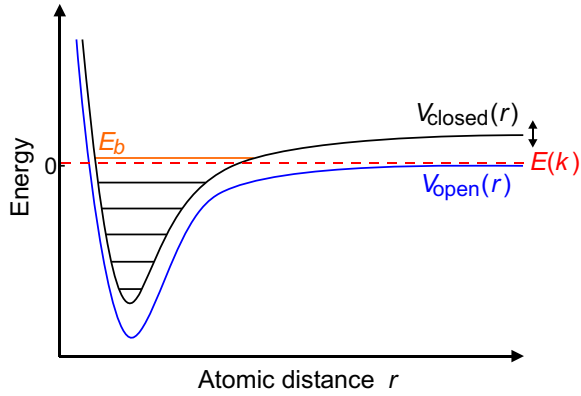
Fig. 2.6: The interaction potentials of the open and closed channel are $V_{\text{open}}(r)$ and $V_{\text{closed}}(r)$, respectively. Feshbach resonances occur when a bound state in a closed channel with the energy $E_b(B)$ is in resonance with the dissociation energy of the open channel.

2.2.2 Feshbach resonances

Optical lattices offer an ideal testing ground for condensed matter theories, due to the controllability and tunability of optical potentials. In addition, experiments with ultracold gases allow to tune the interaction of particles by means of Feshbach resonances. The scattering length is adjustable over a wide range from strongly attractive to strongly repulsive, which provides unique possibilities. The underlying concept was originally introduced by Feshbach [96] in the context of compound nucleus reactions and by Fano [97] for the description of multielectron atoms. In experiments with ultracold atoms, the scattering can be tuned by changing the magnetic field, due to different magnetic moments of the involved molecular states, which allows an easy and precise control. Experiments using Feshbach resonances have been realized in this context in Refs. [22, 23] and recently in more and more experimental setups. However, e.g., for the investigation of spinor condensates, the magnetic field is already an experimental parameter controlling the dynamics. In this case, Feshbach resonances can also be induced optically via one- and two-photon transitions [98–100]. Spontaneous emission resulting from this technique might, however, cause an additional heating of the atomic gas. Reviews on this subject are given in Refs. [101–103].

Feshbach resonances occur when a closed scattering channel and a bound state in an open channel couple resonantly as depicted in Fig. 2.6. The two channels correspond, e.g., to two different spin configurations, i.e., a singlet and a triplet state. Scattering without a Feshbach resonance corresponds to the open channel, where the atoms experience the unaltered scattering potential $V_{\text{open}}(r)$. This potential leads to the so-called background scattering length a introduced in the last section and denoted here a_{bg}. At large distances $r \to \infty$, the potential is chosen to be zero, so that only the kinetic energy of the relative motion

$$E(k) = \frac{\hbar^2 k^2}{2m_r} \tag{2.35}$$

remains, where m_r is the reduced mass. The potential of the closed channel $V_{\text{closed}}(r)$ at $r \to \infty$ is assumed to be larger than the thermal energy for the ultracold collision and is therefore not accessible.

For alkali atoms this potential difference arises from the Zeeman and the hyperfine energy of

coupled states. In the presence of a magnetic field $\mathbf{B}$ along one axis this energy emerge originally from the Hamiltonian of a single atom

$$\hat{H}_B = a_{\text{hf}} \, \hat{\mathbf{S}} \, \hat{\mathbf{I}} + 2\mu_B B \hat{S}_z - \mu_n B \hat{I}_z, \tag{2.36}$$

where $\hat{\mathbf{I}}$ is the operator of the nuclear spin and $\hat{\mathbf{S}}$ the spin operator of the single valence electron [101], assuming zero orbital momentum. The Bohr magneton is labeled by μ_B and is much larger than the nuclear magneton μ_n. For large magnetic fields (Paschen-Back regime), the Hamiltonian has eigenstates labeled by the quantum numbers m_s and m_I, which are the projections of electron and nuclear spin, respectively, rather than by the coupled hyperfine spin quantum number f and its projection m_f (Zeeman regime). Because of the large Bohr magneton, states with $m_s = -1/2$ have a much lower energy in the Paschen-Back regime and are energetically well-separated from the $m_s = 1/2$ states. Atoms, prepared in the $m_s = -1/2$ states, form molecular orbitals during the collision. The respective molecular potentials show a van-der-Waals behavior at large distances but can considerably differ from each other at short distances. Moreover, the potentials are offset at $r \to \infty$ due to the hyperfine and Zeeman energy (Fig. 2.7).

Let us assume only one closed channel, which is valid for the description of an isolated Feshbach resonance. As depicted in Fig. 2.6, two molecular potentials form an open and a closed channel. The effective scattering in the open channel can be strongly modified due to a strong coupling of valence electrons. The atoms can temporarily be captured in a quasibound state in the closed channel. As usual, the coupling of the two channels [102–104] can be described in a Hamiltonian of the form

$$\hat{H} = \begin{pmatrix} \hat{E}_{\text{kin}} + V_{\text{open}}(r) & W(r) \\ W(r) & \hat{E}_{\text{kin}} + V_{\text{closed}}(r) \end{pmatrix}, \tag{2.37}$$

where $\hat{E}_{\text{kin}}$ is the kinetic energy operator and $W(r)$ is the coupling between open and closed channel, which is nonzero on the order of the atomic scale r_c. Typically, the magnetic moments of the open channel μ_{open} and closed channel μ_{closed} differ by $\Delta\mu$. The tunability of the Feshbach resonance enters, since a change in the magnetic field by δB shifts the open channel by an energy $\Delta\mu \, \delta B$. At $B = B_{\text{res}}$ the bound state in the closed channel shall be exactly in resonance with the open channel at $r \to \infty$. For large background scattering, the exact solution for the Hamiltonian (2.37) leads, however, to a shifted magnetic field B_0 at which the scattering amplitude diverges. Approximately, it is related to the *bare* magnetic field B_{res} by

$$B_0 \approx B_{\text{res}} + \Delta B \frac{(1-x)x}{(1-x)^2 + 1}, \tag{2.38}$$

where $x = a_{\text{bg}}/\bar{a}$ and ΔB is defined in equation (2.42) [105]. In the vicinity of B_0 the energy of the bound state is given by

$$E_b(B) = \Delta\mu \, (B - B_0). \tag{2.39}$$

The nearly resonant scattering of a continuum state with a bound state for a low-energetic particle is known as Breit and Wigner problem and leads to a resonant shift of the scattering phase by

$$\delta_{\text{res}}(k) = -\text{atan} \left(\frac{\Gamma(k)/2}{E(k) - E_b(B)} \right) \tag{2.40}$$
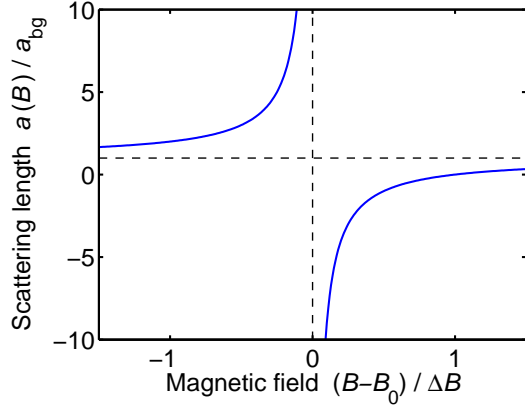
Fig. 2.7: Magnetic field dependence of the scattering length $a(B)$ due to an isolated Feshbach resonance. According to equation (2.43), $a(B)$ depends on the magnetic resonance position B_0, its width ΔB, and the background scattering a_{bg}.

with the resonance width $\Gamma(k)$ [66]. The resonance width for small k is linear, which allows to define a characteristic length r^* by

$$\Gamma(k \rightarrow 0) = \frac{\hbar^2 k}{m_r r^*}. \tag{2.41}$$

Its inverse $1/r^*$ is a measure how strong the two channels are coupled. The total scattering length, due to the resonant phase shift δ_{res} and the background phase shift δ_{bg}, is $a = \lim_{k\to 0} \tan(\delta_{\mathrm{bg}} + \delta_{\mathrm{res}})/k$. Defining the width of a Feshbach resonance as

$$\Delta B = \frac{\hbar^2}{2 m_r r^* a_{\mathrm{bg}} \mu} \tag{2.42}$$

leads to a simple expression for the magnetic-field-dependent scattering length

$$a(B) = a_{\mathrm{bg}} \left(1 - \frac{\Delta B}{B - B_0} \right). \tag{2.43}$$

With the assumptions above, the position B_0 and the width ΔB of a Feshbach resonance together with the background scattering a_{bg} give therefore full information on the scattering amplitude $a(B)$ as depicted in Fig. 2.7. In particular, these parameters are experimentally well accessible. Therefore, Feshbach resonances are an excellent tool for tunable interactions applicable to a wide range of atoms. It should be noted that this also includes scattering between different atomic species.

2.3 Hamiltonian for spin-polarized atoms

2.3.1 Hamiltonian for bosons and fermions

As discussed in section 2.2.1, the interaction between neutral atoms can in good approximation be captured by a δ interaction potential

$$V_{\mathrm{int}}(\mathbf{r}, \mathbf{r}') = g\, \delta(\mathbf{r} - \mathbf{r}'), \tag{2.44}$$

where $\mathbf{r}$ and $\mathbf{r}'$ are the coordinates of two scattering atoms. The scattering constant g is given in equation (2.34), namely

$$g = \frac{4\pi\hbar^2 a_s}{2m_r}, \tag{2.45}$$

with a_s being the s-wave scattering length and m_r the reduced mass. For ^{87}Rb atoms the s-wave scattering length is $a_s \approx 100a_0$. Although ^{87}Rb is one of the most frequently used species for Bose-Einstein condensates, the value for a_s given by recent calculations varies, i.e., $(100.4 \pm 0.1)a_0$ in Ref. [106] and $(102.4 \pm 0.5)a_0$ in Ref. [107]. For identical particles, i.e., $m_r = m_{\mathrm{B}}/2$ the interaction potential reads

$$V_{\mathrm{int}}(\mathbf{r}, \mathbf{r}') = \frac{4\pi\hbar^2 a_s}{m_{\mathrm{B}}} \delta(\mathbf{r} - \mathbf{r}'). \tag{2.46}$$

For the further treatment, the potential is translated into the language of second-quantization, assuming bosonic particles. Using the bosonic field operator $\hat{\psi}_{\mathrm{B}}(\mathbf{r})$, which creates a particle at coordinate $\mathbf{r}$, and its hermitian conjugate $\hat{\psi}_{\mathrm{B}}^\dagger(\mathbf{r})$, which annihilates a particle at $\mathbf{r}$, the two-particle interaction reads

$$\frac{1}{2} g \int d^3r \, d^3r' \, \hat{\psi}_{\mathrm{B}}^\dagger(\mathbf{r})\hat{\psi}_{\mathrm{B}}^\dagger(\mathbf{r}') \, \delta(\mathbf{r} - \mathbf{r}') \, \hat{\psi}_{\mathrm{B}}(\mathbf{r}')\hat{\psi}_{\mathrm{B}}(\mathbf{r}). \tag{2.47}$$

Including the kinetic and potential single-particle energies, the Hamiltonian is given by

$$\hat{H}_{\mathrm{B}} = \int d^3r \, \hat{\psi}_{\mathrm{B}}^\dagger(\mathbf{r}) \left[\frac{\hat{\mathbf{p}}^2}{2m_{\mathrm{B}}} + V_P(\mathbf{r}) + V_C(\mathbf{r}) + \frac{g}{2}\hat{\psi}_{\mathrm{B}}^\dagger(\mathbf{r})\hat{\psi}_{\mathrm{B}}(\mathbf{r}) \right] \hat{\psi}_{\mathrm{B}}(\mathbf{r}). \tag{2.48}$$

Here, by the virtue of equation (2.18), the single-particle potential of the optical lattice is split into a periodic sinusoidal potential $V_P(\mathbf{r})$ and a slowly varying confinement $V_C(\mathbf{r})$.

As already mentioned, the interaction of spin-polarized ultracold fermions is relatively small and can be neglected in most approaches. Consequently, the Hamiltonian for fermions is a one-particle operator containing kinetic and potential energy, namely

$$\hat{H}_{\mathrm{F}} = \int d^3r \, \hat{\psi}_{\mathrm{F}}^\dagger(\mathbf{r}) \left[\frac{\hat{\mathbf{p}}^2}{2m_{\mathrm{F}}} + V_P^{\mathrm{F}}(\mathbf{r}) + V_C^{\mathrm{F}}(\mathbf{r}) \right] \hat{\psi}_{\mathrm{F}}(\mathbf{r}) \tag{2.49}$$

using the fermionic field operator $\hat{\psi}_{\mathrm{F}}(\mathbf{r})$. The potential $V_P^{\mathrm{F}}(\mathbf{r}) + V_C^{\mathrm{F}}(\mathbf{r})$ is not necessarily the same as for bosons, as it depends on the detuning of atomic and laser frequency. An interesting and nontrivial situation emerges when the fermionic atoms are loaded together with bosonic atoms in an optical lattice. Due to the interaction between fermions and bosons, the fermionic subsystem responses to the bosonic one and vice versa. The interaction between bosons and fermions can be expressed by

$$\hat{H}_{\mathrm{BF}} = g_{\mathrm{BF}} \int d^3r \, \hat{\psi}_{\mathrm{B}}^\dagger(\mathbf{r})\hat{\psi}_{\mathrm{F}}^\dagger(\mathbf{r})\hat{\psi}_{\mathrm{F}}(\mathbf{r})\hat{\psi}_{\mathrm{B}}(\mathbf{r}), \tag{2.50}$$

due to the s-wave scattering of distinguishable particles with

$$g_{\mathrm{BF}} = \frac{2\pi\hbar^2}{m_{\mathrm{BF}}} a_{\mathrm{BF}}, \tag{2.51}$$

the boson-fermion scattering length a_{BF}, and the reduced mass $m_{BF} = m_B m_F / (m_B + m_F)$. Hence, the total Hamiltonian for a Bose-Fermi mixture of atoms is

$$\hat{H} = \hat{H}_B + \hat{H}_F + \hat{H}_{BF}. \tag{2.52}$$

For explicit calculations, the bosonic and fermionic field operators are expanded in the spatial bases

$$\hat{\psi}_B(\mathbf{r}) = \sum_i \chi_i(\mathbf{r}) \hat{b}_i, \tag{2.53}$$

and

$$\hat{\psi}_F(\mathbf{r}) = \sum_i \phi_i(\mathbf{r}) \hat{f}_i, \tag{2.54}$$

respectively. Thereby, $\hat{b}_i$ annihilates a bosonic atom in the state with the wave function $\chi_i(\mathbf{r})$ and $\hat{f}_i$ annihilates a fermionic atom in the state $\phi_i(\mathbf{r})$.

2.3.2 The Hubbard model

The idea of the Hubbard model is to describe the physics in a lattice by the tunneling of particles to neighboring sites and by the interaction particles experience when occupying the same site. To realize this model basis functions are used that are optimally localized at the lattice sites, which are the Wannier functions given in equation (2.28). The starting point for discussing the Bose-Hubbard model [20, 21, 75] is the full bosonic Hamiltonian (2.48), which is expanded according to equation (2.53) in a Wannier basis of the lowest band $w^{(0)}(\mathbf{r} - \mathbf{r}_j)$. Commonly higher bands are neglected as the on-site interaction is considerably smaller than the band gap to the first excited band. The influence of higher bands, which leads to remarkable modifications of the single-band Hubbard physics, is discussed in chapters 4, 5, and 7. Using the lowest-band Wannier basis, the Hamiltonian can be written as

$$\hat{H}_B = -\sum_{i,j} J_{ij} \hat{b}_i^\dagger \hat{b}_j + \frac{1}{2} \sum_{i,j,k,l} U_{ijkl} \hat{b}_i^\dagger \hat{b}_j^\dagger \hat{b}_k \hat{b}_l, \tag{2.55}$$

where

$$J_{ij} = -\int d^3r\, w^{(0)*}(\mathbf{r} - \mathbf{r}_i) \left(\frac{\hat{\mathbf{p}}^2}{2m_B} + V_P(\mathbf{r}) + V_C(\mathbf{r}) \right) w^{(0)}(\mathbf{r} - \mathbf{r}_j) \tag{2.56}$$

and

$$U_{ijkl} = g \int d^3r\, w^{(0)*}(\mathbf{r} - \mathbf{r}_i) w^{(0)*}(\mathbf{r} - \mathbf{r}_j) w^{(0)}(\mathbf{r} - \mathbf{r}_k) w^{(0)}(\mathbf{r} - \mathbf{r}_l). \tag{2.57}$$

Since the Wannier functions are well localized in deep lattices (commonly this assumes $V_0 \gtrsim 5E_R$), the hopping integral J_{ij} of nonnearest neighbors is small and $U_{iiii} \gg U_{ijkl}$ for not all $\{i, j, k, l\}$ equal. Neglecting these minor terms, this leads to the Hamiltonian of the Bose-Hubbard model

$$\hat{H}_{BHM} = -J \sum_{\langle i,j \rangle} \hat{b}_i^\dagger \hat{b}_j + \frac{1}{2} U \sum_i \hat{n}_i (\hat{n}_i - 1) + \sum_i \epsilon_i \hat{n}_i, \tag{2.58}$$
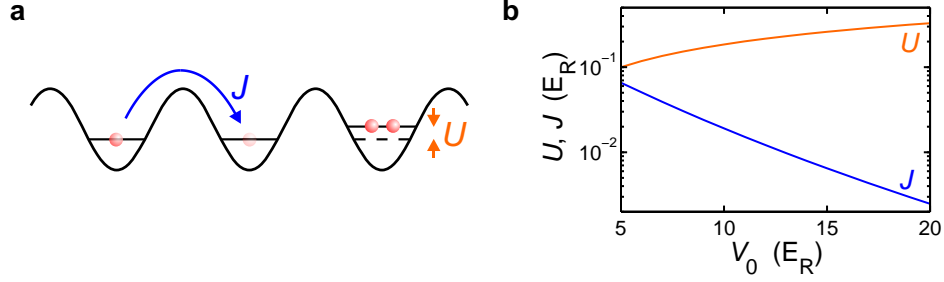
Fig. 2.8: (a) The Bose-Hubbard model with the hopping integral J and the on-site interaction U. (b) The Bose-Hubbard parameter J and U as a function of the lattice depth V_0 for ^{87}Rb and a lattice spacing $a = \pi/k_L = 515$ nm.

due to $\hat{b}_i^\dagger \hat{b}_i^\dagger \hat{b}_i \hat{b}_i = \hat{n}_i(\hat{n}_i - 1)$. Thereby, $\langle i, j \rangle$ denotes the sum over nearest neighbors with the hopping integral

$$J \equiv J_{01} = -\int d^3r \, w^{(0)*}(\mathbf{r}) \left(\frac{\hat{\mathbf{p}}^2}{2m_B} + V_P(\mathbf{r}) \right) w^{(0)}(\mathbf{r} - a\,\mathbf{e}_k) \qquad (2.59)$$

for $V_C(\mathbf{r}) = 0$ with a the lattice constant and $\mathbf{e}_k$ the unit vector along one of the lattice axes. In principle, J may depend on the direction so that, in general, $J_x \neq J_y \neq J_z$. In the following, however, the lattice is assumed to be isotropic. The last term in the Hamiltonian (2.58) arises from the term J_{ii} and describes the slowly varying confinement $V_C(\mathbf{r})$, where $\epsilon_i \approx V_C(\mathbf{r}_i)$, whereas other contributions of J_{ii} lead to a constant offset energy. The full interaction integral (2.57) is approximated by the on-site interaction

$$U \equiv U_{0000} = g \int d^3r \, |w^{(0)}(\mathbf{r})|^4. \qquad (2.60)$$

For a homogeneous lattice, the Bose-Hubbard model therefore depends only on the two parameters U and J. While U describes the interaction of particles at the same site, J reflects the gain in kinetic energy due to the tunneling of particles. Qualitatively, the absolute value of the on-site interaction U increases with increasing lattice depth, whereas the hopping J decreases roughly exponentially. Their quantitative dependency is shown in Fig. 2.8b and analytical expressions are given in equation (2.117) and (2.118).

The same approach can be used to derive the Bose-Fermi-Hubbard model [31, 32] from the full Hamiltonian (2.52). Using the parameters J_B and J_F for bosonic and fermionic tunneling, respectively, U_B for the bosonic on-site interaction, and

$$U_{BF} = g_{BF} \int d^3r \, \left| w_B^{(0)}(\mathbf{r} - \mathbf{r}_i) w_F^{(0)}(\mathbf{r} - \mathbf{r}_i) \right|^2 \qquad (2.61)$$

for the boson-fermion on-site interaction, the Bose-Fermi-Hubbard Hamiltonian reads

$$\begin{aligned} \hat{H}_{BFHM} = &- J_B \sum_{\langle i,j \rangle} \hat{b}_i^\dagger \hat{b}_j - J_F \sum_{\langle i,j \rangle} \hat{f}_i^\dagger \hat{f}_j + \sum_i \epsilon_i^B \hat{n}_i + \sum_i \epsilon_i^F \hat{n}_i \\ &+ \frac{1}{2} U_B \sum_i \hat{n}_i(\hat{n}_i - 1) + U_{BF} \sum_i \hat{n}_i \hat{m}_i. \end{aligned} \qquad (2.62)$$
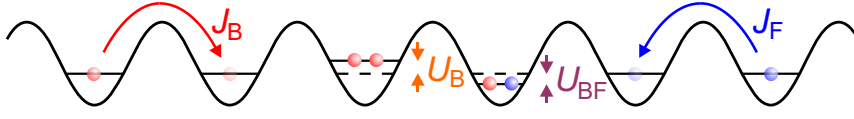
Fig. 2.9: The Bose-Fermi-Hubbard model with bosonic and fermionic hopping J_{B} and J_{F}, respectively, bosonic on-site interaction U_{B}, and boson-fermion on-site interaction U_{BF}.

Here, the operators $\hat{n}_i = \hat{b}_i^\dagger \hat{b}_i$ and $\hat{m}_i = \hat{f}_i^\dagger \hat{f}_i$ count the number of bosons and fermions at site i, respectively.

2.4   Exact diagonalization

The main numerical results in this thesis are obtained using the method of exact diagonalization, which allows to solve the many-particle Schrödinger equation numerically exact. In particular, it includes the full correlations of particles neglected in mean-field approaches and permits to compute accurately excited states. The drawback is the numerical expense, which is enormous and restricts the applicability to few-particle systems. However, exact diagonalization allows the precise treatment of strong interactions and finite systems. For systems with orbital degrees of freedom, the basis of the Hilbert space may have infinite dimensions, so that the numerical treatment has to be restricted to a suitable finite subspace. In this section the basic aspects are highlighted, whereas a more comprehensive description of this method is given in Refs. [81, 108, 109] including also several technical aspects. The computer program implementing a finite-size multiorbit exact diagonalization algorithm was mainly designed in my diploma thesis [81], although it was also improved and extended afterwards. In addition, a Bose-Fermi Hubbard model was implemented using periodic boundary conditions.

The exact diagonalization method solves the stationary many-particle Schrödinger equation $\hat{H}|\Psi\rangle = E|\Psi\rangle$ by expanding it in a basis set $|N\rangle$. Projecting the Schrödinger equation on the state $\langle N|$, it follows

$$\langle N|\hat{H} \sum_{N'} |N'\rangle\langle N'|\Psi\rangle = E\langle N|\Psi\rangle. \tag{2.63}$$

Using the coefficient vector $c_N = \langle N|\Psi\rangle$, this can be rewritten in a matrix equation for the coefficient c_N

$$\sum_{N'} \langle N|\hat{H}|N'\rangle \, c_{N'} = E \, c_N. \tag{2.64}$$

This equation is solved by diagonalization of the matrix $\langle N|\hat{H}|N'\rangle$, which gives the energy eigenvalues E and the eigenvectors c_N.

As discussed in detail in section 2.4.2, the Hamiltonian $\hat{H}$ contains only one- and two-particle operators, so that $\langle N|\hat{H}|N'\rangle$ vanishes for most pairs of states $|N\rangle$ and $|N'\rangle$. Numerically, this allows to use a sparse matrix representation, where only the nonzero elements are stored together

with their respective column or row indices. For the numerical diagonalization, the Arnoldi package is used developed at Rice University in Houston, Texas [110].

2.4.1   Single- and many-particle basis

To solve the many-particle problem a Fock basis is used, which consists of fully (anti-) symmetrized occupation number states for bosons (fermions). The occupation numbers reference three-dimensional single-particle basis states $|\phi_i\rangle$, often referred to as orbitals, that are indexed by a single integer number. For simplicity, we assume that the energy e_i corresponding to $|\phi_i\rangle$ increases with this index, i.e, $e_{i+1} \geq e_i$. Due to the separable potential, the three-dimensional single-particle basis states can be build up from the basis states in x, y, and z directions, i.e.,

$$|\phi_i\rangle = |\varphi_j(x)\rangle \, |\varphi_k(y)\rangle \, |\varphi_l(z)\rangle \tag{2.65}$$

with j, k, $l = 0, 1, \dots$. Using the occupation number representation, the many particle-basis is constructed using a Dijkstra-like algorithm [111]. It starts with the ground state of the system, where all particles occupy the energetically lowest single-particle state $|\phi_0\rangle$, and considers possible one-particle excitations. Iteratively, the lowest excitation is added to the basis set, while its excitations are added to the list of possible excitations. The procedure stops at a given number of basis states thereby ensuring that all omitted states have a higher energy than the included basis states, i.e., $E_i^{\mathrm{omitted}} \geq \max_j E_j^{\mathrm{basis}}$. If the Hilbert space is finite and all states shall be included in the basis set a faster and simpler algorithm can be used. Starting with the vacuum state, it expands recursively the whole tree of possible occupations by adding a particle to one of the sites.

For Bose-Fermi mixtures, the product space of bosons and fermions must be generated, unless a self-consistent approach is used as introduced in section 2.4.4, where boson and fermion subspace are diagonalized separately. Restricting the basis for a lattice with N_S sites to the lowest band, such as in the Bose-Hubbard (2.58) and Bose-Fermi-Hubbard (2.62) model, the separate Fock spaces have the finite dimension

$$D_{\mathrm{B}} = \frac{(N_{\mathrm{B}} + N_S - 1)!}{N_{\mathrm{B}}!(N_S - 1)!} \tag{2.66}$$

for N_{B} bosonic atoms and

$$D_{\mathrm{F}} = \frac{N_S!}{N_{\mathrm{F}}!(N_S - N_F)!} \tag{2.67}$$

for N_{F} fermionic atoms. The latter is reduced substantially due to Pauli's exclusion principle, allowing only the occupations zero and one. To describe the system in the whole parameter range, e.g., the bosonic transition from a superfluid to a Mott insulator (see section 2.6), all lowest-band states must be included in the calculation irrespectively of the fact that a Wannier or a Bloch basis is used.

For the Bose-Hubbard and the Bose-Fermi-Hubbard model, the Hamiltonian exclusively depends on $U_{\{\mathrm{B,BF}\}}$ and $J_{\{\mathrm{B,F}\}}$. The many-particle basis in this model consists of the occupation numbers of the lattice sites. This is advantageous, since observables such as the filling or particle fluctuations can easily be calculated. Moreover, the two-particle operators in the Hubbard model, (2.58) or

(2.62), are diagonal in the Wannier basis. As the implementation of the lowest-band Hubbard model is rather straight forward, I will concentrate in the following on finite lattices with orbital degrees of freedom. To allow the treatment of arbitrary separable potentials, a variable problem-adapted single-particle basis is used. In this context, it is important to realize that the calculation of the single-particle interaction integrals (2.73) is numerically inexpensive due to the δ function in the interaction potential.

To allow for an inclusion of orbital degrees of freedom, the single-particle eigenbasis is used to build up the many-particle basis for the finite system, which is most flexible ranging from the treatment of particles in a harmonic trap to finite lattice systems with arbitrary perturbations. However, it is not well suited for periodic boundary conditions or algebraic calculations, where localized Wannier states are the common choice. The single-particle eigenbasis of the system can be found by exact diagonalization of the single-particle problem using adequate wave functions. For finite sinusoidal potentials without additional perturbations the single-particle eigenfunctions correspond to Bloch functions (2.22). More precisely, they are the finite size correspondents with a defined parity because of the symmetric potential. The many-particle basis consists of subspaces of states with even and odd parity in each spatial direction, which are not mixed by the interaction (2.47). Therefore, the basis can be reduced to a single-parity subspace, which accelerates the diagonalization substantially. The basis functions in momentum space, being the Fourier transforms of the wave functions, show sharp peaks at certain quasimomenta q and $-q$. Additionally, higher order peaks at multiples of the reciprocal lattice vectors appear with less intensity. The potential for finite lattices is truncated to $(n_x, 1, 1)$ sites for one-dimensional and $(n_x, n_y, 1)$ sites for two-dimensional lattices. It is continued at its boundary by a harmonic confinement potential[1].

The width of the lowest Bloch band, i.e., the energy difference of the lowest and highest energetic state, of an infinite one-dimensional lattice determines the value of the Hubbard hopping integral $4J$ within the tight-binding approximation. For a double well the band width is only $2J$ and converges rapidly with increasing number of sites to $4J$. In practice, a number of 30 sites gives a reasonable agreement with the definition (2.59) for lattice depths $V_0 \gtrsim 5E_R$.

2.4.2   Calculation of matrix elements

As mentioned above, it is necessary for the diagonalization to calculate the elements of the Hamiltonian matrix $\langle N|\hat{H}|N'\rangle$ in the Fock basis $\{|N\rangle\}$. Thereby, $\{|N\rangle\}$ is the product space of bosonic and fermionic subspaces $\{|N\rangle\} = \{|N_B\rangle\} \otimes \{|N_F\rangle\}$. The many-particle states $|N_{\{B,F\}}\rangle$ are represented by vectors $|n_1, n_2, n_3, ...\rangle$, where n_i corresponds to the occupation of a bosonic or fermionic single-particle orbital. The Hamiltonian (2.52) consists of bosonic and fermionic one-particle operators $\hat{\psi}^\dagger_{\{B,F\}}(\mathbf{r})\hat{\psi}_{\{B,F\}}(\mathbf{r})$ and two-particle operators $\hat{\psi}^\dagger_B(\mathbf{r})\hat{\psi}^\dagger_{\{B,F\}}(\mathbf{r})\hat{\psi}_{\{B,F\}}(\mathbf{r})\hat{\psi}_B(\mathbf{r})$.

---

[1]The confining potential $V(x) = \gamma V_{0x}\left(\frac{2kx}{n\pi}\right)^2$ continues the periodic potential at $|x| = x_0$, where n is the number of sites (see Ref. [81]). The potential is continuously differentiable which determines γ (≈ 1) and x_0 ($\approx na/2$).

For a bosonic one-particle operator, it follows due to the expansion (2.53)

$$\langle N_{\mathrm{B}}| \int d^3r \; \hat{\psi}_{\mathrm{B}}^\dagger(\mathbf{r}) \hat{O} \hat{\psi}_{\mathrm{B}}(\mathbf{r}) |N_{\mathrm{B}}'\rangle = \sum_{j,k} \langle \chi_j | \hat{O} | \chi_k \rangle \langle N_{\mathrm{B}} | \hat{b}_j^\dagger \hat{b}_k | N_{\mathrm{B}}'\rangle \tag{2.68}$$

and the respective expression for fermions. The latter term can be evaluated for bosons

$$\langle N_{\mathrm{B}} | \hat{b}_j^\dagger \hat{b}_k | N_{\mathrm{B}}'\rangle = \delta_{N_{\mathrm{B}}N_{\mathrm{B}}'} \, \delta_{jk} \, n_j + \Delta_{N_{\mathrm{B}}N_{\mathrm{B}}'}^{jk} \sqrt{n_j(n_k+1)}, \tag{2.69}$$

where $\delta_{N_{\mathrm{B}}N_{\mathrm{B}}'}$ is the Kronecker δ and $\Delta_{N_{\mathrm{B}}N_{\mathrm{B}}'}^{jk} = 1$ if $|N'\rangle = |..., n_j - 1, ..., n_k + 1, ...\rangle$ and $\Delta_{N_{\mathrm{B}}N_{\mathrm{B}}'}^{jk} = 0$ otherwise with $n_i = n_i'$ for $i \neq j$ and $i \neq k$. For fermions holds

$$\langle N_{\mathrm{F}} | \hat{f}_j^\dagger \hat{f}_k | N_{\mathrm{F}}'\rangle = \delta_{N_{\mathrm{F}}N_{\mathrm{F}}'} \, \delta_{jk} \, n_j + \Delta_{N_{\mathrm{F}}N_{\mathrm{F}}'}^{jk} \, (-1)^{\epsilon_{jk}}, \tag{2.70}$$

where

$$\epsilon_{jk} = \sum_{\xi=\min(j,k)+1}^{\max(j,k)-1} n_\xi \tag{2.71}$$

due to the anticommutation relation of the fermionic operators.

While the two-particle boson-fermion interaction is discussed in section 2.4.4, the exact evaluation of the boson-boson interaction is elaborated here shortly (see Refs. [81, 108, 109] for details). The boson-boson interaction matrix element becomes

$$\langle N_{\mathrm{B}} | \frac{g}{2} \int d^3r \; \hat{\psi}_{\mathrm{B}}^\dagger(\mathbf{r}) \hat{\psi}_{\mathrm{B}}^\dagger(\mathbf{r}) \hat{\psi}_{\mathrm{B}}(\mathbf{r}) \hat{\psi}_{\mathrm{B}}(\mathbf{r}) |N_{\mathrm{B}}'\rangle = \frac{g}{2} \sum_{i,j,k,l} \chi_{ijkl} \langle N_{\mathrm{B}} | \hat{b}_i^\dagger \hat{b}_j^\dagger \hat{b}_k \hat{b}_l | N_{\mathrm{B}}'\rangle, \tag{2.72}$$

where the interaction integral is given by

$$\chi_{ijkl} = \int d^3r \; \chi_i^*(\mathbf{r}) \chi_j^*(\mathbf{r}) \chi_k(\mathbf{r}) \chi_l(\mathbf{r}). \tag{2.73}$$

Comparing with one-particle operators, a larger number of states $|N_{\mathrm{B}}\rangle$ and $|N_{\mathrm{B}}'\rangle$ exists for which $\langle N_{\mathrm{B}} | \hat{b}_i^\dagger \hat{b}_j^\dagger \hat{b}_k \hat{b}_l | N_{\mathrm{B}}'\rangle$ does not vanish. It gives a nonzero contribution, if $|N_{\mathrm{B}}\rangle$ and $|N_{\mathrm{B}}'\rangle$ are related as follows

$$
\begin{aligned}
|N_{\mathrm{B}}'\rangle &= |N_{\mathrm{B}}\rangle, \\
|N_{\mathrm{B}}'\rangle &= |..., n_i - 2, ..., n_k + 2, ...\rangle, \\
|N_{\mathrm{B}}'\rangle &= |..., n_j - 1, ..., n_k + 1, ...\rangle, \\
|N_{\mathrm{B}}'\rangle &= |..., n_i - 1, ..., n_j - 1, ..., n_k + 2, ...\rangle, \\
|N_{\mathrm{B}}'\rangle &= |..., n_i - 2, ..., n_k + 1, ..., n_l + 1, ...\rangle, \\
|N_{\mathrm{B}}'\rangle &= |..., n_i - 1, ..., n_j - 1, ..., n_k + 1, ..., n_l + 1, ...\rangle.
\end{aligned}
\tag{2.74}
$$

Thus, for each class of nonvanishing matrix elements, the sum $\sum_{ijkl} \chi_{ijkl} \hat{b}_i^\dagger \hat{b}_j^\dagger \hat{b}_k \hat{b}_l$ must be calculated. The algorithm, which computes the Hamiltonian matrix, has to determine if a given pair of states $\{|N_{\mathrm{B}}\rangle, |N_{\mathrm{B}}'\rangle\}$ belongs to one of the classes in (2.74), which causes a major contribution to the calculation time. Subsequently, the program evaluates the matrix elements (2.72), which are derived in appendix A.1 (see also Refs. [81, 108, 109]). To allow a fast computation, the interaction integrals χ_{ijkl} are precalculated numerically and stored in a look-up table. It should be noted that the matrix $\langle N_{\mathrm{B}} | \hat{H} | N_{\mathrm{B}}'\rangle$ is symmetric (or, in general, hermitian) so that only the upper or lower triangle of the matrix has to be computed.

2.4.3   One-particle density matrix

The many-particle eigenvectors that are obtained by exact diagonalization give full information about the system. In contrast to an eigenvalue, an eigenvector is, in general, a quite complicated quantity, which does not give intuitive insight into the physical system. Therefore, usually several expectation values are calculated subsequent to the diagonalization such as the density, the momentum distribution, and two-particle correlation functions. The single-particle expectation values of density and momentum distribution are determined using the one-particle density matrix. In the case of bosons, the density matrix for an eigenvector $|\Psi_{\rm B}\rangle = \sum_N c_N |N\rangle$ reads

$$\langle\Psi_{\rm B}|\hat{b}_j^\dagger \hat{b}_k|\Psi_{\rm B}\rangle = \sum_{N,N'} c_N^* c_{N'} \langle N|\hat{b}_j^\dagger \hat{b}_k|N'\rangle. \tag{2.75}$$

Any expectation value of an operator of the form $\sum_{j,k} a_{jk}\hat{b}_j^\dagger \hat{b}_k$ can be expressed using the one-particle density matrix

$$\langle\Psi_{\rm B}|\sum_{j,k} a_{jk}\hat{b}_j^\dagger \hat{b}_k|\Psi_{\rm B}\rangle = \sum_{j,k} a_{jk}\langle\Psi_{\rm B}|\hat{b}_j^\dagger \hat{b}_k|\Psi_{\rm B}\rangle. \tag{2.76}$$

Assuming $a_{jk} = a_{kj}^*$ and using (2.69), this can be rewritten for the numerical calculation as

$$\langle\Psi_{\rm B}|\sum_{j,k} a_{jk}\hat{b}_j^\dagger \hat{b}_k|\Psi_{\rm B}\rangle = \sum_{j,k} \rho_{jk}^{\rm B}\,{\rm Re}(a_{jk}) \tag{2.77}$$

with

$$\rho_{jk}^{\rm B} = \delta_{jk}\sum_N |c_N|^2 n_j + \sum_{N<N'} 2\,{\rm Re}(c_N^* c_{N'})\,\Delta_{N_{\rm B}N_{\rm B}'}^{jk}\sqrt{n_j(n_k+1)}. \tag{2.78}$$

The sum over $N < N'$ restricts the calculation to the the upper triangular matrix, which is also used for the diagonalization of $\langle N|\hat{H}|N'\rangle$. Note that the matrix $\rho_{jk}^{\rm B}$ is not symmetric in j and k but either $\rho_{jk}^{\rm B} = 0$ or $\rho_{kj}^{\rm B} = 0$.

Correspondingly, for fermions the one-particle density matrix is given by

$$\langle\Psi_{\rm F}|\hat{f}_j^\dagger \hat{f}_k|\Psi_{\rm F}\rangle = \sum_{N,N'} c_N^* c_{N'} \langle N|\hat{f}_j^\dagger \hat{f}_k|N'\rangle \tag{2.79}$$

and with (2.70) one obtains

$$\langle\Psi_{\rm F}|\sum_{j,k} a_{jk}\hat{f}_j^\dagger \hat{f}_k|\Psi_{\rm F}\rangle = \sum_{j,k} \rho_{jk}^{\rm F}\,{\rm Re}(a_{jk}), \tag{2.80}$$

where

$$\rho_{jk}^{\rm F} = \delta_{jk}\sum_N |c_N|^2 n_j + \sum_{N<N'} 2\,{\rm Re}(c_N^* c_{N'})\,\Delta_{N_{\rm B}N_{\rm B}'}^{jk}\,(-1)^{\epsilon_{jk}}. \tag{2.81}$$

With these expressions, one easily obtains the expectation value for the density, namely

$$\rho_{\rm B}(\mathbf{r}) = \langle\hat{\psi}_{\rm B}^\dagger(\mathbf{r})\hat{\psi}_{\rm B}(\mathbf{r})\rangle = \sum_{j,k} \rho_{jk}^{\rm B}\,{\rm Re}(\chi_j^* \chi_k), \tag{2.82}$$

$$\rho_{\mathrm{F}}(\mathbf{r}) = \langle \hat{\psi}_{\mathrm{F}}^{\dagger}(\mathbf{r})\hat{\psi}_{\mathrm{F}}(\mathbf{r}) \rangle = \sum_{j,k} \rho_{jk}^{\mathrm{F}} \, \mathrm{Re}(\phi_j^* \phi_k), \tag{2.83}$$

for bosons and fermions, respectively. Using the momentum basis functions, which are the Fourier transformed wave functions $\tilde{\chi}_i(\mathbf{p})$ and $\tilde{\phi}_i(\mathbf{p})$, i.e., for bosons

$$\tilde{\chi}_i(\hbar\mathbf{k}) = \frac{1}{(2\pi\hbar)^{3/2}} \int d^3r \, \chi(\mathbf{r})e^{-i\mathbf{k}\mathbf{r}}, \tag{2.84}$$

the momentum distribution is given by

$$\rho_{p,\mathrm{B}}(\mathbf{p}) = \langle \hat{\psi}_{\mathrm{B}}^{\dagger}(\mathbf{p})\hat{\psi}_{\mathrm{B}}(\mathbf{p}) \rangle = \sum_{j,k} \rho_{jk}^{\mathrm{B}} \, \mathrm{Re}(\tilde{\chi}_j^* \tilde{\chi}_k), \tag{2.85}$$

$$\rho_{p,\mathrm{F}}(\mathbf{p}) = \langle \hat{\psi}_{\mathrm{F}}^{\dagger}(\mathbf{p})\hat{\psi}_{\mathrm{F}}(\mathbf{p}) \rangle = \sum_{j,k} \rho_{jk}^{\mathrm{F}} \, \mathrm{Re}(\tilde{\phi}_j^* \tilde{\phi}_k). \tag{2.86}$$

2.4.4 Self-consistent effective potentials

Instead of solving the full Bose-Fermi Hamiltonian (2.52)

$$\hat{H} = \hat{H}_{\mathrm{B}} + \hat{H}_{\mathrm{F}} + \hat{H}_{\mathrm{BF}} \tag{2.87}$$

in the product basis of bosons and fermions $\{|N_{\mathrm{B}}\rangle\} \otimes \{|N_{\mathrm{F}}\rangle\}$, one can also use an approximative self-consistent method. In this approach, the bosonic and the fermionic subspace are diagonalized separately using a self-consistent interaction potential for the boson-fermion interaction. For a given fermion density $\rho_{\mathrm{F}}(\mathbf{r}) = \langle \hat{\Psi}_{\mathrm{F}}^{\dagger}\hat{\Psi}_{\mathrm{F}} \rangle$, the effective Hamiltonian of the bosonic subsystem reads

$$\hat{H}_{\mathrm{B}}^{\mathrm{eff}}(\rho_{\mathrm{F}}) = \hat{H}_{\mathrm{B}} + g_{\mathrm{BF}} \int d^3r \, \rho_{\mathrm{F}}(\mathbf{r}) \, \hat{\psi}_{\mathrm{B}}^{\dagger}(\mathbf{r})\hat{\psi}_{\mathrm{B}}(\mathbf{r}). \tag{2.88}$$

The latter term represents the interaction with the fermion density and leads to a bosonic effective potential

$$V_{\mathrm{B}}^{\mathrm{eff}}(\rho_{\mathrm{F}}) = V(\mathbf{r}) + g_{\mathrm{BF}}\rho_{\mathrm{F}}(\mathbf{r}). \tag{2.89}$$

Consequently, the effective bosonic Hamiltonian (2.48) can be written as

$$\hat{H}_{\mathrm{B}}^{\mathrm{eff}} = \int d^3r \, \hat{\psi}_{\mathrm{B}}^{\dagger}(\mathbf{r}) \left[\frac{\hat{\mathbf{p}}^2}{2m_{\mathrm{B}}} + V_{\mathrm{B}}^{\mathrm{eff}}(\rho_{\mathrm{F}}) + \frac{g}{2}\hat{\psi}_{\mathrm{B}}^{\dagger}(\mathbf{r})\hat{\psi}_{\mathrm{B}}(\mathbf{r}) \right] \hat{\psi}_{\mathrm{B}}(\mathbf{r}). \tag{2.90}$$

Starting with the density of noninteracting fermions ρ_{F}^0, the boson density $\rho_{\mathrm{B}}^0(\mathbf{r}) = \langle \Psi_{\mathrm{B}}^{\dagger}\Psi_{\mathrm{B}} \rangle$ is determined by diagonalization of $\langle N_{\mathrm{B}}'|\hat{H}_{\mathrm{B}}^{\mathrm{eff}}|N_{\mathrm{B}}\rangle$. Subsequently, a new fermion density ρ_{F}^1 can be calculated using the fermionic effective potential

$$V_{\mathrm{F}}^{\mathrm{eff}}(\rho_{\mathrm{B}}) = V(\mathbf{r}) + g_{\mathrm{BF}}\rho_{\mathrm{B}}(\mathbf{r}) \tag{2.91}$$

and the effective Hamiltonian

$$\hat{H}_{\mathrm{F}}^{\mathrm{eff}} = \int d^3r \, \hat{\psi}_{\mathrm{F}}^{\dagger}(\mathbf{r}) \left[\frac{\hat{\mathbf{p}}^2}{2m_{\mathrm{F}}} + V_{\mathrm{F}}^{\mathrm{eff}}(\rho_{\mathrm{B}}) \right] \hat{\psi}_{\mathrm{F}}(\mathbf{r}). \tag{2.92}$$
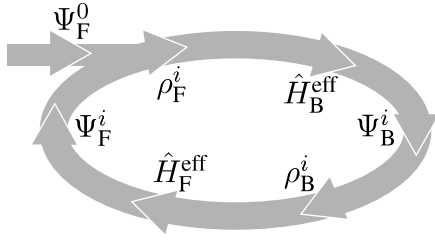
Fig. 2.10: The bosonic and the fermionic subspace are diagonalized separately using a self-consistent interaction potential, which converges within a few cycles.

This cycle, which is visualized in Fig. 2.10, is repeated until the effective potentials, the energies, and densities converge. In practice, the convergence is achieved after few cycles. This method is advantageous, since the number of basis states for each diagonalization can be reduced. In addition, the effective potentials give an intuitive insight into the interaction of bosons and fermions. However, only the ground state is accessible and several diagonalizations of the bosonic and fermionic system must be performed. Moreover, the method is only an approximation, which works well if bosons and fermions are weakly correlated.

2.5 Detection methods

As mentioned in the previous chapters the versatile tunability of system parameters makes optical lattices an optimal model system, which demands reliable detection techniques to probe the actual state of the quantum system. In this section, the most frequently used method, the time-of-flight expansion, is described including the adiabatic mapping and the possibility to detect two-particle correlations by analyzing shot-noise fluctuations. In addition, spectroscopic methods permit to probe excited states of the system. The Bragg spectroscopy, recently applied to optical lattice experiments, is discussed in chapter 6.

2.5.1 Time-of-flight experiments

In a time-of-flight experiment, the lattice potential and all additional trapping potentials are switched off abruptly, which causes the atomic cloud to expand. Neglecting interaction effects in the expanding cloud, the Bloch states (2.22) with quasimomentum $\mathbf{q}$ expand according to their momentum distribution with contributions $\mathbf{p} = \hbar(\mathbf{q} + n\mathbf{G})$, where $\mathbf{G}$ is a reciprocal lattice vector. The ballistic expansion for each plane wave with momentum $\mathbf{p}$ is given by $r = \hbar \mathbf{k} t/m$ with $\mathbf{p} = \hbar \mathbf{k}$. After a certain time-of-flight, the expanded atomic cloud is observed using absorption imaging. If the initial extend of the atomic cloud in the optical lattice is small compared with its size after the ballistic expansion, the momentum distribution is related to the imaged density [19, 112] via

$$\rho^p(\mathbf{k}) \approx \left(\frac{\hbar t}{m}\right)^3 \rho^{\mathrm{TOF}}\left(\mathbf{r} = \frac{\hbar \mathbf{k} t}{m}\right). \tag{2.93}$$

Therefore, a time-of-flight experiment images the momentum distribution in the lattice. Due to the small lattice spacing in most experiments, an imaging of the density distribution in the lattice, i.e., directly after switching off the trapping potentials, does not offer single-site resolution.
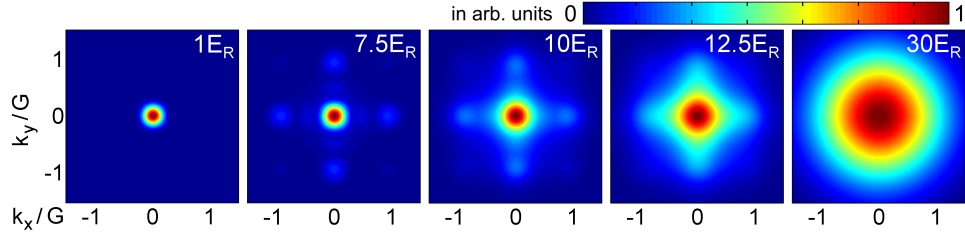
Fig. 2.11: The momentum distribution for a finite two-dimensional lattice for several lattice depths V_0 (see chapter 3).

Using the lowest band Wannier basis (2.28), the momentum distribution can be written as

$$\rho_p(\mathbf{k}) = \sum_{i,j} \tilde{w}_i^{(0)*}(\mathbf{k})\, \tilde{w}_j^{(0)}(\mathbf{k})\, \langle \hat{b}_i^\dagger \hat{b}_j \rangle \tag{2.94}$$

due to equation (2.76), where $\tilde{w}_i^{(0)}(\mathbf{k})$ is the Fourier transformation of the Wannier function $w^{(0)}(\mathbf{r} - \mathbf{r}_i)$ and $\langle \hat{b}_i^\dagger \hat{b}_j \rangle = \langle \Psi | \hat{b}_i^\dagger \hat{b}_j | \Psi \rangle$ [113]. Writing the Fourier transformation explicitly

$$\rho_p(\mathbf{k}) = \frac{1}{(2\pi)^3} \int d^3r \int d^3r' \sum_{i,j} w^{(0)*}(\mathbf{r} - \mathbf{r}_i)\, w^{(0)}(\mathbf{r}' - \mathbf{r}_j)\, e^{i\mathbf{k}(\mathbf{r} - \mathbf{r}')}\, \langle \hat{b}_i^\dagger \hat{b}_j \rangle \tag{2.95}$$

and by substitution of $\mathbf{r} - \mathbf{r}_i$ and $\mathbf{r}' - \mathbf{r}_j$, one obtains the simple expression

$$\rho_p(\mathbf{k}) = |\tilde{w}_0^{(0)}(\mathbf{k})|^2 \sum_{i,j} e^{i\mathbf{k}(\mathbf{r}_i - \mathbf{r}_j)}\, \langle \hat{b}_i^\dagger \hat{b}_j \rangle. \tag{2.96}$$

Thus, the momentum distribution can be described by means of the envelope function $|\tilde{w}_0^{(0)}(\mathbf{k})|^2$ and an interference pattern

$$S(\mathbf{k}) = \sum_{i,j} e^{i\mathbf{k}(\mathbf{r}_i - \mathbf{r}_j)}\, \langle \hat{b}_i^\dagger \hat{b}_j \rangle. \tag{2.97}$$

For a Bose-Einstein condensate or a quasicondensate with a macroscopic occupation of the Bloch state with quasimomentum $\mathbf{q} = 0$, the momentum distribution shows a sharp interference pattern, since the one-particle density matrix $\langle \hat{b}_i^\dagger \hat{b}_j \rangle$ is constant at large separations due to the long-range order (see section 2.6.1). Restricting ourselves to the first Brillouin zone, a single sharp peak at $k = 0$ is observable, which represents the fraction of condensed atoms. To measure the interference pattern quantitatively one defines the visibility of interference fringes

$$\nu = \frac{\rho_p(\mathbf{k}_{max}) - \rho_p(\mathbf{k}_{min})}{\rho_p(\mathbf{k}_{max}) + \rho_p(\mathbf{k}_{min})}. \tag{2.98}$$

In two-dimensions, the maximum value $\rho_p(\mathbf{k}_{max})$ can be found at the center of the second Brillouin zone, e.g., $\mathbf{k}_{max} = (G, 0)$, and the minimum $\rho_p(\mathbf{k}_{min})$ at $\mathbf{k}_{min} = (G/\sqrt{2}, G/\sqrt{2})$. Both extremes lie at the same distance from the center, which ensures that the Wannier envelope $|\tilde{w}_0^{(0)}(\mathbf{k})|^2$ cancels in the ratio (2.98) [112, 114]. Thus, the visibility can be written as

$$\nu = \frac{S(\mathbf{k}_{max}) - S(\mathbf{k}_{min})}{S(\mathbf{k}_{max}) + S(\mathbf{k}_{min})}. \tag{2.99}$$

Instead of switching off the lattice potential suddenly, it can also be turned off slowly. This adiabatically transforms a deep lattice into a shallow one and finally releases the atoms from the trapping potential. In this process the quasimomentum $\mathbf{q}$ is conserved and a Bloch state is mapped onto the free-particle state with corresponding momentum $\mathbf{p}$ in the nth Brillouin zone [115, 116]. If the lowest band of a cubic lattice is homogeneously filled, one can observe a mapping of the first Brillouin zone, i.e., the absorption image exhibits a square, where the length of the edge corresponds to the length of the reciprocal lattice vector G. Just as well, a partially filled lowest band or the population of higher bands can be visualized using this technique.

2.5.2 Two-particle correlations

In strongly interacting quantum systems, it is also desirable to explore the higher-order correlations, which complements the information contained in the one-particle density matrix. The density-density correlation is given by

$$
\begin{aligned}
\langle \rho(\mathbf{r})\rho(\mathbf{r}') \rangle &= \langle \hat{\psi}^\dagger(\mathbf{r})\hat{\psi}(\mathbf{r})\hat{\psi}^\dagger(\mathbf{r}')\hat{\psi}(\mathbf{r}') \rangle \\
&= \langle \hat{\psi}^\dagger(\mathbf{r})\hat{\psi}^\dagger(\mathbf{r}')\hat{\psi}(\mathbf{r}')\hat{\psi}(\mathbf{r}) \rangle + \delta(\mathbf{r} - \mathbf{r}')\langle \rho(\mathbf{r}) \rangle.
\end{aligned}
\tag{2.100}
$$

The last term in this equation is the self-correlation term, whereas the first part is the pair distribution function $g_2(\mathbf{r}, \mathbf{r}')$, which is commonly normalized by the particle density. The matrix elements needed for the calculation of $g_2(\mathbf{r}, \mathbf{r}')$ in a many-particle basis are given in appendix A.2. The pair distribution function reveals detailed information on the spatial two-particle correlations, i.e., the probability of finding a second atom at $\mathbf{r}'$, if a first atom is located at $\mathbf{r}$.

In a time-of-flight experiment, the correlations in momentum space are accessible rather than the spatial correlations. The momentum pair correlation function reads

$$
g_2^p(\mathbf{k}, \mathbf{k}') = \langle \hat{\psi}^\dagger(\mathbf{k})\hat{\psi}^\dagger(\mathbf{k}')\hat{\psi}(\mathbf{k}')\hat{\psi}(\mathbf{k}) \rangle
\tag{2.101}
$$

and equals the expectation value $\langle \rho_p(\mathbf{k})\rho_p(\mathbf{k}') \rangle$ when omitting the self-correlation term $\delta(\mathbf{k} - \mathbf{k}')$ $\langle \rho_p(\mathbf{k}) \rangle$. In the following, the signature of a state with a fixed occupation number per site, e.g., a Mott insulator, is discussed. Expanding the bosonic field operators in a lowest-band Wannier basis $\hat{\psi}(\mathbf{k}) = \sum_i \tilde{w}_i^{(0)}(\mathbf{k})\hat{b}_i$ and using the relation

$$
\tilde{w}_i^{(0)}(\mathbf{k}) = \int d^3r \; e^{-i\mathbf{k}\mathbf{r}} w^{(0)}(\mathbf{r} - \mathbf{r}_i) = e^{-i\mathbf{k}\mathbf{r}_i} w_0^{(0)}(\mathbf{k}),
\tag{2.102}
$$

one gets

$$
g_{2,\text{Mott}}^p(\mathbf{k}, \mathbf{k}') = N^2 |\tilde{w}_0^{(0)}(\mathbf{k})|^2 |\tilde{w}_0^{(0)}(\mathbf{k}')|^2 \left(1 + \frac{1}{N^2}\big| \sum_i e^{i(\mathbf{k}-\mathbf{k}')\mathbf{r}_i}\, n_i \big| \right)
\tag{2.103}
$$

for a state with fixed occupation numbers [66]. In experiments, the recorded absorption image is a single realization of momentum distribution and not an average. Therefore, several images of the same experiment differ by shot-noise fluctuations, yielding second-order correlations. From the

recorded time-of-flight images, one can extract the experimental momentum correlation function using

$$g_{2,\text{exp}}^{p}(\Delta k) = \frac{\int d^3k \, \langle \rho^{\text{TOF}}(\mathbf{k} + \Delta\mathbf{k}/2)\rho^{\text{TOF}}(\mathbf{k} - \Delta\mathbf{k}/2)\rangle}{\int d^3k \, \langle \rho^{\text{TOF}}(\mathbf{k} + \Delta\mathbf{k}/2)\rangle\langle \rho^{\text{TOF}}(\mathbf{k} - \Delta\mathbf{k}/2)\rangle}. \tag{2.104}$$

In Refs. [117, 118], the bosonic Mott insulator has been observed by analyzing this correlation function, which shows sharp correlation peaks at reciprocal lattice vectors $\mathbf{k} - \mathbf{k}' = \mathbf{G}$ caused by the sum in equation (2.103). In contrast, for a superfluid state an unmodulated correlation function is expected. The same technique has also been applied to observe the fermionic band isolator [119], where dips emerge in the noise correlation functions, since the sum in equation (2.103) changes sign for fermions.

2.6 Superfluid and Mott insulator

One of the most interesting phenomena that occurs in optical lattices is the quantum phase transition of bosonic atoms from a superfluid to a Mott-insulator phase at zero temperature, where all thermal fluctuations are frozen out. This macroscopic phase transition is remarkable since it is driven purely by the increase of interaction relative to tunneling energy, which causes the long-range phase coherence of the superfluid to break down. In the Mott-insulator phase the particles localize at individual lattice sites, due to their repulsive interaction. Originally, this behavior was predicted for liquid helium on a porous surface [20]. More recently, it was proposed that this quantum phase transition might be observable in optical lattices [21], where a relatively perfect realization of a periodic potential is present. Furthermore, the interaction between the atoms as well as the tunneling can be tuned directly by varying the strength of the potential, which is proportional to the laser power and therefore precisely adjustable. Experimentally, the superfluid to Mott-insulator transition was observed in a three-dimensional optical lattice in Ref. [19] and subsequently in one [120] and two dimensions [118, 121]. In three dimensions, the phase transition has been further analyzed in Refs. [112, 122, 123]. From a theoretical point of view, the investigation of the phase transition is based on the Bose-Hubbard model described in section 2.3.2.

2.6.1 Superfluidity

The existence of superfluidity is strongly connected to the Bose-Einstein condensation of particles. In the following, this relationship is discussed including the basic definition of both phenomena following Refs. [48, 66]. In experiments with ultracold bosonic atoms, the quantum degeneracy is achieved by cooling the atoms below a critical temperature T_c. In a homogeneous gas, the critical temperature for a Bose-Einstein condensate (BEC) is reached when the de Broglie wavelength $\lambda_T = h/\sqrt{2\pi m k_B T}$ is comparable to the average interparticle distance $n^{-1/3}$, i.e., $\lambda_T^3 n = n_s \zeta(3/2)$, where n_s is the spin degree of freedom and $\zeta(3/2) \approx 2.61$.[2] In experimental realizations, where the gas is trapped, the BEC transition is, in principle, smooth. However, for

---

[2]The Riemann zeta function is defined as $\zeta(s) = \frac{1}{\Gamma(s)} \int_0^\infty \frac{x^{s-1}}{e^x - 1} \, dx$.

typical particle numbers N a rather sharp transition temperature $k_B T_c = \hbar \bar{\omega} (N/\zeta(3))^{1/3}$ exists, where $\bar{\omega}$ is the average trapping frequency by geometric means. It should be noted that in a homogeneous system a real BEC exists only in three dimensions due to the density of states. However, the trapping geometry of two-dimensional system changes the density of states so that one expects even for weakly repulsive interaction a BEC at very low temperatures, whereas at higher temperatures a quasicondensate with an algebraically decaying one-particle density matrix is existent. In one-dimension, quasicondensation can be achieved only at $T = 0$ or even at finite temperatures, if the cloud size is smaller than the phase coherence length [66].

The microscopic definition of a Bose-Einstein condensate states that there is exactly one eigenvalue φ_0 of the one-particle density matrix $\langle \hat{\psi}^\dagger(\mathbf{x}) \hat{\psi}(\mathbf{x}') \rangle$ of order N, while all other eigenvalues are nonextensive. This property is only well defined in the thermodynamic limit, but for typical experimental particle numbers a distinction of normal phase and BEC is possible. In other words, the condensation goes along with a macroscopic occupation of a single-particle state, which is usually the ground state of the system. In principle, more than one eigenvalue can be extensive, e.g., in multicomponent spinor condensates [65], which is denoted as fragmented BEC. In translational invariant systems the single-particle levels are plain waves, while in an optical lattice Bloch waves are present. In both cases, the eigenvectors correspond to states with defined (quasi)momentum $\mathbf{k}$ and occupation number $\langle \hat{b}_\mathbf{k}^\dagger \hat{b}_\mathbf{k} \rangle$. Therefore, a BEC in the ground state is reflected in a momentum distribution with a sharp peak at $\mathbf{k} = 0$ for a trapped BEC and an interference pattern with peaks at $\mathbf{k} = 0 + \mathbf{G}$ for a BEC in a lattice. The one-particle density matrix in an uniform system

$$\langle \hat{\psi}^\dagger(\mathbf{x}) \hat{\psi}(\mathbf{x}') \rangle = \int d^3k \, n(\mathbf{k}) \, e^{-i\mathbf{k}(\mathbf{x}-\mathbf{x}')} \tag{2.105}$$

depends only on the distance $\mathbf{x} - \mathbf{x}'$ and vanishes for a normal system when $|\mathbf{x} - \mathbf{x}'| \to \infty$. For systems which exhibit a singularity in the momentum distribution, i.e., $n(\mathbf{k}) = n_0 \, \delta(\mathbf{k}) + \tilde{n}(\mathbf{k})$, the density matrix

$$\langle \hat{\psi}^\dagger(\mathbf{x}) \hat{\psi}(\mathbf{x}') \rangle = n_0 + \int d^3k \, \tilde{n}(\mathbf{k}) \, e^{-i\mathbf{k}(\mathbf{x}-\mathbf{x}')} \tag{2.106}$$

approaches a finite value $n_0 = N_0/V$ when $|\mathbf{x} - \mathbf{x}'| \to \infty$. This behavior, which evolves nondiagonal matrix elements $(\mathbf{x} \neq \mathbf{x}')$ of the one-particle density matrix, is called off-diagonal long-range order. In a trapped BEC, this quantity has been observed experimentally for two points separated on the order of micrometers [16]. In interacting bosonic systems, the existence of off-diagonal long-range order in the one-particle density matrix defines the Bose-Einstein condensation.

The definition of superfluidity on a microscopic footing is rather subtle, but an intuitive picture can be given on a macroscopic phenomenological level by introducing a complex order parameter $\psi(\mathbf{x}) = \sqrt{n(\mathbf{x})} e^{i\phi(\mathbf{x})}$ [48, 66]. While $n(\mathbf{x}) = |\psi(\mathbf{x})|^2$ is the superfluid density, $\phi(\mathbf{x})$ defines the superfluid velocity $\mathbf{v}_{\text{SF}} = (\hbar/m)\nabla\phi(\mathbf{x})$. The latter expression leads directly to one of the most interesting phenomenon of superfluidity, which is the quantization of the circulation $\oint d\mathbf{s} \, \mathbf{v}_{\text{SF}}$ in integer multiples of h/m. Assuming now that we can identify the order parameter of superfluidity $\psi(\mathbf{x})$ with the extensive eigenvector of the one-particle density matrix $\psi(\mathbf{x}) = \sqrt{N_0}\varphi_0(\mathbf{x})$, we see that the BEC and the superfluid seems to be equivalent. However, this assumption holds only in the

Gross-Pitaevskii regime. A more subtle theoretical description, covering also superfluidity in low dimensions, deals with response of a system to a change in the boundary conditions. This probes the stiffness of the system to an additional phase shift $e^{i\Phi}$, which offers a microscopic definition of superfluidity (see Refs. [124–126]). It turns out that superfluidity and a finite compressibility $\kappa = \partial n/\partial \mu$ are sufficient conditions for the existence of a BEC in three dimensions or a quasicondensate in one or two dimensions. This means that superfluidity is also necessary for the existence of a BEC or a quasicondensate.

In the superfluid phase, the particles are spread out over the entire lattice, which goes hand in hand with the macroscopic occupation of the lowest Bloch wave. The superfluidity manifests itself in the long-range phase coherence of atoms throughout the lattice. As long as the interaction energy is small compared with the gain in kinetic energy due to the delocalization, the atoms can be described by a superfluid wave function. When the interaction can be neglected, the superfluid state is a perfect BEC state $|\Psi_{\mathrm{SF}}\rangle = \frac{1}{\sqrt{N!}}(\hat{b}_{q=0}^{\dagger})^{N}|0\rangle$, where all atoms occupy the Bloch state $\phi_{\mathbf{q}=0}(\mathbf{r})$. In the Wannier basis, where the single-particle wave functions are optimally localized at the lattice sites, the superfluid state can be written as

$$|\Psi_{\mathrm{SF}}\rangle = \frac{1}{\sqrt{N!}}\left(\frac{1}{\sqrt{N_s}}\sum_i \hat{b}_i^{\dagger}\right)^{N}|0\rangle \qquad (2.107)$$

using relation (2.29).

2.6.2 Mott insulator

To describe the effect of strong interaction in the lattice, the Bose-Hubbard model is used (section 2.3.2), which depends on the two parameters U and J, which change when ramping up the optical lattices as depicted in Fig. 2.12. The tunneling parameter J describes the gain in kinetic energy due to the hopping of particles and the corresponding spatial extend of the wave function, whereas the on-site interaction U captures the interaction of particles in the lattice. In the case, where the repulsive interaction energy dominates the kinetic energy, the system minimizes its interaction energy $\langle \hat{H}_{\mathrm{int}} \rangle = \frac{1}{2}U\langle \sum_i \hat{n}_i(\hat{n}_i - 1)\rangle$ with $U > 0$. For integer filling $n = N/N_s$ and vanishing tunneling ($J = 0$), the Fock state with the same filling at all lattice sites

$$|\Psi_{\mathrm{MI}}\rangle = \Big(\prod_i \frac{1}{\sqrt{n!}}\, b_i^{\dagger n}\Big)|0\rangle \qquad (2.108)$$

is the ground state. In particular, for filling $n = 1$, where each lattice site is occupied with one particle, the interaction energy $\langle \hat{H}_{\mathrm{int}} \rangle$ vanishes completely. As long as the tunneling J is small compared to the interaction U of two particles at one site, the atoms remain localized, but $|\Psi\rangle$ can not be written as the simple product state (2.108). The process, where localization is driven by interaction, was firstly discovered by N. F. Mott [127, 128] and the associated phase is called Mott-insulator phase.

A crucial property of the Mott insulator is that there is a finite energy gap of U between the ground state and the first excited state. This excitation corresponds to the creation of a particle-hole pair,
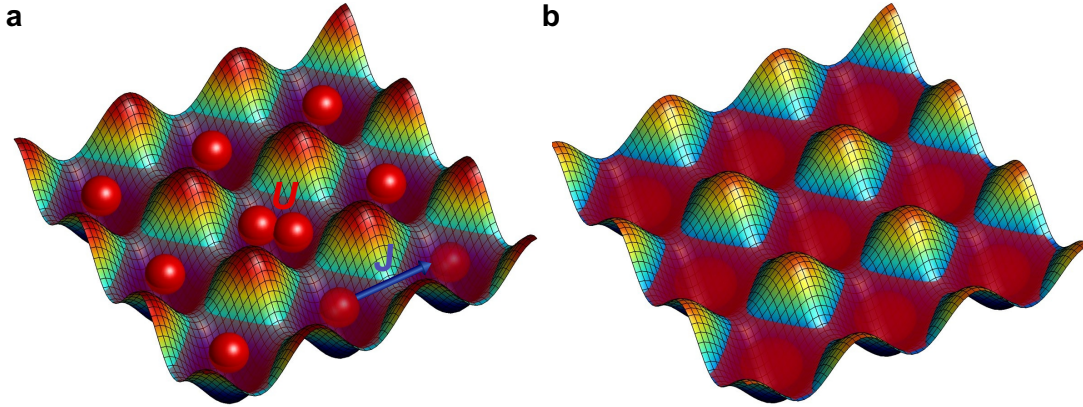
Fig. 2.12: (a) Optical lattice depicting the hopping parameter J and the on-site interaction U. For deep lattices, the atoms tend to localize at individual lattice sites. In the Mott-insulator phase, each lattice site is filled with the same integer number of atoms. (b) In the superfluid phase, which exists below a critical lattice depth, the atoms are delocalized and are spread over the lattice.

where the hole leads to a gain in energy of $(n-1)U$ and the additional particle on one of the other sites requires the energy nU. The energy nU for adding an additional particle causes that the density remains unchanged when the chemical potential is infinitesimally altered. Because of $\partial n / \partial \mu = 0$, the system is incompressible, which defines the Mott insulator, rather than the existence of a state with integer local filling.

Furthermore, the localization of atoms on lattice sites causes the long-range order in the one-particle density matrix to vanish. With increasing tunneling, however, the Mott state at $J = 0$ is modified by an admixture of particle-hole pairs, which induces significant short-range coherence [112, 122, 129]. This means that the created particles and holes are rather tightly bound to each other, which is due to the large gap in the excitation spectrum. Using first order perturbation theory, where the tunneling J is treated as a small perturbation on the interaction, the admixture of particle-hole pairs can be expressed quantitatively as

$$|\Psi\rangle_{U/J} \approx |\Psi_{\mathrm{MI}}\rangle + \frac{J}{U} \sum_{\langle i,j \rangle} \hat{b}_i^\dagger \hat{b}_i |\Psi_{\mathrm{MI}}\rangle, \tag{2.109}$$

where $|\Psi_{\mathrm{MI}}\rangle$ is the Mott-insulator state at $J = 0$ and $\langle i,j \rangle$ indicates the sum over nearest neighbors.

2.6.3 Superfluid to Mott-insulator transition

The discussion of the superfluid phase on the one hand and of the Mott insulator on the other hand implies a transition between both phases driven by the ratio of kinetic to interaction energy. In the Bose-Hubbard model (section 2.3.2) this is reflected by the ratio of on-site interaction U to tunneling energy J when neglecting additional site offsets ϵ_i. For $J \gg U$ the system is superfluid,

whereas for $J \ll U$ the phase coherence is lost and atoms localize at individual lattice sites required by the minimization of interaction energy. Although the model depends only on one parameter, namely the ratio U/J, it is not exactly solvable.

In the following, the boundary of the superfluid phase and the Mott insulator is discussed using a mean-field approach [20, 21, 49, 130]. The derivation of the phase diagram follows van Oosten et al. [49]. By introducing the superfluid order parameter $\psi = \sqrt{\langle n_i \rangle} = \langle \hat{b}_i^\dagger \rangle = \langle \hat{b}_i \rangle$, the hopping operator $\hat{b}_i^\dagger \hat{b}_j$ in the Bose-Hubbard Hamiltonian (2.58) can be substituted by the mean-field expression $\psi(\hat{b}_i^\dagger + \hat{b}_j) - \psi^2$. For $z = 2d$ equivalent nearest neighbors, where d is the dimension of the lattice, it follows

$$-J \sum_{\langle i,j \rangle} \hat{b}_i^\dagger \hat{b}_j = -J \sum_{\langle i,j \rangle} \left(\psi(\hat{b}_i^\dagger + \hat{b}_j) - \psi^2 \right) = -zJ \left(\sum_i \hat{b}_i^\dagger + \hat{b}_i \right) \psi + zJN_s\psi^2 \quad (2.110)$$

with N_s the total number of lattice sites. In this decoupling approximation, the Bose-Hubbard Hamiltonian becomes an effective single-site Hamiltonian $\hat{H}^{\mathrm{eff}} = \sum_i \hat{H}_i^{\mathrm{eff}}$ with

$$\hat{H}_i^{\mathrm{eff}} = -zJ(\hat{b}_i^\dagger + \hat{b}_i)\psi + zJ\psi^2 + \frac{1}{2}U\hat{n}_i(\hat{n}_i - 1) - \mu\hat{n}_i, \quad (2.111)$$

where μ is the chemical potential. To apply perturbation theory with respect to the superfluid order parameter, we write the Hamiltonian as $\hat{H}_i^{\mathrm{eff}}/zJ = \hat{H}_i^{(0)} - (\hat{b}_i^\dagger + \hat{b}_i)\psi$ with

$$\hat{H}_i^{(0)} = \frac{1}{2}\bar{U}\hat{n}_i(\hat{n}_i - 1) - \bar{\mu}\hat{n}_i + \psi^2. \quad (2.112)$$

The energies in this expression are scaled by $1/zJ$, i.e., $\bar{U} = U/zJ$ and $\bar{\mu} = \mu/zJ$. The unperturbed ground state is a local Fock state that minimizes the energy $\langle \hat{H}_i^{(0)} \rangle$. For $\bar{U}(n-1) < \bar{\mu} < \bar{U}n$, the state is given by $|\Psi_i^{(0)}\rangle = \hat{b}_i^{\dagger n}|0\rangle = |n\rangle$. The first order correction in ψ vanishes since $\langle n|(\hat{b}_i^\dagger + \hat{b}_i)|n\rangle = 0$. The second-order perturbation in energy gives

$$E^{(2)} = \sum_{m \neq n} \frac{|\langle m|(\hat{b}_i^\dagger + \hat{b}_i)|n\rangle|^2}{E_n^{(0)} - E_m^{(0)}} = \frac{n+1}{-\bar{U}n + \bar{\mu}} + \frac{n}{\bar{U}(n-1) - \bar{\mu}} \quad (2.113)$$

since only $m = n \pm 1$ contributes. As all odd powers of the expansion are zero, it follows

$$E(\psi) = \left(\frac{1}{2}\bar{U}n(n-1) - \bar{\mu}n\right) + \left(E^{(2)} + 1\right)\psi^2 + O(\psi^4). \quad (2.114)$$

Minimizing $E(\psi)$ gives $\psi = 0$ for $E^{(2)} + 1 > 0$ and $\psi \neq 0$ if $E^{(2)} + 1 < 0$, so that the phase boundary is defined by $E^{(2)} + 1 = 0$. Solving this expression for the chemical potential, one obtains

$$\bar{\mu}_\pm = \frac{1}{2}[\bar{U}(2n-1) - 1] \pm \frac{1}{2}\sqrt{\bar{U}^2 - 2\bar{U}(2n+1) + 1}, \quad (2.115)$$

which defines the upper and the lower boundary of the Mott-insulator phase. The Mott lobes in phase space $(\bar{\mu}/\bar{U}, 1/\bar{U})$ are depicted in Fig. 2.13 for $n = 1$ to $n = 4$. The smallest $\bar{U}$, where the system enters the Mott-insulator phase for a given n corresponding to the tips of the lobes, requires $\hat{\mu}_+ = \hat{\mu}_-$, i.e., a vanishing square root in equation (2.115). Consequently, the critical $\bar{U}_c = (U/zJ)_c$ is given by

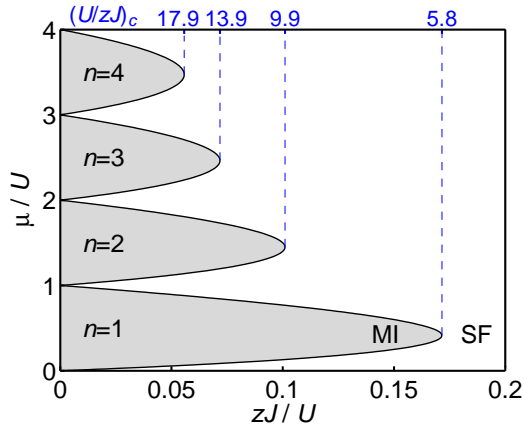$$(U/zJ)_c = 2n + 1 + \sqrt{(2n+1)^2 - 1} \quad (2.116)$$

Fig. 2.13: Phase diagram showing the Mott insulator (MI) and the superfluid phase (SF). The critical points $(U/zJ)_c$ for integer filling n correspond to the tips of the Mott lobes.

and yields $(U/zJ)_c = 5.83$ for $n = 1$ [20, 49, 130].

In the case of integer filling n, the system enters the Mott-insulator phase by varying zJ/U on a line with a constant chemical potential. For a constant filling $n' = n + \epsilon$, however, the value of the chemical potential bends around the Mott lobe with increasing zJ/U to the final value of $\mu/U = n$. Hence, the ground state of the system remains in the superfluid phase although only a small fraction of atoms remains delocalized [20]. The idea, that these atoms tend to localize when a disorder potential is present, is addressed in the fundamental article by Fisher *et al.* [20]. It turns out, that the Mott lobes are surrounded by a glass phase, where the extend of the Bose-glass phase depends on the disorder parameter. Thus, in the presence of disorder, the transition from a superfluid to a Mott insulator occurs via the Bose glass phase. In addition to the localization process caused by interaction, the atoms localize due to random site offsets of the lattice sites. This leads to gapless excitations with a finite compressibility, but also with an infinite superfluid susceptibility.

The transition point separating the superfluid phase from the Mott insulator has been studied with several beyond mean-field methods reaching from quantum Monte Carlo in three dimensions to DMRG in one dimension. These calculations have found substantial deviations from equation (2.116), in particular, for the one-dimensional case. An accurate value for the critical ratio $(U/zJ)_c$ for a three-dimensional lattice was obtained by quantum Monte Carlo simulation in Ref. [131] which determines $(U/J)_c^{3D}$ as 29.36 for $n = 1$, being noticeably lower than the mean-field result $(U/J)_c^{3D} = 6 \times 5.83$. In two dimensions an accurate value is given by $(U/J)_c^{2D} = 16.74$ [132]. The transition in one dimension is of Kosterlitz-Thouless type [20, 74]. Using DMRG (density-matrix renormalization group) calculations, a precise value for the critical point $(U/J)_c^{1D} = 3.37$ can be obtained [133, 134]. The value is, in principle, supported by infinite-sized DMRG using periodic boundary conditions [135, 136], exact diagonalization [137], quantum Monte Carlo [138], the Bethe ansatz [139], and by a strong-coupling expansion [132]. Note that in one dimension the result deviates drastically from the mean field value above. As a new feature, in one-dimension a reentrant behavior occurs [133].

In experiments, the ratio U/J is altered by tuning the depth of the lattice potential. In contrast to the symmetric case in three dimensions, high potential barriers in one or two directions lead to two- or three-dimensional systems, since the tunneling J in the other directions is strongly suppressed.

The values for U and J can be obtained using equations (2.59) and (2.60), respectively, by means of the Wannier functions for a given lattice depth V_0. For $V_0 \gg E_R$, the tunneling integral J can be determined from the bandwidth of the one-dimensional Mathieu equation which tends to $4J$, i.e.,

$$J = \frac{4}{\sqrt{\pi}} \left(\frac{V_0}{E_R} \right)^{3/4} e^{-\sqrt{4V_0/E_R}} E_R \tag{2.117}$$

with $k_L = \pi/a$. An analytical expression for U [74] can be obtained by approximating the Wannier functions as the ground state of a harmonic oscillator

$$U = \sqrt{\frac{8}{\pi}} k_L a_s \left(\frac{V_0}{E_R} \right)^{3/4} E_R, \tag{2.118}$$

which yields good results for deep lattices. It is important to realize that the tunneling parameter J depends exponentially on V_0, whereas U scales with $V_0^{3/4}$. Combining both equations, an analytical expression for the ratio U/J is given by

$$\frac{U}{J} = \frac{\pi a_s}{\sqrt{2}a} e^{\sqrt{4V_0/E_R}}, \tag{2.119}$$

which holds for $V_0 \gg E_R$. However, more accurate values can be computed numerically using equations (2.59) and (2.60).

3

Bosonic atoms in finite optical lattices

3.1   Motivation

As a fascinating new development, experiments with a small number of lattice sites and in particular finite optical chains have become focus of current research. Prominent examples are quantum registers in the context of quantum information processing [38–40], the manipulation of single atoms within a few sites [43, 44], and experiments with double well unit cells [41, 42]. In this context a fundamental question arises: How similar are finite compared with macroscopic systems? In this chapter, the problem of few repulsively interacting bosonic atoms in finite one-dimensional and small two-dimensional lattices is studied. The central point is how finite size effects influence the precursors of the Mott-insulator and the Bose-glass transition. The rich physics of the crossover from a double well to mesoscopic systems is investigated by exact diagonalization using a multiband basis, as described in the previous chapter. This allows accurate results and the discussion of orbital effects, which have been widely neglected so far.

As shown in the following, small systems exhibit a surprisingly strong similarity to the localization process in macroscopic systems. The momentum distribution, the formation of an energy gap, and the pair correlation function show only a weak size dependence. A great advantage of studying these systems by means of exact diagonalization is that we can gain intuitive insight into the excitation spectrum and the nature of excited states. Finite systems offer also the possibility to study the effects of noncommensurate filling, in which the localization is suppressed by the equivalence of lattice sites. In deep lattices, a mixture of localized and delocalized particles can be observed that is sensitive to lattice imperfections. Breaking the lattice symmetry causes the localization of atoms in a Bose-glass-like phase [20, 140–143].

3.2   Theoretical approach

The calculations are performed for repulsively interacting ^{87}Rb atoms, which are present in many experimental setups. Following the theoretical description in section 2.3, the Hamiltonian including the full two-particle interaction in a periodic potential V_P reads

$$\hat{H} = \int d^3r \, \hat{\psi}^\dagger(\mathbf{r}) \left[\frac{\hat{\mathbf{p}}^2}{2m} + V_P(\mathbf{r}) + \frac{g}{2}\hat{\psi}^\dagger(\mathbf{r})\hat{\psi}(\mathbf{r}) \right] \hat{\psi}(\mathbf{r}), \tag{3.1}$$

where $V_P(\mathbf{r})$ is the periodic lattice potential. Thereby, the short range interaction potential is approximated by a contact potential $g\delta(\mathbf{r} - \mathbf{r}')$ with the interaction parameter $g = \frac{4\pi\hbar^2}{m}a_s$, where a_s is the s-wave scattering length and m the mass of the atoms. The periodic potential

$$V_P(\mathbf{r}) = V_{0x}\cos^2(kx) + V_{0y}\cos^2(ky) + V_{0z}\cos^2(kz) \tag{3.2}$$

is truncated to $(n_x, 1, 1)$ sites for chains and $(n_x, n_y, 1)$ sites for two-dimensional lattices (see inset of Fig. 3.1). At the boundaries, $V_P(\mathbf{r})$ is continued by a harmonic confinement (section 2.4.1). The modeled optical lattice has the periodicity $a = 515$ nm, where $k = \pi/a$, and the depth of the wells is varied from $1E_R$ to $40E_R$ given in units of the ^{87}Rb recoil energy $E_R = \frac{\hbar^2 k^2}{2m} = 2.16\,h$ kHz. The one-dimensional and two-dimensional lattices have a transversal confinement $V_{0,y} = V_{0,z} = 40E_R$ and $V_{0,z} = 40E_R$, respectively, so that the transversal tunneling can be neglected. Exact diagonalization is performed in the Bloch representation of the optical lattice (see section 2.4.1). By using a few-particle basis, the two-particle interaction is fully included. The truncation of the basis at a sufficiently high energy allows the inclusion of orbital effects. In this chapter, up to 100 000 many-particle basis states and parity conservation if applicable are used for the calculation. These basis states include the formed Bloch bands and the lowest bound states in the confinement (corresponding to "continuum" states in an open system).

3.3   Precursor of the Mott insulator in finite systems

3.3.1   The double well problem

Let us start the discussion with atoms in a double well which exhibit a crossover reminiscent of the superfluid to Mott-insulator transition. Although the double well with commensurate filling represents an intuitive and easy-to-handle model, the eigenstates and the spectrum have already a structure similar to the studied one-dimensional lattices with three to ten sites. A double well with two particles can easily be treated analytically with the restriction to the lowest band. The Hilbert space separates into states with even and odd parity that do not couple. The subspace with even parity comprises of the states

$$|2,0\rangle = \frac{1}{\sqrt{2}}b_{\mathrm{s}}^{\dagger 2}|0\rangle \qquad \text{and} \qquad |0,2\rangle = \frac{1}{\sqrt{2}}b_{\mathrm{as}}^{\dagger 2}|0\rangle, \tag{3.3}$$

where $b_{\mathrm{s}}^\dagger$ is the creation operator of particles in the symmetric state and $b_{\mathrm{as}}^\dagger$ in the antisymmetric state (see inset of Fig. 3.1). Since the energy difference between symmetric and antisymmetric
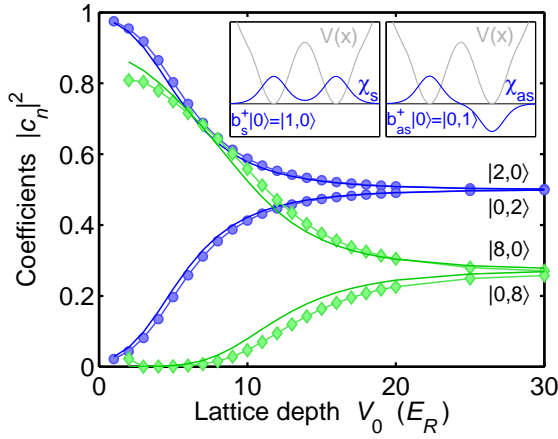
Fig. 3.1: Major coefficients c_n for two ($\circ$) and eight atoms ($\diamond$) in a double-well potential in dependency on the lattice depth V_0 calculated by exact diagonalization. The lines without markers are obtained using the LBA. The inset shows a symmetric and an antisymmetric basis wave function.

single-particle states χ_s and χ_as is twice the tunneling energy J, the energy of the states $|2,0\rangle$ and $|0,2\rangle$ differs by $2\Omega = 4J + \Delta$. The difference in the interaction energies Δ is given by

$$\Delta = g \int d^3r \left[\chi_\mathrm{as}^4(\mathbf{r}) - \chi_\mathrm{s}^4(\mathbf{r}) \right] \tag{3.4}$$

using the real space representation. The off-diagonal matrix element between both states is

$$I = g \int d^3r \; \chi_\mathrm{s}^2(\mathbf{r}) \chi_\mathrm{as}^2(\mathbf{r}). \tag{3.5}$$

Thus, by diagonalization of the respective 2×2 matrix the ground state reads

$$\Psi_0 = \cos\theta \, |2,0\rangle + \sin\theta \, |0,2\rangle, \tag{3.6}$$

where

$$\theta = \mathrm{atan}\left(\frac{\Omega - \sqrt{\Omega^2 + I^2}}{I} \right). \tag{3.7}$$

For very shallow lattices, where J approaches infinity, θ vanishes and $\Psi_{0,V_0 \to 0}$ equals $|2,0\rangle$, i.e., both particles occupy the energetically lower symmetric one-particle state.

In the limit of deep lattices, where $J \to 0$, the difference between the symmetric and anti-symmetric wave function $\chi_\mathrm{s}^2(x) - \chi_\mathrm{as}^2(x)$ vanishes, i.e., $\Delta \to 0$, and θ approaches $-\pi/4$. Consequently, the ground state is given by

$$\Psi_0(V_0 \to \infty) = \frac{1}{\sqrt{2}} |2,0\rangle - \frac{1}{\sqrt{2}} |0,2\rangle. \tag{3.8}$$

Using the creation operators of a particle in the left and the right well $b_{l/r}^\dagger = \frac{1}{\sqrt{2}}(b_\mathrm{s}^\dagger \pm b_\mathrm{as}^\dagger)$, respectively, the ground state can be rewritten as

$$\Psi_0(V_0 \to \infty) = b_l^\dagger b_r^\dagger |0\rangle. \tag{3.9}$$

Therefore, one particle is localized at the left site and one particle at the right site of the double well. In addition to the localization, a fundamental property of a Mott-insulator-like state is an excitation gap, which is given here by $2I$. Because of its uneven parity, the first
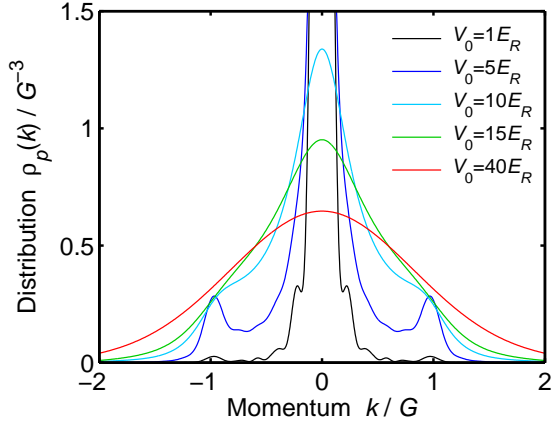
Fig. 3.2: Ground-state momentum distribution of six bosons in a quasi-one-dimensional chain with six sites. The crossover from a delocalized wave function ($V_0 \lesssim 5E_R$) to a localized wave function ($V_0 \gtrsim 10E_R$) can be observed.

excited state $\Psi_1 = |1,1\rangle = b_s^\dagger b_{as}^\dagger |0\rangle$ remains unchanged. The second excited state is given by $\Psi_2 = \cos\theta'|2,0\rangle + \sin\theta'|0,2\rangle$ with $\theta' = \mathrm{atan}[(\Omega + \sqrt{\Omega^2 + I^2})/I]$. In deep lattices, the first and second excited state

$$\Psi_{1/2}(V_0 \to \infty) = \frac{1}{2}(b_l^{\dagger 2} \mp b_r^{\dagger 2})|0\rangle \tag{3.10}$$

are therefore degenerate. Both states are symmetric-antisymmetric combinations of doubly occupied sites and thus represent particle-hole excitations. In lattices these linear combinations of particle-hole excitations build up the excited band as discussed further below.

Some of the coefficients c_n in the expansion of the many-body wave function of the ground state are plotted in Fig. 3.1. Already for a double well, it is instructive to compare these analytical results obtained using the lowest band approximation (LBA) with numerical multiband calculations. For filling factor $\nu = 1$, deviations are well noticeable for shallow potentials ($V_0 \lesssim 10E_R$), whereas for deep potentials the LBA leads to nearly perfect results. For higher filling factors the total interaction energy and consequently the deviations increase, since higher one-particle bands are occupied in order to minimize the interaction energy. Exemplarily, the coefficients of the states $|8,0\rangle$ and $|0,8\rangle$ for filling factor $\nu = 4$ are plotted in Fig. 3.1. Additionally, the lowest band coefficients $|6,2\rangle$, $|4,4\rangle$, and $|2,6\rangle$, which are not shown in Fig. 3.1, contribute. For filling factors higher than $\nu = 1$, the deviations do not vanish in deep lattices, since in that case ν interacting particles are trapped at each site, leading to a modification of the effective single-particle orbitals. This has direct implications for the Bose-Hubbard model (section 2.3.2) which is widely used in this context and is commonly restricted to the lowest band. Figure 3.1 shows that for higher filling factors ($\nu \gtrsim 3$) this restriction leads to noticeable deviations from a multiband calculation, whereas for low filling factors the deviations are small. Experimentally, deviations for higher fillings have been observed, e.g., by measuring the interaction energy U on a single lattice site. The experimental observation and calculation in Ref. [144] can be confirmed restricting the exact diagonalization to a single site. The on-site energy U of filling factor $\nu = 5$ is, e.g., roughly 17% smaller than for $\nu = 1$ at $V_0 = 30E_R$.
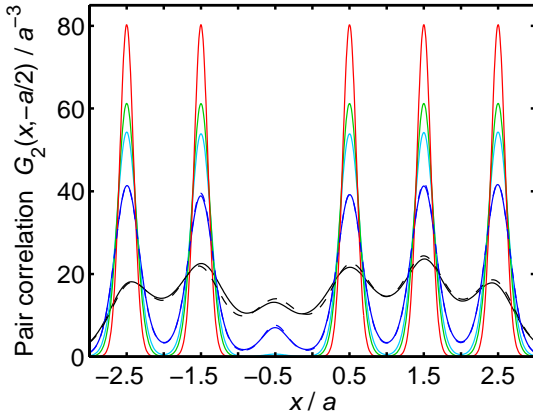
Fig. 3.3: The pair correlation function of six bosons in a lattice with six sites shows the localization of particles for $V_0 \gtrsim 10E_R$ (see Fig. 3.2 for a legend). Due to the low filling factor $\nu = 1$, the deviation from results obtained using the LBA (dashed lines) are only noticeable for $V_0 \lesssim 5E_R$.

3.3.2 Finite one-dimensional lattices

In the following, let us extend the double well to a one-dimensional lattice or rather a chain with $N_s = 6$ lattice sites and six particles. The momentum distribution $\rho_p(k_x)$ of the chain is shown for different lattice depths V_0 in Fig. 3.2, where $k_y = k_z = 0$. For very shallow lattices ($V_0 = 1E_R$) a narrow central peak indicates the delocalization of all particles over the lattice, whereas for deep lattices a broad Gaussian momentum distribution is observable. The latter can be assigned to particles that are localized in the center of a single lattice site. Although the system is very small the similarity to macroscopic experimental results, e.g., Refs. [19, 120], is striking. This is a first indication that the localization mechanism is not strongly dependent on the number of lattice sites (see also [145]) which is discussed in detail below.

For $V_0 = 1E_R$, minor dips in the momentum distribution at $k_n = nG/N_s$ are observable (Fig. 3.2), where $G = 2\pi/a$ is the reciprocal lattice vector. These dips originate from the suppression of standing waves with odd parity in the confinement with wavelengths $\lambda_n = N_s a/n$, where $n = 1, 2, ...$, because of the even parity of the ground state. Increasing the lattice depth to $V_0 = 5E_R$, Bragg peaks located at the reciprocal lattice vector appear. At the same time, the central peak drops rapidly in height and becomes broader, i.e., the particles begin to separate to different sites as the interaction grows relative to the tunneling. At $V_0 = 10E_R$, the minima are smeared out and only a small modulation of momentum density due to delocalized particles remains. This progress proceeds with increasing lattice depth, so that for approximately $V_0 = 30E_R$ the momentum distribution has a Gaussian shape[1], corresponding to completely localized particles.

3.3.3 Two-particle correlations

However, a Gaussian momentum distribution may also arise from a superposition of delocalized states and does not prove the localization at single lattice sites. Therefore, the pair correlation

---

[1] The density on one site corresponds to the density of a single particle in a single-sited $\cos^2$ potential, but deviates slightly from a harmonic approach.
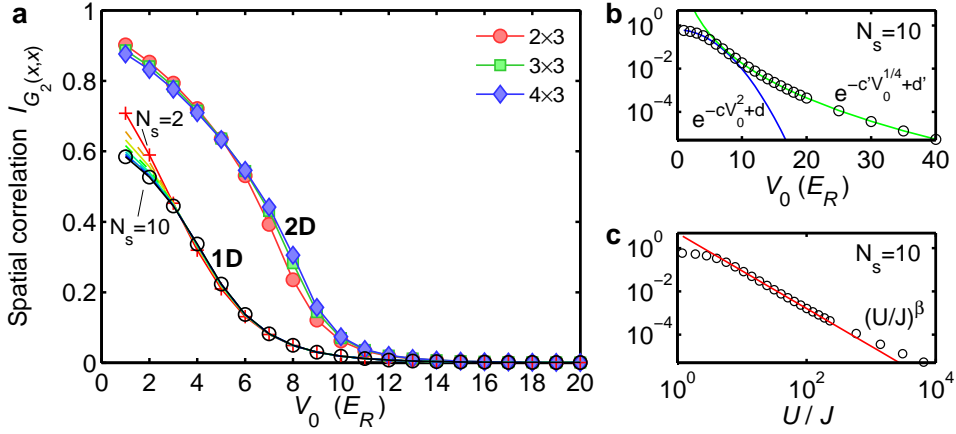
Fig. 3.4: (a) The integral over the local correlation function for chains with N_s sites and small two-dimensional lattices (6, 9, and 12 sites) with filling factor $\nu = 1$ (in LBA). (b) Logarithmic plot in units of V_0/E_R and (c) double-logarithmic plot in units of U/J for a chain with ten sites.

function

$$G_2(\mathbf{r}, \mathbf{r}') = \frac{1}{\rho(\mathbf{r}')} \langle \hat{\psi}^\dagger(\mathbf{r})\hat{\psi}^\dagger(\mathbf{r}')\hat{\psi}(\mathbf{r}')\hat{\psi}(\mathbf{r}) \rangle \qquad (3.11)$$

at $y = z = 0$ is studied, which reflects the conditional density of $N - 1$ particles if one particle can be found at $\mathbf{r}'$. In Fig. 3.3 the pair correlation is shown for $x' = -a/2$, i.e., for one particle located at the third site. For $V_0 \lesssim 5E_R$ other particles can be found at the same site, whereas for $V_0 \gtrsim 10E_R$ the pair correlation completely vanishes on the third site. Hence, that site and consequently all sites are occupied with exactly one particle in deep lattices.

The integral over the *local* correlation function

$$I_{G_2(x,x)} = \frac{N/(N-1)}{\int dx\, \rho(x)} \int dx\, G_2(x, x) \qquad (3.12)$$

measures the average probability of finding two particles at the same position and is consequently a good measure for the total spatial correlation of particles. In Fig. 3.4a the local correlation integral is shown for chains with N_s sites and filling factor $\nu = 1$. The calculations are restricted to the lowest band which is quite accurate due to the low filling (see Fig. 3.3).

Overall, we see an exponential decay of the correlation integral with increasing lattice depth. In deep lattices, the integral vanishes which reflects the localization of all particles. For $V_0 \lesssim 6E_R$ the correlation decreases with an exponent $-cV_0^2$ (see fit for $N_S = 10$ in Fig. 3.4b). Thus, an increase of the potential barriers causes a relatively strong separation of the particles in this regime due to the strong overlap of wave functions. For $V_0 \gtrsim 8E_R$ the particles are located predominately at single lattice sites and the extent to neighboring sites is small. In this region, the exponential decay is weaker and the correlation drops with an exponent $-c'V_0^{1/4}$. It is remarkable that this calculation shows a crossover between two different correlation regimes already for such a small-sized system.

In the studied systems, we observe a partial loss of spatial correlations in the region corresponding to the superfluid phase (see also Ref. [145]). Moreover, finite correlations above the transition
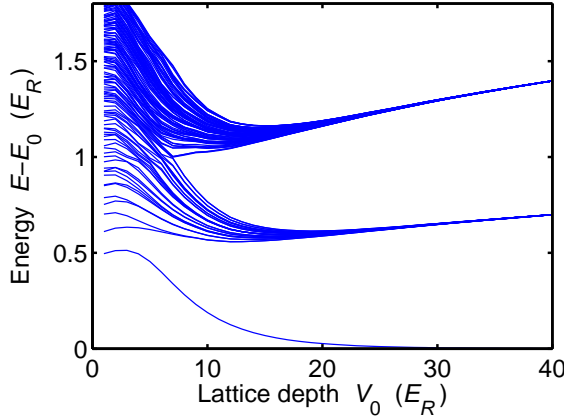
Fig. 3.5: The energy spectrum of six bosons in an one-dimensional lattice with six sites relative to the energy E_0 of the noninteracting system. The spectrum shows the ground state and the two lowest bands.

point are present, which can be understood quantitatively by using a perturbative ansatz to first order in J/U [112, 118], where J is the tunneling matrix element and U the on-site interaction energy. The perturbed wave function can be written as

$$\Psi' = \Psi_{MI}^{\nu=1} + \frac{J}{U} \sum_{ij} b_i^\dagger b_j \Psi_{MI}^{\nu=1}, \tag{3.13}$$

where $\Psi_{MI}^{\nu=1}$ is the pure Mott insulator state at infinite lattice depth which has a vanishing local correlation (see section 2.6.2). The operator $b_i^\dagger b_j$ creates a particle-hole state with a hole at site j and a doubly occupied site i. For doubly occupied sites, the pair correlation has a constant value if neglecting the interaction. Hence, the expectation value of the correlation integral is roughly proportional to $(J/U)^2$. In a double-logarithmic plot in units of U/J (Fig. 3.4c) the correlation integral shows a linear behavior between $V_0 = 6E_R$ and $17E_R$, i.e., the integral is proportional to $(U/J)^\beta$. We observe a value for β that is slightly above $\beta = -2$ (about 13%). For shallow lattices, this simple perturbative ansatz is obviously not suited and for very deep lattices ($V_0 > 20E_R$) the expectation values are slightly above the power law fit (see also Ref. [112]).

Only in very shallow lattices the correlation integral varies noticeably with the number of lattice sites, whereas for $V_0 > 3E_R$ the integral is nearly size-independent (even for a double well system). In addition, the differences for $V_0 < 3E_R$ are quite small for more than four lattice sites. Thus, the localization of particles depends very weakly on the number of lattice sites N_s, which indicates that the localization may occur in the same manner also in one-dimensional lattices of macroscopic size. We conclude that the blocking mechanism, which is caused by the tunneling prohibiting repulsion, is to a large extend insensitive to changes of the system size. Apparently, the coherence length in the insulating region drops below the extend of the system. Consequently, small systems become a good representation of larger ones. This explains the similarity of the presented momentum distributions and experimental results.

3.3.4 Energy spectrum and two-dimensional lattices

Further insight can be gained by probing the excitations of the many-body system, which has been addressed experimentally, e.g., in Ref. [120]. Exemplarily, the energy spectrum of a system with
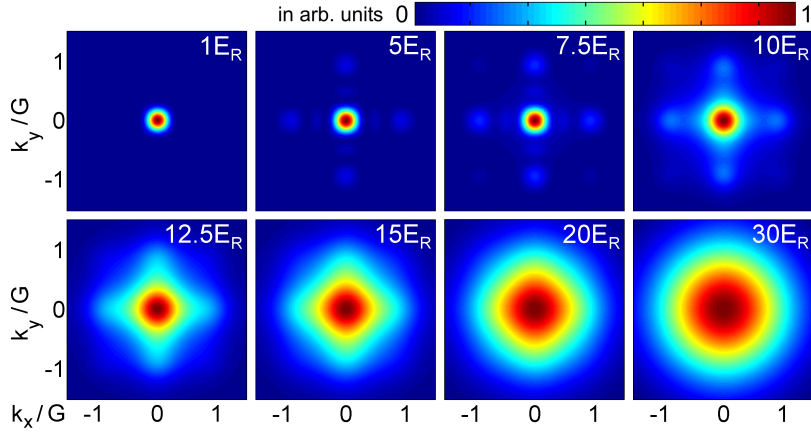
Fig. 3.6: The momentum distribution (normalized to 1) of a two-dimensional 3×3 lattice with nine atoms for various lattice depths V_0 using the LBA.

$N_s = 6$ sites, plotted in Fig. 3.5, shows the formation of narrow many-particle bands for deep lattices. The bands are gapped by the interaction energy U of two particles on the same site. For example, the first excited band consists of states where one particle interacts on average with one other particle at the same site. The number of states in each band is given by the possibilities to remove a certain number of particles and put them onto other sites resulting in an interaction energy of nU (e.g., the first band has 30 states due to 6 possible sites for a hole and 5 possible sites with double occupation). In particular, the energy of the nondegenerate ground state decreases and the ground state becomes separated from the excited states which is characteristic for an incompressible Mott-insulating state. In the limit of deep lattices, the interaction energy of the ground state vanishes, since the wave function overlap decreases due to the localization at single sites. The energy of the excited bands slowly increases due to the stronger confinement. Since the sites are equivalent, the eigenstates of the bands are delocalized. These delocalized states that form the excited bands in this commensurate system reappear within the ground-state band of noncommensurate systems, which are discussed in the next section.

The results obtained so far for momentum distributions, correlation functions, and energy spectra of quasi-one-dimensional chains can be generalized to two- or three-dimensional lattices. As an example, a quasi-two-dimensional lattice with 3×3 lattice sites and integer filling factor $\nu = 1$ is studied. The momentum distribution is presented in Fig. 3.6 for different potential depths. It shows the crossover from delocalization to localization and compares well with experimental results [118]. For $5E_R$ and $7.5E_R$ Bragg peaks at $\mathbf{k} = \pm G\hat{\mathbf{k}}_x$ and $\mathbf{k} = \pm G\hat{\mathbf{k}}_y$ appear in the distribution. Due to the finite number of sites per lattice direction, additional dips at $k = \frac{n}{3}G$ can be observed. Increasing the lattice depth, the momentum distribution smears out due to the localization of particles. This starts at approximately $10E_R$ and is far advanced at $12.5E_R$, which is in accordance with the critical point for infinite systems [132]. The two-dimensionality of the system becomes apparent for a lattice depth V_0 between $10E_R$ and $15E_R$. Here, the momentum distribution reflects the square symmetry of the boundary of a single lattice site. At roughly $V_0 = 30E_R$ the distribution becomes a Gaussian, which indicates that the particles are located

deep in the wells. Then the confining potential experienced by the particles is circular symmetric and can be approximated by a two-dimensional harmonic oscillator, which is reflected in the momentum distribution.

Further information on the localization process is contained in the integral over the local correlation function $I_{G_2(x,x)}$ that is plotted in Fig. 3.4. Compared with the quasi-one-dimensional chain, the localization process is shifted towards deeper potentials because of two reasons: The interaction energy on each lattice site is diminished due to a smaller confinement in the y direction and the tunneling is enhanced, since tunneling to four nearest neighbors is possible. For the two-dimensional lattice, the formation of gapped excited bands in deep lattices and the energetic separation of the ground state is observable in the same way as discussed for chains.

3.4   Noncommensurate filling

3.4.1   The noncommensurate double well

When a noncommensurate filling of the lattice is present the physical situation becomes more complicated. The localization of all particles as in the Mott-insulator-like regime is suppressed by the symmetry of the potential, since the equivalence of sites requires the same filling on all sites. Consequently, particles which in principle would prefer localization must delocalize over the whole lattice. The differences to commensurate filling can be illuminated by considering a double well with three atoms restricted to the lowest band. The basis of even parity states comprises of the two states

$$|3,0\rangle = \frac{1}{\sqrt{6}} b_{\mathrm{s}}^{\dagger 3} |0\rangle \qquad \text{and} \qquad |1,2\rangle = \frac{1}{\sqrt{2}} b_{\mathrm{s}}^{\dagger} b_{\mathrm{as}}^{\dagger 2} |0\rangle. \tag{3.14}$$

The difference in energy between both basis states is $2\Omega = 4J + \Delta$ with

$$\Delta = g \int d^3r \, [\chi_{\mathrm{as}}^4(\mathbf{r}) + 4\chi_{\mathrm{s}}^2(\mathbf{r})\chi_{\mathrm{as}}^2(\mathbf{r}) - 3\chi_{\mathrm{s}}^4(\mathbf{r})] \tag{3.15}$$

and the off-diagonal matrix element

$$I = \sqrt{3} g \int d^3r \, \chi_{\mathrm{s}}^2(\mathbf{r})\chi_{\mathrm{as}}^2(\mathbf{r}). \tag{3.16}$$

Thus, the solution for the ground state is given by the same expression as for two particles, i.e.,

$$\Psi_0 = \cos\theta \, |3,0\rangle + \sin\theta \, |1,2\rangle. \tag{3.17}$$

In deep lattices the tunneling energy J vanishes, but Δ, which had vanished for two particles, becomes $4I/\sqrt{3}$.

The ground state in the limit of deep lattices reads

$$\Psi_0(V_0 \to \infty) = \frac{\sqrt{3}}{2} |3,0\rangle - \frac{1}{2} |1,2\rangle = \frac{1}{2} b_l^{\dagger} b_r^{\dagger} (b_l^{\dagger} + b_r^{\dagger}) |0\rangle, \tag{3.18}$$

since θ becomes $2\pi/3$. This represents a wave function with two localized atoms and one atom that is delocalized between both wells. Consequently, the ground state is a mixture of localized

and delocalized particles. Of great importance in this context is that in this limit the first excited state, which has odd parity and is given by

$$\Psi_1(V_0 \to \infty) = \frac{1}{2} b_l^\dagger b_r^\dagger (b_l^\dagger - b_r^\dagger)|0\rangle, \tag{3.19}$$

becomes degenerate with the ground state. Small asymmetries lead to linear combinations of the two quasidegenerate states and result in the nonsymmetric states $\frac{1}{\sqrt{2}} b_l^{\dagger 2} b_r^\dagger |0\rangle$ and $\frac{1}{\sqrt{2}} b_l^\dagger b_r^{\dagger 2}|0\rangle$. Consequently, in a potential with broken symmetry the *third* particle can always localize in one of the wells, if the lattice is deep enough. This localization process depends on the potential difference between the two wells compared with the energy difference between ground and first excited state $E_1(V_0) - E_0(V_0)$. The third and fourth excited state which form the "first excited band" are separated from the ground state by $4I/\sqrt{3}$.

3.4.2   Finite systems

These intuitive results for a double well transfer nicely to one- and two-dimensional lattices. Exemplarily, a chain with $N_s = 5$ sites filled by five to ten particles is studied. The momentum distribution for deep lattices ($V_0 = 40 E_R$) obtained by exact diagonalization is shown in Fig. 3.7a. For integer filling factors ($N = 5$ and $N = 10$) a Mott-insulator momentum distribution can be observed as discussed in the previous section. When, for example, adding a sixth particle to a chain with filling factor $\nu = 1$, the additional particle cannot localize, since all lattice sites are equivalent. Despite being delocalized at different sites, the particle has a high probability density at the lattice site centers. Therefore, the momentum distribution reflects the lattice structure very clearly. Correspondingly, it shows peaks at 0 and $\pm G$ as well as smaller peaks at $\pm nG$ with $n = 2, 3, ...$, which originate from the delocalized particle. Additional to this peak structure, the momentum distribution has an underlying Gaussian background, which arises from the localized particles. Recapitulating the ground state for three particles in a double well $\Psi_0(V_0 \to \infty) = \frac{1}{2} b_l^\dagger b_r^\dagger (b_l^\dagger + b_r^\dagger)|0\rangle$, the interpretation is straight forward: For noninteger filling factors ν, the number of particles may be written as $N = \kappa N_s + N_{\text{add}}$ with the corresponding integer filling factor κ and the number of additional particles N_{add}. In deep lattices κN_s particles localize in the wells of the lattice and the remaining N_{add} are delocalized.

The plotted momentum distribution for $V_0 = 40 E_R$ in Fig. 3.7a shows that for $N = 6$ particles the Gaussian background is noticeably smaller than for five particles. This indicates that the localized particles are influenced by the delocalized hopping particle, which experiences the same repulsive interaction on all lattice sites and consequently interacts with all localized particles. For seven particles the height of the peaks increases due to two hopping particles, whereas for eight particles the background increases, since more sites are doubly occupied. Finally, for nine particles all sites except one are doubly occupied which is equivalent to the tunneling of a hole in a lattice with filling $\nu = 2$. We also find the delocalization in deep lattices by analyzing the pair correlation function $G_2(x, x')$ with one particle fixed in the middle of a specific site. As seen before, the spatial correlations vanish at that site for filling factor $\nu = 1$. For noninteger filling ($6 \leq N \leq 9$) the height of the correlation function varies for each site. Thus, regarding the integer number of particles, at least some particles must be delocalized between the sites.
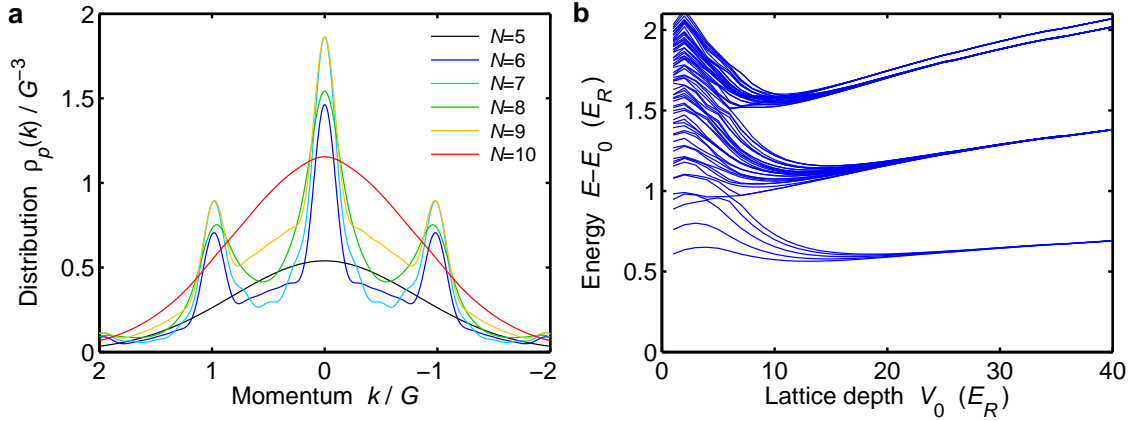
Fig. 3.7: (a) Momentum distribution of $N = 5$ to 10 atoms in a chain with five sites at $V_0 = 40E_R$. For a perfectly symmetric potential the localization of all particles can only be observed at integer filling. (b) The energy spectrum for six particles on five sites shows the formation of a lowest many-particle band.

The energy spectrum for six particles in a chain with $N_s = 5$ sites is shown in Fig. 3.7b. For deep lattices the formation of bands can be observed, which are roughly separated by the two-particle interaction energy U. An interesting feature is the splitting of the second excited band which would not be observable in the LBA. The states with higher energy have three doubly occupied sites whereas the other states have one triply occupied site. Their energy is reduced by a stronger deformation of the wave function accounting for the effective repulsive potential created by the two other atoms at the same site. As seen before for a double well, the ground state becomes quasidegenerate and lies within a band of N_s states. Therefore, the ground state is extremely sensitive to small perturbations of the lattice potential, which is discussed in the next section.

It is hardly surprising that the rich physics of noncommensurate filling can also be found in two-dimensional lattices, including the formation of a degenerate lowest band with the implications discussed above. For a two-dimensional lattice it is interesting to explore the quantum mechanical nature of the states that are contributing to the lowest band. For a 3×3 lattice with ten particles the lowest band consists of nine states due to one particle exceeding commensurate filling. Similar to Fig. 3.7a these states become quasidegenerate with increasing lattice depth representing all delocalized combinations with the two-particle interaction energy U. In Fig. 3.8 the momentum distribution of the lowest band states is plotted at $V_0 = 30E_R$ (the seventh state is not shown). The first and second excited state, the third and fourth excited state as well as the sixth and seventh excited state are exactly degenerate. The strong interference pattern of the momentum distribution is in eye-catching contrast with the Gaussian shape of a Mott insulator state and reflects the delocalization. The general structure of the shown band states can be generalized to larger noncommensurately filled lattices and to particle-hole excitations for commensurate filling.
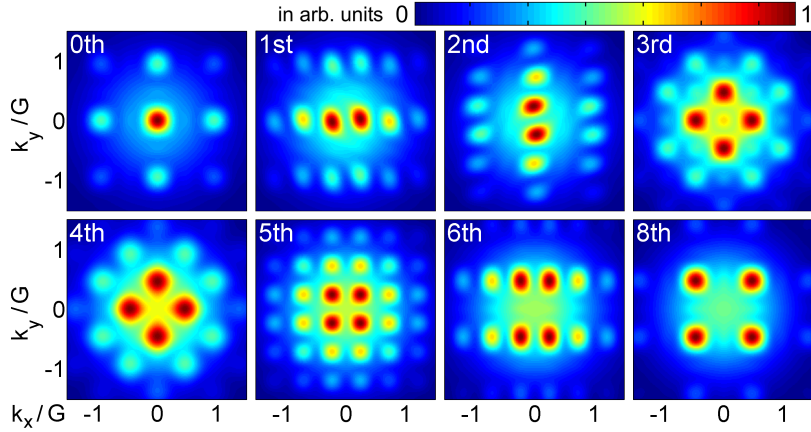
Fig. 3.8: The momentum distribution (normalized to 1) of the lowest band states of a two-dimensional 3×3 lattice with ten atoms at $V_0 = 30E_R$ (in LBA). The seventh excited state, which corresponds to the sixth excited state (rotated by $\pi/2$), is not shown here.

3.4.3 Noncommensurate filling in a harmonic confinement

As indicated in the discussion above, an additional symmetry-breaking potential forces the localization in noncommensurate systems. Perturbations of the periodic potential can cause linear combinations of the lowest band states that allow the localization of the additional particles at specific sites. Consequently, a small external confinement can destroy the partly delocalized phase in the same way as small random site offsets caused by lattice fluctuations in a Bose glass [20]. The parameter which triggers the localization of the additional N_{add} particles is the bandwidth of the lowest band which must be similar or smaller than the site offsets to attain localized particles. In experimental setups perfectly flat potentials are hard to achieve, due to the finite waist of the laser beams, which establish the optical lattice, and additional external fields. We investigate this effect by using a chain with five sites and six particles that experience an additional potential

$$V_{\mathrm{add}} = -2V_T e^{-2x^2/W_0^2} \tag{3.20}$$

with $V_T = 40E_R$. The potential is motivated by the Gaussian beam waist W_0 given in units of the lattice constant a, but it can also be approximated by the harmonic potential $\frac{4V_T}{W_0^2}x^2$. The momentum distribution at $V_0 = 20E_R$ is shown in Fig. 3.9 for different beam widths W_0 ranging from $W_0 = 10a$ to $W_0 = 200a$. The corresponding offset energies relative to the central site are given by $\epsilon_1 = \frac{160}{W_0^2/a^2}E_R$ and $\epsilon_2 = 4\epsilon_1$ (see inset of Fig. 3.9). The width of the ground state band at $V_0 = 20E_R$ is roughly $\frac{1}{50}E_R$.

In order to localize the additional particle, the offset ϵ_1 is important with respect to the bandwidth. For $W_0 = 200a$ and $W_0 = 120a$ peaks due to delocalization can be well identified in the momentum distribution, but at $W_0 = 80a$ ($\epsilon_1 = \frac{1}{40}E_R$) this structure is smeared out. At $W_0 = 40a$ ($\epsilon_1 = \frac{1}{10}E_R$) the momentum distribution matches the distribution for commensurate filling shown in Fig. 3.2 (at $V_0 \approx 15E_R$), i.e., the sixth particle is localized in the center of the lattice. Below $W_0 = 40a$ the momentum distribution does not change noticeably. Instead, the *density* changes
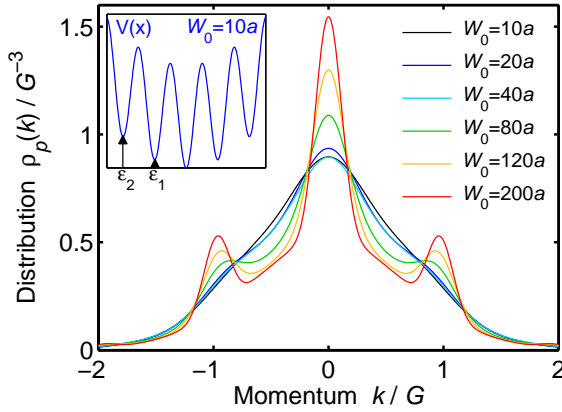
Fig. 3.9: The momentum distribution of six atoms in a chain with five sites at $V_0 = 20E_R$ for a laser beam with a finite Gauss width W_0. The inset shows the corresponding site offsets ϵ_1 and ϵ_2.

drastically, since the gain in potential energy ϵ_2 exceeds the repulsive interaction U of two particles on the same site. At $W_0 = 20a$ the density on the two outer sites vanishes and the inner sites are doubly occupied, due to a total energy gain of roughly $2(\epsilon_2 - U) \approx 2 \times (1.6E_R - 0.6E_R)$. For the stronger confinement $W_0 = 10a$, the central site is even occupied by four particles.

In addition to a harmonic potential, the lattice symmetry can also be broken by applying different moderate perturbation potentials (such as single site offsets or a linear potential). The localization process remains qualitatively the same for the studied finite systems, since basically local site offsets are responsible for the localization. Consequently, in perturbed lattices a Bose-glass-like localization of all particles can always be achieved in sufficiently deep lattices triggered by the ratio of offset energies and bandwidth. However, at intermediate lattice depth a mixed phase with N_{add} delocalized particles can be observed, if the lattice fluctuations are smaller than the bandwidth. Increasing the lattice depth (decreasing the bandwidth) first κN_s particles and in deeper potentials the remaining N_{add} particles localize. Experimentally, the observation of the mixed phase may be hindered by the finite temperature of the BEC. In stronger harmonic confinements in which the offset energies match the interaction energy U ($W_0 \lesssim 20a$ for the system above) a precursor of a shell structure can be observed, which shows regions with different occupations per site. This is further discussed in the next chapter.

3.5   Conclusions

In this chapter, bosonic atoms in finite optical lattices were studied using an exact treatment which includes the effects of higher bands. Due to the equivalence of sites, finite lattices with integer filling factors exhibit a fundamentally different behavior than those with noninteger filling factors. The well-studied superfluid to Mott-insulator transition can be recovered in finite commensurately filled one- and two-dimensional lattices with few lattice sites. The reader should be aware that the finite systems discussed here cannot exhibit macroscopic phases or a phase transition. Nonetheless, the precursors to the superfluid phase and the Mott insulator map on many aspects known from macroscopic systems. The results show the localization of atoms in deep lattices

and reveal a striking similarity to the momentum distribution observed in macroscopic systems. Furthermore, the local correlation is widely independent of the system size, which indicates that the localization process in small systems compares with that in infinite systems. The localization is also reflected by the formation of an energy gap in the energy spectrum. Finite-size effects can be observed but do not dominate the behavior of the system. Therefore, simulations with few lattice sites are also quite applicable to larger systems and offer an intuitive and detailed insight due to the accuracy and the inclusion of orbital effects.

For noninteger filling factors only the particles that correspond to integer filling localize in deep lattices whereas the additional particles are delocalized. The coexistence of localized and delocalized particles in the ground state can be observed in the momentum distribution and the pair correlation function. The energy spectrum shows the formation of a narrow lowest band in deep lattices. This causes that the ground state is extremely sensitive to perturbations of the potential such as lattice imperfections or additional confinements. Triggered by the ratio of bandwidth to site offsets, one observes the localization of all particles which is similar to the localization process in a Bose glass. In weakly confined systems this leads to a localization which occurs in deeper potentials than in lattices with commensurate filling.

Briefly, the macroscopic physics of the Mott insulator and of the Bose glass transfer to finite systems. Consequently, the detailed simulation of small systems offer important information about larger ones. In addition, using exact diagonalization allows to gain detailed insight into the localization behavior of experimentally relevant finite systems.

Excitation spectrum of Mott-insulator shells

4.1 Motivation

The equivalence of lattice sites is the foundation of solid state physics as it causes bands and lattice-periodic wave functions. Interesting physics emerges when the band is bend caused by the inhomogeneity of the system, e.g., in clusters, where bulk and surface electrons show a different physical behavior. In optical lattices, the inhomogeneity comes naturally due to the finite waist of the lattice-establishing laser beams or due to an additional dipole trap. It has been shown in a series of pioneering work [19, 21, 120] that the bosonic Mott-insulator phase can be realized in optical lattices. However, further measurements [42, 144, 146] have demonstrated that the situation is more subtle and Mott-insulator shells appear, i.e., plateaus with constant filling factors descending in integer steps from the center of the trap. The existence of superfluid regions between the Mott shells has been theoretically predicted [113, 122, 134, 147–149]. The system has previously been studied numerically, using quantum Monte Carlo [113, 147, 148] and DMRG [134], and analytically in Refs. [122, 149]. In addition to condensed matter aspects, the coexistence of compressible and incompressible regions has important implications on adiabatic heating in optical lattices [150].

This chapter presents a multiband exact diagonalization study of small systems exploring the exact excitation spectrum and the precursor of shell formation. Based on this calculation, a fast numerical method is proposed to calculate the ground-state filling and excitation energies in the limit of deep lattices. Thereby, many-particle on-site energies are incorporated capturing multiband effects. This approach is suitable for optical lattices with millions of atoms in arbitrary spatial dimensions and allows a perturbative treatment of tunneling using an effectively restricted Hilbert space. Results for small one-dimensional lattices obtained by this method are in good agreement with the exact multiband diagonalization of the Hamiltonian. For large three-dimensional systems, the formation of shells, local excitation gaps, and particle fluctuations are
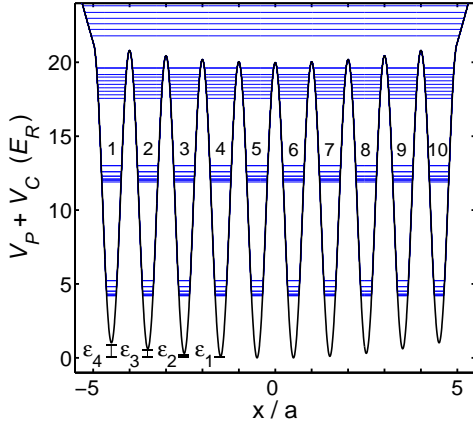
Fig. 4.1: The periodic potential V_P is superposed by a harmonic potential V_C leading to site offsets ϵ_i. The single-particle spectrum for $V_h = 0.06 E_R$ containing discrete bands is plotted within the potential.

discussed reflecting the strong inhomogeneity of the system. In particular, interfaces between the shells exhibit gapless local excitations characterized by strong particle fluctuations. Compared with algorithms such as quantum Monte Carlo [113, 147, 148] and DMRG [134], this technique gives numerically inexpensive results for large three-dimensional lattice systems in a specific parameter regime.

4.2 Exact diagonalization

As mentioned previously, the interaction of the ultracold bosonic atoms with mass m is modeled by a contact potential $g\delta(\mathbf{r}-\mathbf{r}')$ with $g = \frac{4\pi\hbar^2}{m}a_s$ and the s-wave scattering length a_s (section 2.3). Using the bosonic field operator $\hat{\psi}(\mathbf{r})$, the Hamiltonian including the repulsive two-particle interaction reads

$$\hat{H} = \int d^3r \left(\hat{\psi}^\dagger(\mathbf{r}) \left[\frac{\hat{\mathbf{p}}^2}{2m} + V_P(\mathbf{r}) + V_C(\mathbf{r}) \right] \hat{\psi}(\mathbf{r}) \right.$$
$$\left. + \frac{g}{2} \hat{\psi}^\dagger(\mathbf{r})\hat{\psi}^\dagger(\mathbf{r})\hat{\psi}(\mathbf{r})\hat{\psi}(\mathbf{r}) \right), \tag{4.1}$$

where the periodic potential V_P of the optical lattice is given by $V_{0,x}\cos^2(\pi x/a) + V_{0,y}\cos^2(\pi y/a) + V_{0,z}\cos^2(\pi z/a)$ with the lattice spacing a. The atoms experience an additional confinement potential V_C caused by the finite Gaussian beam waist W_0 of the laser beams and/or an additional dipole trap with frequency ω_d (see section 2.1.3). Using a harmonic approach, the confining potential in x direction is given by

$$V_C = V_h \frac{x^2}{a^2}, \tag{4.2}$$

where $V_h = \frac{1}{2}m\omega_{\text{eff}}^2 a^2$ with $\omega_{\text{eff}}^2 \approx \frac{4(V_{0,y}+V_{0,z})}{mW_0^2} + \omega_{d,x}^2$.

For the exact diagonalization, the potential is truncated to an one-dimensional lattice with $m_x = 10$ and $m_y = m_z = 1$ sites by adding a smooth boundary (see section 2.4.1). The calculation is performed for ^{87}Rb atoms with $a_s = 100a_0$, where a_0 is the Bohr radius, $N = 10$ particles,
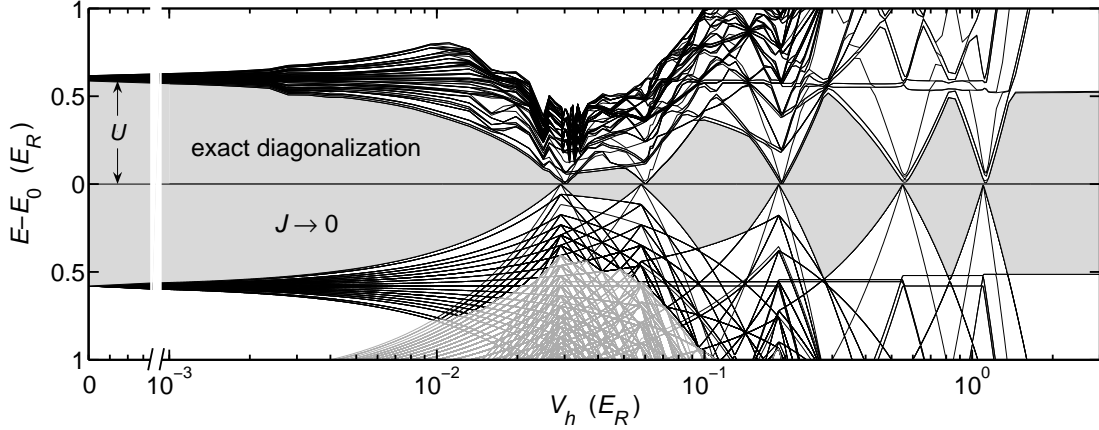
Fig. 4.2: The many-particle energy spectrum (91 states) obtained by exact diagonalization (upper half) and for vanishing tunneling (lower half) as a function of the harmonic confinement strength V_h. Additional states in the $J \to 0$ spectrum are plotted in gray. The energy scale is relative to the ground-state energy E_0 and the gap to the first excited state is depicted in gray.

a lattice constant $a = 515$ nm, and a transversal lattice depth $V_{0,y} = V_{0,z} = 40 E_R$, where $E_R = \frac{h}{8ma^2}$ is the recoil energy. The lattice depth in the longitudinal direction is $V_{0,x} = 20 E_R$, leading to a system deep within the Mott-insulator phase for a vanishing harmonic confinement ($V_h = 0$). The potential of the one-dimensional lattice, shown in Fig. 4.1, depicts the energy offsets ϵ_i of the modeled chain, which are labeled $\epsilon_0 = 0$ for the two equivalent central sites and ϵ_4 for the outermost sites. The parabolic shape of the confinement leads to large energy offsets of outer sites, although the offsets are small for central ones. At $V_h = 0$, the single-particle spectrum shows three discrete bands that comprise ten delocalized Bloch states each (corresponding to the number of sites), where the width of the lowest band is $4J \approx 2.4 \times 10^{-3} E_R$. Due to the symmetry of the potential, the two lowest bands contain nearly degenerate symmetric and antisymmetric states localized at two equivalent sites. For larger values of V_h the "band" width is given basically by the offset of the outermost sites (see Fig. 4.1). At $V_h \gtrsim 0.4 E_R$, the outermost site offset $\epsilon_4 \gtrsim 8 E_R$ causes the lowest two single-particle bands to overlap.

To calculate the many-particle spectrum by means of exact diagonalization, the many-particle basis is limited to $500\,000$ Fock states with lowest energy and the orbital degrees of freedom in y and z direction are frozen out. Afterwards, the matrix elements of (4.1) are calculated and the 91 lowest eigenvalues determined (the ground state and the 90 states of the first band for $V_h \to 0$). The exact diagonalization method includes particle correlations and the admixture of higher bands, i.e., orbital changes taking place for higher fillings, but is strongly limited to systems with few lattice sites. The many-particle spectrum is plotted in Fig. 4.2 (upper half) relative to the ground-state energy E_0 as a function of the harmonic confinement V_h using a logarithmic scale. For convenience, the band gap between the ground state and the first excited state is depicted in gray.

For vanishing confinement ($V_h = 0$), the spectrum shows that the first excited band is gapped from the ground state by the on-site interaction energy of two particles $U \approx 0.6 E_R$, which corresponds

to the gap of the macroscopic Mott-insulator phase. The atoms are strongly localized at single lattice sites, so that all lattice sites are occupied by exactly one particle per site. Increasing the harmonic confinement leads to abrupt crossovers to states with higher integer occupation numbers, i.e., finite size correspondents to Mott shell configurations. In the many-particle spectrum these crossover points are reflected by vanishing energy gaps. In between these points lobe-like energy gaps can be observed, where the lobes correspond to the occupation number configurations 1-1-1-2-2-1-1-1, 1-2-2-2-2-1, 2-3-3-2, 1-4-4-1, and finally for $V_h > 1E_R$ a states with 5 particles on the two central sites.[1] For $V_h < 0.03E_R$ the lattice is commensurately filled with one particle per site. In this region, the excited band broadens with increasing V_h leading to a slowly decreasing energy gap. At $V_h \approx 0.03E_R$, where the energy gap vanishes, a multitude of low-lying excitations are possible leading to a compressible system. At this point, the double occupation of the central sites, which corresponds to the on-site energy U, becomes energetically preferable to the occupation of the outermost sites with $\epsilon_4 = 20V_h$. Analogous situations exist at the other crossovers, so that the shell structure is dominated by the ratio of on-site interaction $\frac{n_i(n_i-1)}{2}U$ to individual site offsets ϵ_i. The critical behavior separating different filling configurations manifests itself in the disappearance of the excitation gap.

4.3   Classical approach

The nature of the excited states, however, is more complicated and the energy spectrum, which contains important physics, is rather complex. Let us therefore consider the "classical" case of vanishing tunneling ($J \to 0$) which is valid deep within the Mott-insulator phase. Using this approach, the basic features of the spectrum can be uncovered. Furthermore, larger systems can be studied, for which finite tunneling can be reintroduced perturbatively in a second step, dealing with a drastically reduced basis set. For $J \to 0$, the truncated Bose-Hubbard Hamiltonian is given by

$$\hat{H} = \sum_i \frac{\hat{n}_i(\hat{n}_i - 1)}{2}U + \epsilon_i \hat{n}_i \tag{4.3}$$

and the localized occupation number basis $|n_1, n_2, ..., n_M\rangle$ is an eigenbasis of the Hamiltonian, where $M = m_x m_y m_z$ denotes the number of sites. In principle, finding the ground state requires to calculate the total energy $E = \langle \hat{H} \rangle$ of all possible basis states. The efficiency of this method is very limited due to the huge number of basis states $\frac{(N+M-1)!}{N!(M-1)!}$ for large lattices, where N is the number of particles. Following Refs. [122, 149], in the local density approximation an effective local chemical potential $\tilde{\mu}(\mathbf{r}) = \mu - V_C(\mathbf{r})$ can be introduced, and the ground state is then constructed via filling each lattice site up to the local chemical potential $\tilde{\mu}$ separately. Using the continuous limit, the chemical potential $\mu(N)$ is calculated analytically in Ref. [149] and numerically in Ref. [122]. The continuous limit is, however, only applicable to smooth confining potentials. In general, the self-consistent determination of $\mu(N)$ is tedious. Therefore, the following iterative algorithm can be used for the solution of (4.3) directly in the microcanonical ensemble with a fixed total particle number $N = \sum_i n_i$. It allows us also to construct the lowest

---

[1]For certain system parameters (N, m_x, V_h) a degeneracy of the ground state can occur.
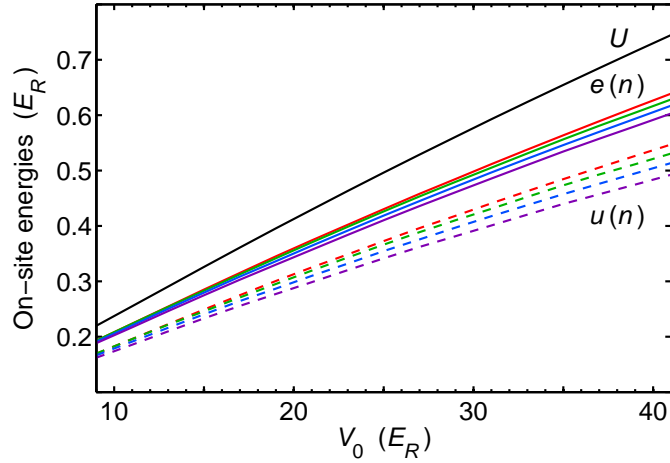
Fig. 4.3: A comparison of Hubbard on-site interaction U, the many-particle interaction energy $u(n)$, and the total on-site energy $e(n)$ per atom pair. The single-site many-particle wave function is determined by exact diagonalization for $n = 2$ particles (highest energy) to $n = 5$ particles (lowest energy).

excited states of the system, which we can compare with the exact calculation shown in the upper half of Fig. 4.2. Starting with an empty lattice, the N particles are added successively to that site j of the lattice, where the expense of energy $\mu_j^+ = n_j U + \epsilon_j$ is presently minimal. This procedure gives the lowest energy occupation for any particle number N, since $\mu_j^+ > 0$ and all sites are uncorrelated. The complexity of this algorithm is given by $O(NM)$, since each step adds one particle to one of M possible sites. This allows the calculation of the exact occupation numbers for a million particles, e.g., $N = M = 100^3$, within seconds on an ordinary desktop computer. Hence, this method is considerable useful for the design and interpretation of experiments.

4.4 Orbital degrees of freedom

Compared with the exact diagonalization results for the one-dimensional lattice, the crossover points can, in principle, be reproduced with this method but their positions are shifted. To study this effect, which is enhanced for higher filling factors, the on-site interaction is calculated for n particles by exact diagonalization using a multiorbital basis. Since the lattice is sufficiently deep, it is valid to approximate the multiband Wannier functions $w_i(\mathbf{r})$ by the wave functions of a single sinusoidal lattice site using hard boundary conditions, i.e, infinite walls at $\pm a/2$. The correlationless Hubbard on-site interaction

$$U = g \int d^3r \, |w_0(\mathbf{r})|^4 \tag{4.4}$$

does not incorporate that particles tend to avoid each other for repulsive interaction. This causes broadening of the particle density and was addressed experimentally in Ref. [144]. Using the correct many-particle wave function Ψ_n for n particles, the expectation value of the on-site

interaction becomes

$$u(n) = \frac{g}{n(n-1)} \int d^3r \, \langle \hat{\psi}^\dagger(\mathbf{r}) \hat{\psi}^\dagger(\mathbf{r}) \hat{\psi}(\mathbf{r}) \hat{\psi}(\mathbf{r}) \rangle, \tag{4.5}$$

which is normalized to the interaction energy per atom pair. The results that are depicted in Fig. 4.3 show that $u(n)$ determined by exact diagonalization deviates strongly from the Hubbard on-site interaction U. As expected, the interaction energy $u(n)$ decreases with an increasing number of particles per site. However, not only $u(n)$ changes when the modification of wave functions is taken into account. In fact, the admixture of correlated states and the broadening of the density change the expectation value of on-site kinetic and potential energy. The total on-site energy is the eigenvalue of the many-particle Schrödinger equation

$$\hat{H}_i \, \Psi_n = E_n \, \Psi_n \tag{4.6}$$

restricted to single-site wave functions and using the full Hamiltonian (4.1) with $V_h = 0$. The normalized on-site energies

$$e(n) = \frac{2(E_n - E_n^0)}{n(n-1)} \tag{4.7}$$

are plotted in Fig. 4.3, where E_n^0 is the energy of the noninteracting system. It shows that the total interaction energy $e(n)$ lies between U and $u(n)$. Nevertheless, the deviation of $e(2)$ from the Hubbard U is large. Using $U = e(2)$, the crossovers are still shifted noticeably for higher fillings (large V_h) comparing with the results of the fully quantum mechanical calculation (upper half of Fig. 4.2). Therefore, the correct total interaction energy $e(n_j)$ for a single site with the occupation n_j is incorporated in the "classical" approach. Note that the optimization problem remains the same if substituting the energy $\mu_j^+ = n_j U + \epsilon_j$ for adding one particle by $\mu_j^+ = e(n_j + 1) - e(n_j) + \epsilon_j$. In the lower half of Fig. 4.2 the energy spectrum for vanishing tunneling ($J \to 0$) is shown using the corrected values of the on-site interaction. In this case the crossover energies corresponding to the vanishing gaps for $J \to 0$ are in good agreement with the exact diagonalization of the one-dimensional lattice. This result shows, in general, that the introduced filling-dependent on-site interaction $e(n)$ is appropriate to describe effects arising from orbital changes. The small remaining shift of the crossover energies in Fig. 4.2 is due to the "classical" treatment of the states in our approach.

The energy gap can be obtained by removing one particle from site j and adding it to site $k \neq j$. Finding the minimum excitation energy $\Delta E_{j,k}$ for all possible j and k has, in general, the complexity $O(M^2)$. The excitation energy is given by $\Delta E_{j,k} = \mu_j^+ + \mu_k^-$, where

$$\mu_j^+ = e(n_j + 1) - e(n_j) + \epsilon_j > 0 \tag{4.8}$$

for adding a particle at site j and

$$\mu_k^- = e(n_k - 1) - e(n_k) - \epsilon_k < 0 \tag{4.9}$$

for removing a particle from site k. Thus, it is sufficient to minimize μ_j^+ and μ_k^- separately, which reduces the complexity to linear order in M. Finding the next excited state is more complicated, since this state may be an excitation of the ground state but also of the first excited
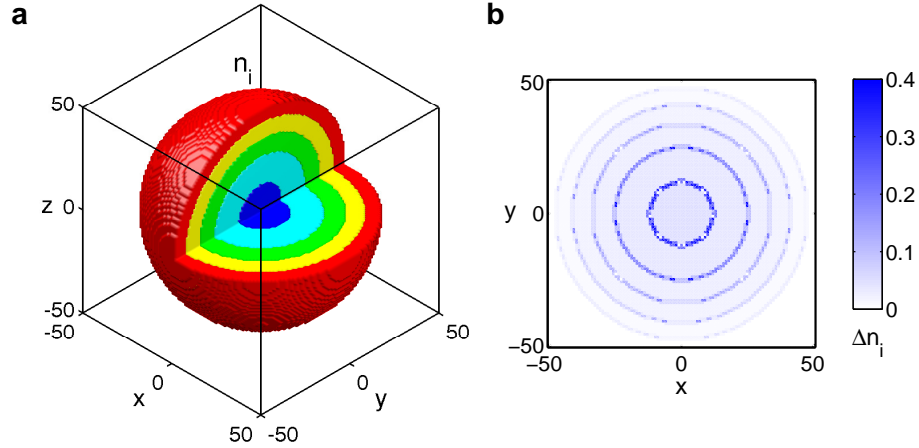
Fig. 4.4: (a) Cut through the occupation number distribution n_i of a three-dimensional lattice ($N = 10^6$, $J = 0$, $V_h = 7.5 \times 10^{-4} E_R$, and $V_0 = 25 E_R$) showing fillings $n_i = 1$ (red) to $n_i = 5$ (blue). (b) Particle fluctuations Δn_i due to finite tunneling ($J = 10^{-3} E_R \approx 2 \times 10^{-3} U$) appear at the surfaces of the shells ($z = 0$ plane).

state. For the calculation of the spectrum, a slightly modified Dijkstra algorithm can be used, where one considers the ground state as the node of a graph. This node is expanded according to all possible excitations. Iteratively, the node with the minimum energy, which is not expanded yet, is expanded. Consequently, the list of expanded nodes represents the states with the lowest energy. It is necessary, however, to check whether a created excited state is already a node in the graph, which is a major contribution to the complexity of the Dijkstra algorithm, but can numerically be highly optimized. Using this procedure, the resulting energy spectrum (lower half of Fig. 4.2) reproduces well the basic features, i.e., the band gap, the overall shape, and the density of states, of the exact calculation (upper half). Because of interactions, the degeneracy of states is lifted in the exact spectrum, so that the actual energies of many states are shifted.

4.5 Macroscopic lattices

Transferring the above results to macroscopic lattices is not straightforward. Enlarging the system's size causes the differences in offset energies of neighboring sites $\epsilon_j - \epsilon_k$ to decrease substantially when keeping the offset of the outermost sites fixed. This causes the width and the height of the energy lobes in the spectrum to decrease because a huge number of configurations become possible when increasing the number of particles and lattice sites. This process is drastically enhanced in two- and three-dimensional lattices, where practically the band gap vanishes for all confinement strengths V_h. The only exception is the real Mott-insulator phase, where the outermost sites have an offset smaller than U. In fact, the excitation spectrum of the total system becomes more or less continuous. This might appear contradictory to the insulating property at first glance but the system is inhomogeneous and only some of the atoms can perform
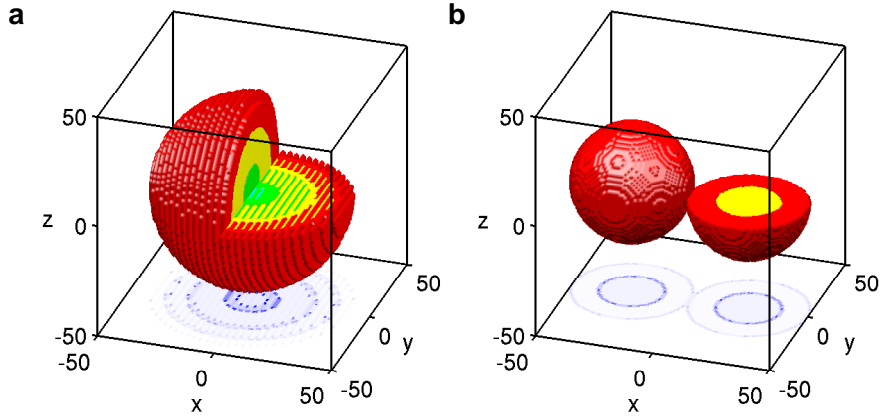
Fig. 4.5: (a) An additional standing wave with periodicity $3a$ and amplitude U causes alternating fillings in x direction ($N = 3.5 \times 10^5$). (b) An added $-50V_h|x|$ potential leads to two separate atom spheres ($N = 1.5 \times 10^5$). The fluctuations Δn_i for $J = 10^{-3}E_R$ and $z = 0$ are shown at the bottom (see Fig. 4.4 for the color map and other parameters).

gapless excitations. Therefore, local properties are more suited to describe the system, such as particle number fluctuations and the local excitation spectrum. It has already been pointed out [113, 134, 148, 149] that the regions with fixed occupation number, the Mott-insulator shells, are surrounded by compressible shells for nonnegligible tunneling.

Exemplarily, the occupation number distribution n_i for $N = 10^6$ particles in a three-dimensional lattice is depicted in Fig. 4.4a. It shows the expected shell structure with filling factors five (in the center) to one. An advantage of the presented numerical algorithm is that it is also applicable to confining potentials which vary rapidly in space. It can thus be used to tailor more sophisticated shell configurations for experiments. Since the on-site interaction energy U is relatively small compared with the depth of the lattice wells, the local filling factors can be adjusted without a stronger perturbation of the three-dimensional lattice. Additional laser beams or magnetic fields can thus be used to obtain complex spatial distributions of atoms with specific filling factors. Figure 4.5a shows the occupation number distribution for an added periodic potential in x direction $V_C = V_h x^2/a^2 + U \cos^2(\pi x/a')$ with the periodicity $a' = 3a$ motivated by Ref. [89]. The superlattice structure leads to alternating local fillings. As a second example, an added hat-shaped ($-|x|$) potential causes the formation of two separate atomic clouds, shown in Fig. 4.5b, that are in touch with each other at the origin.

4.6 Excitations and finite tunneling

At the outer surface of each shell, almost gapless excitations are possible via the hopping of a particle to another site, whereas the inner surface can easily absorb particles. This is shown quantitatively in Fig. 4.6a (upper half), where $\Delta E_i^- = \mu_i^- + \min_j(\mu_j^+)$ is the minimal energy for removing one particle from site i and adding it to another site j. The minimal energy for adding one particle to site i (and removing it from site j) is denoted as $\Delta E_i^+ = \mu_i^+ + \min_j(\mu_j^-)$
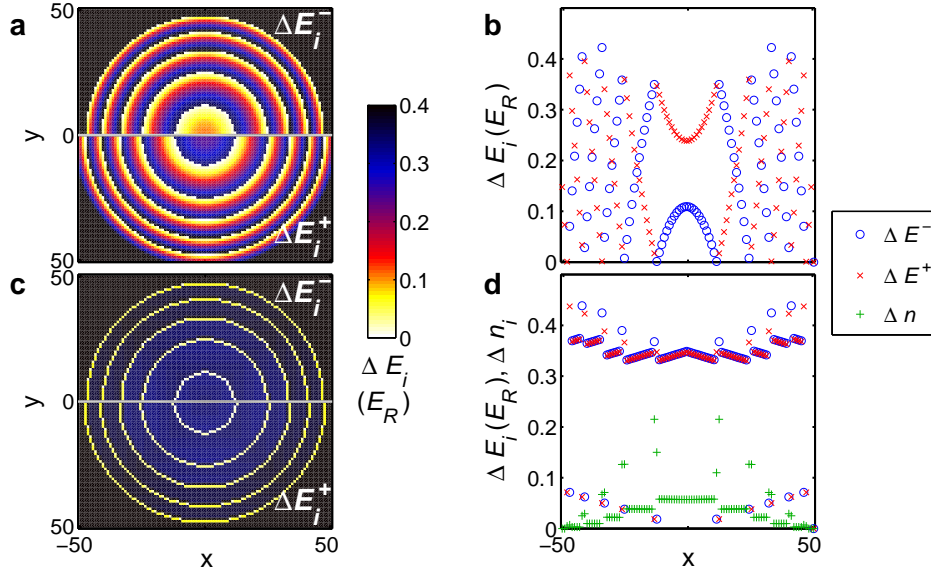
Fig. 4.6: The minimal excitation energy in the $z = 0$ plane (a) and for $y = z = 0$ (b) for particles hopping from site i (E_i^-) and to site i (E_i^+). The excitation energies only accounting for nearest-neighbor hopping in the $z = 0$ plane (c) and for $y = z = 0$ including particle fluctuations Δn_i for $J = 5 \times 10^{-3} E_R$ (d).

(lower half of Fig. 4.6a). The local excitation gap vanishes at the outer and inner surfaces and increases strongly within the shells. The excitation energies $\Delta E_i^{\pm}$ are explicitly shown for sites with $y = z = 0$ in Fig. 4.6b. It reflects basically the harmonic shape of the confinement, so that ΔE_i^+ and ΔE_i^- are positive and negative parabolas, respectively, subtracted by integer multiples of the on-site interaction. The situation changes drastically, if accounting only for excitations to nearest neighbors as shown in Figs. 4.6c and 4.6d. Low energy excitations (either ΔE_i^+ or ΔE_i^-) can occur exclusively on sites directly at the boundary between different shells. Within the bulk the single-particle excitation gap is wide and nearly constant. Therefore, the nearest-neighbor tunneling is, in general, strongly suppressed at these sites, where the system is a good insulator.

In the following, a perturbative approach is used to obtain particle fluctuations for finite tunneling J. For each site i the subsystem containing the site i and all neighboring sites is considered. The diagonalization of this subsystem with finite tunneling $-J \sum_{\langle i,j \rangle} \hat{b}_i^\dagger \hat{b}_j$ allows an approximative calculation of the particle fluctuations $\Delta n_i = \sqrt{\langle \hat{n}_i^2 \rangle - \langle \hat{n}_i \rangle^2}$. For the example above, weak tunneling causes finite fluctuations Δn_i at the boundaries of the shells, which is shown in Figs. 4.4b and 4.5 for $J = 10^{-3} E_R$ and in Fig. 4.6d for $J = 5 \times 10^{-3} E_R$. Note that due to the finite cell size of the lattice, the results are not completely spherically symmetric. In accordance with the nearest-neighbor excitation energies, the fluctuations affect only sites directly at the surfaces of the shells. Because of the larger slope of the confinement and the lower filling, the tunneling decreases for outer shells. Within the bulk of the Mott shells small particle fluctuations can be observed due to the finite tunneling. However, the fluctuations on the surface enhance the tunneling of atoms next to the surface, which is not covered by this perturbative approach and would require a self-consistent calculation. The narrow energy gaps of particles close to the surface can in principle

cause near-resonant tunneling to nonnearest neighbors, so-called variable range hopping [151]. Due to the relatively strong V_h (compared with J) and the regularity of the potential, only sites on the surface, which are dominated by nearest-neighbor hopping, have suitably low excitation energies.

The presented method provides the lowest energetic states (including particle-hole excitations) and is suitable to restrict the Hilbert space effectively. The obtained states can be used as a starting point for exact diagonalization, quantum Monte Carlo, and dynamical mean-field calculations including tunneling and finite temperatures. In particular, the diagonalization of the one-dimensional lattice (Fig. 4.2) could be performed with much fewer basis states.

4.7   Conclusions

In summary, the excitation spectrum and exact site occupation numbers for confined optical lattices deep within the Mott-insulator regime have been studied. In good agreement with the exact diagonalization for small one-dimensional lattices, a numerical method has been presented that allows for negligible tunneling the exact treatment of macroscopic optical lattices with arbitrary shape of the confining potential. Adding slowly varying potentials to the optical lattice can give rise to complex filling structures. I have calculated the numerically exact many-particle on-site energies and have shown that introducing a filling factor depending on-site interaction can be incorporated to cover orbital changes. For small systems, the many-particle spectrum contains lobes, whereas for macroscopic systems nearly gapless excitations are always possible at the boundaries of the Mott shells. Within a given Mott shell the local excitation energy varies strongly leading to compressible sites close to the surface and incompressible inner sites. A perturbative treatment for finite tunneling shows strong particle fluctuations at the boundaries between the shells, where the Mott-insulator gap vanishes. Finally, the presented method can serve as a reduction scheme for the Hilbert space for further numerical treatments.

Self-trapping of bosonic and fermionic atoms

*The main results in this chapter have been published in Refs. [2] D.-S. Lühmann, K. Bongs, K. Sengstock, and D. Pfannkuche, Self-Trapping of Bosons and Fermions in Optical Lattices, Physical Review Letters **101**, 050402 (2008) and [3] T. Best, S. Will, U. Schneider, L. Hacker-müller, D. van Oosten, I. Bloch, and D.-S. Lühmann, Role of Interactions in ^{87}Rb-^{40}K Bose-Fermi Mixtures in a 3D Optical Lattice, Physical Review Letters **102**, 030408 (2009).*

5.1 Motivation

Degenerate mixtures of bosonic and fermionic atoms in optical lattices offer new insight into a novel many-body system with strong particle correlations. The constituents behave contrary to each other with respect to quantum statistics and intraspecies interaction. The coupling by interspecies interaction gives rise to a fascinating system, which recently has become accessible in ultracold atom experiments [3, 29, 30]. In its solid-state counterpart electrons interact with lattice vibrations, where prominent examples are the superconductivity and the formation of polarons. In optical lattices, bosons and fermions are more alike and allow to study the effect that fermions induce on bosons and vice versa on an equal footing. In particular, the interplay between intra- and interspecies interaction and tunneling of both components is reflected in a complex phase diagram. The Bose-Fermi-Hubbard model, which is introduced in section 2.3.2 and serves as the simplest description of Bose-Fermi mixtures in lattices, has been studied theoretically using various approaches [31–37, 152–166]. In particular, the phase separation between bosons and fermions, the supersolid phase [32–34], the charge-density wave [34, 35], and the pairing of bosons and fermions forming phases of composite particles [36, 37] have been investigated.

Recently, the first experiments with bosonic ^{87}Rb and fermionic ^{40}K atoms have been realized in optical lattices [29, 30] and have drawn much attention due to an unexpected large shift of the bosonic phase transition between the superfluid phase and the Mott insulator. The effect, which is

substantial even for a small ratio of fermionic to bosonic atoms, was controversially discussed [30, 156, 161, 167], and a relatively small influence of the boson-fermion interaction on the transition was proposed. Within the Bose-Fermi-Hubbard model, the repulsive on-site interaction of bosons is partially screened by the attractive boson-fermion interaction, which was studied numerically in Ref. [156] and analytically in Refs. [159, 162]. This effect reduces the effective repulsive on-site interaction energy of the bosonic atoms U and extends the superfluid phase in the phase diagram. In addition, a redistribution of the bosons due to a pinning to fermion occupied sites must be taken into account, which can cause a bosonic accumulation [156]. Consequently, the Bose-Fermi-Hubbard model predicts a moderate shift of the Mott-insulator phase transition towards deeper lattice depths, whereas in experiments a large shift towards shallower lattices has been found [29, 30]. Moreover, the loss of coherence due to an adiabatic heating in the optical lattice was addressed [156, 161]. Due to the different temperature dependence of bosonic and fermionic contributions to the entropy, the effective temperature of the ^{87}Rb -^{40}K mixture rises, assuming that the lattice is ramped up fully adiabatically. This increase of temperature can lead to a decrease of the bosonic visibility.

In preference for the single-band Hubbard-type Hamiltonian, the influence of interaction induced orbital changes was widely neglected in calculations performed for optical lattices. In the following, the enhanced localization of bosonic atoms by fermionic atoms in three-dimensional optical lattices is investigated by means of exact diagonalization. In this chapter, I show that the attractive interaction between bosons and fermions causes substantially modified single-site densities. The nonlinearity of the interaction leads to a mutual trapping of ^{87}Rb and ^{40}K atoms in the centers of the wells. Because of this mutual interaction, the fermion orbitals are substantially squeezed, which results in a strong deformation of the effective potential for bosons. This effect is enhanced by an increasing bosonic filling factor and causes a self-trapping of the bosons mediated by the attractive boson-fermion interaction. Using renormalized Bose-Hubbard parameters, this leads to a large shift of the transition between the superfluid and the Mott-insulator phase, which coincides with first experimental results in 2006 [29, 30]. A nonlinear dependency of the critical potential depth on the boson-fermion interaction strength is found, which is directly tunable in experimental setups applying Feshbach resonances (section 2.2.2).

Succeeding the first two experiments with Bose-Fermi mixtures, a new experimental setup [3] permits optical lattices with a rather homogeneous filling. In particular, using a Feshbach resonance enables to tune the interspecies interaction. Analyzing the condensate fraction of the bosonic atoms, this experiment shows an increasing shift of the Mott-insulator transition towards shallower lattices with increasing attractive boson-fermion interaction. The results are in good quantitative agreement with the presented renormalization of the Hubbard parameter and the self-trapping behavior found in the exact diagonalization calculation. The results in this chapter, in general, demonstrate the important role of higher Bloch bands for the physics of attractively interacting quantum gas mixtures in optical lattices and are of direct relevance to experiments with ^{87}Rb - ^{40}K mixtures.

5.2   Self-trapping in Bose-Fermi mixtures

5.2.1   Exact diagonalization

The interaction between fully spin-polarized neutral atoms in the ultracold regime can be described by a contact potential $g\delta(\mathbf{r} - \mathbf{r}')$ as discussed in section 2.2.1. The strength of the repulsive intraspecies interaction between ^{87}Rb atoms is given by $g_B = \frac{4\pi\hbar^2}{m_B}a_B$, where $a_B \approx 100a_0$ is the bosonic scattering length and a_0 the Bohr radius. Neglecting p-wave scattering between ^{40}K atoms, the fermionic particles do not interact with each other. The interspecies interaction between ^{87}Rb and ^{40}K atoms far from a Feshbach resonance is attractive with the strength $g_{BF} = \frac{2\pi\hbar^2}{\mu}a_{BF}$, where $\mu = \frac{m_B m_F}{m_B + m_F}$ is the reduced mass and $a_{BF} \approx -205a_0$ [168]. The Hamiltonian of a Bose-Fermi mixture in an optical lattice is given by

$$\hat{H} = \hat{H}_B + \hat{H}_F + \hat{H}_{BF}, \tag{5.1}$$

where $\hat{H}_B$ describes the system of interacting bosons, $\hat{H}_F$ the system of noninteracting fermions, and $\hat{H}_{BF}$ the interaction between bosons and fermions [31, 32]. Using the bosonic and fermionic field operators $\hat{\psi}_B(\mathbf{r})$ and $\hat{\psi}_F(\mathbf{r})$, the three parts of the Hamiltonian can be written as

$$\hat{H}_B = \int d^3r \, \hat{\psi}_B^\dagger(\mathbf{r}) \left[\frac{\hat{\mathbf{p}}^2}{2m_B} + V(\mathbf{r}) + \frac{g_B}{2}\hat{\psi}_B^\dagger(\mathbf{r})\hat{\psi}_B(\mathbf{r}) \right] \hat{\psi}_B(\mathbf{r}),$$

$$\hat{H}_F = \int d^3r \, \hat{\psi}_F^\dagger(\mathbf{r}) \left[\frac{\hat{\mathbf{p}}^2}{2m_F} + V(\mathbf{r}) \right] \hat{\psi}_F(\mathbf{r}),$$

$$\hat{H}_{BF} = g_{BF} \int d^3r \, \hat{\psi}_B^\dagger(\mathbf{r})\hat{\psi}_F^\dagger(\mathbf{r})\hat{\psi}_F(\mathbf{r})\hat{\psi}_B(\mathbf{r}), \tag{5.2}$$

with the periodic potential $V(\mathbf{r})$ of the optical lattice.

As described in section 2.4, the exact diagonalization of the Hamiltonian (5.2) is performed in a many-particle basis that includes higher orbital states and is truncated at a sufficiently high energy. In the calculation, the bosonic and the fermionic subspace are diagonalized separately using a self-consistent interaction potential, which converges within a few cycles. This method is presented in section 2.4.4 and is recapitulated here shortly. For a known fermionic density $\rho_F(\mathbf{r}) = \langle\hat{\Psi}_F^\dagger\hat{\Psi}_F\rangle$ the effective Hamiltonian of the bosonic subsystem is given by

$$\hat{H}_B^{\text{eff}}(\rho_F) = \hat{H}_B + g_{BF} \int d^3r \, \rho_F(\mathbf{r}) \, \hat{\psi}_B^\dagger(\mathbf{r})\hat{\psi}_B(\mathbf{r}). \tag{5.3}$$

The latter term represents the interaction with the fermionic density and leads to a bosonic effective potential

$$V_B^{\text{eff}}(\rho_F) = V(\mathbf{r}) + g_{BF}\rho_F(\mathbf{r}). \tag{5.4}$$

Starting with the density of noninteracting fermions, we determine the boson density $\rho_B(\mathbf{r}) = \langle\Psi_B^\dagger\Psi_B\rangle$ by diagonalization of $\hat{H}_B^{\text{eff}}$. Afterwards, the fermionic subsystem can be diagonalized using the fermionic effective potential

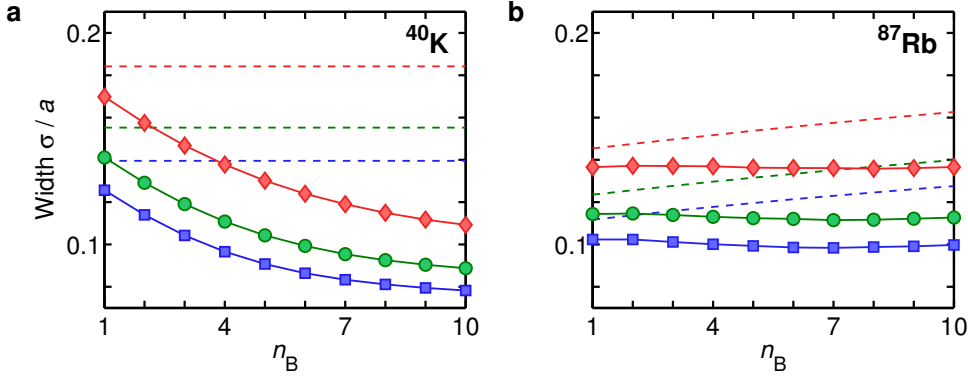$$V_F^{\text{eff}}(\rho_B) = V(\mathbf{r}) + g_{BF}\rho_B(\mathbf{r}), \tag{5.5}$$

Fig. 5.1: The width of the density profile for (a) one fermionic ^{40}K atom and (b) n_B bosonic ^{87}Rb atoms for $V_0 = 8E_R$ (♦), $V_0 = 14E_R$ (●), and $V_0 = 20E_R$ (■). The dashed lines are obtained for vanishing boson-fermion interaction. Because of the mutual attraction, the densities are substantially squeezed.

which leads to a new fermion density. This loop is iterated until effective potentials and energies are converged.

In the following, I concentrate on orbital changes in experiments with red detuned optical lattices as used in Refs. [29, 30] with a lattice constant $a = \pi/k = 515$ nm [30]. Note that orbital effects, in general, depend on the density, which varies with the lattice constant. In the experimental setup, one fermion ($n_F = 1$) and several bosons are present at each lattice site. The maximal number of bosons at a lattice site varies due to the applied confinement and the boson-fermion interaction and is reported to be $n_B \gtrsim 5$ in Ref. [30]. Here, we address the range $1 \leq n_B \leq 10$, although in experiments the loss rate increases substantially for high filling factors [29]. To study the effect caused by the mutual interaction, it is instructive to restrict the particles to a single lattice site. Hence, the diagonalization[1] is performed for atoms in a symmetric well with the shape

$$V(\mathbf{r}) = V_0 \left[\sin^2(kx) + \sin^2(ky) + \sin^2(kz) \right],$$ (5.6)

since a simple harmonic approach as in Refs. [30, 167] leads to noticeably narrower ^{40}K densities. A smooth boundary is attached to the $\sin^2$-shaped single-site potential as described in section 2.4.1.

To illustrate the orbital changes, Gaussians are fitted to the calculated densities for bosons and fermions

$$\rho_{B/F}(\mathbf{r}) = n_{B/F}(\sqrt{2\pi}\sigma_{B/F})^{-3} \exp(-r^2/2\sigma_{B/F}^2),$$ (5.7)

where deviations from the real shape are relatively small using

$$\sigma_{B/F} = \frac{1}{\sqrt{2\pi}} \left(\frac{n_{B/F}}{\rho_{B/F}(0)} \right)^{1/3},$$ (5.8)

where $\rho_{B/F}(0)$ is the peak density at the center of a site. Although all results are obtained using the computed expectation value for the densities $\rho_{B/F}$, a Gaussian shape of the densities is assumed in

---

[1] We use parity conservation and up to 25 000 bosonic basis states for ten bosons.
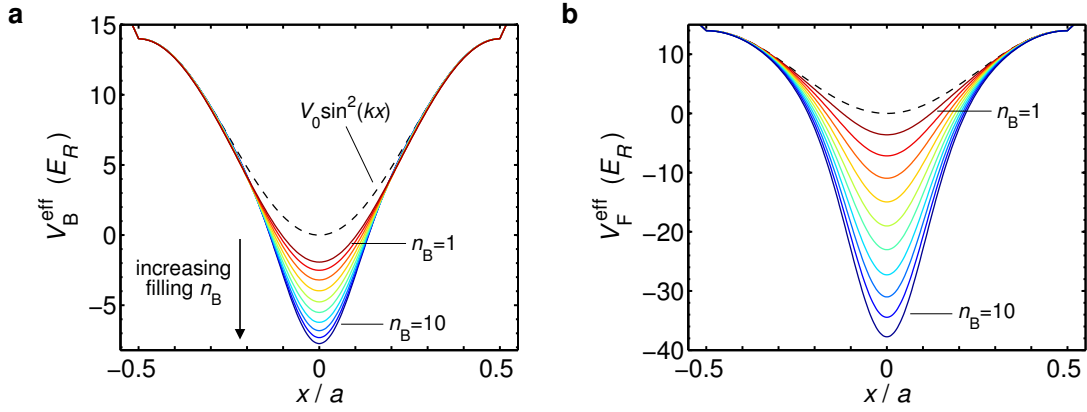
Fig. 5.2: (a) The effective potential V_B^{eff} for n_B bosonic ^{87}Rb atoms at one symmetric site created by one fermionic ^{40}K atom. The dashed line represents the unperturbed lattice potential $V(x)$ with $V_0 = 14E_R$ for vanishing boson-fermion interaction. (b) The effective potential V_F^{eff} experienced by the fermion.

the discussion for simplicity. The width of the Gaussians $\sigma_{B/F}$ as a function of the bosonic filling n_B is shown in Fig. 5.1 for the lattice depths $V_0 = 8E_R$, $14E_R$, and $20E_R$, where $E_R = \frac{\hbar^2 k^2}{2m_B}$ is the recoil energy of ^{87}Rb atoms. Since ^{40}K atoms are much lighter than ^{87}Rb atoms, the resulting density profile for a ^{40}K atom on a single lattice site is much broader than for the ^{87}Rb atoms. For a pure bosonic system (dashed lines), we observe an increase of the bosonic width with an increasing number of ^{87}Rb atoms, due to the boson-boson repulsion. The interaction with the single fermion leads to a compression of the boson density (solid lines), which becomes even narrower than the single-particle boson density. In fact, the bosonic width decreases slightly with an increasing n_B and reaches a minimum at $n_B = 7 - 8$. This effective attractive behavior is surprising, since the attractive interaction between bosons and fermions scales linearly with n_B, whereas the repulsion of the bosons is proportional to n_B^2. This effect is caused by the strong squeezing of the density of the fermion due to its effective potential

$$V_F^{\text{eff}} = V(\mathbf{r}) + g_{BF}\rho_B(\mathbf{r}) \approx V(\mathbf{r}) + n_B g_{BF}(\sqrt{2\pi}\sigma_B)^{-3} \exp(-r^2/2\sigma_B^2), \qquad (5.9)$$

that is deepened linearly with the number of bosons n_B as shown quantitatively in Fig. 5.2b. The increasing curvature of the fermionic effective potential, which equals

$$\frac{\partial^2}{\partial x^2}V_F^{\text{eff}}|_{\mathbf{r}=0} \approx 2V_0 k^2 + (2\pi)^{-3/2}|g_{BF}|\,n_B/\sigma_B^5 \qquad (5.10)$$

using the Gaussian approach, causes the width of the fermion density to be similar to the bosonic one for $n_B = 3 - 4$ and even narrower for $n_B > 4$. In our calculation, the occupation of higher single-particle fermion orbitals, due to the squeezing of the fermion density, is roughly 10% for $n_B = 4$ and up to 40% for the filling factor $n_B = 10$.

The effective potential experienced by the ^{87}Rb atoms

$$V_B^{\text{eff}}(\rho_F) = V(\mathbf{r}) + g_{BF}\rho_F(\mathbf{r}) \approx V(\mathbf{r}) + g_{BF}(\sqrt{2\pi}\sigma_F)^{-3} \exp(-r^2/2\sigma_F^2) \qquad (5.11)$$

is plotted in Fig. 5.2a for $V_0 = 14E_R$. The curvature of the bosonic effective potential

$$\frac{\partial^2}{\partial x^2} V_{\mathrm{B}}^{\mathrm{eff}}|_{\mathbf{r}=0} \approx 2V_0 k^2 + (2\pi)^{-3/2} |g_{\mathrm{BF}}|/\sigma_{\mathrm{F}}^5 \tag{5.12}$$

is strongly enhanced by the nonlinear dependence on the fermion width σ_F^5, which leads to a deepening of the bosonic effective potential with increasing n_{B}. The resulting energy gain in $\langle \hat{H}_{\mathrm{BF}} \rangle$ overcompensates the repulsion energy of the bosons. Instead of a stronger repulsion, an increasing n_{B} causes a self-trapping of the bosons in the deepened center of the effective potential. This effect is mediated by the squeezing of the fermion orbital due to the higher boson density. The compression of boson and fermion densities should be observable in the experiments directly by imaging a broadened momentum distribution or by using atomic clock shifts to measure the peak density [144].

5.2.2   Variational approach

It is interesting how strong the self-trapping effect depends on correlations between the bosons. Therefore, in addition to the exact calculation, a variational mean-field approach is presented and discussed in this section, where the particle correlations are neglected. In the mean-field ansatz, the wave functions of bosons and fermions are replaced by the root of the density

$$\psi_{\mathrm{B}}(\mathbf{r}) = \sqrt{\rho_{\mathrm{B}}(\mathbf{r})} \qquad \text{and} \qquad \psi_{\mathrm{F}}(\mathbf{r}) = \sqrt{\rho_{\mathrm{F}}(\mathbf{r})}. \tag{5.13}$$

To obtain an analytical expression for the energy functional $\langle \hat{H} \rangle$, the sinusoidal single-site potential is approximated as a spherically symmetric harmonic oscillator potential yielding

$$V_{\mathrm{ho}} = V_0 k^2 r^2 \tag{5.14}$$

with $k = \pi/a$. Let us assume a Gaussian shape of the density, which seems not to be a strong restriction following the results above. Consequently, the wave functions of bosons and fermions are written as

$$\begin{aligned}
\rho_{\mathrm{B}}(\mathbf{r}) &= n_{\mathrm{B}} \left(\sqrt{2\pi}\sigma_{\mathrm{B}}\right)^{-3} \exp(-r^2/2\sigma_{\mathrm{B}}^2) \\
\rho_{\mathrm{F}}(\mathbf{r}) &= \left(\sqrt{2\pi}\sigma_{\mathrm{F}}\right)^{-3} \exp(-r^2/2\sigma_{\mathrm{F}}^2).
\end{aligned} \tag{5.15}$$

Thus, the energy functional depends on σ_{B} and σ_{F} and reads

$$E(\sigma_{\mathrm{B}}, \sigma_{\mathrm{F}}) = \langle \hat{H}_{\mathrm{B}} + \hat{H}_{\mathrm{F}} + \hat{H}_{\mathrm{BF}} \rangle, \tag{5.16}$$

where the three parts of the Hamiltonian are given in equation (5.2). Using a mean-field ansatz, the bosonic and fermionic field operator in the Hamiltonian are substituted by

$$\hat{\psi}_{\mathrm{B}}(\mathbf{r}) \rightarrow \phi_{\mathrm{B}}^{\mathrm{mf}}(\mathbf{r})\hat{b}_{\mathrm{mf}} \qquad \text{and} \qquad \hat{\psi}_{\mathrm{F}}(\mathbf{r}) \rightarrow \phi_{\mathrm{F}}^{\mathrm{mf}}(\mathbf{r})\hat{f}_{\mathrm{mf}}, \tag{5.17}$$

where $\phi_{\mathrm{B/F}}^{\mathrm{mf}}(\mathbf{r})$ are the bosonic and fermionic mean-field orbitals, respectively. Consequently, one obtains the expectations values for the products of field operators

$$\begin{aligned}
\langle \hat{\psi}_{\mathrm{B}}^{\dagger} \hat{\psi}_{\mathrm{B}} \rangle &= |\phi_{\mathrm{B}}^{\mathrm{mf}}|^2 \, n_{\mathrm{B}} = |\psi_{\mathrm{B}}|^2, \\
\langle \hat{\psi}_{\mathrm{F}}^{\dagger} \hat{\psi}_{\mathrm{F}} \rangle &= |\phi_{\mathrm{F}}^{\mathrm{mf}}|^2 \, n_{\mathrm{F}} = |\psi_{\mathrm{F}}|^2, \\
\langle \hat{\psi}_{\mathrm{B}}^{\dagger} \hat{\psi}_{\mathrm{B}}^{\dagger} \hat{\psi}_{\mathrm{B}} \hat{\psi}_{\mathrm{B}} \rangle &= |\phi_{\mathrm{B}}^{\mathrm{mf}}|^4 \, n_{\mathrm{B}}(n_{\mathrm{B}}-1) = \frac{n_{\mathrm{B}}-1}{n_{\mathrm{B}}} |\psi_{\mathrm{B}}|^4.
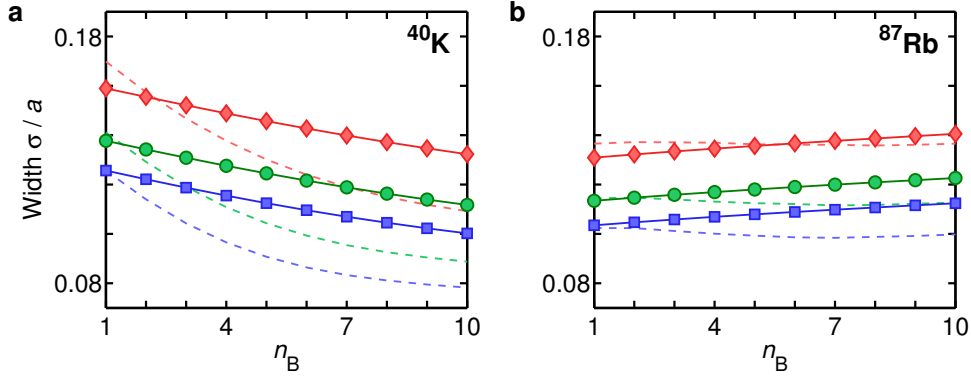\end{aligned} \tag{5.18}$$

Fig. 5.3: The width of the density profile for (a) one fermionic ^{40}K atom and (b) n_B bosonic ^{87}Rb atoms for $V_0 = 8E_R$ (♦), $V_0 = 14E_R$ (●), and $V_0 = 20E_R$ (■). The solid lines are obtained using a variational mean-field ansatz and the dashed lines correspond to the exact calculation in Fig. 5.1. The variational approach, which neglects particle correlations, shows substantial deviations.

Inserting these expressions in equation (5.16) and integrating over spherical coordinates leads to the energy functional

$$\langle \hat{H} \rangle = \frac{3}{8} \hbar^2 \left(\frac{n_B}{\sigma_B^2 m_B} + \frac{1}{\sigma_F^2 m_F} \right) + 3V_0 k^2 \left(\sigma_B^2 + \sigma_F^2 \right) + \frac{g_B \, n_B (n_B - 1)}{16 \pi^{3/2} \sigma_B^3}$$
$$+ \frac{g_{BF} \, n_B}{(2\pi)^{3/2} (\sigma_B^2 + \sigma_F^2)^{3/2}}. \tag{5.19}$$

It depends exclusively on the free parameters σ_B and σ_F, which can be determined by minimizing $\langle \hat{H} \rangle$. Thus, the solution must satisfy the conditions

$$\frac{\partial \langle \hat{H} \rangle}{\partial \sigma_B} = 0 \qquad \text{and} \qquad \frac{\partial \langle \hat{H} \rangle}{\partial \sigma_F} = 0. \tag{5.20}$$

As these equations can not be solved analytically, σ_B and σ_F are calculated numerically.

The results are plotted in Fig. 5.3 for a lattice constant $a = 515$ nm, a bosonic scattering length $a_B = 100a_0$, and an interspecies scattering length $a_{BF} = -205a_0$. In the figure, the variational approach (solid lines) is compared with the exact calculation (dashed lines). For $n_B = 1$, the width σ_B of the ^{87}Rb atoms and the width σ_F of the ^{40}K atoms computed with both methods agree quite well. This appears reasonable since each mean-field wave function represents a single particle. Only for shallow lattices ($V_0 = 8E_R$) the widths obtained by variation of the energy functional are considerably narrower. This can be attributed to the harmonic shape of the potential which leads, in general, to a stronger compression of the density. With increasing number of bosons n_B, the variational ansatz shows a broadening of the bosonic wave function, whereas the exact results show a compression of the boson density. Here, it becomes apparent that the mean-field wave function does not incorporate the correlations of the ^{87}Rb atoms, which partly avoid each other in a correlated quantum mechanical state. As a consequence, the mean-field repulsion is considerably larger. Mediated by the fundamentally different behavior of the bosons in the mean-field picture, the changes on the fermion side are even more dramatic. The fermion width σ_F for more than two
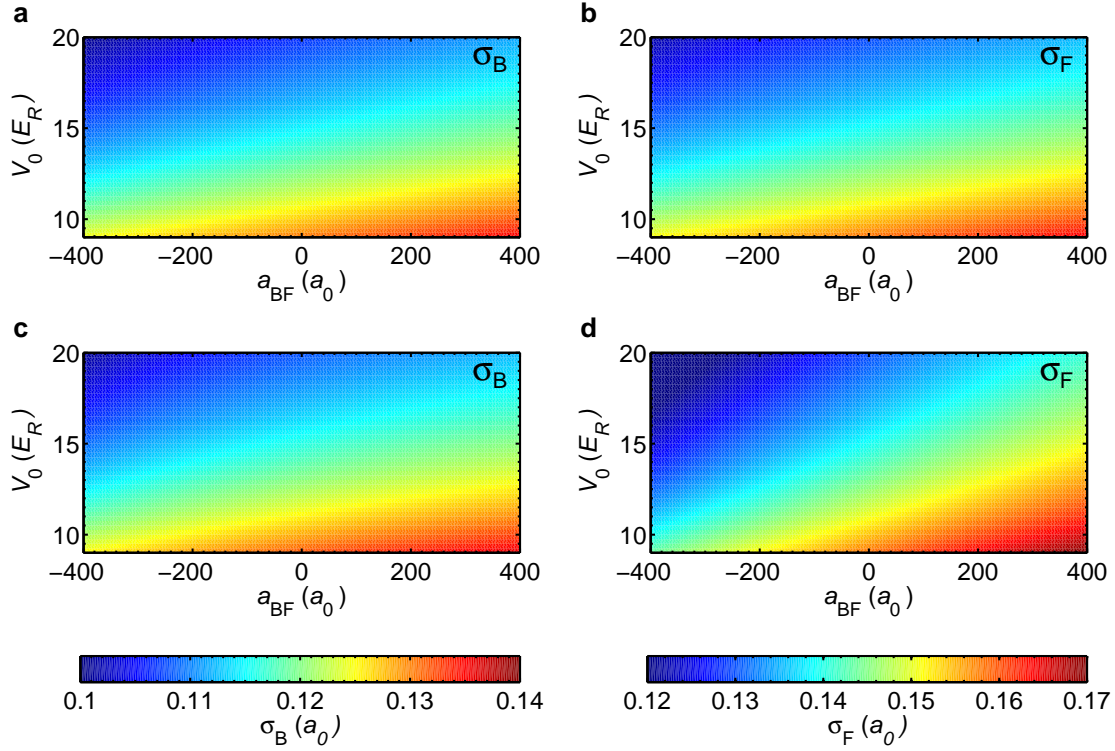
Fig. 5.4: (a) Bosonic width σ_B and (b) fermionic width σ_F in dependency on the interspecies scattering length a_{BF} and the lattice depth V_0 for $n_B = 1$ and $a_B = 100a_0$ using the variational mean-field approach. The results for $n_B = 2$ are shown in figure (c) and (d). The color bars for σ_B and σ_F are shown left and right, respectively.

^{87}Rb atoms is substantially less compressed than in the exact calculation. The latter has strong implications for the Mott transition, since it influences directly the bosonic effective potential

$$V_B^{\mathrm{eff}} = V(\mathbf{r}) + g_{BF}|\psi_F(\mathbf{r})|^2, \qquad (5.21)$$

which is deepened only to a minor extent with increasing n_B (see Fig. 5.13). We can conclude that no (or only a weak) self-trapping behavior is found using a variational approach. This indicates that the mean-field ansatz neglects important physics and can not describe the system accurately enough for our purpose. However, the variational approach can serve as a simple description for a basic discussion of effects caused by the boson-fermion interaction. In general, it is restricted to weak intra- and interspecies scattering.

For the lattice parameters above, the variational approach gives quite reasonable results for one and two ^{87}Rb atoms at a lattice site for intermediate lattice depths. Here, numerical inexpensive results can be obtained for a large parameter space, which are shown in Fig. 5.4. The change of both, σ_B and σ_F, are depicted as a function of the potential depth V_0 and the boson-fermion scattering length a_{BF}. For one ^{87}Rb atom, a squeezing of boson and fermion orbitals is caused by an increase of one of these parameters (Fig. 5.4a and b). Note, that the color scale is different for both species. Adding a second ^{87}Rb atom, where the intraspecies scattering length is $a_B = 100a_0$,
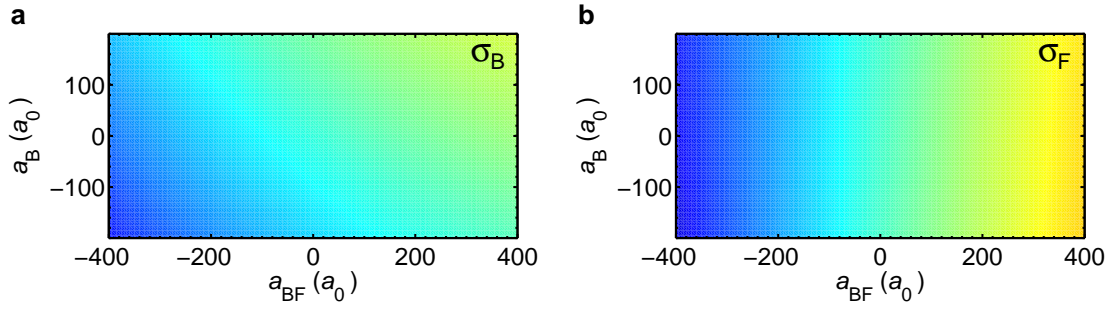
Fig. 5.5: The dependency of (a) the bosonic width σ_B and (b) the fermionic width σ_F on the scattering lengths a_B and a_{BF} for $n_B = 2$. See Fig. 5.4 for the color scales.

causes a larger gradient of the fermion width in the direction of a_{BF}, while the bosonic width is, overall, slightly broader (Fig. 5.4c and d). The interplay between boson-boson and boson-fermion interaction, i.e., a_B and a_{BF}, is depicted in Fig. 5.5a and b. It shows that the boson density is broadened with both, an increasing a_B and an increasing a_{BF}, whereas the fermion density is mainly influenced by a_{BF}.

5.3 Composite particles

Until now, the interaction of ^{87}Rb and ^{40}K atoms is studied restricted to a single lattice site, which is applicable to commensurately filled systems. Multisite physics becomes important, when, e.g., a redistribution of atoms within the lattice can occur, which is addressed in the following including the orbital degrees of freedom. The same diagonalization method is used for small quasi-one-dimensional chains as performed in section 3, where the scattering parameters of section 5.2.1 are applied. For only one fermionic "impurity", lattices are studied with $5 - 7$ sites, a bosonic filling factor $1 \leq n_B \leq 3$, and $15E_R \leq V_0 \leq 20E_R$. In this systems, an additional effect caused by the interspecies interaction becomes apparent. It has been shown that the self-trapping behavior causes a local deepening of the bosonic effective potential for the fermion occupied site. The gain in energy, due to the boson-fermion interaction, leads to a binding of several bosons to one fermion, which is a phenomenon resembling polaron physics [169, 170]. Remarkably, we find that the fermionic impurity causes, for the above parameters, the localization of six additional bosons at its site.

For more than one fermion in the lattice, the binding effect remains but the gain in energy is largest if all fermions interact with bosons, which causes that the bosons are rather equally distributed at fermion occupied sites. E.g., a situation with two fermions interacting with three bosons each is energetically preferable to one fermion bound to six bosons and a lonely fermion. Exemplarily, this behavior is shown in Fig. 5.6 for a one-dimensional lattice with seven sites, $N_B = 12$ bosonic atoms, i.e., bosonic filling $n_B = 12/7$, and a variable number N_F of fermionic atoms. For one fermion, one observes that the central site, where the fermion is localized, is occupied by eight bosons where the remaining four bosons are delocalized at the other six sites. In this
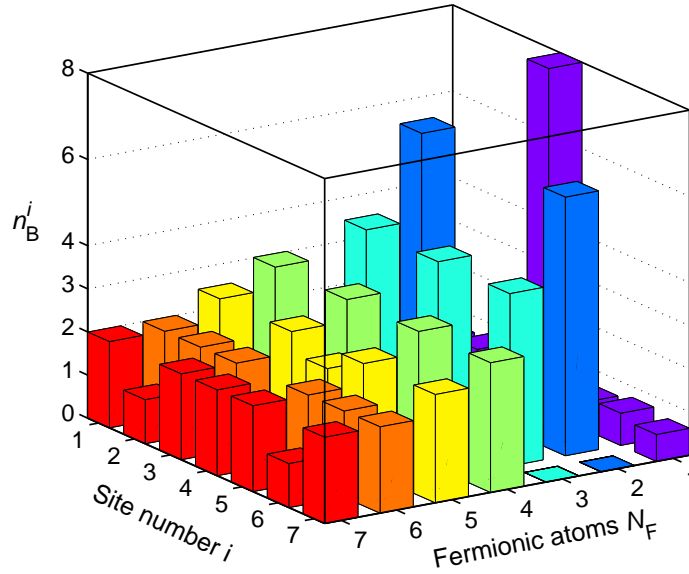
Fig. 5.6: Bosonic site occupation n_B^i for a one-dimensional lattice with seven sites and $N_B = 12$ bosons. The N_F fermions are localized at the sites with $n_B^i \geq 1$.

context, it is important to notice that the fermions always localize at individual sites due to the interaction with the bosons, since for the chosen parameters the energy gain due to tunneling is small. This resembles the localization of polarons in solids, which is also referred to as "self-trapping" in the context of the Fröhlich Hamiltonian [171]. The self-trapping of the fermionic atom causes its localization at a single site although all sites are equivalent (see discussion below). The interspecies interaction leads therefore to a "spontaneous" symmetry breaking. For $N_F = 2$ $(3, 4, 6)$ fermions, each fermion shares its site with 6 $(4, 3, 2)$ fermions and the other sites are empty. For noncommensurate situations, the remaining bosons are delocalized ($N_F = 5$) or the fermion occupied sites are not equally filled ($N_F = 7$). Furthermore, a superstructure occurs as a very interesting feature which is most pronounced for $N_F = 2$ to 4. However, since self-consistent methods tend to break the spatial symmetry, this emerging structure might also be an artifact of the calculation. This means, that ground states with (nearly) the same energy exist, where the fermions and the respective bosons occupy different sites. Exemplarily, states for $N_F = 2$, where the two compounds (of one fermion and six bosons) are located at site i and site $j \neq i$, respectively, have comparable energies. Regarding the results for $N_F \leq 4$, this leads to the assumption that near-resonant hopping can occur, where a compound of one fermion and several bosons tunnels. Such a behavior indicates a real composite particle as predicted in Ref. [36]. A break-up of such a compound corresponds to the tunneling of a single boson or a fermion into an energetically higher state. The self-trapping effect stabilizes therefore the formation of composite particles due to a substantial gain in energy.

Nonetheless, the localization of fermions mediated by their interaction with the bosonic atoms applies also to the experimental situation, where the symmetry is broken, in particular, by the confinement which establishes a finite atomic cloud [29, 30]. Since bosons are attracted to sites

that are occupied by fermions, bosons and fermions occupy only the central lattice sites. If the fermionic filling $n_F < 1$ or the fermionic cloud is smaller than the bosonic one (as in Ref. [30]), this leads to an increase of the bosonic filling factor in mixtures in comparison with pure bosonic systems. In experiments, the predicted high bosonic site occupation will be accompanied by high losses due to three-body recombinations.

5.4 Shift of the critical potential depth

5.4.1 Renormalization of the Bose-Hubbard model

In the following, I discuss commensurately filled macroscopic cubic lattices and the implications on the Mott-insulator phase transition that result from the deformation of the effective potential. In optical lattices, the bosonic superfluid to Mott-insulator transition is triggered by the boson-boson interaction strength relative to the hopping amplitude. In the Bose-Hubbard framework [21, 74, 75], this is described by the ratio between the on-site interaction U and the hopping parameter J that both depend on the depth of the lattice potential V_0. For boson-fermion mixtures, both U and J also depend explicitly on the filling factor. However, to estimate how the interaction with the fermions influences the phase transition, an effective Bose-Hubbard model is used, where the lattice potential is substituted by the bosonic effective potential $V_B^{eff}(n_B)$ for a specific static filling factor n_B. This approach leads to a renormalization of the parameters U and J in the effective bosonic system. The on-site interaction U is obtained directly from $V_B^{eff}(n_B)$ and the hopping J by band-structure calculations using a finite periodic continuation of $V_B^{eff}(n_B)$. Thereby, the parameter J is determined as $1/4$ of the width of the lowest Bloch band of a one-dimensional lattice with 30 sites [75], and U is the interaction of two particles

$$U = \langle \frac{g_B}{2} \int d^3r \; \hat{\psi}_B^{\dagger 2}(\mathbf{r}) \hat{\psi}_B^2(\mathbf{r}) \rangle. \tag{5.22}$$

Qualitatively, the bosonic effective potential, which is shown in Fig. 5.2a, reveals two important aspects: First, even for a single boson the minimum is deepened substantially and decreases further with an increasing number of ^{87}Rb atoms; second, the shape of the effective potential deviates strongly from the $V_0 \sin^2(kx)$ potential, leading to a broader barrier between neighboring lattice sites. Both effects lead to a reduced hopping between neighboring sites, whereas the on-site interaction energy is mainly increased by the stronger curvature of the effective potential. The decrease in J, which is larger than the effect on U (inset of Fig. 5.7), causes narrower bands.

Using the effective potential $V_B^{eff}(n_B)$, the ratio U/J is plotted in Fig. 5.7 as a function of the lattice depth V_0, where the dashed black line corresponds to a pure bosonic system. The interacting system is represented by solid lines which are split for different filling factors n_B, since the deformation of the effective potential grows with an increasing filling factor n_B. Even for $n_B = 1$ the self-trapping causes a large shift of $U/J\,(V_0)$ towards higher values, which is further enhanced with an increasing n_B. In the following, the renormalized values of U/J are used and known results for the critical point $(U/J)_c$ to calculate the shift of the critical potential
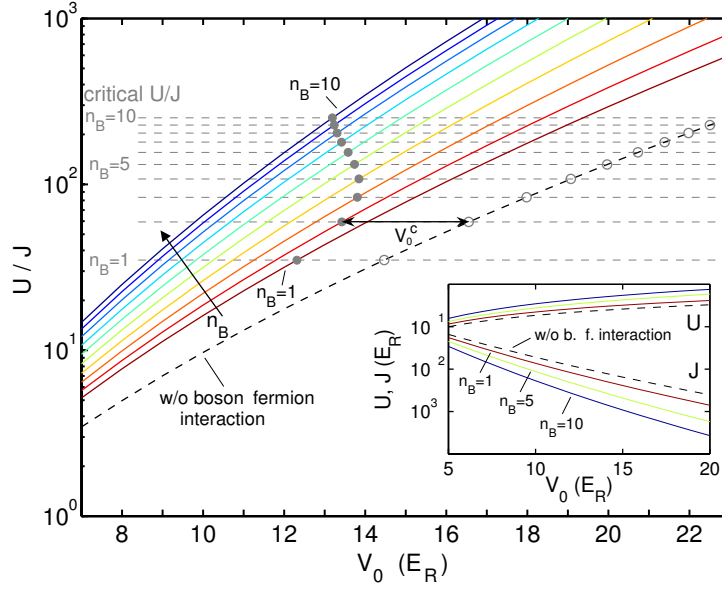
Fig. 5.7: Calculated ratio U/J plotted against the lattice depth V_0 for filling factors $n_B = 1$ to $n_B = 10$ and $n_F = 1$ (solid lines). The dashed black line represents a pure bosonic system. The boson-fermion interaction causes a large shift of the critical potential depth V_0^c. The inset shows U and J separately for the filling factors $n_B = 1, 5, 10$ and for vanishing interaction. The lattice constant is $a = 515$ nm.

depth V_0^c. Following the mean field results derived in section 2.6.3, the critical ratio depends on the filling factor n_B and obeys the relation

$$(U/J)_c = z \left[2n_B + 1 + 2\sqrt{n_B(n_B + 1)} \right], \qquad (5.23)$$

where $z = 6$ for a cubic lattice [49, 130]. In Fig. 5.7, the critical values for different filling factors n_B are depicted as horizontal gray lines. The critical lattice depths $V_0^c(n_B)$ for the pure bosonic system are given by the intersections of the dashed black line with the horizontal lines (open circles). According to the relation above, the phase transition for a pure bosonic system shifts to deeper lattices for an increasing filling factor n_B. For Bose-Fermi mixtures, the intersections representing the critical potential depths are indicated by solid circles. In comparison with the pure bosonic system, the phase transition in mixtures is shifted substantially towards shallower lattices.

5.4.2   Loss of coherence in red detuned lattices

The parameters in the following have been chosen such that a comparison with the experiment in Ref. [30] is possible, where a red detuned optical lattice with $a = 515$ nm is used. The critical potential depth can be estimated from Fig. 5.7 as $12.3 E_R$ for $n_B = 1$, increases to $13.8 E_R$ for $n_B = 4$, and decreases slightly for higher fillings. Comparing the boson-fermion mixture and the pure bosonic system with the same bosonic filling, the shift ΔV_0^c of the phase transition is
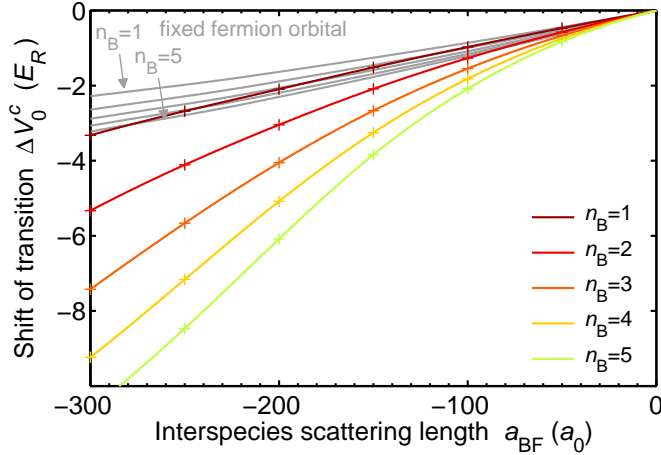
Fig. 5.8: The shift of the superfluid to Mott-insulator phase transition ΔV_0^c in dependence on the boson-fermion scattering length a_{BF} for the filling factors $n_B = 1$ to $n_B = 5$. The gray lines are obtained by keeping the fermion orbital fixed.

given by the difference of the respective critical lattice depths (see arrow for $n_B = 2$). The expected shift increases substantially with the filling factor, e.g., $\Delta V_0^c = -2.2E_R$ for $n_B = 1$ and $\Delta V_0^c = -5.2E_R$ for $n_B = 4$. In Refs. [29, 30], pure bosonic systems are compared to Bose-Fermi mixtures with the same number of bosonic atoms, not accounting for the increase of the local bosonic filling factor due to self-trapping, as discussed above. In addition, the confinement in experiments causes the formation of shells with different filling factors n_B. Therefore, the reported shift in Ref. [30] of approximately $-5E_R$ is an average value of a system, where at the center of the lattice $n_B > 5$ and $n_F = 1$. Accounting for the inhomogeneous filling, we average our results for $n_B \leq 5$ to $n_B \leq 7$ leading to a shift between $-4.2E_R$ and $-5.1E_R$, which is in good agreement with the experiment. In principle, the experimental local filling factors can be determined, e.g., using atomic clock shifts [144], which would allow a more accurate comparison of experiment and theory.

Uniquely, experiments with ultracold atoms allow the precise tuning of the interaction strength by Feshbach resonances. Hence, the shift of the critical potential depth ΔV_0^c can also be studied in dependence on the scattering length a_{BF} between bosons and fermions, while the bosonic scattering length $a_B = 100a_0$ is kept constant. Such an experiment allows a closer investigation of the mutual interaction and the effects due to orbital changes. In Fig. 5.8, I present the calculated shifts ΔV_0^c for bosonic filling factors $n_B = 1$ to $n_B = 5$, where the solid lines are calculated allowing for orbital deformations and the gray lines by using a rigid fermion orbital obtained for $V_F^{eff}(\mathbf{r}) = V(\mathbf{r})$. The latter corresponds to a single-band approach for fermions, leaving the orbital degrees of freedom only to the bosonic subsystem. Because of a much weaker deformation of the bosonic effective potential, both U and J are less affected than in the previous discussion. For a rigid fermion orbital, U/J is independent of n_B, but the difference from the pure bosonic system increases with the lattice depth. Thus, ΔV_0^c increases slightly with n_B. The scattering length a_{BF}, which enters linearly in the Hamiltonian (5.2), leads to an almost linear shift ΔV_0^c. In great contrast, the dependence on a_{BF} for the self-consistent calculation (solid lines), which fully includes the orbital degrees of freedom, is superlinear due to self-trapping. Thus, the mutual deformation of the effective potential is enhanced by a larger scattering length as well as by a higher bosonic filling factor as discussed above. Therefore, the assumption of a fixed fermion
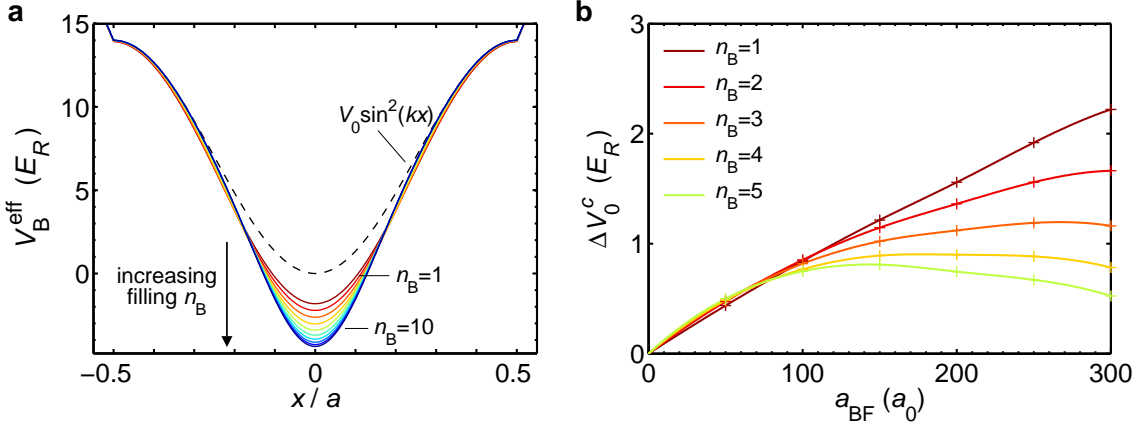
Fig. 5.9: (a) The effective potential $V_{\mathrm{B}}^{\mathrm{eff}}$ for a site with n_{B} bosonic ^{87}Rb atoms and *two* fermionic ^{40}K atoms for attractive interspecies interaction. (b) The shift of the phase transition ΔV_0^{c} for repulsive interspecies scattering lengths a_{BF} for filling factors $n_{\mathrm{B}} = 1$ to $n_{\mathrm{B}} = 5$.

orbital is only suited for weak interaction and low bosonic filling.

So far, results for the *fermionic* filling $n_{\mathrm{F}} = 1$ are presented, which is the typical experimental situation. In principle, the number of fermionic atoms can exceed the number of bosonic atoms which poses the problem of a fermionic filling factor larger than one for a suitable confining potential. For two fermionic ^{40}K atoms in a symmetric single well, the effective bosonic potential is shown in Fig. 5.9a. For these calculations, a finite temperature (10nK) is applied that mixes the degenerate fermionic orbitals. Surprisingly, one observes that the bosonic effective potential is less deformed than for a single fermion. This counter-intuitive behavior is caused by the density of the second fermion in the higher orbital, which hinders a stronger deformation of the boson density. It indicates that the shift of the critical potential depth for the fermionic filling factor $n_{\mathrm{F}} = 2$ is even slightly diminished in comparison with $n_{\mathrm{F}} = 1$.

5.4.3   Repulsive interspecies scattering

Feshbach resonances allow to tune the interaction between ^{87}Rb and ^{40}K atoms from attractive to repulsive. For repulsive interspecies interaction, the separation of bosons and fermions plays a role, which is not accounted for in our single-site calculation. However, the change of the on-site interaction due to the mutual interaction is also important when considering models with particle hopping. Applying the renormalization of the Hubbard parameters for repulsive interaction between bosons and fermions ($a_{\mathrm{BF}} > 0$) the shift ΔV_0^{c} becomes positive, which is plotted in Fig. 5.9b. Overall, it remains quite small ($\Delta V_0^{\mathrm{c}} \lesssim 2E_R$) and has a sublinear dependence on the interspecies scattering length a_{BF}. For $0a_0 < a_{\mathrm{BF}} < 50a_0$, the shift is nearly equal for different fillings n_{B}, but for stronger interspecies repulsion the shift is the smaller, the higher the bosonic filling. While V_0^{c} is almost linear for $n_B = 1$, it saturates for $n_B \geq 3$ and even decreases for large a_{BF}.

While a self-amplified interaction effect is found for interspecies attraction, the broadening of orbitals for repulsive interaction is hindered by the relatively steep on-site potential.
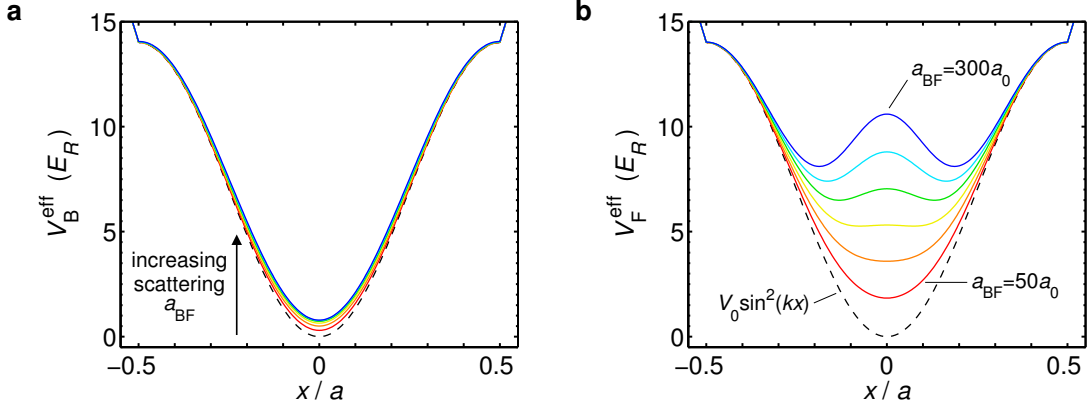
Fig. 5.10: (a) The bosonic effective potential $V_{\mathrm{B}}^{\mathrm{eff}}$ and (b) the fermionic effective potential $V_{\mathrm{F}}^{\mathrm{eff}}$ for $n_{\mathrm{B}} = 3$ bosons and one fermion. The results are plotted for repulsive interspecies scattering in the range $a_{\mathrm{BF}} = 50a_0$ to $a_{\mathrm{BF}} = 300a_0$.

Figure 5.10 shows the bosonic and fermionic effective potentials for three bosonic atoms per site. Recapitulating that a ^{40}K atom is much lighter than a ^{87}Rb atom, the fermion density is broader than the bosonic one even without interaction. Because of the repulsion, the fermionic effective potential becomes shallower with increasing a_{BF} as depicted in Figure 5.10b causing a further broadening of the fermion density. For strong repulsion, the fermionic effective potential has the shape of a double well. Due to the broad fermion density, the bosonic effective potential is much less affected. This causes only a small change in the boson density and a relatively small shift in the critical potential depth V_0^c as shown in Fig. 5.9b.

5.5 Experiments with tunable interactions

5.5.1 Experimental setup and particle losses

Recently, the first experiment with boson-fermion mixtures in a three-dimensional lattice and the possibility of tunable interactions has been carried out in the group of I. Bloch (University of Mainz) [3]. In this experiment a degenerate mixture of 4×10^5 ^{87}Rb and up to 3×10^5 ^{40}K atoms are prepared in the hyperfine ground states $|F = 1, m_F = +1\rangle$ and $|F = 9/2, m_F = -9/2\rangle$, respectively. In order to tune the interaction between ^{87}Rb and ^{40}K atoms [168, 172], a Feshbach resonance at $B_0 = 546.9$ G with $\Delta B = 2.9$ G has been used. This allows to tune the interspecies scattering length in accordance with equation (2.43), i.e.,

$$a_{\mathrm{BF}}(B) = a_{\mathrm{bg}} \left(1 - \frac{\Delta B}{B - B_0} \right) \tag{5.24}$$

with an accuracy of $\pm 10a_0$ between $-800a_0$ and $-200a_0$ (below) and between $-170a_0$ and $800a_0$ (above the resonance). Thus, the experimental setup permits to tune the bosons-fermion interaction in a wide range from strongly attractive to strongly repulsive, while the boson-boson scattering length $a_{\mathrm{B}} \approx 100a_0$ remains unchanged. The lattice laser operates at a wavelength $\lambda = 755$ nm,
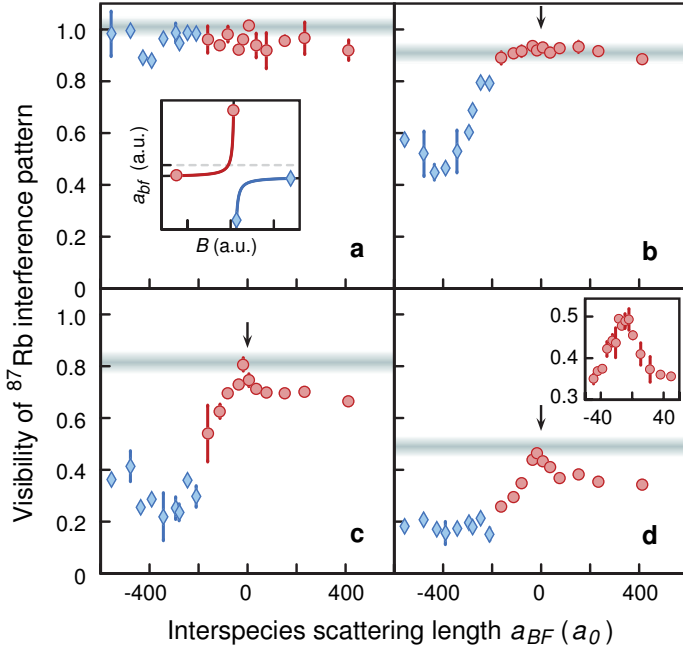
Fig. 5.11: Visibility decay for lattices depths (a) $3E_R$, (b) $5 E_R$, (c) $9 E_R$, and (d) $12 E_R$ for $N_F = 3/4 N_B$. The shaded regions correspond to the visibility of a pure ^{87}Rb system, which is compatible with the maximum visibility of the mixture at $a_{BF} \approx 0$ (indicated by arrows). The red circles and blue diamonds represent data taken below and above the resonance, respectively, with an uncertainty of $\pm 10 a_0$ as depicted in the inset of part a. The figure is taken from Ref. [3].

which is blue detuned with respect to the atomic frequencies causing a trapping in the nodes of the lattice. At this specific wavelength, the lattice depth for bosons and fermions measured in the respective recoil energies of ^{87}Rb and ^{40}K atoms, i.e., $E_R^{B/F} = \hbar k_L^2/2m_{B/F}$, are the same. This means that the single-particle Wannier functions of both species have the same width and therefore maximum overlap. The optical potentials for ^{87}Rb and ^{40}K are given by

$$
\begin{aligned}
V_B(\mathbf{r}) &= V_0 \left[\sin^2(kx) + \sin^2(ky) + \sin^2(kz)\right], \\
V_F(\mathbf{r}) &= \frac{m_B}{m_F} V_B(\mathbf{r}).
\end{aligned}
\tag{5.25}
$$

As usual, all energies are given in units of the recoil energy of ^{87}Rb, i.e., $E_R/h = 4.027$ kHz. The blue detuned optical lattice causes an anticonfinement which is overcompensated by an elliptical dipole trap that compensates also the gravitational sag. The lattice is ramped up adiabatically within 100 ms to a final lattice depth V_0 between $2E_R$ and $17E_R$ in all three spatial directions. After another 100 ms hold time, the trapping potentials and the magnetic field are switched off instantaneously. Finally, the momentum distribution is observed using standard time-of-flight absorption imaging (see section 2.5.1). The extracted visibility data from Ref. [3] is shown in Fig. 5.11.

In the experiment, the ratio of ^{87}Rb to ^{40}K atoms has been $N_F = 1/4 N_B$, $N_F = 1/2 N_B$, and, $N_F = 3/4 N_B$. For shallow lattices ($V_0 \lesssim 3E_R$), the visibility shows a rather constant value for all scattering lengths a_{BF}. Furthermore, the visibility of the mixture at $a_{BF} = 0$ is compatible with the Mott transition in a pure bosonic system for all lattice depths. This means that bosonic and fermionic system are in fact transparent for each other. For $V_0 \gtrsim 9E_R$, this transparency is accompanied by a rather symmetric decay of the visibility in a small interval around $a_{BF} = 0$ for repulsive and attractive interaction, where $|U_{BF}| \lesssim U_B$. For stronger repulsive interaction, the visibility remains constant and is slightly below the value for $a_{BF} = 0$. For stronger attraction, the

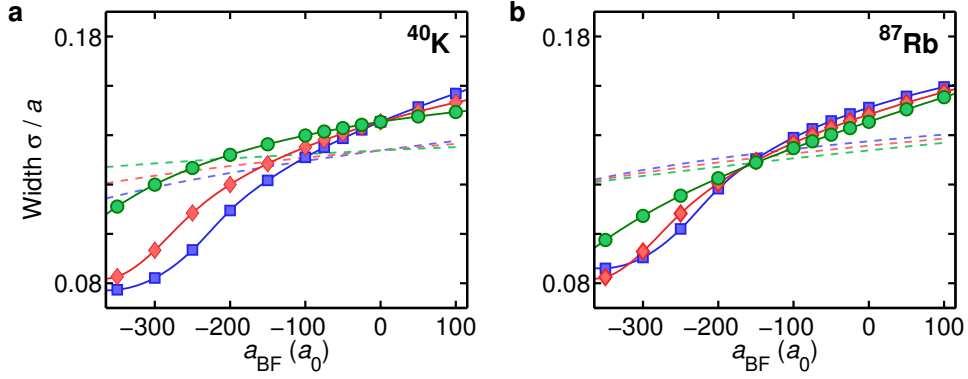**Fig. 5.12:** Width of the density for (a) one ^{40}K atom and (b) n_B ^{87}Rb atoms as function of the interspecies interaction strength a_{BF}. The results are plotted for a bosonic filling $n_B = 1$ (●), $n_B = 2$ (◆), and $n_B = 3$ (■). The dashed lines with respective colors are obtained using a variational approach, which underestimates the orbital changes substantially.

decay of visibility proceeds until $a_{BF} = -300a_0$ to $-400a_0$ (for $V_0 \gtrsim 5E_R$). As the visibility has been connected with the localization process in the Mott transition [19, 112], this rapid decrease of visibility seems qualitatively to be compatible with the enhanced localization presented in this chapter. However, a more profound analysis can be given by studying the fraction of condensed atoms, which is discussed in section 5.5.3. First, the situation of very strong attractive interaction is discussed, where the visibility increases again with larger attractive scattering.

While the visibility decrease is reversible for repulsive and intermediate attractive scattering, for strongly attractive scattering high losses of ^{87}Rb atoms have been observed experimentally. The scattering length, where these losses become significant, corresponds roughly to the visibility minimum in Fig. 5.11. Therefore, one can identify the visibility minimum as a critical value for the loss regime. The observed ratio of lost ^{87}Rb to ^{40}K atoms is between three and four, which means that three-body losses with two bosons and one fermion do not play a major role, which was also observed in Ref. [29]. The loss coefficient for three-body collisions of ^{87}Rb atoms is in the range $K_3 = 4\text{-}7 \times 10^{-30}$ cm^6/s [173], so that, even without fermions, lattice sites with four and more ^{87}Rb atoms decay faster than the experimental hold time. Therefore, the dominating process is presumably the three-body recombination of three ^{87}Rb atoms in the presence of a ^{40}K atom.

The enhanced loss of atoms is caused by the on-site density accumulation due to the boson-fermion interaction as described in the previous sections. Thereby, two distinct effects have to be taken into account: first, a higher peak density due to the squeezing of the effective atomic orbitals and, second, a higher bosonic occupation number per site as discussed in section 5.3. While an occupation of one or two ^{87}Rb atoms per site is dominant at $a_{BF} \approx 0$, the strongly attractive interaction leads to an occupation of three or more atoms per site and, therefore, causes three-body losses. In the experiment, a site will decay within the hold time τ if $\dot{N}_3\tau \gg 1$. The three-body loss rate $\dot{N}_3$ is proportional to σ_B^{-6} and is strongly enhanced by the compressed ^{87}Rb densities due to the boson-fermion interaction. Using a variational model (see section 5.2.2), the boundary
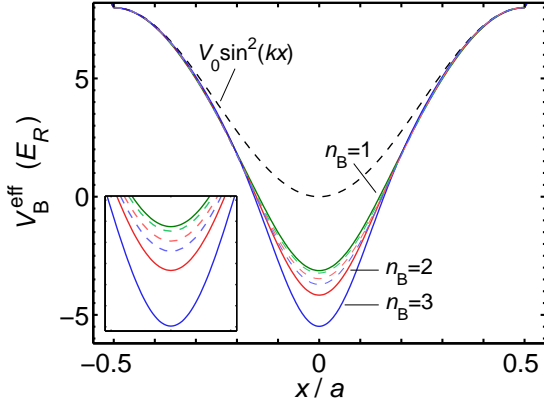
Fig. 5.13: Effective potential experienced by ^{87}Rb atoms for filling factors $n_B = 1$ to $n_B = 3$ at $a_{BF} = -200a_0$. It is substantially altered due to the deformation of the fermion density. The dashed lines correspond to the variational model.

of the loss dominated regime with respect to the lattice depth V_0 and the scattering length a_{BF} has been calculated in Ref. [3]. This approach agrees well with the experimentally measured values. The increase of the visibility for interaction strengths beyond this critical value can thus be associated with the removal of highly occupied sites with high peak densities. This leads to a lower average filling factor and may cause an enhanced bosonic mobility due to defects and local incommensurability.

5.5.2 Interaction induced orbital changes

In the following, I discuss interaction induced orbital changes and the shift of the transition point for the blue detuned lattice used in the experiment [3]. While for the red detuned optical lattices discussed before with $a = 515$ nm the single-particle on-site densities are different for both species, they are equivalent when using a blue detuned lattice with $a = 377.5$ nm. Consequently, the density overlap at small interspecies scattering a_{BF} is maximal, which causes a large effect on the Mott-insulator phase transition even for small values of the interspecies scattering length a_{BF}. First, let me concentrate on the direct interaction effect which manifests itself in the change of the effective atomic orbitals and the effective potentials. The same exact diagonalization technique is used as described in section 5.2.1 for one to three bosonic atoms per site and, of course, with a variable interspecies interaction.

In Fig. 5.12 the Gaussian widths σ_B and σ_F of the respective ^{87}Rb and ^{40}K densities are shown for $V_0 = 8E_R$, displaying the density compression with an increasing attractive interspecies scattering length a_{BF}. For $a_{BF} = 0$, the broadening of the bosonic density due to boson-boson scattering $a_B = 100a_0$ with an increasing number n_B of ^{87}Rb atoms per site is observable, while the width of the ^{40}K atoms is constant due to the vanishing interspecies interaction. For increasing attractive scattering, the bosonic width decreases. The mutual interaction causes that the effect is enhanced with a higher bosonic filling. For the background scattering $a_{BF} = -205a_0$ a higher occupation goes along with a narrower density although the repulsive boson-boson interaction energy increases. For $n_B = 2$ and $n_B = 3$, a saturation of the decrease is observable for $a_{BF} < -300a_0$, which depends also critically on the lattice depth V_0. Here, the ^{87}Rb atoms are strongly localized, which causes the kinetic energy and the repulsion to increase substantially.
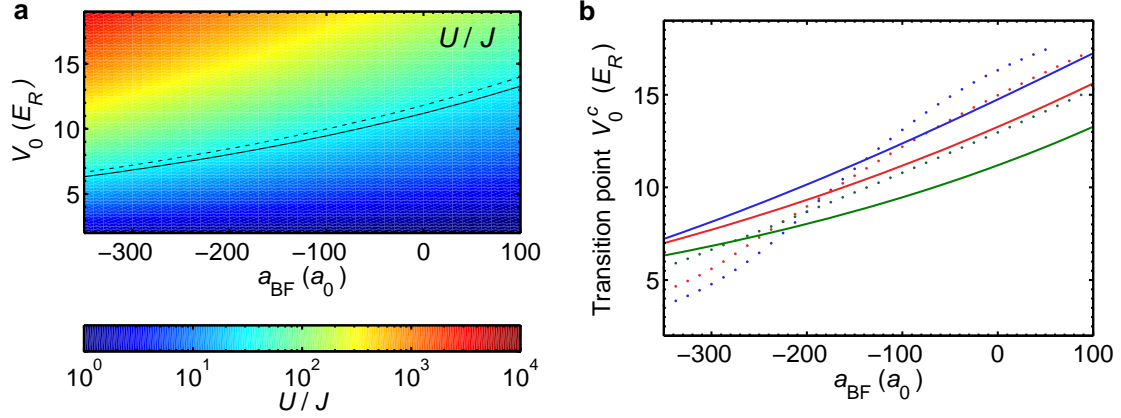
Fig. 5.14: (a) Ratio U/J obtained by variation in dependence on the lattice depth V_0 and the interspecies scattering length a_{BF} for $n_B = 1$ and $a_B = 100a_0$. The solid black line corresponds to a critical $U/J = 29.36$, whereas the dashed line represents the mean-field value. (b) Critical lattice depth V_0^c for a bosonic filling $n_B = 1$ (–), $n_B = 2$ (–), and $n_B = 3$ (–) using equation (5.28). For comparison, the dotted lines represent results obtained by exact diagonalization (see Fig. 5.16).

Comparing the widths of bosons and the fermion, we see that the bosonic filling n_B has a stronger effect on the fermion than on the boson density. The decrease of the fermionic width with an increasing bosonic filling n_B as well as with the strength of the attractive scattering a_{BF} is quite expected, since both parameters directly influence the strength of the fermionic effective potential via

$$V_F^{\text{eff}} \approx V_F(\mathbf{r}) + n_B \, a_{BF} \frac{2\pi\hbar^2}{(\sqrt{2\pi}\sigma_B)^3 \mu} \exp(-r^2/2\sigma_B^2), \tag{5.26}$$

where $\mu = \frac{m_B m_F}{m_B + m_F}$ is the reduced mass. Additionally, the fermionic effective potential depends on the bosonic width σ_B and vice versa. The strength of the decrease is nonetheless remarkable, which becomes apparent when comparing with results obtained by the variational approach in section 5.2.2. The latter indicates the same general behavior but in great contrast it predicts only small changes of the width for both ^{87}Rb and ^{40}K as depicted in Fig. 5.12 (dashed lines). The deviation between both methods at $a_{BF} = 0$ is due to the harmonic approximation within the variational approach, which causes narrower particle densities. Because of this, the values of σ_B and σ_F obtained by variation and by diagonalization are quite comparable in the range between $a_{BF} = -200a_0$ and $0a_0$, although the variational approach completely underestimates interaction induced changes in σ_B and σ_F.

The effective bosonic potential in Fig. 5.13 shows the self-trapping of the ^{87}Rb atoms with increasing n_B for $a_{BF} = -200a_0$. The effective lattice potential

$$V_B^{\text{eff}} \approx V_B(\mathbf{r}) + a_{BF} \frac{2\pi\hbar^2}{(\sqrt{2\pi}\sigma_F)^3 \mu} \exp(-r^2/2\sigma_F^2) \tag{5.27}$$

is strongly altered, which is enhanced by the deformation of the fermion density shown in Fig. 5.12. The effect is drastically reduced for the variational approach (dashed lines), due to the small changes in σ_F. Here, the change with increasing bosonic filling n_B is small. The accidental
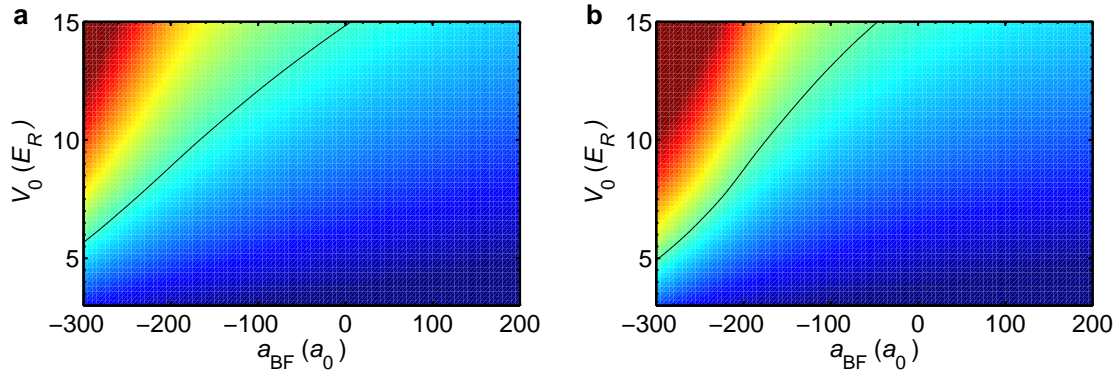
Fig. 5.15: The ratio U/J calculated by exact diagonalization as a function of V_0 and a_{BF} for a bosonic filling (a) $n_B = 2$ and (b) $n_B = 3$. The respective critical potential depths are depicted by a solid line. Here, the initial resolution $(50a_{BF}, 1E_R)$ is interpolated and U is obtained directly from the n_B-particle wave function. See Fig. 5.14a for a color scale.

agreement of both approaches for $n_B = 1$ and $a_{BF} = -200a_0$ is due to the narrower harmonic potential in the variational model.

5.5.3   Shift of the phase transition

From the discussion above, it is quite obvious that the transition from the superfluid to the Mott insulator is strongly influenced by the boson-fermion interaction. As the fringe visibility offers a relatively indirect access to the phase transition point, the time-of-flight images have been used in Ref. [3] to extract the condensate fraction of bosonic atoms yielding a direct relation to superfluidity. The condensate fraction can be defined experimentally as the sum of atoms corresponding to quasimomentum zero divided by the total atom number [121]. With increasing lattice depth, this value monotonically decays to zero for all a_{BF} and number of fermions N_F. The kink position, where the condensate fraction of atoms vanishes, can be identified with the critical lattice depth of the Mott-insulator transition (see inset of Fig. 5.17).

The influence of the mutual interaction on the superfluid to Mott-insulator phase transition, is analyzed in the following using the renormalization of the Bose-Hubbard parameters U and J developed in section 5.4.1. Thereby, the bosonic effective potential is used to determine the hopping J from the band structure. The bosonic on-site interaction U is the expectation value of the interaction energy of two ^{87}Rb atoms in the effective single-site potential. Since a direct comparison with the critical lattice depth V_0^c observed in experiment is possible, it is, however, not sufficient to use the mean-field result for the critical ratio $(U/J)_c^{3D} \approx 35.0$ for $n_B = 1$, leading to a shift in the order of $0.5E_R$ to $1E_R$ and a slightly modified dependency on a_{BF}. For a bosonic filling $n_B = 1$, a quantum Monte-Carlo calculation has been performed in Ref. [131] determining the critical point $(U/J)_c^{3D} = 29.36$ with great accuracy. Similar calculations for higher filling factors are not available, so that we have to scale the quantum Monte-Carlo result with the mean-field
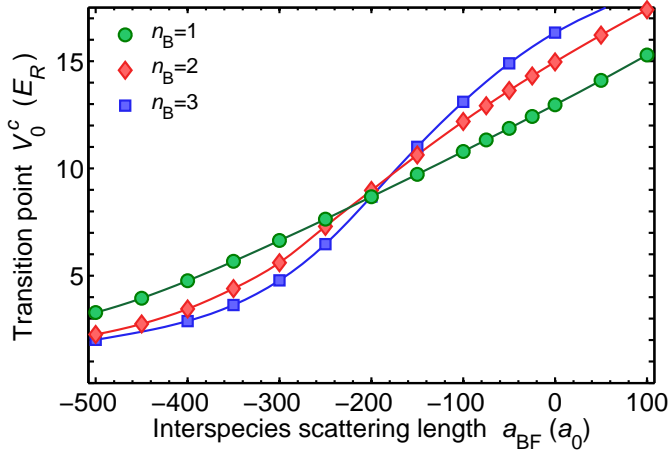
Fig. 5.16: Critical potential depth V_0^c for a bosonic filling factor $n_B = 1$ to $n_B = 3$ in dependence on the interspecies scattering length a_{BF}. At $a_{BF} = 0$, the results are split only due to different critical U/J. For attractive scattering, the interaction induced change of the fermion density causes a larger shift of the Mott transition for higher fillings.

formula (2.116) for higher filling factors, i.e.,

$$(U/J)_c^{3D} = \frac{29.36}{3 + \sqrt{8}} \left(2n_B + 1 + \sqrt{(2n_B + 1)^2 - 1}\right). \qquad (5.28)$$

This equation should give a reasonable rescaling of (2.116) for $n_B = 2$ with $(U/J)_c = 49.86$ and $n_B = 3$ with $(U/J)_c = 70.16$ but, in principle, more accurate values would be highly desirable.

Let us start with the ratio U/J determined from the bosonic effective potential (5.27) using the variational approach. The ratio is plotted for $n_B = 1$ in Fig. 5.14a using a logarithmic scale. In addition to the increase with the lattice depth V_0, the effective potential depends on the interspecies scattering length a_{BF} and on the fermionic width σ_F. While the direct dependency on a_{BF} is strong, the effect of $\sigma_F(a_{BF}, n_B)$ on the bosonic effective potential is weak for the variational approach as depicted in Figure 5.13. Therefore, the value of U/J is not strongly influenced by the bosonic filling. The critical lattice depth, where the Mott transition occurs, is plotted in Fig. 5.14a using the critical quantum Monte-Carlo value (solid line) and the mean-field value (dashed line). For higher fillings n_B, the critical potential depths V_0^c are shown in Fig. 5.14b. Note that the major difference between the curves comes from the scaling of V_0^c with n_B in equation (5.28) rather than from a direct dependence of U/J on n_B. The variational approach describes the shift of the Mott-insulator transition qualitatively correct, but differs up to several E_R from results obtained by exact diagonalization. In fact, the shift of the transition in comparison with $a_{BF} = 0$ is substantially underestimated by the variation model.

Using the self-consistent exact diagonalization presented in section 5.2.1 to determine particle densities and the effective potentials leads to a considerably larger shift of the critical potential depth. The ratio U/J is shown in Fig. 5.15 in dependence on both V_0 and a_{BF}. Figure 5.16 depicts the critical potential depth V_0^c for bosonic filling $n_B = 1$ to 3 in the range from strongly attractive interspecies scattering $a_{BF} = -500a_0$ to repulsive scattering $a_{BF} = 100a_0$. For vanishing a_{BF}, V_0^c is split for different n_B because of the increase of the critical U/J with higher filling according to equation (5.28). As discussed above, for attractive scattering the mutual trapping of bosons and the fermion causes a compression of densities, an altering of the effective potentials, and thus a notable change of the function $U/J(V_0)$. As a consequence, the critical potential depth $V_0^c(a_{BF})$ decreases
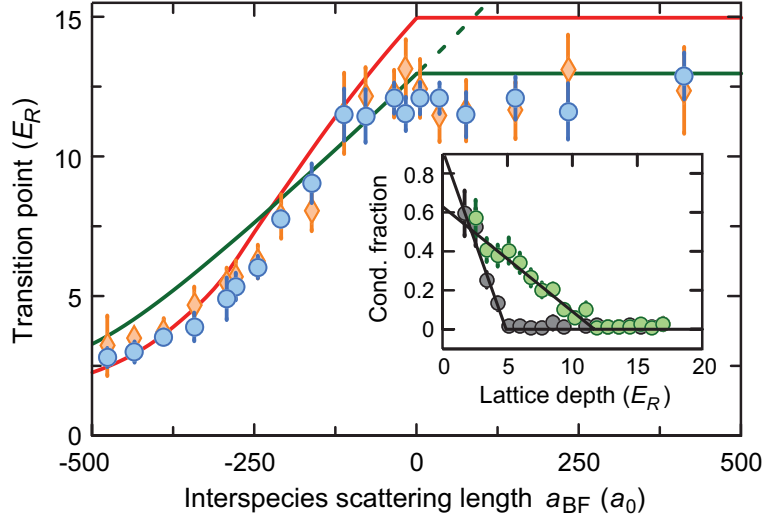
Fig. 5.17: Comparison of the experimentally observed critical lattice depth V_0^c for $N_F = 1/2\,N_B$ (orange diamonds) and $N_F = 3/4\,N_B$ (blue circles) with the theoretical predictions from exact diagonalization, where the green and red lines represent a bosonic filling factor $n_B = 1$ and $n_B = 2$, respectively. Considering the redistribution the bosonic atoms (see text) and a separation of bosons and fermions for repulsive a_{BF}, the agreement is remarkably good. The dashed line for $a_{BF} > 0$ represents a fictive scenario, where bosons and fermions occupy the same sites. The inset shows the condensed fraction of bosonic atoms for $a_{BF} = -295a_0$ (black circles) and $a_{BF} = 235a_0$ (green circles) at $N_F = 1/2\,N_B$. The linear fits depict the experimental determination of V_0^c. The figure is taken from Ref. [3].

faster, the higher the filling n_B. At roughly $a_{BF} = -200$, V_0^c is equal for filling factors $n_B = 1$ to 3. For stronger attractive scattering, the transition occurs even at a shallower lattice if the filling is increased. The theory predicts a remarkable shift of the superfluid to Mott-insulator phase transition of up to $11E_R$ comparing with vanishing interspecies interaction. Therefore, a clear signature of this behavior must be observable in experiments with tunable ^{87}Rb -^{40}K scattering. It is remarkable that for strongly attractive interaction the Mott-insulator transition occurs in shallow lattices with $V_0 < 4E_R$, where the trapping potential is created mainly by ^{40}K atoms and to a lesser extend by light forces. Thereby, the deepening of the effective potential is strongly amplified by the presented self-trapping effect.

Figure 5.17 shows the experimental data obtained in the group of I. Bloch [3]. Exemplarily, the inset depicts the decay of the condensate fraction for $a_{BF} = -295a_0$ (black circles) and $a_{BF} = 235a_0$ (green circles). For each interaction strength, a linear fit is applied to determine the kink position, which can be attributed to the critical potential depth V_0^c of the Mott transition. The critical points V_0^c are represented in Fig. 5.17 by blue circles and orange diamonds for $N_F = 3/4\,N_B$ and $N_F = 1/2\,N_B$, respectively. Although the experiment was designed to enable a setup with a weak confining potential, some effects due to inhomogeneity must be taken into account. One can assume that at $a_{BF} = 0$ the lattice is predominately filled with one ^{87}Rb atom per site with a small admixture of doubly occupied sites irrespectively of N_F. Therefore, a critical

lattice depth of V_0^c corresponding to the filling one is expected around $a_{BF} = 0$. The experimental data is compared with theoretical predictions from Fig. 5.16 for bosonic filling $n_B = 1$ (green line) and $n_B = 2$ (red line). Around $a_{BF} = 0$, the observed transition seems to occur up to $1 E_R$ below the theoretical prediction for $n_B = 1$. Considering the experimental uncertainties and, in particular, the systematical error in attributing the kink position to the critical potential depth, experiment and theory agree well. Additionally, the nonzero confinement may cause the entrance into the Mott phase to occur via a localized Bose-glass phase, which would give rise to an earlier decay of the condensate fraction. In other words, localization by disorder might play an additional role in the experiment. Of course, also the theoretical calculation of $U/J(V_0)$ may contain methodical and numerical inaccuracies.

Of particular interest is the shift of the transition point for attractive interspecies scattering. Overall, the experimental results follow the theoretical curves with surprisingly good agreement. This indicates that orbital degrees of freedom play in fact the major role in the shift of the Mott-insulator phase transition. Further, the mutual interaction of bosons and fermions via the effective potentials and the self-trapping behavior are of great importance, which becomes apparent when comparing the experimental data with the variational approach in Fig. 5.14. With increasing attractive scattering between ^{87}Rb and ^{40}K , ^{87}Rb atoms are drawn to ^{40}K occupied sites, since the interspecies interaction U_{BF} increases whereas the boson-boson repulsion U, which is explicitly denoted as U_B in the following, remains roughly constant. The process


$$\tag{5.29}$$
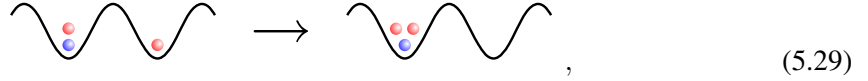
where ^{87}Rb is colored red and ^{40}K blue, occurs if

$$U_B^{n_B=2} + 2U_{BF}^{n_B=2} - U_{BF}^{n_B=1} \approx U_B^{n_B=2} + U_{BF}^{n_B=2} < 0. \tag{5.30}$$

Considering the exact interaction at each lattice site, the boson-boson interaction U_B and the boson-fermion interaction U_{BF} depend on the bosonic filling indicated in the superscript. Both exact diagonalization and the variational model predict that the occupation of a site with two ^{87}Rb atoms is preferable for a_{BF} below $-50a_0$ to $-60a_0$.

Thus, below this value each site should be occupied by two bosons and one fermion for $N_F = 1/2\, N_B$ (orange diamonds). The experimental critical points support this shift to higher filling (red curve) for $a_{BF} \lesssim -60a_0$, although the experimental uncertainties make an estimate difficult. For a larger number of ^{40}K atoms (blue circles), a coexistence of sites with one fermion and one or two bosons is expected. Here, the following redistribution can occur

$$\tag{5.31}$$
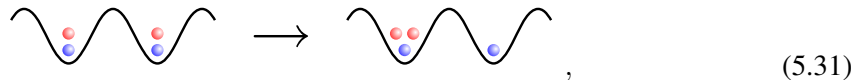
which becomes possible if

$$U_B^{n_B=2} + 2U_{BF}^{n_B=2} - 2U_{BF}^{n_B=1} < 0. \tag{5.32}$$

Note that this process is impossible within the Bose-Fermi-Hubbard model (2.62), where the interaction energies $U_B^{n_B}$ and particularly $U_{BF}^{n_B}$ are independent of n_B. Within the model, the
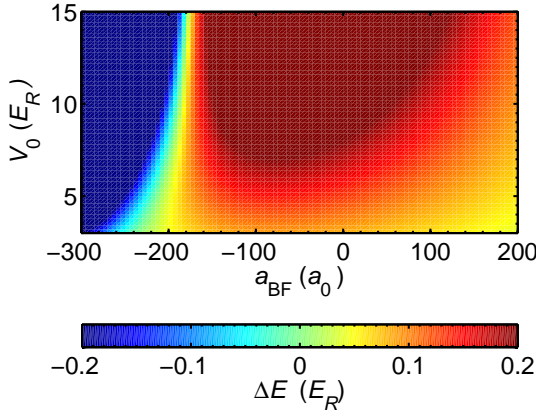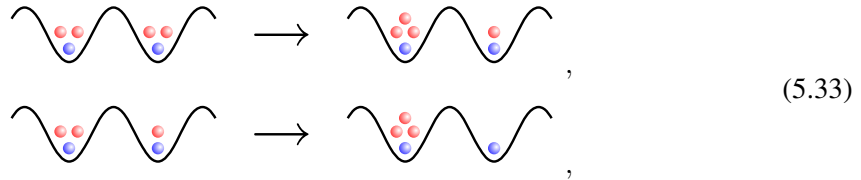
Fig. 5.18: The energy balance of the process (5.31) obtained by exact diagonalization (interpolated) shows that a redistribution of bosonic atoms becomes possible below $a_{\mathrm{BF}} \approx -200 a_0$.

energy gain equals exactly U_{B} which is greater than zero for repulsive boson-boson scattering. Due to the mutual compression of the on-site densities, the gain in energy $2U_{\mathrm{BF}}^{n_{\mathrm{B}}=2} - 2U_{\mathrm{BF}}^{n_{\mathrm{B}}=1}$ can overcome the boson-boson repulsion $U_{\mathrm{B}}^{n_{\mathrm{B}}=2}$. The variational model estimates that this process occurs below $a_{\mathrm{BF}} \approx -400 a_0$ for a critical value of U_{B}/J. Since the difference $U_{\mathrm{BF}}^{n_{\mathrm{B}}=2} - U_{\mathrm{BF}}^{n_{\mathrm{B}}=1}$ depends critically on the orbital changes, this model underestimates this effect substantially. The net energy of the process (5.31) is shown in Fig. 5.18 obtained by exact diagonalization, which determines its criticality around $a_{\mathrm{BF}} = -200 a_0$. This is also compatible with the experiment, since both results for intermediate and high fermion numbers follow the theoretical prediction for $n_{\mathrm{B}} = 2$ below $a_{\mathrm{BF}} \approx -250 a_0$, while for $a_{\mathrm{BF}} \approx -200 a_0$ the theoretical predictions are to close to tell.

One important aspect of the experiment are three-body losses, which require a bosonic filling equal or higher than three. Therefore, also the processes

$$
\begin{array}{c}
\text{(diagram)} \longrightarrow \text{(diagram)} \quad , \\[1em]
\text{(diagram)} \longrightarrow \text{(diagram)} \quad ,
\end{array}
\tag{5.33}
$$

are important favoring the filling factor $n_{\mathrm{B}} = 3$, which are possible if

$$
\begin{aligned}
3U_{\mathrm{B}}^{n_{\mathrm{B}}=3} + 3U_{\mathrm{BF}}^{n_{\mathrm{B}}=3} + U_{\mathrm{BF}}^{n_{\mathrm{B}}=1} - \left(2U_{\mathrm{B}}^{n_{\mathrm{B}}=2} + 4U_{\mathrm{BF}}^{n_{\mathrm{B}}=2} \right) &< 0, \\
3U_{\mathrm{B}}^{n_{\mathrm{B}}=3} + 3U_{\mathrm{BF}}^{n_{\mathrm{B}}=3} - \left(U_{\mathrm{B}}^{n_{\mathrm{B}}=2} + 2U_{\mathrm{BF}}^{n_{\mathrm{B}}=2} + U_{\mathrm{BF}}^{n_{\mathrm{B}}=1} \right) &< 0,
\end{aligned}
\tag{5.34}
$$

respectively. In the Bose-Fermi-Hubbard model, these processes correspond to an energy expense of one and two times U_B and are consequently energetically not allowed. The variational approach estimates $a_{\mathrm{BF}} \lesssim -400 a_0$ for both processes, whereas exact diagonalization predicts $a_{\mathrm{BF}} \lesssim -200 a_0$. The latter shows a critical behavior similar to process (5.31). This explains the high three-body losses for $a_{\mathrm{BF}} \lesssim -200 a_0$ in the experiment. Furthermore, the admixture of Mott-insulator sites with $n_{\mathrm{B}} = 3$ with a lower transition depth (see Fig. 5.16) are possible in a certain region below $a_{\mathrm{BF}} < -200 a_0$, where the losses are not yet dominating. Sites with bosonic fillings higher than three, although energetically possible, must not be considered as they decay

within the hold time of the experiment. For attractive scattering, we can conclude that there is an excellent agreement of the experiment with the presented theoretical predictions. Nonetheless, several aspects would be an interesting subject for further theoretical and experimental studies, in particular, the bosonic redistribution and temperature effects.

On the repulsive side of the interspecies interaction a_{BF}, the situation is quite different and the experimental results show a roughly constant critical lattice depth. Although some structure is perceptible for both intermediate and high fermion numbers the experimental uncertainties hinder a definite interpretation. The exact diagonalization results imply a further increase of the critical potential depth for all filling factors, which is surely not observable in the experiment. This deviation is expected, since the theoretical description assumes that ^{87}Rb and ^{40}K atoms occupy the same sites. As the ^{40}K atoms create a repulsive effective potential for the ^{87}Rb atoms, the bosons and fermions separate. Theoretically, two distinct scenarios are predicted depending on boson-boson and boson-fermion on-site interaction energies: first, a complete phase separation of fermions and bosons with two or more domains, and second, a supersolid order [32–34], where bosons and fermions are aligned in a checkerboard pattern. These theoretical descriptions, however, exclude the confining potential, which could disfavor a supersolid order. On the basis of the experimental results both scenarios are not distinguishable. However, the absence of a shift of the Mott-insulator transition to deeper lattices indicates that bosons and fermions do not occupy the same lattice sites.

5.6   Conclusions

In conclusion, it has been shown that orbital changes in attractive Bose-Fermi mixtures (^{87}Rb - ^{40}K) are nonnegligible as they lead to a substantial deformation of the effective potential and a squeezing of the effective orbitals. We found a self-trapping behavior of the bosons in their effective potential mediated by the interaction with the fermions. Using a model with effective Bose-Hubbard parameters U and J, the expected shift of the critical potential depth separating the superfluid phase from the Mott insulator was estimated. It depends strongly on the width of the fermion orbital, which is substantially altered due to the mutual interaction. The results reveal a strong dependence of the critical potential depth on the boson-fermion interaction strength a_{BF} and the bosonic filling factor n_B. The theoretical model uses exact diagonalization to determine the few-particle wave function, which is used to calculate the effective potential, the tunneling energy J, and the on-site interaction energies. A variational approach, which has been discussed in this chapter, shows a qualitatively similar behavior but underestimates the interaction induced orbital changes strongly. The theoretical predictions are compatible with the large shift reported in the first two experiments with ^{87}Rb - ^{40}K mixtures [29, 30]. The results of a recent experiment with a tunable boson-fermion scattering length a_{BF} [3] are discussed on the basis of the orbital renormalization of the Bose-Hubbard parameters U and J and an excellent agreement of theory and experiment has been found. Furthermore, processes that allow a redistribution of atoms in the lattice have been studied. For repulsive interspecies interaction, the disagreement between experiment and predictions of the renormalized Bose-Hubbard model indicates the separation of bosons and fermions to different sites of the lattice. In general, it is shown that interaction induced

orbital changes are of fundamental importance for attractively interacting quantum gas mixtures in optical lattices. Theoretically, the full inclusion of orbital changes is a challenge for the efficient calculation of lattice systems.

6

Momentum-resolved Bragg spectroscopy

*The main results in this chapter have been published in Ref. [5] P. T. Ernst, S. Götze, J. S. Krauser, K. Pyka, D.-S. Lühmann, D. Pfannkuche, and K. Sengstock, Probing superfluids in optical lattices by momentum-resolved Bragg spectroscopy, Nature Physics **6**, 56 (2010).*

6.1 Motivation

The experimental toolbox for manipulating atom-atom interactions and optical potentials has rapidly developed in the last decade. Experiments with atomic mixtures, tunable interactions, and optical lattices have become possible, which has also stimulated theoretical studies predicting various phases with strong connections to condensed matter physics. On the detection side, the time-of-flight mapping of the ground-state momentum distribution (section 2.5.1) is used in most experiments with relatively few but notable exceptions, e.g., Refs. [120, 174]. This technique gives good access to the ground-state properties of the system but offers no information on the excitations of the systems. Particularly, in strongly correlated systems, the knowledge of the excitations is crucial to understand the underlying physics. One way to access these excitation is to perform a two-photon process which couples ground and excited state over a virtual third state [175]. Thereby, a tunable amount of energy $\hbar\omega$ as well as momentum $\hbar\mathbf{k}$ are transfered to the system, which allows to probe the dynamic structure factor $S(\omega, k)$. In ultracold atoms experiments without periodic potentials, this technique has been used to investigate Bose-Einstein condensates [176–179]. In optical lattices, Bragg spectroscopy has been applied with only one or two different momenta [45–47].

Following a description of the experimental realization, interaction effects in the superfluid phase are discussed, which lead to a modification of the band structure. In section 6.3, two different mean-field approaches are discussed, the Bogoliubov-de Gennes equations and a tight-binding approximation, being valid in the weakly interacting superfluid regime. The results are compared with experimental results [5] for the two lowest bands in a two-dimensional lattice. For strongly interacting systems (section 6.4), where the mean-field description is not appropriate, exact diagonalization is used to compute the dynamic structure factor.
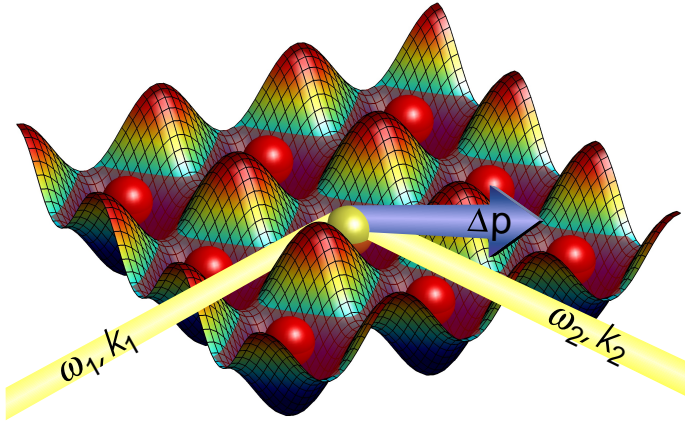
Fig. 6.1: Two-photon Bragg spectroscopy with two detuned laser beams at an angle θ. The atomic ensemble absorbs photons with ω_1 and $\mathbf{k}_1$ and stimulated emits photons with ω_2 and $\mathbf{k}_2$ resulting in an energy and momentum transfer.

6.2 Experimental realization

Recently, the first fully momentum-resolved Bragg spectroscopy, which allows to investigate the band structure of superfluids in optical lattices, has been performed in the group of K. Sengstock (University of Hamburg) [5, 180, 181]. The applied two-photon Bragg process is depicted in Fig. 6.1. It shows the atomic sample which is illuminated by two phase-coherent laser beams enclosing an angle θ. The intersecting beams have frequencies ω_1 and ω_2 and wave vectors $\mathbf{k}_1$ and $\mathbf{k}_2$, respectively. The process of absorption and stimulated emission couples resonantly states with an energy difference $\hbar\delta = \hbar(\omega_1 - \omega_2)$ and a difference in momentum

$$\hbar\mathbf{k}_{\text{Bragg}} = \hbar(\mathbf{k}_1 - \mathbf{k}_2) \approx 2\hbar k \sin(\theta/2)\, \frac{\mathbf{e}_{k_1} - \mathbf{e}_{k_2}}{|\mathbf{e}_{k_1} - \mathbf{e}_{k_2}|} \tag{6.1}$$

assuming $k = k_1 \approx k_2$ for small δ and unit vectors $\mathbf{e}_{k_1}$ and $\mathbf{e}_{k_2}$. It is important to note that this technique permits the independent tuning of energy transfer via the laser detuning δ and of momentum transfer by varying the angle θ. In the experiment, an average particle number of 1.5×10^5 ^{87}Rb atoms are loaded in two- or three-dimensional optical lattices, which are ramped up adiabatically. The Bragg lasers are aligned to excite atoms in the $[1, 1]$ direction of the lattice. Hence, the momentum transfer can be tuned from zero to the edge of the Brillouin zone at $\mathbf{k}_{\text{BZ}} = (\pi/a, \pi/a)$ with the lattice spacing $a = 515$ nm. For each momentum, the resonance position is determined by measuring the transfer efficiency for various values of the laser detuning δ, where two methods are employed: the coherent momentum transfer mapping and the energy transfer mapping. In the first case, the Bragg pulse is applied for 1 ms and afterwards all trapping potentials are switched off. Performing detection via time-of-flight allows to measure the population of the quasimomentum state with $\mathbf{q} = \hbar\mathbf{k}_{\text{Bragg}}$. At small momenta this technique is not applicable, since the momentum distribution of excited atoms and the ground state do not separate. Here, the second method is used, where the system is given time to rethermalize before the traps are switched off. The width of the condensate fraction of atoms gives information on the amount of energy deposited in the system and therefore indirectly on the number of transfered atoms.

6.3   Mean-field description of excitations

6.3.1   Bogoliubov-de Gennes equations

In the following, let us concentrate on the description of excitations on a mean-field level, where the excitations are small perturbations of the ground state. The condensate mean-field wave function Ψ fulfills the time-dependent Gross-Pitaevskii equation

$$i\hbar\frac{\partial\Psi}{\partial t} = \left(-\frac{\hbar^2}{2m}\nabla^2 + V(\mathbf{r}) + gN|\Psi|^2\right)\Psi, \tag{6.2}$$

where $V(\mathbf{r})$ is the potential, N the number of atoms in the condensate, and g the scattering constant (see section 2.3.1). Time-dependent excitations of the stationary solution Ψ_{GPE} with a characteristic frequency ω can be included using the ansatz

$$\Psi(\mathbf{r},t) = e^{-i\mu t/\hbar}\left(\Psi_{\mathrm{GPE}} + u_q\, e^{-i\omega t} + v_q^*\, e^{i\omega t}\right) \tag{6.3}$$

with μ being the chemical potential and complex functions $u_q(\mathbf{r})$ and $v_q(\mathbf{r})$. By inserting $\Psi(\mathbf{r},t)$ and $|\Psi(\mathbf{r},t)|^2\Psi(\mathbf{r},t)$ in the time-dependent Gross-Pitaevskii equation, where only linear order terms in u_q and v_q are kept, it follows

$$\begin{aligned}
\mu\Psi_{\mathrm{GPE}} + (\mu + \hbar\omega)u_q\, e^{-i\omega t} + (\mu - \hbar\omega)v_q^*\, e^{i\omega t} = \\
\left(-\frac{\hbar^2}{2m}\nabla^2 + V(\mathbf{r})\right)\left(\Psi_{\mathrm{GPE}} + u_q\, e^{-i\omega t} + v_q^*\, e^{i\omega t}\right) \\
+ gN|\Psi_{\mathrm{GPE}}|^2\left(\Psi_{\mathrm{GPE}} + 2u_q\, e^{-i\omega t} + 2v_q^*\, e^{i\omega t}\right) \\
+ gN\Psi_{\mathrm{GPE}}^2\left(v_q\, e^{-i\omega t} + u_q^*\, e^{i\omega t}\right).
\end{aligned} \tag{6.4}$$

Comparison of coefficients leads to

$$\mu\Psi_{\mathrm{GPE}} = \left(-\frac{\hbar^2}{2m}\nabla^2 + V(\mathbf{r}) + gN|\Psi_{\mathrm{GPE}}|^2\right)\Psi_{\mathrm{GPE}}, \tag{6.5}$$

which defines Ψ_{GPE} as the solution of the stationary Gross-Pitaevskii equation. Further, by assuming a real wave function Ψ_{GPE} we obtain the coupled Bogoliubov-de Gennes equations [50–53]

$$\begin{aligned}
(L + 2M)\, u_q + M v_q &= \hbar\,\omega_q u_q \\
(L + 2M)\, v_q + M u_q &= -\hbar\,\omega_q v_q
\end{aligned} \tag{6.6}$$

using

$$L = -\frac{\hbar^2}{2m}\nabla^2 + V(\mathbf{r}) - \mu \tag{6.7}$$

and

$$M = gN|\Psi_{\mathrm{GPE}}|^2. \tag{6.8}$$

The Bogoliubov-de Gennes equations (6.6) are linear so that, due to the periodic potential $V(\mathbf{r})$, the functions u_q and v_q are subject to Bloch's theorem. To solve (6.6) numerically, it is

advantageous to decouple the equations by applying a transformation to the functions ψ_q and ϕ_q with

$$u_q = \frac{1}{\sqrt{2}}(\phi_q + \psi_q) \quad \text{and} \quad v_q = \frac{1}{\sqrt{2}}(\phi_q - \psi_q), \tag{6.9}$$

which leads to

$$\begin{aligned}
(L + M)\,\psi_q &= \hbar\,\omega_q \phi_q \\
(L + 3M)\,\phi_q &= \hbar\,\omega_q \psi_q
\end{aligned} \tag{6.10}$$

and finally to the decoupled equation

$$(L + 3M)\,(L + M)\,\psi_q = (\hbar\,\omega_q)^2\,\psi_q. \tag{6.11}$$

Due to their periodicity, ψ_q, $V(\mathbf{r})$, and M can be expanded in Fourier series, which leads to an algebraic equation for the Fourier coefficients of ψ_q. This algebraic equation, which can easily be solved numerically, is derived in appendix A.3.

6.3.2 Bose-Hubbard approximation

A simpler expression than the Bogoliubov-de Gennes equations (6.6) can be obtained for the lowest band by using a Hubbard approach for the Hamiltonian, which is valid if the atomic orbitals are tightly bound to the lattice sites. Slightly different approaches [48, 49, 54, 55] can be used to derive the dispersion relation, where Ref. [55] is followed here. Using the Bose-Hubbard Hamiltonian (2.58) within a time-dependent mean-field approach, where the operator $\hat{b}_i$ is replaced by a complex number c_i, leads to a set of coupled Schrödinger equations

$$i\hbar \frac{\partial}{\partial t} c_j = -J(c_{j+1} + c_{j-1}) + U c_j^\dagger c_j c_j \tag{6.12}$$

by variation with respect to c_j^*. The stationary solution can be found by writing $c_j = e^{-i\mu t/\hbar} z_j$, which results in

$$\mu z_j = -J(z_{j+1} + z_{j-1}) + U z_j^* z_j z_j. \tag{6.13}$$

As the ground-state wave function must be equal for all lattice sites, we can define $z_i \equiv z_0 = \sqrt{n}$, where n is the filling per site, which leads to

$$\mu = nU - 2J. \tag{6.14}$$

Bogoliubov excitations can be incorporated by replacing

$$c_j \rightarrow e^{-i\mu t/\hbar}\,(z_j + \hat{\delta}_j), \tag{6.15}$$

where $\hat{\delta}_j$ is the amplitude of the time-dependent Bogoliubov excitation. Evaluating

$$\begin{aligned}
c_j^\dagger c_j^2 &\rightarrow e^{-i\mu t/\hbar}\,(z_j^* + \hat{\delta}_j^\dagger)\,(z_j^2 + 2z_j\hat{\delta}_j + \hat{\delta}_j^2) \\
&\approx e^{-i\mu t/\hbar}\,(z_j^* z_j^2 + 2z_j^* z_j\hat{\delta}_j + z_j^2\hat{\delta}_j^\dagger),
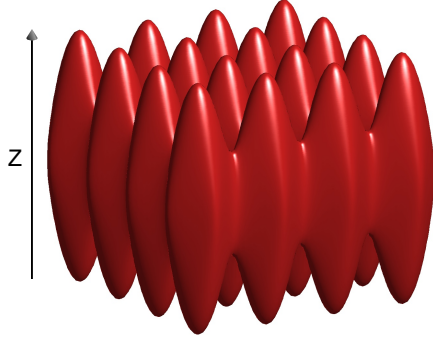\end{aligned} \tag{6.16}$$

Fig. 6.2: The isosurface of the density within the Thomas-Fermi approximation for a two-dimensional lattice with a harmonic confinement in the direction perpendicular to the lattice plane.

where quadratic and higher powers of $\hat{\delta}_j$ are neglected, it follows an equation for the Bogoliubov excitations

$$\mu\hat{\delta}_j + i\hbar\frac{\partial}{\partial t}\hat{\delta}_j = -J(\hat{\delta}_{j+1} + \hat{\delta}_{j-1}) + 2nU\hat{\delta}_j + nU\hat{\delta}_j^\dagger \tag{6.17}$$

using the relation for the ground-state solution (6.13). This equation can be solved by defining quasiparticles

$$\hat{\delta}_j^{(q)} = u_q e^{ijqa - i\omega_q t}\hat{\alpha}_q + v_{-q}^* e^{-ijqa + i\omega_q t}\hat{\alpha}_q^\dagger \tag{6.18}$$

with a wave vector q, energy $\hbar\omega_q$, and amplitudes u_q and v_{-q}. Comparison of coefficients and using $4\sin(qa/2) = 2 - e^{iqa} - e^{-iqa}$ result in two coupled equations for u_q and v_{-q}

$$\begin{aligned}
\left[nU + 4J\sin^2(qa/2)\right]u_q + nUv_{-q} &= \hbar\omega_q u_q \\
\left[nU + 4J\sin^2(qa/2)\right]v_{-q} + nUu_q &= -\hbar\omega_q v_{-q}.
\end{aligned} \tag{6.19}$$

The diagonalization of this matrix equation for (u_q, v_{-q}) leads finally to an algebraic form of the dispersion relation [48, 49, 54, 55]

$$\hbar\omega_q = \sqrt{4J\sin^2\left(\frac{qa}{2}\right)\left[2nU + 4J\sin^2\left(\frac{qa}{2}\right)\right]}. \tag{6.20}$$

6.3.3 Ground-state band

Experimentally, Bragg spectroscopy of superfluid ^{87}Rb atoms in Ref. [5] has mainly been performed in a two-dimensional lattice, where the lattice depths $V_{0,x}$ and $V_{0,y}$ are equal. To compare the predictions of equation (6.20) with the experimental results, the on-site interaction U must be calculated for the two-dimensional geometry. The magnetic dipole trap with frequency $\omega_{d,z}$ and the Gaussian beam waist W_0 cause a confining potential in the z direction with an angular frequency

$$\omega_z^2 \approx \frac{8V_0}{mW_0^2} + \omega_{d,z}^2, \tag{6.21}$$

where $V_0 = V_{0,x} = V_{0,y}$. Therefore, the atoms are distributed in a two-dimensional array of tubes, which is illustrated in Fig. 6.2. Due to an additional confinement within the lattice plane, the tubes in the experiment are filled with a varying number of N particles. Due to the weak confinement
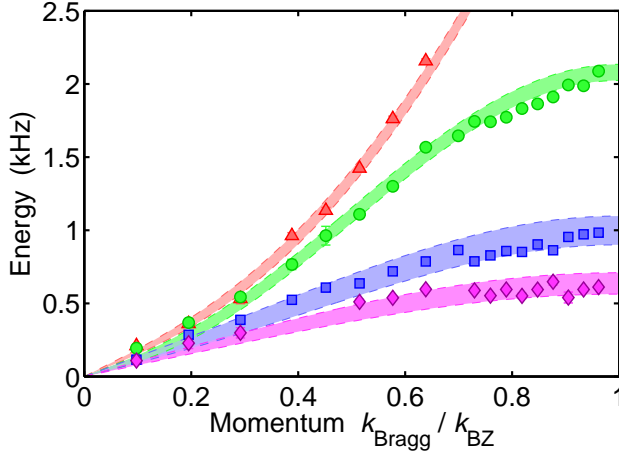
Fig. 6.3: Energy spectrum for resonant Bragg excitations in the $[1, 1]$ direction with momentum $\hbar k_{\text{Bragg}}$ for harmonic trapping (▲) and optical lattices with $V_0 = 3E_R$ (●), $V_0 = 7E_R$ (■), and $V_0 = 11E_R$ (◆). The experimental data (symbols) agrees well with theoretical predictions (shaded areas).

in the z direction, the Thomas-Fermi limit can be applied, where the kinetic energy is neglected. This requires that the Thomas-Fermi radius

$$Z = \left(\frac{3Na_s l_z^4}{l_r^2} \right)^{1/3} \tag{6.22}$$

is much larger than the axial oscillator length l_z [48], i.e., $Z/l_z \gg 1$, which is approximately fulfilled for an adequate number of particles. Thereby, the radial oscillator length of a single site is given by $l_r = \sqrt{\hbar/m\omega_r}$ with

$$\omega_r = \frac{\pi}{a} \sqrt{\frac{2V_0}{m}}. \tag{6.23}$$

The Thomas-Fermi density profile in the axial direction, i.e., perpendicular to the lattice plane, is described by [48]

$$n_z(z) = \frac{1}{4a_s} \left(\frac{3Na_s l_r}{l_z^2} \right)^{2/3} \left(1 - \frac{z^2}{Z^2} \right), \tag{6.24}$$

which is an inverted parabola, whereas the radial motion is frozen out. Here, we use the harmonic approximation leading to a Gaussian radial density

$$n_r(x, y) = \frac{1}{\pi l_r^2} e^{-(x^2 + y^2)/l_r^2}. \tag{6.25}$$

Thus, the on-site interaction per particle pair is given by

$$U \approx \frac{g}{2N(N-1)} \frac{1}{2\pi l_r^2} \int_{-Z}^{Z} dz\, n_z^2(z), \tag{6.26}$$

which has a strong influence on the band structure.

Figure 6.3 shows the experimentally observed resonance positions of the Bragg process [5] together with theoretical predictions for the lowest band. As the Bragg process excites the atoms along the $[1, 1]$ direction in the lattice plane, the ground-state band is an equal superposition of the lowest bands in x and y directions, i.e., $\hbar\omega_{\text{2D}} = \hbar\omega(k_x) + \hbar\omega(k_y)$ with $k_x = k_y = k_{\text{Bragg}}/\sqrt{2}$ (see equation (6.30)). The transfered momentum k_{Bragg} is given in units of $k_{\text{BZ}} = |\mathbf{k}_{\text{BZ}}|$, where
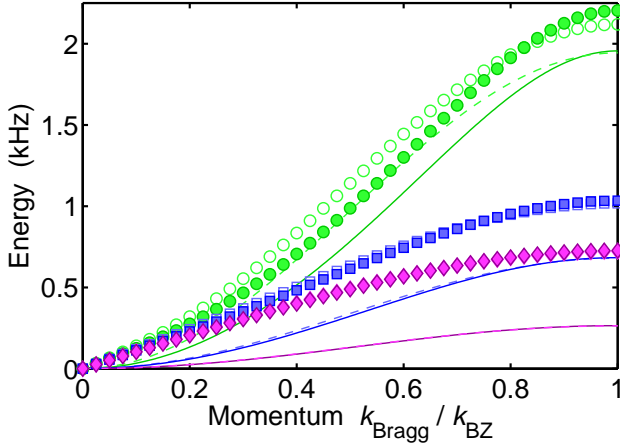
Fig. 6.4: Theoretical dispersion relation for $V_0 = 3E_R$ (green), $V_0 = 7E_R$ (blue), and $V_0 = 11E_R$ (magenta). The solid lines depict the single-particle band-structure solution and the dashed lines correspond to the tight-binding approach. Interaction induced changes are incorporated using the Bogoliubov-de Gennes equations (open symbols) and by a Hubbard-type approximation (solid symbols).

$\mathbf{k}_{BZ}$ corresponds to the Brillouin zone edge at $(\pi/a, \pi/a)$. For comparison, the red triangles correspond to a the case, where the lasers establishing the lattice are turned off and the atoms are trapped only in the harmonic confinement, which has been investigated before in Refs. [176–179]. The shaded red area shows the lattice-free dispersion relation including interactions for 1×10^5 to 3×10^5 particles [5]. For all lattice depths, a phonon-like behavior is observable at low momentum reflected by the linear slope of the dispersion relation [48, 178]. The influence of the lattice manifests itself at the edge of the Brillouin zone, where the periodicity fundamentally changes the excitation spectrum and a band gap appears. Using the dispersion relation (6.20) derived within the Bose-Hubbard model and equation (6.26) for the on-site interaction U, a good agreement with experimental data is obtained. The boundaries of the theoretical predictions assume a particle number per tube of $N = 5\text{-}25$ for $V_0 = 3E_R$ (dashed green lines), $N = 15\text{-}50$ for $V_0 = 7E_R$ (blue), and $N = 25\text{-}60$ for $V_0 = 11E_R$ (magenta). An increase of the particle number per tube with increasing lattice depth V_0 is expected, due to a stronger in-plane confinement, which grows as

$$\omega_{x/y}^2 = \frac{4V_0}{mW_0^2} + \omega_{d,x/y}^2. \tag{6.27}$$

In fact, the confinement causes the tubes to be filled with different numbers of atoms decreasing from the center of the lattice. Therefore, the particle number per tube N is to be understood as an average over the lattice. In principle, the resonance frequency ω_{2D} as a function of N must be weighted with the occupation number distribution in the two-dimensional lattice, which gives, however, quite similar results.

The strong influence of the interaction becomes apparent when comparing with the single-particle dispersion relation. Figure 6.4 depicts the single-particle solution (2.27) (solid lines) and the Hubbard-type approximation (6.20) with $U = 0$ (dashed lines) for $V_0 = 3E_R$, $7E_R$, and $11E_R$. Note that these interaction-free solutions deviate for $V_0 = 3E_R$, where the tight-binding approximation is not fully valid, whereas for $V_0 = 7E_R$ and $11E_R$ both solutions agree almost perfectly. It turns out that the tight-binding approximation is probably also responsible for the deviation of relation (6.20) (solid symbols) from the numerical solution of the Bogoliubov-de Gennes equations (6.6) (open symbols). For $V_0 = 7E_R$, both approaches agree quite well and for $11E_R$ no noticeable difference is observable. Although both solutions are slightly different for
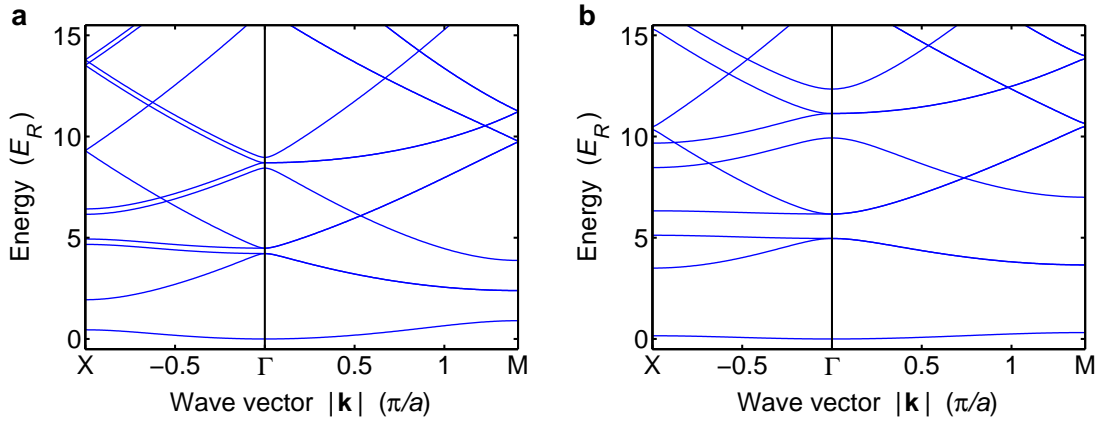
Fig. 6.5: Band structure for (a) $V_0 = 3E_R$ and (b) $V_0 = 7E_R$ for wave vectors $\mathbf{k}$ along Γ-X and Γ-M, i.e., in $[1, 0]$ and $[1, 1]$ direction, respectively.

$3E_R$, they are experimentally not clearly distinguishable. Regardless of the model, the interaction changes the excitation spectrum notably. Whereas for $V_0 = 3E_R$ the interaction effects are relatively small, interactions modify the dispersion substantially in deeper lattices. For $11E_R$, the energies are several times larger than for vanishing interaction. At the edge of the Brillouin zone, where the relative change is smallest, the excitation energies are considerably higher, e.g., about $11J$ for $V_0 = 11E_R$, than the single-particle band width $4J$.

6.3.4 Excited bands

As the two-photon Bragg process is not restricted to lowest band excitations, this method offers excellent access to the physics of higher bands. Neglecting the interaction, the band structure is given by the momentum-resolved single-particle excitation spectrum (see section 2.1.4). Here, let us restrict ourselves to the case of two-dimensional lattices not regarding excitations orthogonal to the lattice plane. Within the plane, three points of high symmetry are of special interest in the Brillouin zone: the center (Γ), the centers of the edges (X), and the corners of the square (M). The
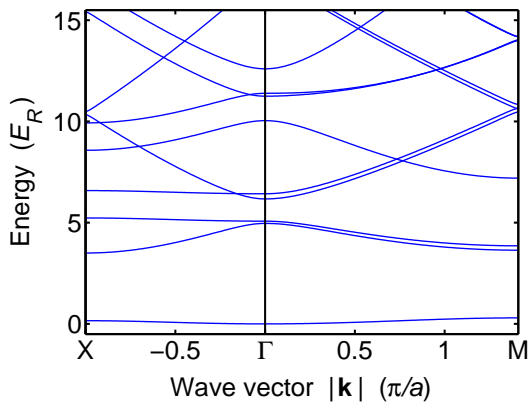

Fig. 6.6: Band structure plotted for asymmetric lattice depths $V_{0,x} = 7E_R$ and $V_{0,y} = 7.5E_R$, where X and M denote the points $(\pi/a, 0)$ and $(\pi/a, \pi/a)$ in the Brillouin zone, respectively.
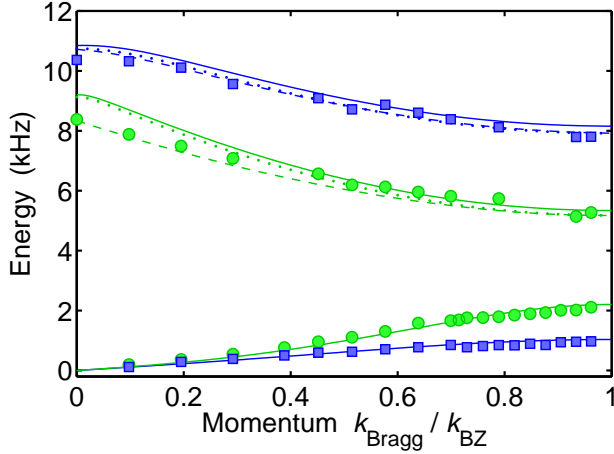
Fig. 6.7: Excitation spectrum of the lowest two bands for $V_0 = 3E_R$ (green) and $V_0 = 7E_R$ (blue). The dotted lines show the single-particle band structure, whereas the solid lines include interaction effects. Influences of the confinement for the first excited band are depicted by dashed lines.

band structure can be calculated using equation (2.27) and is plotted in Fig. 6.5 for $3E_R$ and $7E_R$. In general, the two-dimensional band structure can be obtained from the one-dimensional problem via

$$\omega_{2D}^{(n_x, n_y)}(k_x, k_y) = \omega^{(n_x)}(k_x) + \omega^{(n_y)}(k_y), \tag{6.28}$$

where the $n_i = 0, 1, ...$ denote the band indices, provided that the potential is separable in the axis directions and interaction effects are not dominant. Thus, along the Γ-X direction we have

$$\omega_{\Gamma\text{-}X}^{(n_x, n_y)} = \omega^{(n_x)}(k) + \omega^{(n_y)}(0) \tag{6.29}$$

and along the Γ-M direction

$$\omega_{\Gamma\text{-}M}^{(n_x, n_y)} = \omega^{(n_x)}(k/\sqrt{2}) + \omega^{(n_y)}(k/\sqrt{2}), \tag{6.30}$$

where $k = \sqrt{k_x^2 + k_y^2}$. Therefore, $\omega_{\Gamma\text{-}M}^{(n_x, n_y)}$ is two-fold degenerate for $n_x \neq n_y$. For broken symmetry, these bands split up, which is depicted in Fig. 6.6. This effect is also experimentally observable, when the intensities of the lattice beams are not equally adjusted.

In the experiment, the momentum transfer is in the $[1, 1]$ direction, i.e., the atoms are excited solely along the Γ-M direction. The experimental results for the first excited band are shown in Fig. 6.7 for $3E_R$ and $7E_R$, where the dotted lines represent the single-particle band structure. The solid lines are the numerical solution of the Bogoliubov-de Gennes equations (6.6). Compared with the lowest band, the relative changes of the excitation energies due to interaction are relatively small. Therefore, already the single-particle energies provide, in principle, a good description of the measured spectrum, while the small interaction effects can not be clearly resolved in the present experiment. Surprisingly, both descriptions overestimate the excitation energies noticeably for small momenta, which is most pronounced for $V_0 = 3E_R$. The shift of the experimental data can be attributed to the influence of the confinement. For $3E_R$, the energies of the first excited band lie energetically above the barriers between the lattice sites but still low enough that a clear band structure evolves. Therefore, a large effect of the confining potential is expected, which is incorporated by solving the single-particle problem using a finite lattice with an attached harmonic potential (see Fig. 4.1). For $3E_R$, the dispersion relation is governed by the strength

of the harmonic confinement and only to a much lesser extend by the size of the lattice, where $N_s = 100$ sites are used. The dashed green line in Fig. 6.7 depicts the finite-size solution and can explain the experimental results, which lie below the single-particle band structure. By contrast, at $7E_R$ the effect of the confinement is drastically reduced, since the first excited band lies only partly above the potential barriers, where results for $N_s = 30$ are plotted. It should be noted that the finite-size calculation does not include interactions. However, it seems to be justified to expect the same amount of interaction induced shift as in the infinite case, which corresponds to the difference between single-particle solution (dotted lines) and the Bogoliubov-de Gennes solution (solid lines).

6.4 Exact diagonalization

The Bogoliubov theory described in the last section offers a good description for weakly interacting atomic gases such as superfluids in optical lattices. However, the regime of strong interactions and correlations is not accessible within this description. The two-photon Bragg spectroscopy is an excellent tool to investigate these systems as it provides insight into the excitation spectrum and correlations by measuring the dynamic structure factor $S(\omega, k)$. Theoretically, exact diagonalization of the Hamiltonian is suited to describe systems with strong correlations and to compute the excitations for a variable range of interaction parameters. Exact diagonalization has been applied to determine the dynamic structure factor $S(\omega, k)$ in Refs. [56, 182]. Furthermore, $S(\omega, k)$ has been addressed using perturbation theory [182], an extended fermionization treatment [183], and quantum Monte Carlo [183, 184]. The aim is to identify signatures of strong correlations which are present, e.g., in the Mott-insulator phase or in the supersolid phase [32–34, 185–195].

6.4.1 The dynamic structure factor

In the following, the exact numerical solution for one-dimensional lattices is obtained. Thereby, the Hamiltonian (2.58) is diagonalized using a Wannier basis, where the many-particle basis states are represented by vectors $|N\rangle = |n_1, ..., n_i, ..., n_{N_s}\rangle$, where n_i corresponds to the occupation of site i (see section 2.4). The exact diagonalization is performed for lattices with $N_s = 10$ sites using periodic boundary conditions, which means that a particle can hop from the first site $i = 0$ to the last site $i = N_s$ and vice versa. The study of a single-component Bose gas is analogue to results presented in Ref. [56].

The excitation of atomic gases by a photon with energy $\hbar\omega$ and momentum $\hbar\mathbf{k}$ probes the dynamic density-density response of the system. Its signature is imprinted on the dynamic structure factor [56]

$$S(\omega, k) = \sum_{\nu} |\langle \Psi_\nu | \hat{\rho}_k^\dagger | \Psi_0 \rangle|^2 \, \delta(\omega - E_\nu) \tag{6.31}$$

assuming the validity of the linear response regime. The eigenstates Ψ_ν, where Ψ_0 denotes the ground state, and the energies E_ν, which are relative to the ground-state energy, are obtained by

exact diagonalization. The operator $\hat{\rho}_k^\dagger$ describes the Bragg process, which creates an excitation with momentum k, and can be written as

$$\hat{\rho}_k^\dagger = \sum_{q \in \text{BZ}} \hat{c}_{q+k}^\dagger \hat{c}_q. \tag{6.32}$$

Thereby, $\hat{c}_{q+k}^\dagger \hat{c}_q$ annihilates a particle in the Bloch state ϕ_q and creates a particle in the state ϕ_{q+k}. For noninteracting bosons, one finds $S(\omega, k) = N\delta(\omega - E_k)$, where E_k is the energy of the Bloch wave ϕ_k, reflecting the dispersion relation of a single-particle. As the system has a finite extend, the Brillouin zone (BZ) contains N_s different discrete quasimomentum states with

$$q = \frac{2\pi}{a}\frac{m}{N_s} \qquad \text{and} \qquad m = -\frac{N_s}{2} + 1, -\frac{N_s}{2} + 2, ..., \frac{N_s}{2}. \tag{6.33}$$

Due to relation (2.29), we can write the operator

$$\hat{c}_q = \frac{1}{N_s} \sum_{j=1}^{N_s} e^{iqx_j} \hat{b}_j \tag{6.34}$$

as a sum of annihilation operators in a Wannier basis. Inserting this expression in equation (6.32) leads to a simple expression for the Bragg excitation

$$\hat{\rho}_k^\dagger = \frac{1}{N_s} \sum_{q \in \text{BZ}} \sum_{j,l=1}^{N_s} e^{-i(q+k)x_j + iqx_l} \hat{b}_j^\dagger \hat{b}_l = \sum_{j=1}^{N_s} e^{-ikx_j} \hat{n}_j, \tag{6.35}$$

since the sum over the phase factor $\sum_{q \in \text{BZ}} e^{iq(x_l - x_j)}$ vanishes for $j \neq k$, due to $x_l - x_j = na$ with integer n. The computed eigenvectors $|\Psi_\nu\rangle = \sum_N C_N^\nu |N\rangle$ with energies below a cut-off energy $E_{\max}$ are represented by coefficients in the Wannier basis, which leads to

$$\langle \Psi_\nu | \hat{\rho}_k^\dagger | \Psi_0 \rangle = \sum_{j=1}^{N_s} e^{-ikx_j} \sum_N C_N^{\nu*} C_N^0 \, n_j. \tag{6.36}$$

The momentum transfer k is restricted to the N_s discrete vectors in the Brillouin zone given in equation (6.33). Note that the structure factors for k and $-k$ are identical and $S(\omega, k) = N\delta(\omega - E_0)$ for $k = 0$ with $E_0 = 0$. Further, it is convenient to normalize the dynamic structure factor by

$$S_{\text{n}}(\omega, k) = S(\omega, k) / \int d\omega \, S(\omega, k). \tag{6.37}$$

To visualize the results it is necessary to replace the δ function in the definition (6.31) by a smooth function, e.g., a narrow Gauss function

$$\delta(\omega - E_\nu) \rightarrow (\sqrt{2\pi}\Delta)^{-1} e^{-(\omega - E_\nu)^2 / 2\Delta^2}. \tag{6.38}$$

The width of the Gauss function Δ affects the perceptibility of the fine structure. In experiments, the observed Bragg spectrum is mainly broadened by the finite Bragg pulse duration and the inhomogeneous filling in the lattice, which limits the energy resolution in practice. Choosing $\Delta = 0.2J$ allows to visualize the fine structure but also pays tribute to the inevitable experimental
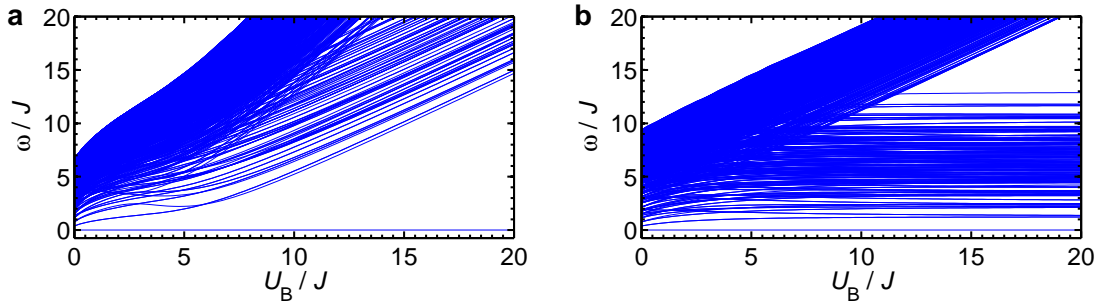
Fig. 6.8: The energy spectrum for an one-dimensional lattice with $N_s = 10$ sites (a) a commensurate filling $n_B = 1$ and (b) for filling $n_B = 0.5$ as a function of the on-site interaction U_B. At $U_{BF} = 0$, the highest computed energy is about $7J$ and $9J$, respectively.

broadening. In addition, the size of the system has an crucial impact on the fine structure, which is discussed below. In experiments, the confinement potential, which can cause Mott shells with superfluid interfaces, influences the observed dynamic structure factor [184].

The dynamic structure factor is shown in Fig. 6.9a-e for a commensurate filling of one atom per site and a varying ratio $U_B/J \geq 0$. The results for $U_B/J = 0, 5, 10$, and 15 are completely analogous to results presented in Ref. [56]. The continuous variation of the parameter U_B turns out to be advantageous with respect to both the interpretation of observed features and its transfer to larger systems. Overall, we see a smooth behavior when varying the ratio U_B/J, which is expected for the Mott transition, in general, and for finite systems, in particular. For $U_B = 0$, the single-particle band dispersion is observable with a single peak for each momentum between $0J$ (for $k = 0$) and $4J$ (for $k = \pi/a$). For small U_B, only one sharp peak is observable at low momenta, whereas for higher momenta already a broadening is noticeable. At intermediate and high momentum, several peaks contribute to $S(\omega, k)$, in contrast to the Bogoliubov picture, where effective single-particle excitations with a well-defined $\omega(k)$ exist. Note that the resonance positions in Fig. 6.9a-e, reflecting excitations in the systems, continuously transform into each other when varying the ratio U_B/J. For $U_B \gtrsim 6E_R$, the resonance positions as a function of U_B/J have the linear slope U_B. Consequently, these excitation can be connected to the Mott-insulator phase, where particle-hole excitations are gapped by U_B. The energy spectrum is shown in Fig. 6.8a, where the energy gap between the ground state and the first band, corresponding to particle-hole excitations, is clearly resolved. In this plot also the second band is shown with a slope $2U_B$ corresponding to two particle-hole excitations. In principle, the full first excited band is accessed in Bragg spectroscopy. While for noninteracting (or weakly interacting) systems, the dynamic structure factor reflects a sharp dispersion relation $\omega(k)$, this is not necessarily the case for strongly interacting particles. Regarding Fig. 6.9a-e, we see that an excitation with a defined k in the Mott-insulator phase corresponds to a superposition of eigenstates in the first excited band, where for higher momenta states in the center of the band dominate $S(\omega, k)$. The number of resonances in the dynamical structure factor is, however, rather size-dependent, so that one can probably expect a rather blurred structure factor $S(\omega, k)$ for large systems with continuous bands (corresponding to $\Delta \gg 0.2J$). In addition, a direct comparison of different system sizes N_s is complicated due to the discrete Brillouin zone vectors that depend also on N_s (see equation (6.33)).
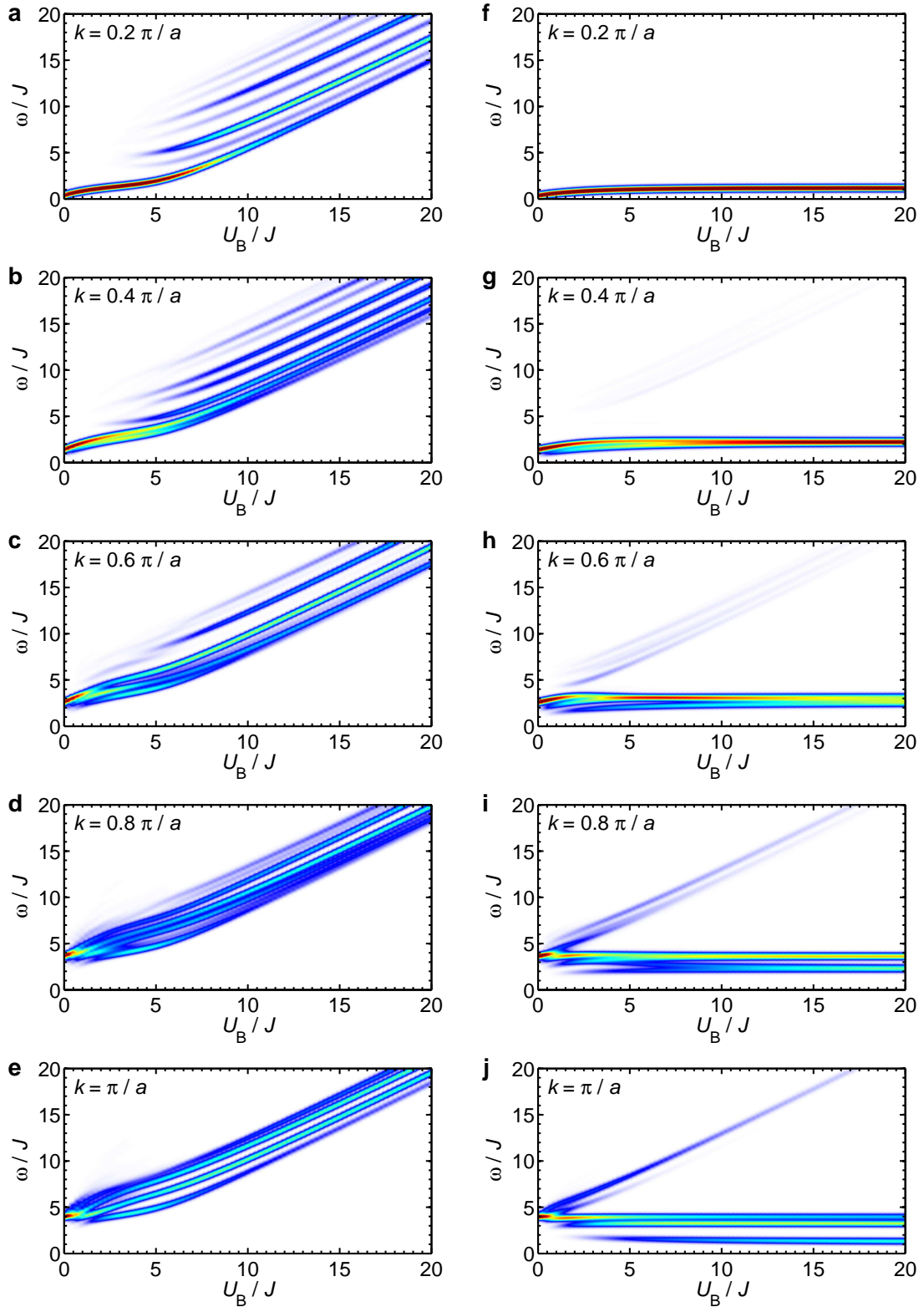
Fig. 6.9: The dynamic structure factor $S_n(\omega, k)$ for a one-dimensional lattice with $N_s = 10$ sites. The plots (a)-(e) show results for a commensurate filling with $n_B = 10$ bosons and column (f)-(j) for half filling with $n_B = 5$ bosons.
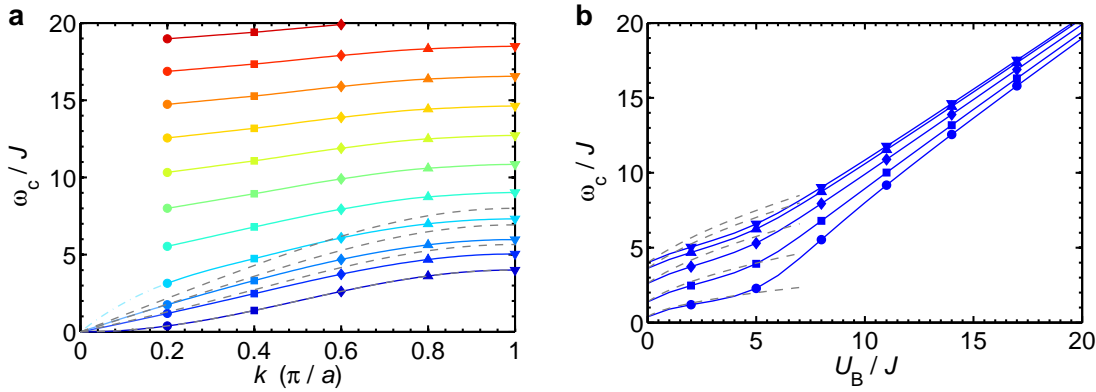
Fig. 6.10: (a) Centroid position ω_c of the dynamic structure factor as a function of the momentum k for $U_B/J = 0, 2, ..., 20$ (bottom to top). The dashed gray lines are Bogoliubov mean-field results of equation (6.20) for $U_B/J = 0, 2, 4$, and 6. (b) Centroid position in dependence on the on-site interaction energy U_B for momentum transfers $k = 0.2\,\pi/a, ..., \pi/a$ (for symbol assignment see left plot). The dashed gray lines correspond to Bogoliubov excitations and predict a fundamentally different behavior for $U_B \gtrsim 6 E_R$.

The overall shape and linear slope of the resonances as a function of U_B/J in the Mott-insulator phase are a more universal property, though, with a weak size dependence.

The basic behavior of $S(\omega, k)$ can in this case be captured in the centroid position of the dynamic structure factor

$$\omega_c = \int d\omega\, \omega\, S_n(\omega, k). \tag{6.39}$$

This quantity is, in particular, useful for the comparison with experimental systems with large broadening. The centroid frequency ω_c is shown in Fig. 6.10 as a function of both the momentum of the excitation k and the on-site interaction energy U_B. In both cases, the formation of an energy gap with increasing U_B is observable reflecting the Mott-insulator phase. Despite the limited resolution in k space, the single-particle band dispersion for $U_B = 0$ is clearly identifiable in Fig. 6.10a, which transforms continuously into a gapped spectrum. For large U_B and $k \neq 0$, the centroid positions reflect the dispersion within the first excited band consisting of particle-hole states (see Fig. 6.8a). In Fig. 6.10b, the linear slope of ω_c for $U_B \gtrsim 6J$ is connected to the excitation gap of the Mott-insulator phase. For large values of U_B, the slope matches precisely U_B. The centroid position allows to compare the results with the Bogoliubov approximation (6.20), which is indicated in Figs. 6.10a and 6.10b by dashed gray lines for $U_B/J \leq 7$. For small k, the mean-field approach matches quite well with the centroid positions of the exact calculation for $U_B/J \leq 4$, whereas at $U_B/J = 6$ the deviation becomes suddenly large (Fig. 6.10a). This can be attributed to the entrance in the Mott-insulator phase that is not covered in the Bogoliubov description. For large values of k, the centroid positions lie above the mean-field values for $U_B/J \lesssim 8$ and below for $U_B/J \gtrsim 8$.

The right column of Fig. 6.9 shows the dynamic structure factor $S_n(\omega, k)$ for the same system with half filling, i.e., $n_B = 5$ bosons. As discussed in detail in chapter 3, noncommensurate

systems show a fundamentally different behavior, which stems from the fact that localization is hindered due the equivalence of lattice sites. In particular, the main contributions to $S_{\mathrm{n}}(\omega, k)$ are within the single-particle band width $4J$, which is only the lower part of the ground-state band (Fig. 6.8b). Although the particles do not localize, they tend to avoid each other with increasing on-site repulsion. Several new features are perceptible at $U_{\mathrm{B}} > 0$ comparing with the single-particle dispersion ($U_{\mathrm{B}} = 0$). While for low momenta, the energy of the resonances rises with increasing U_{B}, for high momenta new excitation below $\omega_{\mathrm{c}}(U_{\mathrm{B}} = 0, k)$ emerge. In addition, a weak resonance with linear slope U_{B} is observable, which is most pronounced at high momentum and arises from the energetically disfavored double occupation of lattice sites. Comparing with the commensurate case, the total strength of $\int d\omega \, S(\omega, k)$ for noncommensurate filling, being connected with properties of the ground state [56], is considerably higher, which must also be considered for inhomogeneous experimental systems.

6.4.2 Bose-Fermi mixtures

In this section, the dynamic structure factor for boson-fermion mixtures is addressed. Here, let us assume that the Bragg excitation is resonant to the bosonic subsystem only and that the fermions do not redistribute as a consequence of the bosonic excitation. For attractive interspecies interaction, we can assume a homogeneous filling of bosons and fermions in the lattice, as discussed in chapter 5. The self-trapping effect causes an strongly altered bosonic effective potential, which leads to a renormalization of the Bose-Hubbard parameters U_{B} and J. Therefore, for attractive interspecies interaction we can apply the results in the last section with effective parameters $U_{\mathrm{B}}(V_0)$ and $J(V_0)$. Here, repulsive interspecies scattering in studied, where at half fermionic filling anticorrelated phases have been predicted [32–34]. For simplicity, we restrict ourselves to the single-band Bose-Fermi-Hubbard model, but, in principle, interaction induced orbital changes can be introduced, which is discussed in chapter 8. Since the Bose-Fermi system is quite complex, I focus the discussion on bosonic excitations for rigid fermionic configurations. Excluding correlated boson-fermion states, this corresponds to the effective potential approach in section 5.2.1 without a self-consistent treatment of boson and fermion subspaces. In particular, it allows to probe the bosonic response to a given fermionic configuration, which is useful for the interpretation of experimental results.

For the exact diagonalization the Bose-Fermi-Hubbard model (2.62) is applied, which depends on the on-site interactions U_{B} and U_{BF} as well as on the hopping parameters J_{B} and J_{F}. The on-site interactions are assumed to be repulsive so that $U_{\mathrm{B}} > 0$ and $U_{\mathrm{BF}} > 0$. The basis states $|N\rangle_{\mathrm{B}} \otimes |\Psi_{\mathrm{F}}^0\rangle$ are used, where $|N\rangle_{\mathrm{B}}$ are all possible bosonic Fock states and $|\Psi_{\mathrm{F}}^0\rangle$ is a single fermion state. Consequently, the system exclusively depends on the ratios U_{B}/J and U_{BF}/J, where J denotes the bosonic tunneling J_{B}.

In particular, for systems with half fermionic filling it is of importance to distinguish between two scenarios: the alternating filling and the alignment of fermions in a single domain. For strong interspecies repulsion, we expect in both cases sites that are either occupied by a boson or by a fermion. However, only when a domain is formed bosons and fermions are spatially separated. To distinguish between both scenarios, the dynamic structure factor for an one-dimensional lattice
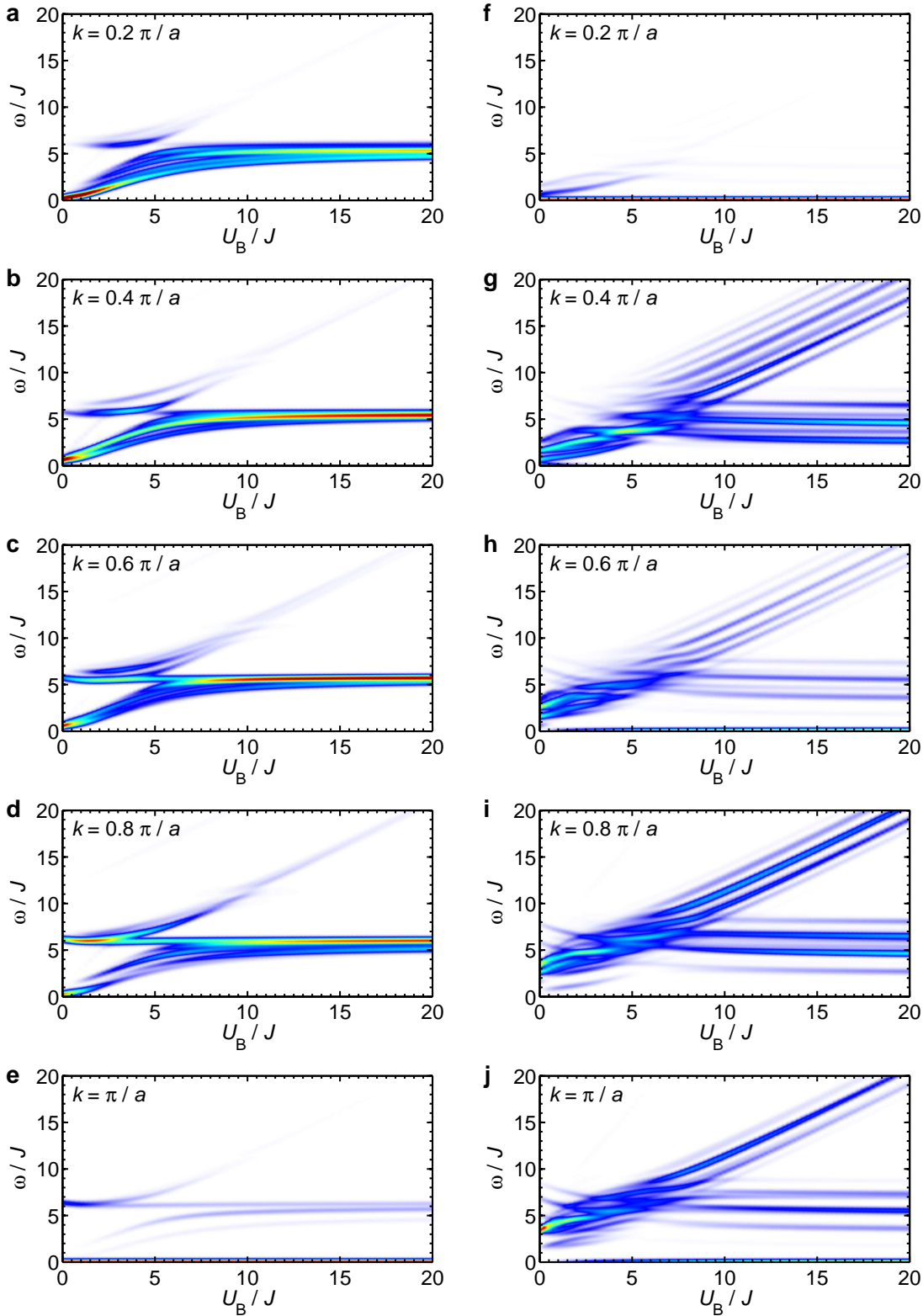
Fig. 6.11: The dynamic structure factor $S_n(\omega, k)$ for a one-dimensional lattice with $N_s = 10$ sites, five bosons and five fermions, and an interspecies interaction $U_{BF} = 5J$. While the first column (a)-(e) shows results for alternating fermionic filling, the plots (f)-(j) depict $S_n(\omega, k)$ for a configuration, where the fermions are aligned next to each other.

Fig. 6.12: The dynamic structure factor $S_{\mathrm{n}}(\omega, k)$ for $U_{\mathrm{BF}} = 10J$ with (a)-(e) alternating fermionic filling and (f)-(j) for fermions aligned in a domain.

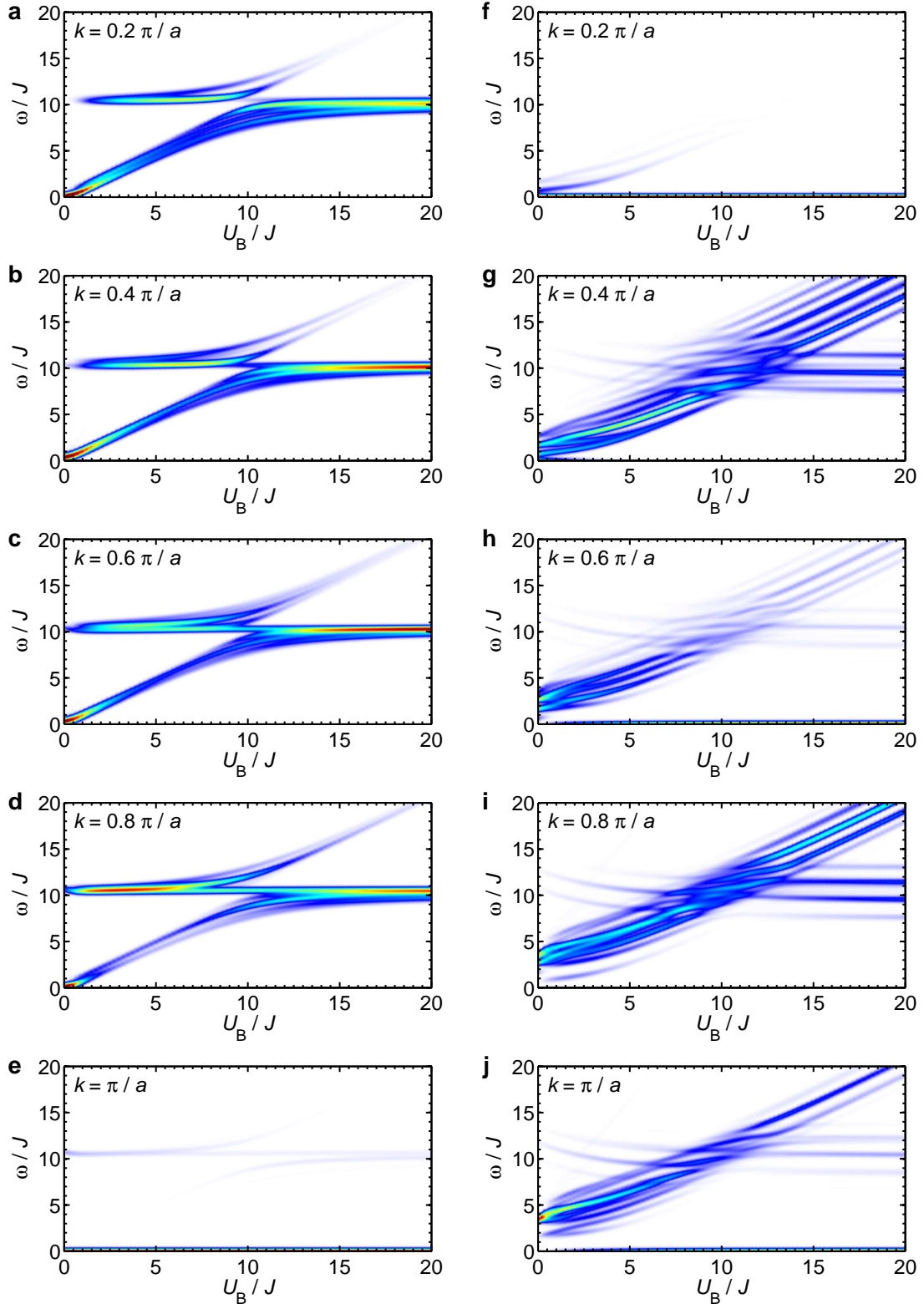with $N_s = 10$ sites, $n_B = 5$ bosons, and $n_F = 5$ fermions is computed, where periodic boundary conditions are applied. Figure 6.11 and 6.12 depict $S_n(\omega, k)$ for both scenarios in dependence on the on-site interaction U_B for $U_{BF} = 5J$ and $10J$. While the columns a-e show results for an alternating fermionic filling, the columns f-j present $S_n(\omega, k)$ for the alignment of fermions in a domain.

For alternating filling, one observes a strong resonance around U_{BF}, which is weaker for small U_B at low momentum. For $U_B < U_{BF}$, a second strong resonance with a slope about U_B is visible. Thus, the basic excitations are given by the double occupation of sites with either two bosons or with a boson and a fermion. For $U_B > U_{BF}$, the resonance with slope U_B is much weaker. Interestingly, the excitations show a pronounced avoided crossing behavior at $U_B = U_{BF}$. In particular, it should be noted that both excitations have a relatively sharp resonance and that for $U_B \gg U_{BF}$ the excitations are dominated by the bosonic excitations to fermionic sites. For $U_B = 0$, no $\sin^2(ka/2)$ shaped dispersion is observable due to the superlattice structure experienced by the bosonic atoms. At the Brillouin zone edge $k = \pi/a$, which corresponds to the superlattice structure $2a$, a strong resonance at $\omega = 0$ occurs for all values of U_B. As a consequence, the relative amplitude for excitations with $\omega > 0$ decreases.

A similar situation can be observed at $k = 0.2\pi/a$ for the scenario in which the fermions are aligned next to each other. Here, the wave vector also corresponds to the superlattice structure, which includes ten lattice sites. Remarkably, the structure factor shows several resonances for all momenta and values of U_B, which is in great contrast to the alternating alignment discussed before. The set of resonances with slope U_B for $U_B/J \gtrsim 6$ can be directly connected to the formation of a Mott insulator as discussed in the previous section (Fig. 6.9a-e). These excitations correspond to particle-hole excitations representing the relatively broad first excited Mott-insulator band. In addition, however, also strong resonances with energy U_{BF} are observable corresponding to excitations of bosons to fermion occupied sites showing a similar band structure.

The differences between both scenarios can be further highlighted by varying the interspecies on-site interaction U_{BF}, which is presented in Fig. 6.13. Note that here the horizontal modes belong to an excitation with energy U_B, whereas the modes with linear slope correspond to U_{BF}. For $U_{BF} \gg U_B$, both fermionic configurations are clearly distinguishable. For fermions being aligned in a domain, only excitations with U_B are observable resembling the purely bosonic system with commensurate filling (Fig. 6.9a-e). This indicates the spatial separation of bosons and fermions. Consequently, we obtain a system where the bosonic atoms behave like a conventional Mott insulator.

For alternating filling, excitations with U_B and U_{BF} are observable for $U_{BF} \gg U_B$, where the resonance scaling with U_{BF} is much stronger despite its much higher energy. This means that bosonic excitations which involve tunneling to nonnearest neighbors are only partly suppressed. The dynamic structure factor is, however, dominated by the occupation of a boson at a fermionic site leading to a band gap energy U_{BF}. The alternating fermionic filling causes, in particular, that the resonances are relatively sharp. This is caused by the small effective tunneling matrix element connecting equivalent sites, i.e., two nearest sites being occupied by fermions or two nearest sites being not occupied by fermions. This is also directly observable in the energy spectrum

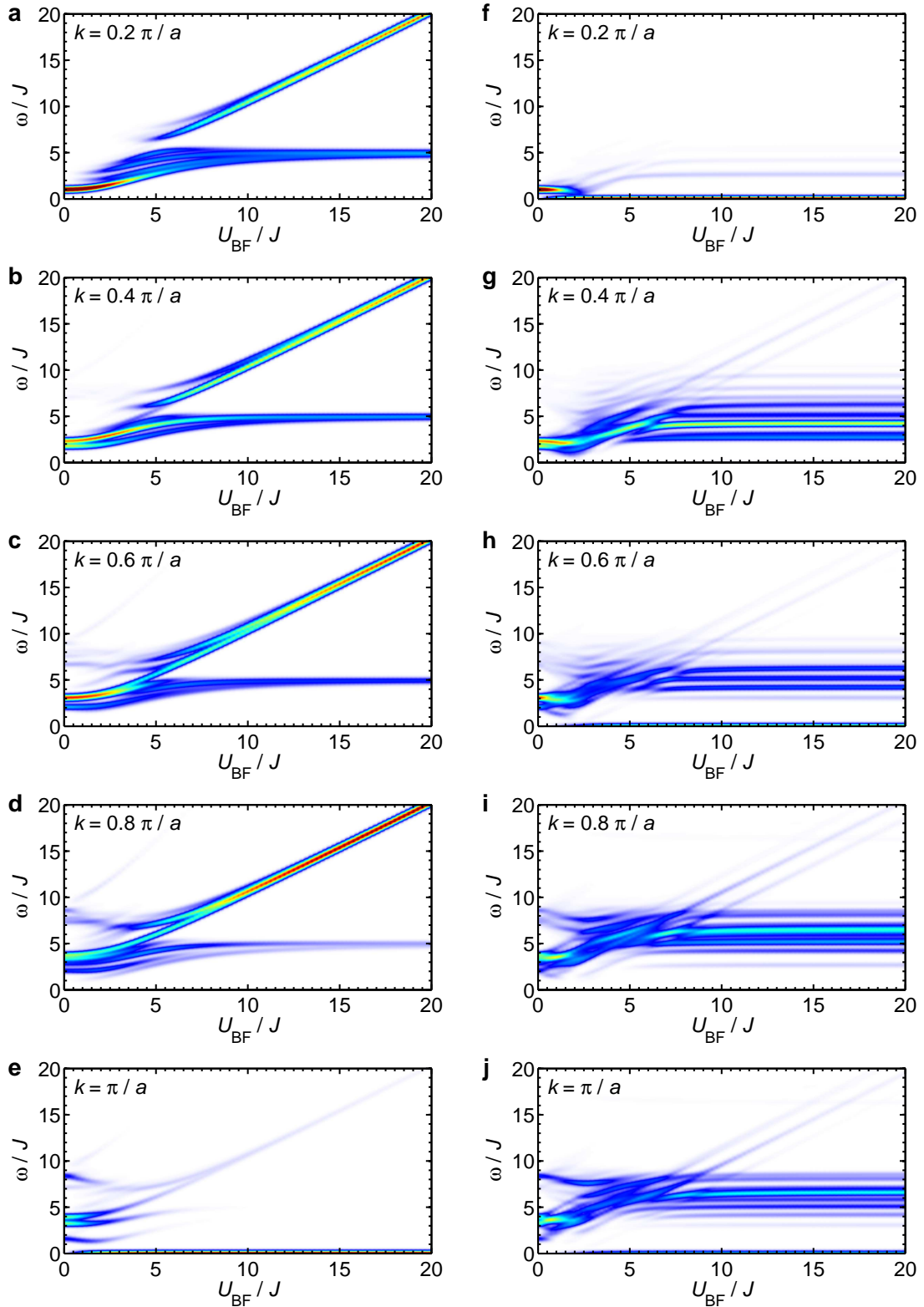**Fig. 6.13:** The dynamic structure factor $S_\mathrm{n}(\omega, k)$ as a function of the interspecies on-site interaction U_BF for $U_\mathrm{B} = 5J$. Plots (a)-(e) depict results for alternating fermionic filling and (f)-(j) for fermions aligned in a domain.
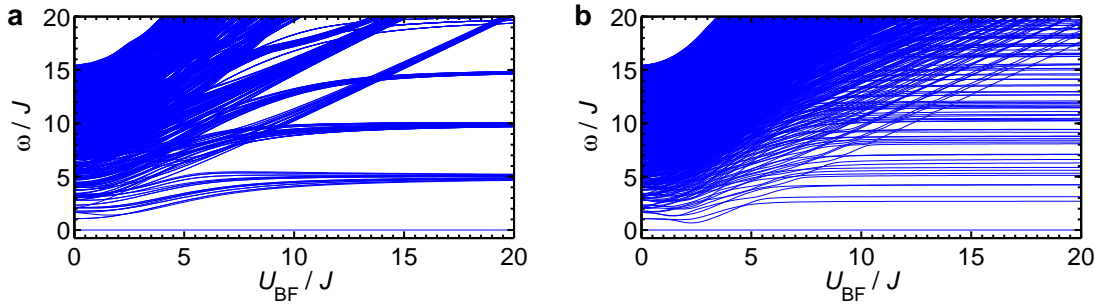
Fig. 6.14: The energy spectrum for (a) alternating fermionic filling and (b) fermions aligned in a domain as a function of U_{BF} at $U_{\mathrm{B}} = 5J$. At $U_{\mathrm{BF}} = 0$, the highest calculated energy is about $15J$.

in Fig. 6.14a, which shows narrow and clearly resolved bands corresponding to excitations with U_{B}, $2U_{\mathrm{B}}$, $3U_{\mathrm{B}}$, U_{BF}, $U_{\mathrm{BF}} + U_{\mathrm{B}}$, and $2U_{\mathrm{BF}}$. In contrast, for the case, where the fermions are aligned in a domain, the bands in the energy spectrum (Fig. 6.14b) are broad and overlap each other.

6.5   Conclusions

For weakly interacting atomic gases in optical lattices, the band structure can be derived using mean-field theory. Two different approaches, the Bogoliubov-de Gennes equations [50–53] and a Hubbard-type approximation [48, 49, 54, 55], have been described and compared with each other using experimental parameters. The band structure is substantially modified by interaction effects and is in good agreement with two-photon Bragg spectroscopy of a superfluid in an optical lattice [5]. In addition, deviations for excited bands arising from to the confinement have been calculated.

Further, we can conclude that Bragg spectroscopy is also a feasible tool to explore the nature of excitations in highly correlated systems. The fingerprint of these correlations, however, give rise to nontrivial structures in the dynamic structure factor $S(\omega, k)$. For one-dimensional finite lattices, $S(\omega, k)$ has been computed for a smoothly varying ratio of tunneling to on-site interaction. It changes notably when driving the system from the superfluid to the Mott-insulator phase, including the formation of an energy gap. Moreover, the presented results show that the dynamic structure factor allows to distinguish systems with a spatial separation of bosons and fermions from a scenario with alternating filling. Although the results in this section are restricted to one-dimensional and, in particular, finite-sized systems, they give valuable information for the experimental verification of complex phases.

7

Multiorbital quantum phase evolution in optical lattices

*The main results in this chapter have been published in Ref. [6] S. Will, T. Best, U. Schneider, L. Hackermüller, D.-S. Lühmann, and I. Bloch, Time-resolved observation of coherent multi-body interactions in quantum phase revivals, Nature **465**, 197 (2010).*

7.1 Motivation

The realization of the quantum phase transition of bosonic atoms from the superfluid to the Mott-insulator phase [19, 118, 120] is one of the most prominent examples that demonstrate the great benefits of optical lattices. Both the accurate tuning of the lattice depth and the modification of the particle-particle interactions open amazing possibilities, which are not easily accessible in solid-state physics. By focusing on a single well of the optical lattice, the fundamentally different behavior of the superfluid and the Mott-insulator phases becomes apparent. The superfluid phase is, in principle, indistinguishable from a coherent state at each lattice site with a Poissonian particle number distribution. This state is clearly not an eigenstate of the particle number operator and exhibits strong particle fluctuations. Being the eigenstate of the annihilation operator, however, the state remains unchanged by the detection of a particle. The atoms in each microtrap can be regarded as a matter wave field. In the Mott phase, the single-site states are local Fock states with a defined particle number. By contrast, for a single-particle Fock state, the detection of a particle eliminates the possibility to detect another. By varying the depth of the optical lattice, we can squeeze the matter wave field from a coherent state to a Fock state and vice versa.

When the lattice is suddenly ramped from shallow to deep, the particle number statistics of the superfluid phase is preserved in the deep lattice. This leads to a coherent superposition of particle number states at each lattice site that evolves in time corresponding to the Hamiltonian at the final lattice depth. Since the tunneling between neighboring sites can be neglected in very deep lattices, the Hamiltonian describes the interaction of particles at single lattice sites. Thereby, each particle number state evolves according to its characteristic interaction energy. Experimentally, the time evolution can be monitored by the visibility of the momentum distribution (see section 2.5.1), which undergoes a characteristic sequence of collapses and revivals [57–60]. This property is directly connected to the evolution of the matter wave field at each lattice site and allows to probe

both the interaction energies and the particle number statistics.

In the Bose-Hubbard model, which is widely used in the context of optical lattices, all number states evolve with multiples of a single on-site energy [60]. In contrast, recent measurements, which are able to detect up to 40 revivals [6], show that different energies contribute to the time evolution. This is a direct evidence for multiband physics causing deviations from the particle-number-independent on-site interaction. Experimentally, the changes of the on-site interaction with the particle number has been addressed before in Ref. [144] by using atomic clock shifts. However, the high resolution of the collapse and revival measurement enables a detailed comparison with accurate theoretical calculations. Since the atoms are tightly confined on the sites for deep lattices, the correlations between the particles due to their interaction become crucial. Performing a diagonalization of the many-particle system, the exact particle-dependent on-site interaction energies are computed, which are in striking agreement with the experimental data [6]. In particular, the influence of kinetic and potential energy, the role of bound and nonbound orbitals, and the broadening of the effective orbitals are addressed.

7.2   Particle fluctuations

As described previously in section 2.6.1, for vanishing on-site interaction U all atoms occupy the lowest Bloch wave $\phi_{\mathbf{q}=0}(\mathbf{r})$. In a Wannier basis, the many-body wave function reads

$$|\Psi_{\text{SF},\,U=0}\rangle = \left(\frac{1}{\sqrt{N_s}}\sum_i \hat{b}_i^\dagger\right)^N |0\rangle, \tag{7.1}$$

which visualizes the strong particle fluctuations at each lattice site. We can approximate this many-body state as

$$|\Psi_{\text{SF},\,U=0}\rangle \approx \prod_i |\phi_i\rangle, \tag{7.2}$$

where the single-site states $|\phi_i\rangle$ consist of a sum of local Fock states with different particle numbers, i. e.,

$$|\phi_i\rangle = \sum_n c_n^{(i)}|n\rangle_i. \tag{7.3}$$

In the limit of large lattices with a constant filling factor, the atom numbers are Poissonian distributed, so that the superfluid state at $U = 0$ can approximately be written as product of coherent states with a constant relative phase to each other, namely

$$|\phi_i\rangle = |\alpha\rangle = e^{-|\alpha|^2/2}\sum_{n=0}^{\infty}\frac{\alpha^n}{\sqrt{n!}}|n\rangle, \tag{7.4}$$

where $\bar{n} = |\alpha|^2$ is the mean particle number per site. As mentioned, the coherent state is the eigenstate of the local annihilation operator $\hat{b}$, i.e.,

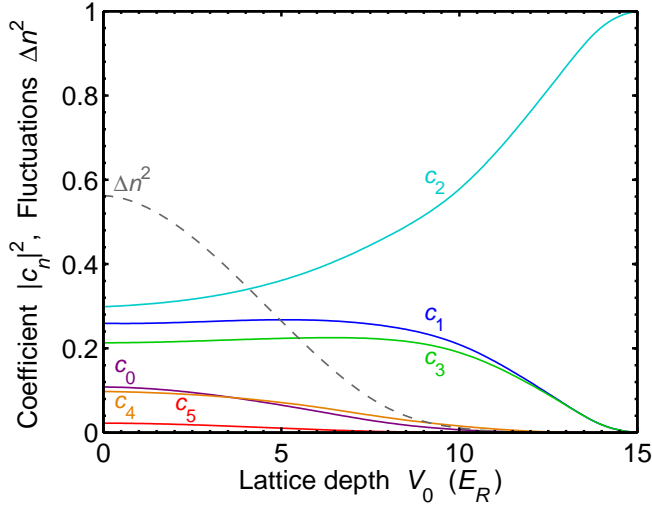$$\hat{b}|\alpha\rangle = \alpha|\alpha\rangle. \tag{7.5}$$

Fig. 7.1: Square of the lowest coefficients $|c_n|^2$ for the mean filling $\bar{n} = 2$ using a Gutzwiller approach and equation (2.119). The dashed gray line depicts the particle fluctuations Δn^2, which vanish in the Mott-insulator phase.

When the ratio of on-site interaction U to tunneling J increases, the distribution of the local particle number states becomes sub-Poissonian [60, 196]. For large values of U/J, when the system forms a Mott-insulator phase (section 2.6.2), the single-site states $|\phi_i\rangle$ have a definite particle number for commensurate integer filling. Consequently, the many-particle state reads

$$|\Psi_{\text{Mott},\, U/J\to\infty}\rangle = \prod_i |n\rangle_i. \tag{7.6}$$

As in both limiting cases $U/J \to 0$ and $U/J \to \infty$ the many-particle state can be written as product of single-site wave functions

$$|\Psi_{\text{GW}}\rangle = \prod_i \sum_n c_n^{(i)} |n\rangle_i, \tag{7.7}$$

it is instructive to choose this ansatz for all values of U/J, which is the so-called Gutzwiller trial wave function [21, 74, 197]. Assuming a homogeneous system, where all single-site wave functions are identical $|n\rangle_i = |n\rangle$, the Hamiltonian can be approximated by an effective single-site Hamiltonian [198]

$$\langle H_{\text{GW}}\rangle = -zJ\Big|\sum_n c_n^* c_{n+1}\sqrt{n+1}\Big|^2 + \frac{U}{2}\sum_n |c_n|^2 n(n-1). \tag{7.8}$$

The energy functional $\langle H_{\text{GW}}\rangle$ can be minimized, where the normalization in respect to the coefficients and the mean particle number,

$$\sum_n |c_n|^2 = 1 \qquad \text{and} \qquad \sum_n |c_n|^2\, n = \bar{n}, \tag{7.9}$$

respectively, must be fulfilled. Exemplarily, for a mean filling $\bar{n} = 2$ the square of the coefficients and the fluctuations Δn^2 are shown in Fig. 7.1, where we assume $|c_n|^2 \approx 0$ for $n \geq 6$. In deep lattices, the particle fluctuations vanish and only the coefficient c_2 contributes. Thus, the system enters the Mott-insulator phase with a commensurate filling of two atoms per site.
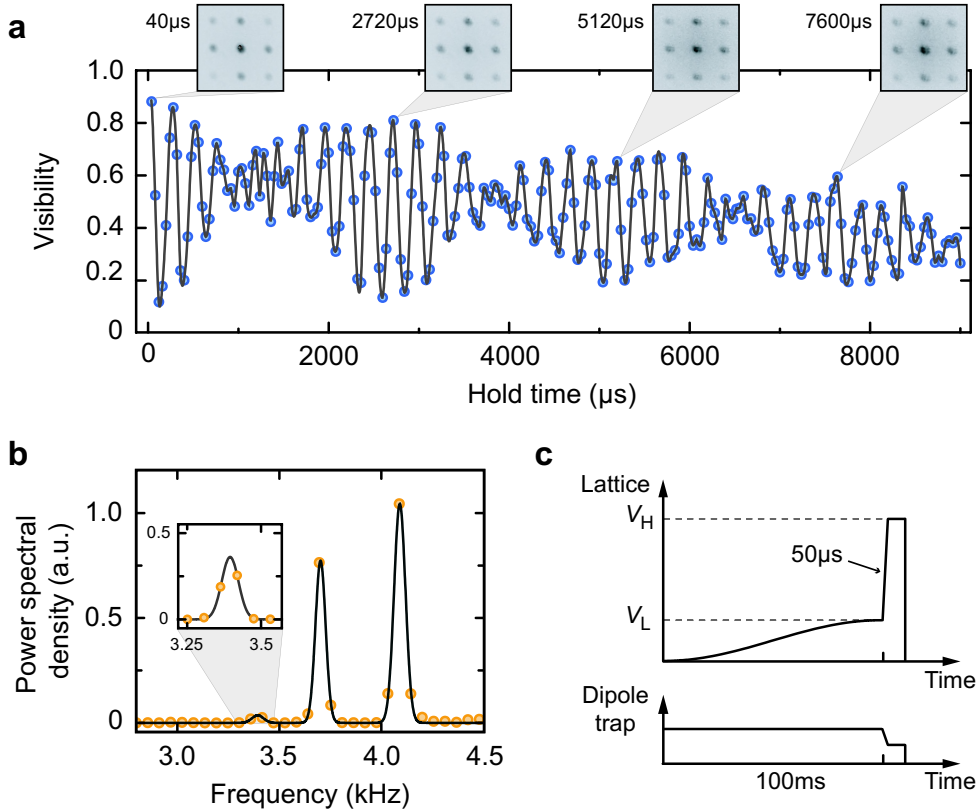
Fig. 7.2: (a) Experimental visibility taken from Ref. [6] as a function of the hold time for a final lattice depth $V_H = 40.3E_R$. Exemplarily, the momentum distributions at certain revival times are shown. Obviously, the experimental data can not be described in a single-band picture with a constant on-site interaction U. (b) A detail of the Fourier transformation and (c) the experimental sequence for the lattice depth and the strength of the dipole potential are shown below. The Fourier-limited peak width is about 100 Hz.

7.3 Time evolution

It has been shown in Ref. [60] that the coherent superposition of particle number states at each lattice site in the superfluid phase can be probed experimentally by performing a nonadiabatic ramp from a shallow to a deep lattice. In a time scale that is fast compared with tunneling time but slow enough that all atoms remain in the vibrational ground state of the lattice wells, the lattice is ramped up from the initial lattice depth V_L to the final lattice depth V_H. This ensures that the atom number distribution is preserved during the rapid increase of the lattice depth. At the final lattice depth, the particle number states at each site evolve separately due to the interaction. In the Bose-Hubbard model, the time evolution at each site can be described by

$$|\phi(t)\rangle = \sum_n c_n e^{-iUn(n-1)t/2\hbar}|n\rangle, \tag{7.10}$$

where U is the on-site interaction per particle pair. Due to the scaling of the on-site interaction U with $n(n-1)/2$ in phase factor, the particle number states dephase leading to a collapse at

$t_{\mathrm{col}} \approx h/\sigma_n U$, where σ_n^2 is the variance of the atom number distribution [57–60]. After an evolution time $t_{\mathrm{rev}} = h/U$ the phase factors become equal modulo 2π and the initial state revives. This leads to periodic collapses and revivals of the matter wave field ψ, which is the expectation value of the atomic field operator

$$\psi = \langle \phi(t) | \, \hat{b} \, | \phi(t) \rangle. \tag{7.11}$$

The macroscopic matter wave field ψ is directly connected to the experimentally accessible fringe visibility of atoms in optical lattices [60]. Therefore, revivals after integer multiples of t_{rev} can be observed in the visibility data. In Ref. [60], the number of revivals is limited to a number of five, which is due to the strong inhomogeneity in the optical lattice caused by the confinement of the lattice lasers at the final lattice depth. This confining potential leads to a varying mean number of atoms from the center to the edge of the lattice and a strong damping of the observed visibility.

Using a new experimental setup described in section 5.5, the group of I. Bloch at the University of Mainz achieves a drastic increase of the number of observable revivals [6]. The progress is mainly due to the advantage of using a blue detuned lattice, causing an anticonfinement, in combination with a red detuned dipole trap, which allows the tunability of the harmonic confinement. In the experiment, a three-dimensional lattice with a lattice spacing $a = 369$ nm is generated and loaded with ultracold ^{87}Rb atoms. By adjusting the elliptical red detuned optical dipole trap for a given lattice depth V_0, optical lattices with very shallow confinements are achieved. The best results for the collapse and revival measurements are even obtained using a weak overall anticonfinement. With this setup it is possible to observe up to 40 revivals, which is shown exemplarily in Fig. 7.2. From these results, it is obvious that more than one frequency is important for the time evolution. Therefore, the single-band Hubbard model (7.10), where the on-site interaction scales precisely with $Un(n-1)/2$, breaks down. The corrections due to higher bands in collapse and revival experiments have been addressed in Ref. [199]. Applying perturbation theory, effective two- and three-body interactions have been predicted leading to a beat frequency behavior. A perturbative approach, however, does not provide an accurate description for the strong interactions considered here. The frequencies arising from the full multiorbital treatment are derived and computed in the following section.

7.4   Exact calculation of on-site energies

Orbital changes cause a reduction of the on-site interaction energy with increasing particle numbers as particles tend to avoid each other for repulsive scattering. Therefore, the interaction energy depends explicitly on the number of atoms per site and an admixture of higher-band orbitals must be considered. Although, the modifications are less pronounced than for boson-fermion mixtures (section 5), they notably change the on-site interaction per particle pair. The problem of n interacting bosons at a lattice site is solved by exact diagonalization yielding a full inclusion of orbital changes and particle correlations. In deep lattices, where the final lattice depth in the collapse and revival experiment is $20 E_R < V_{\mathrm{H}} < 45 E_R$, it is valid to restrict this calculation to a single lattice site. Thus, we can write the single-band Bose-Hubbard on-site interaction as

$$U_{\mathrm{BH}} = g \int d^3r \ |w_0(\mathbf{r})|^4 \approx g \int d^3r \ |\varphi_0(\mathbf{r})|^4, \tag{7.12}$$
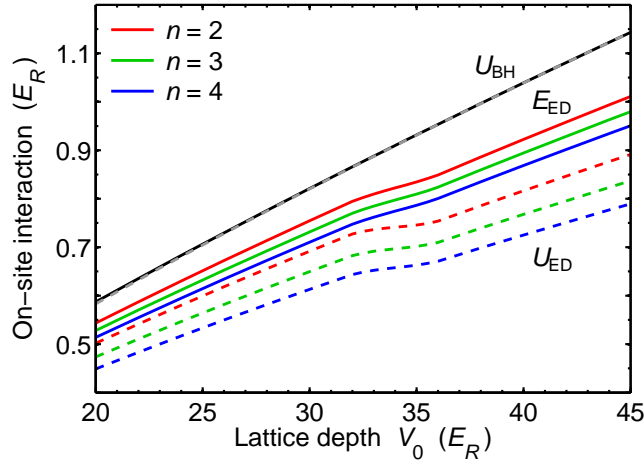
Fig. 7.3: Comparison of the Bose-Hubbard on-site interaction U_{BH}, the many-particle expectation value of the interaction energy U_{ED}, and the total energy E_{ED} obtained by the eigenvalue of the Schrödinger equation. The results are plotted for two to four $^{87}\mathrm{Rb}$ atoms, a lattice spacing $a = 369$ nm, and a scattering length $a_s = 102a_0$. The dashed gray and the solid black lines correspond to the Hubbard interaction U_{BH} computed using Wannier functions $w_0(\mathbf{r})$ and single-site eigenfunctions $\varphi_0(\mathbf{r})$, respectively.

which is shown quantitatively in Fig. 7.3, where the dashed gray line represents the on-site interaction using Wannier functions $w_0(\mathbf{r})$ (section 2.1.4) and the solid black line is obtained using the single-site solutions $\varphi_0(\mathbf{r})$ with hard boundary conditions. Both energies are noticeably higher than indicated by the experiment. With the exact many-particle wave function obtained by diagonalization, the on-site interaction per particle pair can be evaluated using

$$U_{\mathrm{ED}} = \frac{g}{n(n-1)} \int d^3r \, \langle \hat{\psi}^\dagger(\mathbf{r})\hat{\psi}^\dagger(\mathbf{r})\hat{\psi}(\mathbf{r})\hat{\psi}(\mathbf{r})\rangle, \tag{7.13}$$

which fully includes many-particle correlations (see section 4.4). The latter denotes the admixture of many-particle states of the Fock basis, where some or all particles occupy higher single-particle orbitals. The expectation value U_{ED} neglects, however, the changes in potential and kinetic energy due to the broadening of the density. Therefore, the total change of the energy due to the interaction must be taken into account, which is the eigenvalue of the many-particle Schrödinger equation

$$\hat{H}_i \, \Psi_n = e_n \, \Psi_n. \tag{7.14}$$

Normalized to the energy per particle pair, we obtain the correct interaction energies

$$E_{\mathrm{ED}} = \frac{e_n - e_n^0}{n(n-1)/2}, \tag{7.15}$$

where e_n^0 is the energy of noninteracting particles. As shown in Fig. 7.3, the total change in energy is considerably smaller than expected for the interaction integral U_{ED} in equation (7.13).

As mentioned before, in the experimental realization [6] a slight anticonfinement is present, which allows that atoms can leave the system via free-space states or via multiple tunneling processes.

Performing a time-of-flight detection, the fraction of atoms that is lost during the hold time in the experiment does not contribute to the observed signal. It is therefore a good assumption to project the quantum mechanical state on many-particle Fock states with only bound orbitals, while other contributions can be considered as lost. This has a profound influence on the observable interaction energies. Let us consider a confined system, where particle loss occurs only via three-body recombination. Here, an infinite number of orbitals and therefore an infinite number of Fock states contribute causing a notable reduction of the interaction energy. However, the exact diagonalization is restricted to a large but finite number of orbitals in order to achieve convergence. Note that the exact values are therefore always (slightly) lower than the computed ones. Applying this model leads to interaction energies E_{ED} for two ^{87}Rb atoms that are about 8% lower than the experimentally observed values. Experimental errors (see below) and the uncertainty in the scattering length of ^{87}Rb atoms [106, 107] are considerably smaller. Thus, the experimental data supports the assumption that only bound orbitals are occupied.

With the restriction of a finite number of orbitals the diagonalization becomes exact, as all possible many-particle states are included in the calculation. The number of orbitals influences the computed energy, where, in general, the energy is lower, the more orbitals are included. For a separable symmetric three-dimensional optical lattice, the three-dimensional orbitals are simple products of one-dimensional wave functions

$$\psi_{\{j,k,l\}}(\mathbf{r}) = \varphi_j(x)\,\varphi_k(y)\,\varphi_l(z) \tag{7.16}$$

with $j, k, l = 1, ..., s$. The many-particle states $|N\rangle$ can be represented by the occupation numbers of the three-dimensional orbitals $\psi_{\{j,k,l\}}$. The number of many-particle states $|N\rangle$ defines the finite dimension of the Hilbert space

$$\frac{(n+m-1)!}{n!(m-1)!}, \tag{7.17}$$

where $m = s^3$ is the total number of single-particle orbitals. However, only Fock states with even parity in all spatial dimensions can mix with the energetically lowest many-particle state. Of special interest is that the number of bound orbitals changes when the lattice depth is increased. At roughly $V_0 = 34E_R$, the number of bound orbitals changes from three to four per spatial dimension, which is depicted in Fig. 7.4a. Below this threshold, $3^3 = 27$ bound orbitals must be included, whereas $4^3 = 64$ orbitals contribute above $V_0 = 34E_R$. Between $32E_R$ and $36E_R$, the energies in Fig. 7.3 are interpolated, which leads to smooth crossover from 3^3 to 4^3 orbitals. Below $18E_R$, only two bound orbitals exist per spatial dimension at each lattice well, and the energy difference to the single-band model is drastically reduced. However, this regime is experimentally not accessible, since for shallow final lattice depths only a small number of revivals is observable due to a nonnegligible tunneling.

Regarding the periodicity and the orthogonality of wave functions, hard boundary conditions with infinite walls are chosen. However, also weak boundaries could, in principle, be considered, which influences, in particular, the highest bound orbital in each spatial dimension. The deviation is largest when the highest bound orbital lies just below the edge of the potential barrier. Choosing a very weak confining potential, the deviation in the total interaction energy is roughly between
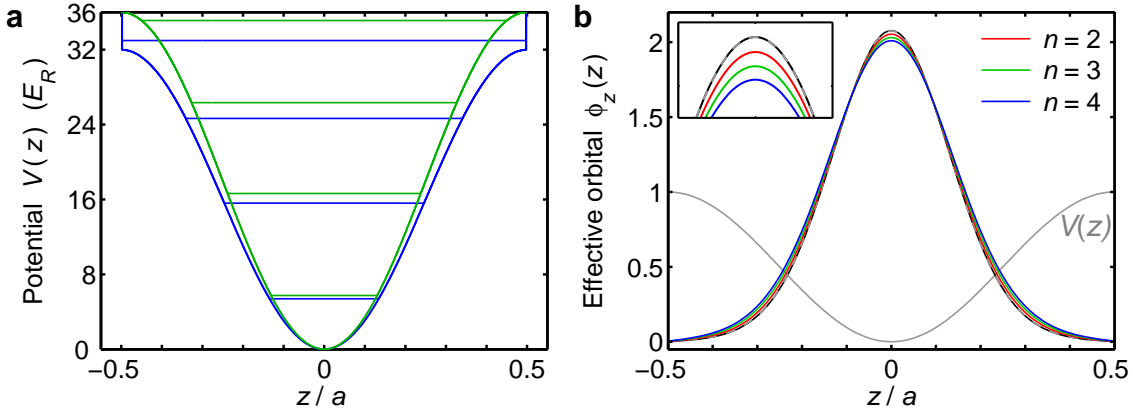
Fig. 7.4: (a) Single-site potential and single-particle energies for $V_0 = 32 E_R$ and $V_0 = 36 E_R$ with three and four bound states, respectively. (b) Effective one-dimensional orbitals for $n = 2$ to 4 ^{87}Rb atoms. The solid black and dashed gray line represent the single-particle single-site wave function $\varphi_0(\mathbf{r})$ and the Wannier function $w_0(\mathbf{r})$, respectively.

0.5% and 1% in comparison with a hard confinement. Furthermore, a weak confinement causes that the crossover from 3^3 to 4^3 orbitals occurs already at $V_0 \approx 31 E_R$.

The admixture of excited many-particle states $\psi_{\{j,k,l\}}$ with $\{j,k,l\} \neq \{1,1,1\}$ is shown in Fig. 7.5a in dependence on the lattice depth and the particle number. The fraction of the particles occupying excited states increases drastically with the atom number, i.e., about 1% for three particles and 5% for five particles. Note that the admixture of states increases also slightly with an increasing lattice depth. Since each of the many-particle states comprises of the occupation numbers of the three-dimensional orbitals, the results can be projected on the single-particle orbitals, which is plotted in Fig. 7.5b for $n = 2$ and $n = 5$ particles using a logarithmic scale. For convenience, the occupation of energetically degenerate orbitals $\psi_{\{j,k,l\}}$ belonging to a permutation of the indices $[jkl]$ are summed up. The occupations comprising only second and third band admixtures are colored in blue and green, respectively. Since the parity is conserved in scattering processes, only many-particle states with the parity of the ground state can contribute. This has also an impact on the projections on single-particle orbitals, where the occupation of the second band being energetically favorable compared to the third band is suppressed.

Another interesting question is how the on-site density changes due to the interaction. Let us focus directly on the change of the effective one-dimensional orbital wave function. Assuming that the three-dimensional wave function is a simple product of one-dimensional ones, which is not strictly the case, the effective orbital wave function can be defined by

$$\phi_z(z) = \sqrt{\frac{\rho(0,0,z)}{\rho^{2/3}(0,0,0)}}. \tag{7.18}$$

These effective orbitals are shown in Fig. 7.4b for $V_0 = 40 E_R$, where a broadening due to interaction for $n = 2$ to 4 particles is perceptible. For comparison, the single-site (solid black) and Wannier wave functions (dashed gray) are shown, which agree perfectly at this lattice depth. Using the effective orbitals in a single-band picture, the broadening changes the value of the on-
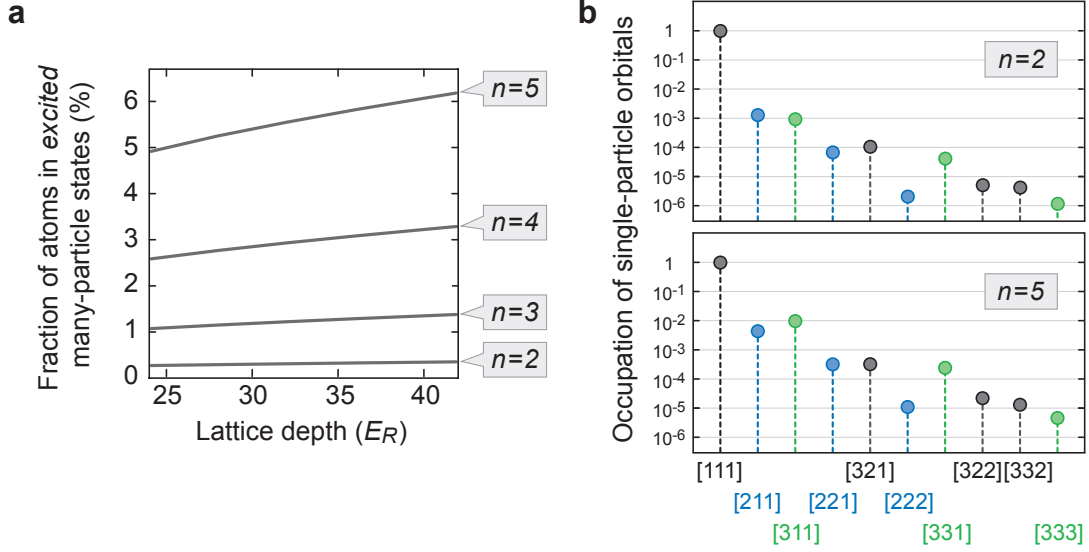
a

b

Fig. 7.5: (a) Fraction of atoms in excited many-particle states as a function of the lattice depth and the number of atoms n for $a_s = 102a_0$ and 4^3 single-particle orbitals. (b) The occupation of single-particle orbitals $\psi_{\{j,k,l\}}$, where all permutations $[jkl]$ are summed up, for $n = 2$ and $n = 5$ particles calculated for 3^3 orbitals, the lattice depth $V_0 = 40E_R$, and $a_s = 102a_0$.

site interaction noticeably. In comparison with the many-particle expectation value for U_{BH} in equation (7.13), this correction of the Hubbard interaction U is, however, considerably smaller. In addition to the broadening, the correlations between the particles play therefore the major role for the reduction of the on-site energy. Thus, we observe a true many-particle correlation effect that can not be captured in an effective mean-field or single-band description.

7.5   Multiorbital time evolution

In the time evolution (7.10), the Hubbard on-site energy can be replaced by the exact particle-number-dependent energy $E_n = E_{\mathrm{ED}}(n)$ for each state $|n\rangle$, namely

$$|\phi(t)\rangle = \sum_{n=0}^{\infty} c_n e^{-i\,E_n t/\hbar}\,|n\rangle. \tag{7.19}$$

Evaluating

$$\hat{b}\,|\phi(t)\rangle = \sum_{n=0}^{\infty} c_{n+1}\sqrt{n+1}\,e^{-i\,E_{n+1}t/\hbar}\,|n\rangle, \tag{7.20}$$

the matter wave field can be expressed as

$$\psi = \langle\phi(t)|\,\hat{b}\,|\phi(t)\rangle = \sum_{n=0}^{\infty} c_n^* c_{n+1}\sqrt{n+1}\,e^{-i(E_{n+1}-E_n)t/\hbar}. \tag{7.21}$$
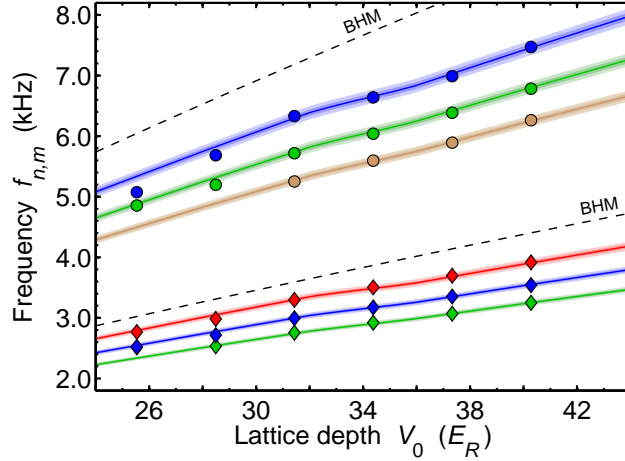
Fig. 7.6: The measured frequencies $f_{n,m}$ (symbols) and the exact calculation for $a_s = 102a_0$ are in excellent agreement. The plotted frequencies are $f_{2,0}$, $f_{3,1}$, $f_{4,2}$, $f_{1,0}$, $f_{2,1}$, and $f_{3,2}$ (from top to bottom). The darker and lighter shaded areas correspond to theoretical values for $(102 \pm 1)a_0$ and $(102 \pm 2)a_0$, respectively. The dashed black lines depict the frequencies predicted by the single-band Hubbard model. A detailed plot for the first-order resonances is show in Fig. 7.7.

The fringe visibility is to first order proportional to the square of the matter wave field

$$|\psi|^2 = \sum_{n,m=0}^{\infty} C_{n,m} \, e^{-i(E_{n+1} - E_n - E_{m+1} + E_m)t/\hbar}, \tag{7.22}$$

where the coefficients read

$$C_{n,m} = c_n^* c_{n+1} c_m c_{m+1}^* \sqrt{n+1} \sqrt{m+1}. \tag{7.23}$$

Further, assuming real coefficients we can write

$$|\psi|^2 = \sum_n C_{n,n} + \sum_{n>m} 2C_{n,m} \cos(\omega_{n,m} t) \tag{7.24}$$

with frequencies

$$\omega_{n,m} = (E_{n+1} - E_n - E_{m+1} + E_m)/\hbar. \tag{7.25}$$

Due to the particle number dependence of the interaction energy, several frequencies $\omega_{n,m}$ can be observed in the experiment [6]. By performing a discrete Fourier transformation of the measured fringe visibility, it is possible to determine the frequencies $\omega_{n,m}$. The finite time interval of the recorded data leads to a finite resolution in energy. Therefore, it is of fundamental necessity to observe the collapses and revivals for a long time, which has become possible with the experimental setup in Ref. [6]. As the mean filling per site $\bar{n}$ is typically small, the coefficients $C_{n,m}$ are negligible for large values of n and m. Therefore, only few frequencies are observable in the Fourier transformation of the visibility data (Fig. 7.2b), where contributions on the order of the on-site energy U are

$$\begin{aligned}
h \, f_{1,0} &= E_2, & C_{1,0} &= \sqrt{2} \, c_0 c_1^2 c_2, \\
h \, f_{2,1} &= E_3 - 2E_2, & C_{2,1} &= \sqrt{6} \, c_1 c_2^2 c_3, \\
h \, f_{3,2} &= E_4 - 2E_3 + E_2, & C_{3,2} &= \sqrt{12} \, c_2 c_3^2 c_4.
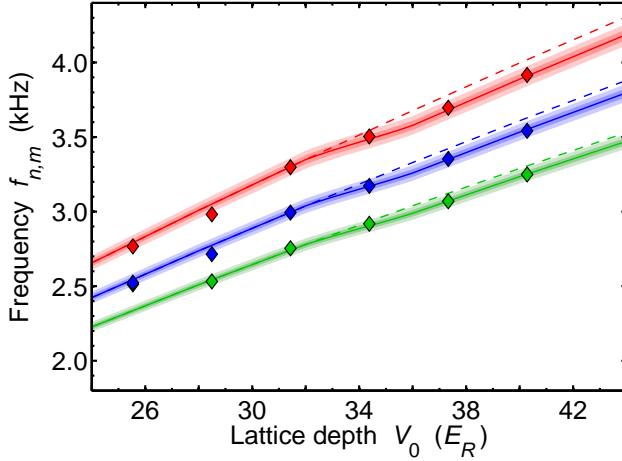\end{aligned} \tag{7.26}$$

Fig. 7.7: Experimental data and theoretical values for the frequencies $f_{1,0}$, $f_{2,1}$, and $f_{3,2}$. The shaded areas are obtained for $(102 \pm 1)a_0$ and $(102 \pm 2)a_0$. Assuming 3^3 orbitals irrespectively of the lattice depth lead to noticeably higher energies for $V_0 > 34E_R$ as depicted by the dashed lines.

Peaks on the order of twice the on-site energy U can be attributed to

$$
\begin{aligned}
h\,f_{2,0} &= E_3 - E_2, & C_{2,0} &= \sqrt{3}\,c_0 c_1 c_2 c_3, \\
h\,f_{3,1} &= E_4 - E_3 - E_2, & C_{3,1} &= \sqrt{8}\,c_1 c_2 c_3 c_4, \\
h\,f_{4,2} &= E_5 - E_4 - E_3 + E_2, & C_{4,2} &= \sqrt{15}\,c_2 c_3 c_4 c_5.
\end{aligned}
\tag{7.27}
$$

While the on-site interaction E_2 for two atoms can be measured directly, other observable frequencies depend on more than a single energy E_n.

The experimental and theoretical results are plotted in Fig. 7.6 for peaks on the order of U (diamonds) and $2U$ (circles). As mentioned, the signal of other contributions is weak due to the smallness of the respective coefficients $C_{n,m}$. It should be noted that there are no free parameters in this comparison, except for the s-wave scattering length a_s of ^{87}Rb atoms. Calculations in Refs. [106, 107] predict for a_s values ranging from $100a_0$ to $103a_0$ (see section 2.3.1). The best agreement of experiment and theory is obtained for a scattering length $102a_0$, which corresponds to the solid lines in Fig. 7.6. The darker and lighter shaded areas are boundaries for $a_s = 101a_0$-$103a_0$ and $a_s = 100a_0$-$104a_0$. The experimental error is mainly due to the calibration of the lattice depth, which is performed by measuring the transition of ^{40}K atoms between the first and the second band. Since the ^{40}K atoms are very weakly interacting, the transition is sharp and can be calculated using the single-particle band structure. However, the edge of the transition has a finite width, which causes an error of about 2% in the calibration. In addition, the lattice depth for ^{40}K atoms must be converted to ^{87}Rb atoms, where the conversion factor is 1.51 with an error of 1.5% [6]. For the measurement of the bosonic energies, the total uncertainty in the lattice depth V_0 is therefore 2.5% and is of a systematic nature, i.e., leading to a shift of all data points. This systematic error is much larger than the statistical error (see Fig. 7.8).

It is striking that the influence of the number of bound states is perceptible in the experimental data. In Fig. 7.7, where the first order peaks in U are shown, the theoretical values for 3^3 orbitals are indicated for $V_0 > 34E_R$ by dashed lines, which are noticeably higher than the experimental frequencies. This is an additional verification that only bound orbitals are occupied. Note that this feature is not influenced by the systematic error in the lattice calibration, which causes an uncertainty in the interaction strength.
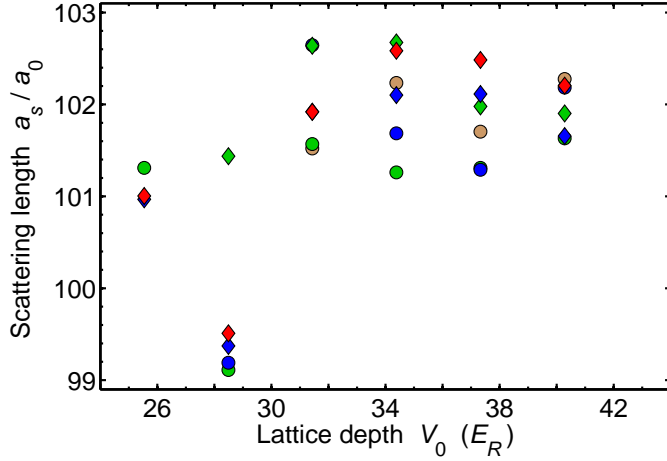
Fig. 7.8: Scattering length extracted from the experimental data applying the theoretical model. Two data points at $V_0 = 25.5E_R$ have large deviations and are not shown. See Fig. 7.6 for an explanation of the symbols.

Since the theoretical calculation is exact, this type of measurement determines directly the s-wave scattering length (2.34). We can see that the measured frequencies for $V_0 = 28.5E_R$ are, in general, slightly too low compared with the theory and in respect to the other data points, which might be caused by an inaccurate calibration of the lattice depth or the confinement. Furthermore, deviations are noticeable for $V_0 = 25.5E_R$, whereas results in deeper lattices are, in general, more accurate due to a smaller tunneling. Despite these small discrepancies, a compelling agreement between experiment and theory is apparent for the scattering length $a_s = 102a_0$. Applying the theoretical model, the s-wave scattering length can be extracted from the experimental results, which is depicted in Fig. 7.8. For the shown data, the scattering length can be estimated as $a_s = 101.5a_0 \pm 1.0a_0$ and without the experimental data at $V_0 = 28.5E_R$ one obtains $a_s = 101.9a_0 \pm 0.5a_0$. However, in addition to the statistical error also systematic uncertainties must be taken into account. The systematic error in the determination of the scattering length a_s caused by the lattice calibration is about 2.3% and dominates therefore the small statical error. Thus, improvements in the calibration procedure can would allow more accurate results for a_s.

The particle-number-dependent multiorbital energies give rive to a Hamiltonian with effective multi-body interactions. The on-site interaction can be expressed as the expansion

$$\hat{H}_{\text{int}} = \frac{U_2}{2}\hat{n}(\hat{n}-1) + \frac{U_3}{6}\hat{n}(\hat{n}-1)(\hat{n}-2) + \frac{U_4}{24}\hat{n}(\hat{n}-1)(\hat{n}-2)(\hat{n}-3) + \dots, \qquad (7.28)$$

where U_2, U_3, and U_4 correspond to an effective two-, three-, and four-body interaction, respectively. In the case where the n-body interaction energy U_n becomes very small for $n > 3$, U_2 and U_3 offer an approximate description for few particles per lattice site [199]. The effective Hamiltonian allows the mapping to systems with direct multi-body interactions, e.g., in the vicinity of Efimov resonances. The calculation and the experimental results are depicted in Fig. 7.9a. The multi-body energies U_n can be derived iteratively from the multiorbital energies E_n, i.e., $U_2 = E_2$, $U_3 = E_3 - 3U_2$, and $U_4 = E_4 - 6U_2 - 4U_3$. Since experimental and theoretical data match excellently, direct multi-body interactions in the experiment can be regarded as negligible. The resulting energies U_n decrease relatively fast with the particle number n, allowing an approximative effective single-band description for few particles on a lattice site by means of multi-body interactions.
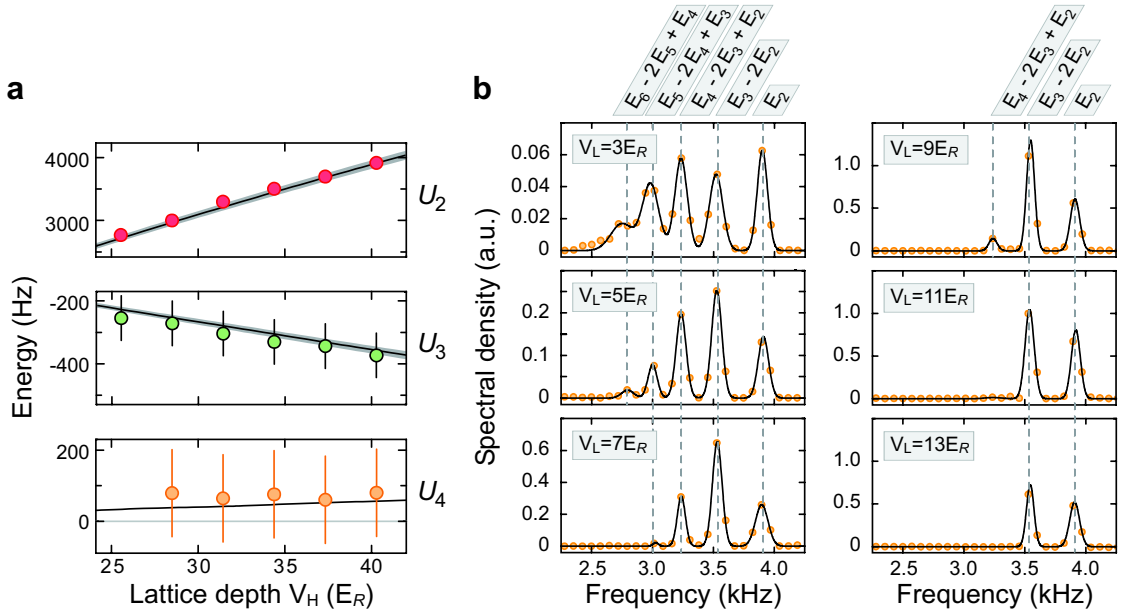
Fig. 7.9: (a) Effective multi-body interaction energies U_n. The experimental values (symbols) are in good agreement with the theoretical predictions (solid lines) for $a_s = (102 \pm 2)a_0$ and 4^3 orbitals. (b) The Fourier spectra for initial lattice depths $V_L = 3E_R$ to $13E_R$ reveal the change in the number statistics from a Poissonian to a strongly number-squeezed distribution indicating the transition from a superfluid to a Mott-insulator. The peak positions measured at a final lattice depth $V_H = 40E_R$ agree with the theoretical predictions (dashed vertical lines) for $a_s = 102a_0$. For shallow lattices, the interaction energy of up to six particles can be determined. The figure is taken from Ref. [6].

Moreover, the experiment allows to probe directly the number squeezing along the superfluid to Mott-insulator transition by varying the initial lattice depth as shown in Fig. 7.9b. In the superfluid phase, one expects a Poissonian distribution of the coefficients c_n, which becomes sub-Poissonian when the ratio of interaction to tunneling is increased. For shallow initial lattices ($V_L = 3E_R$ and $6E_R$) five distinct frequencies are resolved, which allows to measure the interaction energy of up to six particles. Close to the Mott insulator, the distribution c_n becomes strongly number-squeezed and only two frequencies remain, which is imprinted in the Fourier coefficients $C_{n,m}$ by the relations (7.26) and (7.27). In a perfect Mott-insulator phase, all except one coefficient c_n vanish as shown exemplarily in Fig. 7.1 causing a decreasing signal for an increasing lattice depth.

7.6 Conclusions

In general, the results demonstrate the high accuracy of both experimental data and theoretical predictions. Experimentally, a multi-frequency collapse and revival of the matter wave is observable, when ramping the three-dimensional lattice suddenly from shallow to deep, so that the particle number statistics of the superfluid phase is preserved at each lattice site. The phases

of the particle number states evolve in time according to their interaction energy, which can be extracted by Fourier transformation of the measured visibility as a function of time. The different contributing energies are a direct evidence for multiorbital physics, since the Hubbard model predicts only energies that are multiples of the single-band on-site interaction U. Performing an exact diagonalization of the many-particle system, the particle-number-dependent on-site interaction energies are computed including fully the quantum mechanical correlations. The calculation includes also changes of the potential and the kinetic energy that are usually neglected in the on-site interaction energy. It is shown that essentially only bound orbitals are occupied. Thus, a finite number of Fock states contribute to the correlated state for n particles and the diagonalization provides exact values. The observable frequencies computed from the exact particle-number-dependent interaction energies are in excellent agreement with the experimental data. Notably, a kink in the observed frequencies as a function of the final lattice depth is perceptible which can probably be attributed to a crossover from three to four bound orbitals per spatial dimension. In addition to the lattice depth, the computed frequencies depend exclusively on the s-wave scattering for ^{87}Rb atoms. A comparison of theory and experiment determines the s-wave scattering length to $a_s = 102a_0$ with a small statistical error, where the dominating systematic error is about $\pm 2a_0$. The multiorbital particle-number-dependent energies give rise to an effective Hamiltonian with multi-body interactions.

In conclusion, orbital changes in the particle-number-dependent on-site interaction are exactly calculated and are in compelling agreement with a recent high-precision collapse and revival measurement. This demonstrates that highly correlated states can be accurately accessed in ultracold atom experiments. Theoretically, an adequate description requires the exact multiorbital treatment of the interaction as presented in this thesis.

8

Outlook

For attractively interacting Bose-Fermi mixtures in optical lattices, the renormalization of the Bose-Hubbard Hamiltonian (chapter 5) leads to a large shift of the superfluid to Mott-insulator transition. The dependence on the interspecies scattering length predicted by this theory has been verified experimentally for ^{87}Rb - ^{40}K mixtures [3]. The self-trapping, which causes deepened effective potentials with increasing filling, suggests an increase of the bosonic filling per site. Although an indirect experimental evidence for this effect has been found [3], its direct confirmation is still missing. Due to a notable gain in energy, the self-trapping effect stabilizes boson-fermion compounds, which gives rise to physics resembling polaron phenomena in solids. In this field, many interesting questions addressing the fundamental behavior of composite particles are unanswered. In particular, the existence of composite particles in optical lattices is not experimentally confirmed. Theoretically, the dynamics of attractive boson-fermion mixtures could provide evidence of such particle compounds.

Experimentally, the multiorbital renormalization of the Bose-Hubbard parameters can be studied by measuring U and J directly. On the one hand, the collapse and revival experiment presented in chapter 7 is an excellent candidate to determine the on-site interaction energies precisely. In such an experiment both the boson-boson interaction and the boson-fermion interaction contribute to a complex evolution of the quantum phases. In addition, also atomic clock shifts [144] can be used to measure the modified on-site interactions. On the other hand, momentum-resolved Bragg spectroscopy (chapter 6) is an excellent tool to investigate the changes in the tunneling amplitude J due to self-trapping. In particular, it allows to probe directly the band structure of the effective bosonic and fermionic potentials, which would give detailed information on the mutual interaction.

For repulsive interspecies interaction, theoretical studies of the Bose-Fermi-Hubbard model [32–34] predict a competition between a phase separation of bosons and fermions and a supersolid phase, where both species are aligned in a checkerboard pattern. Both, the influence of the confinement and interaction induced changes are neglected so far in these studies but might be of crucial importance for the competition of phases. It has been shown that evidence of a supersolid phase might be found in the dynamic structure factor, which identifies Bragg spectroscopy as a possible experimental tool to detect this phase. The detection of separated fermionic and bosonic clouds could, in principle, also be achieved by in-situ absorption imaging.

Although the renormalization of the Hubbard model due to effective potentials is a very promising way to include orbital effects in the description of bosonic gases and Bose-Fermi mixtures, it

has also certain drawbacks, which are discussed in the following. The great advantage of using the renormalized theory is the reutilization of known results of the Hubbard model being widely used for solids and optical lattices. Furthermore, the Hubbard model depends effectively only on one parameter, namely the ratio U/J, and is therefore relatively easy to handle. However, the renormalization is only applicable when the lattice is locally commensurately filled, i.e., bosonic and fermionic filling factors are constant in larger regions of the lattice. As mentioned this property is not necessarily fulfilled, e.g., when bosonic and fermionic atoms start to separate to different sites of the lattice. Thus, the prediction of an anticorrelated phase is not in the scope of this effective bosonic theory. The use of static filling factors hinders the investigation of the dynamics, i.e., the hopping of particles, which modifies the effective parameters.

A theory which is accurate in all this points is the multiband Hubbard model, which is, however, quite complicated to handle. In recent works, this model has been restricted to only two bands in order to simplify the Hamiltonian [162, 164]. This restriction might, however, not describe the on-site effects accurately enough to allow quantitatively correct results. As a matter of fact, the on-site interaction in deeper lattices is very strong causing also higher bands to be noticeably occupied. A different approach might be promising, though. Assuming that the interaction on each site is strong, the correlated on-site physics must be described accurately. It has been shown that exact diagonalization is suited to compute the on-site wave functions, the on-site energies, and the tunneling from the effective potentials. The idea is to separate the on-site from the intersite physics, which is the basic concept of the Hubbard model and is justified, since on-site and intersite dynamics are subject to different time scales. While the on-site physics can be described by exact diagonalization, which provides precise results for the on-site interaction and the tunneling, the intersite physics gives rise to an effective Hamiltonian, which can be treated using various methods.

For simplicity, let us start the discussion of this point with a purely bosonic system. As pointed out in chapters 4 and 7, it is shown that the on-site energy can be computed as the eigenvalue E_n of the single-site problem. This leads to an effective multiband Bose-Hubbard Hamiltonian

$$\hat{H}_{\text{EBH}} = -\sum_{\langle i,j \rangle} \hat{J}_i(\hat{n}_i, \hat{n}_j)\, \hat{b}_i^\dagger \hat{b}_j + \sum_i \hat{E}(\hat{n}_i), \tag{8.1}$$

where also the particle-number-dependent changes in the hopping matrix element J are included. These corrections can be determined by computing the overlap of higher orbital states according to the definition of J in equation (2.59). In this definition the exact shape of the Wannier functions is assumed, while in this thesis often single-site functions have been used. The presented exact diagonalization technique could, however, easily be modified. An alternative approach is to determine the tunneling from the effective bosonic potential. While the particle-number-dependent on-site energy in bosonic systems is extensively discussed in this thesis, the strength of the effect on the tunneling J is a priori not clear. As discussed in chapter 7, the multiorbital on-site energies can also be modeled by effective multi-body interactions.

For mixtures of bosonic and fermionic atoms with attractive interspecies interaction, we know from discussing the effective potentials that the changes in J are large. In accordance to the effective Bose-Hubbard model above, we can define an effective Hamiltonian for boson-fermion

mixtures

$$\hat{H}_{\text{EBFH}} = -\sum_{\langle i,j \rangle} \hat{J}^{\text{B}}_{i,j}(\hat{n}_i, \hat{m}_i, \hat{n}_j, \hat{m}_j)\, \hat{b}_i^\dagger \hat{b}_j - \sum_{\langle i,j \rangle} \hat{J}^{\text{F}}_{i,j}(\hat{n}_i, \hat{n}_j)\, \hat{f}_i^\dagger \hat{f}_j + \sum_i \hat{E}(\hat{n}_i, \hat{m}_i), \qquad (8.2)$$

where $\hat{n}_i$ and $\hat{m}_i$ count the number of bosons and fermions at site i, respectively, and m_i is zero or one. For the operator $\hat{n}_i$, it can be reasonable to restrict the model to a maximum number of bosons per site. The operator $\hat{E}(\hat{n}_i, \hat{m}_i)$ assigns the total on-site energy including intra- and interspecies interaction obtained by exact diagonalization. In the Bose-Fermi-Hubbard model, it corresponds to $\hat{E}(\hat{n}_i, \hat{m}_i) = \frac{1}{2} U_{\text{B}} \hat{n}_i(\hat{n}_i - 1) + U_{\text{BF}} \hat{n}_i \hat{m}_i$, which is strongly modified by the mutual interaction and the self-trapping behavior as shown in this thesis. As a matter of fact, both bosonic and fermionic tunneling, $\hat{J}^{\text{B}}_{i,j}$ and $\hat{J}^{\text{F}}_{i,j}$, depend on the occupations at site i and j. We can assume that the intrasite dynamics is much faster than the tunneling, so that $\hat{J}^{\text{B}}_{i,j}$ and $\hat{J}^{\text{F}}_{i,j}$ can be calculated from the Wannier orbitals in the effective potentials experienced by bosons and fermions. Since the interaction induced changes on sites occupied by bosons and a fermion are much stronger than on purely bosonic sites, we can approximate $\hat{J}^{\text{B}}_{i,j}(\hat{n}_i, \hat{m}_i = 0, \hat{n}_j, \hat{m}_j = 0)$ as the unmodified Bose-Hubbard tunneling J. At the first glance, the presented model appears to be extremely complex, but the additional expenses for most numerical methods are small, once the effective parameters are calculated. As a trial, this extended Bose-Fermi-Hubbard model has been implemented by exact diagonalization. However, the limitation of the system size hinders an accurate description of the intersite physics, which meets the accuracy of the modeled on-site physics. In particular, quantum Monte Carlo methods are known to yield precise results in three-dimensional systems (see, e.g., Ref. [131]) and could easily incorporate the effective inclusion of multiorbital physics described above.

In general, the precise control of lattice depth and particle interaction permits an excellent comparison of theory and experiment. This allows a detailed study of interaction and correlation effects as well as the limitations of commonly used theoretical models such as the single-band Bose-Hubbard and the Bose-Fermi-Hubbard model. Doubtlessly, the interplay of theory and experiment in this field is very promising to study paradigms of solid-state physics and to address still outstanding questions.

9

Summary

Ultracold bosonic gases and mixtures of bosons and fermions in optical lattices have been studied using a multiorbital exact diagonalization technique. The great accuracy of this method allows a detailed understanding of interaction effects, which have recently become accessible in high-precision experiments [3, 6] with ultracold atoms in optical lattices. In Bose-Fermi mixtures the mutual interaction causes a self-trapping of the bosonic atoms, which leads to a shift of the critical potential depth separating the bosonic superfluid and the Mott-insulator phase in dependence on the bosonic filling and the interspecies scattering length. In bosonic lattice systems, multiorbital effects are revealed in collapse and revival experiments allowing for an accurate extraction of particle-number-dependent on-site interaction energies. Exact diagonalization permits further to explore the excitations in small strongly correlated systems. In particular, the intrinsic differences of commensurate and noncommensurate filling are directly imprinted on the excitation spectrum. Furthermore, a surprising agreement of mesoscopic and macroscopic systems has been found. Experimentally, momentum-resolved Bragg spectroscopy [5] is a promising method to probe excitations in optical lattices, which has been successfully demonstrated for weakly interacting superfluids. Computing the dynamical structure factor for strongly interacting systems using exact diagonalization reveals the typical fingerprint of the Mott-insulator phase in bosonic gases and possible phases in Bose-Fermi mixtures.

In more detail, the localization of ultracold bosonic atoms in finite lattices with commensurate filling resembles in many aspects the macroscopic quantum phase transition between a superfluid and a Mott insulator, including a striking similarity of the momentum distribution and the formation of an energy gap. It is shown that the local correlations are widely independent of the system size, indicating that the detailed simulation of small systems can offer important insight into the physics of large systems. For noncommensurate filling, the physical behavior changes fundamentally and a coexistence of localized and delocalized particles can be observed in deep lattices accounting for the equivalence of lattice sites. Because of a narrow lowest band, the ground state is extremely sensitive to lattice perturbations, which cause the localization of all particles in accordance with the Bose-glass phase. In finite systems with varying harmonic confinement, precursors of Mott-shell configurations are identified, where a vanishing gap in the energy spectrum defines a crossover between two configurations. Using a classical approach with vanishing tunneling, the basic features of the spectrum can be reproduced in deep lattices. Excellent agreement for the crossover points can be obtained, when including orbital changes in the on-site interaction energy. This demonstrates that particle-number-dependent on-site energies

are suitable to cover orbital effects in deep lattices. Furthermore, changes in the kinetic and the potential energy are nonnegligible as they lead to substantial modifications of the on-site energy. For deep lattices, the classical approach allows to obtain the site occupation numbers and the local excitation spectrum of macroscopic lattices for an arbitrary confining potential, where gapless excitations are present at the boundaries of the Mott shells. A perturbative treatment for finite tunneling connects these gapless excitations to strong particle fluctuations.

In Bose-Fermi mixtures with attractive interspecies interaction, orbital induced changes are of fundamental importance as they lead to a strong squeezing of the effective orbitals. The mutual interaction causes a substantial deformation of the effective potentials experienced by both bosons and fermions. Mediated by the strongly altered fermion orbital, the bosonic atoms show a self-trapping behavior, where the repulsive bosonic on-site interaction is overcompensated by the nonlinear dependence on the width of the fermion orbital. It manifests itself in a substantial deepening of the bosonic effective potential with increasing bosonic filling. It is shown that these interaction induced orbital changes can be incorporated in an effective Hubbard model for the bosonic particles. Using a self-consistent multiorbital diagonalization scheme, the renormalized Hubbard parameters, the on-site interaction U and the tunneling J, are calculated. A large shift of the critical potential depth separating superfluid and Mott-insulating phase is found being strongly dependent on the bosonic filling factor and the interspecies scattering length. Estimating these effects by a variational approach shows a qualitatively similar behavior but underestimates the interaction induced changes notably. This demonstrates, in general, the importance of including on-site correlations of particles in lattice models. The predicted shift is compatible with ^{87}Rb - ^{40}K experiments at a fixed interspecies scattering length [29, 30]. Recent experimental results [3] with a tunable scattering length show an excellent agreement with the interaction induced renormalization of the Bose-Hubbard model and support the self-trapping effect in attractively interacting Bose-Fermi mixtures. For repulsive interspecies scattering, the absence of a shift predicted by the same model indicates that bosons and fermions do not occupy the same lattice sites.

By applying momentum-resolved Bragg spectroscopy to superfluids in optical lattices, it has been shown in Ref. [5] that the band structure is notably modified by interaction effects. For the experimental parameters, the Bogoliubov theory of weakly interacting gases is applicable and offers a good description of the probed excitations. Furthermore, Bragg spectroscopy is a feasible tool to explore correlations in strongly interacting systems. These correlations are imprinted on the dynamic structure factor, which is calculated for one-dimensional bosonic systems and Bose-Fermi mixtures. By varying smoothly the ratio of interaction to tunneling, characteristic excitation modes of the Mott insulator have been identified. Moreover, the bosonic response in possible phases for Bose-Fermi mixtures with repulsive interspecies scattering, such as an anticorrelated phase at half filling, has been addressed. In particular, the observed features in the dynamic structure factor for an anticorrelated filling can be distinguished from a phase separation scenario of bosons and fermions.

The breakdown of the single-band Hubbard picture in bosonic gases manifests itself in the time evolution of coherent states in deep optical lattices. In the experimental realization [6] a multi-frequency evolution is observable, which is revealed by a complex pattern of collapses and revivals

of the matter wave field. Each single-site particle-number state evolves in accordance to its exact interaction energy, showing a direct evidence for multiorbital physics in optical lattices. Performing exact diagonalization, the particle-number-dependent on-site energies are calculated including the full quantum mechanical correlations and the corrections from kinetic and potential energy. Caused by the anticonfinement in the experiment, it can be assumed that only bound orbitals are occupied allowing for a highly accurate comparison of theory and experiment. The computed frequencies are in excellent agreement with the experimental results for various lattice depths. The comparison allows to estimate the s-wave scattering length to roughly $102a_0$, where uncertainties are dominated by the lattice calibration. The multiorbital interaction energies give rise to an effective Hamiltonian with multi-body interactions. In general, the results demonstrate the important role of multiorbital physics in optical lattices and its experimental accessibility.

Summary

Appendix

A.1 Two-particle matrix elements

In this section the matrix elements

$$I = \frac{g}{2}\langle N_{\mathrm{B}}| \sum_{i,j,k,l} \chi_{ijkl}\hat{b}_i^\dagger \hat{b}_j^\dagger \hat{b}_k \hat{b}_l |N_{\mathrm{B}}'\rangle, \tag{A.1}$$

are evaluated for the calculation of the boson-boson interaction (see also Refs. [81, 108, 109]). For simplicity, $|N\rangle$ is used in the following as an abbreviation for $|N_{\mathrm{B}}\rangle$. Assuming real wave functions χ_i, the interaction integral.

$$\chi_{ijkl} = \int d^3r \; \chi_i(\mathbf{r})\chi_j(\mathbf{r})\chi_k(\mathbf{r})\chi_l(\mathbf{r}). \tag{A.2}$$

is symmetric in i, j, k, and l.

For the first case given in equation (2.74), i.e., $|N'\rangle = |N\rangle$, the interaction matrix element becomes

$$\begin{aligned}
I_1 &= \frac{g}{2}\langle N| \sum_i \chi_{iiii}\hat{b}_i^\dagger \hat{b}_i^\dagger \hat{b}_i \hat{b}_i + \sum_{i\neq j} \chi_{ijij}\hat{b}_i^\dagger \hat{b}_j^\dagger \hat{b}_i \hat{b}_j + \sum_{i\neq j} \chi_{ijji}\hat{b}_i^\dagger \hat{b}_j^\dagger \hat{b}_j \hat{b}_i \, |N\rangle \\
&= \frac{g}{2}\Big(\sum_i \chi_{iiii}n_i(n_i-1) + 2\sum_{i\neq j} \chi_{ijij}n_i n_j \Big) \\
&= \frac{g}{2}\Big(\sum_i \chi_{iiii}n_i(n_i-1) + 4\sum_{i<j} \chi_{ijij}n_i n_j \Big)
\end{aligned} \tag{A.3}$$

For the second case that $|N'\rangle = |..., n_i-2, ..., n_k+2, ...\rangle$ one gets

$$\begin{aligned}
I_2 &= \frac{g}{2}\langle N| \chi_{iikk}\hat{b}_i^\dagger \hat{b}_i^\dagger \hat{b}_k \hat{b}_k \, |..., n_i-2, ..., n_k+2, ...\rangle \\
&= \frac{g}{2}\chi_{iikk}\sqrt{n_i(n_i-1)(n_k+1)(n_k+2)}
\end{aligned} \tag{A.4}$$

The other classes of interaction matrix elements can be calculated analogously. For $|N'\rangle = |..., n_j-1, ..., n_k+1, ...\rangle$ follows

$$\begin{aligned}
I_3 =&\frac{g}{2}\Big(2\chi_{jjjk}(n_j-1)\sqrt{n_j(n_k+1)} + 2\chi_{kjkk}n_k\sqrt{(n_k+1)n_j} \\
&+ 4\sum_{i(\neq j,\neq k)} \chi_{ijik}n_i\sqrt{n_j(n_k+1)} \Big),
\end{aligned} \tag{A.5}$$

for $|N'\rangle = |..., n_i-1, ..., n_j-1, ..., n_k+2, ...\rangle$

$$I_4 = \frac{g}{2}\,2\chi_{ijkk}\sqrt{n_i n_j(n_k+1)(n_k+2)}, \tag{A.6}$$

for $|N'\rangle = |..., n_i - 2, ..., n_k + 1, ..., n_l + 1, ...\rangle$

$$I_5 = \frac{g}{2} 2\chi_{iikl}\sqrt{n_i(n_i - 1)(n_k + 1)(n_l + 1)},$$

(A.7)

and finally for $|N'\rangle = |..., n_i - 1, ..., n_j - 1, ..., n_k + 1, ..., n_l + 1, ...\rangle$

$$I_6 = \frac{g}{2} 4\chi_{ijkl}\sqrt{n_i n_j(n_k + 1)(n_l + 1)}.$$

(A.8)

A.2 Pair correlation function

In the following, the matrix elements of the pair correlation function are calculated. The pair correlation reflects the conditional density of $N - 1$ particles assuming that one particle is located at $\mathbf{r}'$ and is given by

$$
\begin{aligned}
\hat{g}_2(\mathbf{r}, \mathbf{r}') &= \int d^3x \, d^3x' \, \psi^\dagger(\mathbf{x})\psi^\dagger(\mathbf{x}')\delta(\mathbf{r} - \mathbf{x})\delta(\mathbf{r}' - \mathbf{x}')\psi(\mathbf{x}')\psi(\mathbf{x}) \\
&= \psi^\dagger(\mathbf{r})\psi^\dagger(\mathbf{r}')\psi(\mathbf{r}')\psi(\mathbf{r}) \\
&= \chi_i^*(\mathbf{r})\chi_j^*(\mathbf{r}')\chi_k(\mathbf{r})\chi_l(\mathbf{r}')b_i^\dagger b_j^\dagger b_l b_k.
\end{aligned}
$$

(A.9)

This correspond to density-density correlation (2.100) omitting the self-correlation $\delta(\mathbf{r} - \mathbf{r}')\hat{\rho}(\mathbf{r})$. To calculate the matritx elements, we define for real wave functions

$$f_{ijkl}(\mathbf{r}, \mathbf{r}') = \chi_i(\mathbf{r})\chi_j(\mathbf{r}')\chi_k(\mathbf{r})\chi_l(\mathbf{r}'),$$

(A.10)

where only the indices $\{i, k\}$ and $\{j, l\}$ commute. With this restriction, the calculation of matrix elements $g_2(\mathbf{r}, \mathbf{r}') = \langle N|\hat{g}_2(\mathbf{r}, \mathbf{r}')|N'\rangle$ is completely analogous to the derivation of the Hamiltonian matrix elements in the last section [81]. For the case that $|N'\rangle = |N\rangle$, it follows

$$g_2(\mathbf{r}, \mathbf{r}') = \sum_i f_{iiii} n_i(n_i - 1) + \sum_{i \neq j}(f_{ijij} + f_{ijji})n_{i\alpha}n_{j\beta},$$

(A.11)

for $|N'\rangle = |..., n_i - 2, ..., n_k + 2, ...\rangle$

$$g_2(\mathbf{r}, \mathbf{r}') = f_{iikk}\sqrt{n_i(n_i - 1)(n_k + 1)(n_k + 2)},$$

(A.12)

for $|N'\rangle = |..., n_j - 1, ..., n_k + 1, ...\rangle$

$$
\begin{aligned}
g_2(\mathbf{r}, \mathbf{r}') =&(f_{jjjk} + f_{jjkj})(n_j - 1)\sqrt{n_j(n_k + 1)} + (f_{kjkk} + f_{jkkk})n_k\sqrt{(n_k + 1)n_j} \\
&+ \sum_{i(\neq j, \neq k)}(f_{ijik} + f_{ijki} + f_{jiik} + f_{jiki})n_i\sqrt{n_j(n_k + 1)},
\end{aligned}
$$

(A.13)

for $|N'\rangle = |..., n_i - 1, ..., n_j - 1, ..., n_k + 2, ...\rangle$

$$g_2(\mathbf{r}, \mathbf{r}') = (f_{ijkk} + f_{jikk})\sqrt{n_i n_j(n_k + 1)(n_k + 2)},$$

(A.14)

for $|N'\rangle = |..., n_i - 2, ..., n_k + 1, ..., n_l + 1, ...\rangle$

$$g_2(\mathbf{r}, \mathbf{r}') = (f_{iikl} + f_{iilk})\sqrt{n_i(n_i - 1)(n_k + 1)(n_l + 1)},$$

(A.15)

and finally for $|N'\rangle = |..., n_i - 1, ..., n_j - 1, ..., n_k + 1, ..., n_l + 1, ...\rangle$

$$g_2(\mathbf{r}, \mathbf{r}') = (f_{ijkl} + f_{ijlk} + f_{jikl} + f_{jilk})\sqrt{n_i n_j(n_k + 1)(n_l + 1)}.$$

(A.16)

A.3   Bogoliubov-de Gennes equations

The starting point for the numerical solution of the Bogoliubov-de Gennes equations is the decoupled equation (6.11)

$$\left(-\frac{\hbar^2}{2m}\frac{\partial^2}{\partial z^2} + V(z) - \mu + 3M\right)\left(-\frac{\hbar^2}{2m}\frac{\partial^2}{\partial z^2} + V(z) - \mu + M\right)\psi_q = (\hbar\,\omega_q)^2\,\psi_q \quad \text{(A.17)}$$

with $M(z) = gN|\Psi_{\text{GPE}}(z)|^2$. Due to Bloch's theorem, ψ_q can be expressed as a product of a lattice periodic function $\varphi(z)$ and a plane wave factor e^{-iqzG}, where G is the reciprocal lattice vector $G = 2\pi/a$ and a is the lattice spacing. For each quasimomentum qG in the first Brillouin zone $(-1/2 < q < 1/2)$ a discrete set of eigenfunctions is found. To obtain an algebraic equation, the periodic functions $\varphi(z)$, $V(z)$ and $M(z)$ are expanded in Fourier series

$$\psi_q(z) = \sum_k c_k e^{i(k-q)zG}, \quad \text{(A.18)}$$

$$V(z) = \sum_n \nu_n e^{inzG}, \quad \text{(A.19)}$$

$$M(z) = \sum_\xi \phi_\xi e^{i\xi zG}, \quad \text{(A.20)}$$

where ν_n and ϕ_ξ have the dimension of an energy and are given in units of the recoil energy E_R. The spatial derivative leads to a term $A = \hbar G^2/2M = 4E_R$, which is used in the following. Expanding the parentheses in equation (A.17) and inserting the Fourier series (A.18)-(A.20) lead to the following terms appearing on the left hand side of equation (A.17)

$$\left(\frac{\hbar^2}{2m}\right)^2\frac{\partial^4}{\partial z^4}\psi_q = A^2\sum_k c_k(k-q)^4 e^{i(k-q)zG}, \quad \text{(A.21)}$$

$$-\frac{\hbar^2}{2m}\frac{\partial^2}{\partial z^2}V\psi_q = A\sum_{k,n}c_k\nu_n(k+n-q)^2 e^{i(k+n-q)zG}, \quad \text{(A.22)}$$

$$2\frac{\hbar^2}{2m}\frac{\partial^2}{\partial z^2}\mu\psi_q = -2A\mu\sum_k c_k(k-q)^2 e^{i(k-q)zG}, \quad \text{(A.23)}$$

$$-\frac{\hbar^2}{2m}\frac{\partial^2}{\partial z^2}M\psi_q = A\sum_{k,\xi}c_k\phi_\xi(k+\xi-\mu)e^{i(k+\xi-q)zG}, \quad \text{(A.24)}$$

$$-V\frac{\hbar^2}{2m}\frac{\partial^2}{\partial z^2}\psi_q = A\sum_{k,n}c_k\nu_n(k-q)^2 e^{i(k+n-q)zG}, \quad \text{(A.25)}$$

$$V^2\psi_q = \sum_{k,n,n'}c_k\nu_n\nu_{n'}e^{i(k+n+n'-q)zG}, \quad \text{(A.26)}$$

$$-2V\mu\psi_q = -2\mu\sum_{k,n}c_k\nu_n e^{i(k+n-q)zG}, \quad \text{(A.27)}$$

$$4VM\psi_q = 4 \sum_{k,n,\xi} c_k \nu_n \phi_\xi e^{i(k+n+\xi-q)zG}, \tag{A.28}$$

$$\mu^2 \psi_q = \mu^2 \sum_k c_k e^{i(k-q)zG}, \tag{A.29}$$

$$-4\mu M\psi_q = -4\mu \sum_{k,\xi} c_k \phi_\xi e^{i(k+\xi-q)zG}, \tag{A.30}$$

$$-3M\frac{\hbar^2}{2m}\frac{\partial^2}{\partial z^2}\psi_q = 3A \sum_{k,\xi} c_k \phi_\xi (k-q)^2 e^{i(k+\xi-q)zG}, \tag{A.31}$$

$$3M^2\psi_q = 3 \sum_{k,\xi,\xi'} c_k \phi_\xi \phi_{\xi'} e^{i(k+\xi+\xi'-q)zG}. \tag{A.32}$$

The right hand side of equation (A.17) gives

$$(\hbar\omega_q)^2 \psi_q = (\hbar\omega_q)^2 \sum_k c_k e^{i(k-q)zG}. \tag{A.33}$$

Comparison of coefficients with respect to $e^{i(\beta-q)zG}$ leads to an algebraic equation

$$
\begin{aligned}
[A(\beta-q)^2 - \mu]^2 c_\beta + \sum_i \big[A(\beta-q)^2(\nu_i + \phi_i) \\
+A(\beta-i-q)^2(\nu_i + 3\phi_i) - 2\mu(\nu_i + 2\phi_i) \big] c_{\beta-i} \\
+ \sum_{i,j} \big[\nu_i\nu_j + 4\nu_i\phi_j + 3\phi_i\phi_j \big] c_{\beta-i-j} = (\hbar\omega_q)^2 c_\beta
\end{aligned}
\tag{A.34}
$$

for the coefficients c_β, which can be solved by diagonalization of the respective matrix equation.

Acknowledgments

Many people have contributed to the success of this thesis. I would like to thank everyone involved for support, motivation, and discussions during the last three years. In particular, I would like to express my sincere gratitude to the following people.

First of all, I would like to thank my supervisor Daniela Pfannkuche for the possibility to make my PhD in her group, for all her support, and the numerous discussions. Especially, she made a great effort in correcting my thesis and the publications.

Furthermore, I thank Klaus Sengstock and Kai Bongs for the collaboration with the Institute of Laser-Physics in Hamburg, many discussions, and important ideas. They have contributed to a large extend to my fascination for ultracold atoms.

This work was done in close collaboration with experimentalists. I would like to thank Philipp Ernst and Sören Götze for fascinating insights in the Rb-K experiment in Hamburg and for the very interesting collaboration during the Bragg measurements.

Furthermore, I would like to thank Thorsten Best, Sebastian Will, and Immanuel Bloch from the University of Mainz/Munich for an extremely fruitful collaboration. Without the comparisons with the experiments, I would be still in doubt about a great many things. I acknowledge many interesting (and long) discussions with Thorsten and Sebastian about theoretical and experimental results, their deviations, and how to match both in the end. It has been a great motivation for me!

All people in my group at the I. Institute for Theoretical Physics I thank for the nice time and the great atmosphere, especially, Daniel Becker, Stellan Bohlens, Philipp Knake, Benjamin Krüger, and Peter Moraczewski. Frank Deuretzbacher I would also like to thank for lots of discussions and for setting up the diagonalization technique for bosonic atoms.

For the evaluation of my dissertation, a nice stay in Lund, and the invitation to the symposium at Örenäs castle, many thanks go to Stephanie Reimann.

For numerous corrections of my thesis, I thank Frank Deuretzbacher, Philipp Ernst, Sebastian Will, and my wife Sarah.

Last but not least, I thank my family and friends for supporting me in everything I do.

Finally, I thank Sarah for her everlasting support, motivation, love, and uncountable other things – or simply for spending her life with me!

Acknowledgments

Bibliography

[1] D.-S. Lühmann, K. Bongs, K. Sengstock, and D. Pfannkuche, *Localization and delocalization of ultracold bosonic atoms in finite optical lattices*, Phy. Rev. A **77**, 023620 (2008).

[2] D.-S. Lühmann, K. Bongs, K. Sengstock, and D. Pfannkuche, *Self-Trapping of Bosons and Fermions in Optical Lattices*, Phys. Rev. Lett. **101**, 050402 (2008).

[3] T. Best, S. Will, U. Schneider, L. Hackermüller, D. van Oosten, I. Bloch, and D.-S. Lühmann, *Role of Interactions in ^{87}Rb-^{40}K Bose-Fermi Mixtures in a 3D Optical Lattice*, Phys. Rev. Lett. **102**, 030408 (2009).

[4] D.-S. Lühmann, K. Bongs, and D. Pfannkuche, *Excitation spectrum of Mott shells in optical lattices*, J. Phys. B: At. Mol. Opt. Phys. **42**, 145305 (2009).

[5] P. T. Ernst, S. Götze, J. S. Krauser, K. Pyka, D.-S. Lühmann, D. Pfannkuche, and K. Sengstock, *Probing superfluids in optical lattices by momentum-resolved Bragg spectroscopy*, Nature Phys. **6**, 56 (2010).

[6] S. Will, T. Best, U. Schneider, L. Hackermüller, D.-S. Lühmann, and I. Bloch, *Time-resolved observation of coherent multi-body interactions in quantum phase revivals*, Nature **465**, 197 (2010).

[7] A. Einstein, *Quantentheorie des einatomigen idealen Gases*, Sitzungsber. preuss. Akad. Wiss., phys.-math. Kl. p. 261 (1924).

[8] A. Einstein, *Quantentheorie des einatomigen idealen Gases, 2. Abhandlung*, Sitzungsber. preuss. Akad. Wiss., phys.-math. Kl. p. 3 (1925).

[9] M. H. Anderson, J. R. Ensher, M. R. Matthews, C. E. Wieman, and E. A. Cornell, *Observation of Bose-Einstein Condensation in a Dilute Atomic Vapor*, Science **269**, 198 (1995).

[10] C. C. Bradley, C. A. Sackett, J. J. Tollett, and R. G. Hulet, *Evidence of Bose-Einstein Condensation in an Atomic Gas with Attractive Interactions*, Phys. Rev. Lett. **75**, 1687 (1995).

[11] K. B. Davis, M.-O. Mewes, M. R. Andrews, N. J. van Druten, D. S. Durfee, D. M. Kurn, and W. Ketterle, *Bose-Einstein Condensation in a Gas of Sodium Atoms*, Phys. Rev. Lett. **75**, 3969 (1995).

[12] M. R. Andrews, C. G. Townsend, H.-J. Miesner, D. S. Durfee, D. M. Kurn, and W. Ketterle, *Observation of Interference Between Two Bose Condensates*, Science **275**, 637 (1997).

[13] K. W. Madison, F. Chevy, W. Wohlleben, and J. Dalibard, *Vortex Formation in a Stirred Bose-Einstein Condensate*, Phys. Rev. Lett. **84**, 806 (2000).

[14] M. R. Matthews, B. P. Anderson, P. C. Haljan, D. S. Hall, C. E. Wieman, and E. A. Cornell, *Vortices in a Bose-Einstein Condensate*, Phys. Rev. Lett. **83**, 2498 (1999).

[15] J. R. Abo-Shaeer, C. Raman, J. M. Vogels, and W. Ketterle, *Observation of Vortex Lattices in Bose-Einstein Condensates*, Science **292**, 476 (2001).

[16] I. Bloch, T. W. Hänsch, and T. Esslinger, *Measurement of the spatial coherence of a trapped Bose gas at the phase*, Nature **403**, 166 (2000).

[17] E. P. Gross, *Structure of a quantized vortex in boson systems*, Nuovo Cimento, Suppl. **20**, 454 (1961).

[18] L. P. Pitaevskii, *Vortex lines in an imperfect Bose gas*, Sov. Phys. JETP **13**, 451 (1961).

[19] M. Greiner, O. Mandel, T. Esslinger, T. W. Hänsch, and I. Bloch, *Quantum phase transition from a superfluid to a Mott insulator in a gas of ultracold atoms*, Nature **415**, 39 (2002).

[20] M. P. A. Fisher, P. B. Weichman, G. Grinstein, and D. S. Fisher, *Boson localization and the superfluid-insulator transition*, Phys. Rev. B **40**, 546 (1989).

[21] D. Jaksch, C. Bruder, J. I. Cirac, C. W. Gardiner, and P. Zoller, *Cold Bosonic Atoms in Optical Lattices*, Phys. Rev. Lett. **81**, 3108 (1998).

[22] P. Courteille, R. S. Freeland, D. J. Heinzen, F. A. van Abeelen, and B. J. Verhaar, *Observation of a Feshbach Resonance in Cold Atom Scattering*, Phys. Rev. Lett. **81**, 69 (1998).

[23] S. Inouye, M. R. Andrews, J. Stenger, H.-J. Miesner, D. M. Stamper-Kurn, and W. Ketterle, *Observation of Feshbach resonances in a Bose-Einstein condensate*, Nature **392**, 151 (1998).

[24] B. DeMarco and D. S. Jin, *Onset of Fermi Degeneracy in a Trapped Atomic Gas*, Science **285**, 1703 (1999).

[25] D. M. Stamper-Kurn, M. R. Andrews, A. P. Chikkatur, S. Inouye, H.-J. Miesner, J. Stenger, and W. Ketterle, *Optical Confinement of a Bose-Einstein Condensate*, Phys. Rev. Lett. **80**, 2027 (1998).

[26] J. Stenger, S. Inouye, D. M. Stamper-Kurn, H.-J. Miesner, A. P. Chikkatur, and W. Ketterle, *Spin domains in ground-state Bose-Einstein condensates*, Nature **396**, 345 (1998).

[27] A. G. Truscott, K. E. Strecker, W. I. McAlexander, G. B. Partridge, and R. G. Hulet, *Observation of Fermi Pressure in a Gas of Trapped Atoms*, Science **291**, 2570 (2001).

[28] F. Schreck, L. Khaykovich, K. L. Corwin, G. Ferrari, T. Bourdel, J. Cubizolles, and C. Salomon, *Quasipure Bose-Einstein Condensate Immersed in a Fermi Sea*, Phys. Rev. Lett. **87**, 080403 (2001).

[29] K. Günter, T. Stöferle, H. Moritz, M. Köhl, and T. Esslinger, *Bose-Fermi Mixtures in a Three-Dimensional Optical Lattice*, Phys. Rev. Lett. **96**, 180402 (2006).

[30] S. Ospelkaus, C. Ospelkaus, O. Wille, M. Succo, P. Ernst, K. Sengstock, and K. Bongs, *Localization of Bosonic Atoms by Fermionic Impurities in a Three-Dimensional Optical Lattice*, Phys. Rev. Lett. **96**, 180403 (2006).

[31] A. Albus, F. Illuminati, and J. Eisert, *Mixtures of bosonic and fermionic atoms in optical lattices*, Phys. Rev. A **68**, 023606 (2003).

[32] H. P. Büchler and G. Blatter, *Supersolid versus Phase Separation in Atomic Bose-Fermi Mixtures*, Phys. Rev. Lett. **91**, 130404 (2003).

[33] R. Roth and K. Burnett, *Quantum phases of atomic boson-fermion mixtures in optical lattices*, Phys. Rev. A **69**, 021601(R) (2004).

[34] I. Titvinidze, M. Snoek, and W. Hofstetter, *Supersolid Bose-Fermi Mixtures in Optical Lattices*, Phys. Rev. Lett. **100**, 100401 (2008).

[35] L. Mathey, D.-W. Wang, W. Hofstetter, M. D. Lukin, and E. Demler, *Luttinger Liquid of Polarons in One-Dimensional Boson-Fermion Mixtures*, Phys. Rev. Lett. **93**, 120404 (2004).

[36] M. Lewenstein, L. Santos, M. A. Baranov, and H. Fehrmann, *Atomic Bose-Fermi Mixtures in an Optical Lattice*, Phys. Rev. Lett. **92**, 050401 (2004).

[37] X. Barillier-Pertuisel, S. Pittel, L. Pollet, and P. Schuck, *Boson-fermion pairing in Bose-Fermi mixtures on one-dimensional optical lattices*, Phys. Rev. A **77**, 012115 (2008).

[38] G. K. Brennen, C. M. Caves, P. S. Jessen, and I. H. Deutsch, *Quantum Logic Gates in Optical Lattices*, Phys. Rev. Lett. **82**, 1060 (1999).

[39] D. Jaksch, H.-J. Briegel, J. I. Cirac, C. W. Gardiner, and P. Zoller, *Entanglement of Atoms via Cold Controlled Collisions*, Phys. Rev. Lett. **82**, 1975 (1999).

[40] D. Schrader, I. Dotsenko, M. Khudaverdyan, Y. Miroshnychenko, A. Rauschenbeutel, and D. Meschede, *Neutral Atom Quantum Register*, Phys. Rev. Lett. **93**, 150501 (2004).

[41] J. Sebby-Strabley, M. Anderlini, P. S. Jessen, and J. V. Porto, *Lattice of double wells for manipulating pairs of cold atoms*, Phys. Rev. A **73**, 033605 (2006).

[42] P. Cheinet, S. Trotzky, M. Feld, U. Schnorrberger, M. Moreno-Cardoner, S. Folling, and I. Bloch, *Counting Atoms Using Interaction Blockade in an Optical Superlattice*, Phys. Rev. Lett. **101**, 090404 (2008).

[43] Y. Miroshnychenko, W. Alt, I. Dotsenko, L. Förster, M. Khudaverdyan, D. Meschede, D. Schrader, and A. Rauschenbeutel, *Quantum engineering: An atom-sorting machine*, Nature **442**, 151 (2006).

[44] Y. Miroshnychenko, W. Alt, I. Dotsenko, L. Förster, M. Khudaverdyan, A. Rauschenbeutel, and D. Meschede, *Precision preparation of strings of trapped neutral atoms*, New J. Phys. **8**, 191 (2006).

[45] X. Du, S. Wan, E. Yesilada, C. Ryu, D. J. Heinzen, Z. X. Liang, and B. Wu, *Bragg spectroscopy of a superfluid Bose-Hubbard gas*, arXiv:0704.2623 (2007).

[46] D. Clément, N. Fabbri, L. Fallani, C. Fort, and M. Inguscio, *Exploring Correlated 1D Bose Gases from the Superfluid to the Mott-Insulator State by Inelastic Light Scattering*, Phys. Rev. Lett. **102**, 155301 (2009).

[47] N. Fabbri, D. Clément, L. Fallani, C. Fort, M. Modugno, K. M. R. van der Stam, and M. Inguscio, *Excitations of Bose-Einstein condensates in a one-dimensional periodic potential*, Phys. Rev. A **79**, 043623 (2009).

[48] L. P. Pitaevskii and S. Stringari, *Bose-Einstein condensation* (Oxford University Press, 2003), ISBN 0198507194.

[49] D. van Oosten, P. van der Straten, and H. T. C. Stoof, *Quantum phases in an optical lattice*, Phys. Rev. A **63**, 053601 (2001).

[50] K. Berg-Sørensen and K. Mølmer, *Bose-Einstein condensates in spatially periodic potentials*, Phys. Rev. A **58**, 1480 (1998).

[51] M. L. Chiofalo, M. Polini, and M. P. Tosi, *Collective excitations of a periodic Bose condensate in the Wannier representation*, Eur. Phys. J. D **11**, 371 (2000).

[52] C. Menotti, M. Krämer, L. Pitaevskii, and S. Stringari, *Dynamic structure factor of a Bose-Einstein condensate in a one-dimensional optical lattice*, Phys. Rev. A **67**, 053609 (2003).

[53] M. Modugno, C. Tozzo, and F. Dalfovo, *Role of transverse excitations in the instability of Bose-Einstein condensates moving in optical lattices*, Phys. Rev. A **70**, 043625 (2004).

[54] J. Javanainen, *Phonon approach to an array of traps containing Bose-Einstein condensates*, Phys. Rev. A **60**, 4902 (1999).

[55] K. Burnett, M. Edwards, C. W. Clark, and M. Shotter, *The Bogoliubov approach to number squeezing of atoms in an optical lattice*, J. Phys. B: At. Mol. Opt. Phys. **35**, 1671 (2002).

[56] R. Roth and K. Burnett, *Dynamic structure factor of ultracold Bose and Fermi gases in optical lattices*, J. Phys. B: At. Mol. Opt. Phys. **37**, 3893 (2004).

[57] E. M. Wright, T. Wong, M. J. Collett, S. M. Tan, and D. F. Walls, *Collapses and revivals in the interference between two Bose-Einstein condensates formed in small atomic samples*, Phys. Rev. A **56**, 591 (1997).

[58] A. Imamoḡlu, M. Lewenstein, and L. You, *Inhibition of Coherence in Trapped Bose-Einstein Condensates*, Phys. Rev. Lett. **78**, 2511 (1997).

[59] Y. Castin and J. Dalibard, *Relative phase of two Bose-Einstein condensates*, Phys. Rev. A **55**, 4330 (1997).

[60] M. Greiner, O. Mandel, T. W. Hänsch, and I. Bloch, *Collapse and revival of the matter wave field of a Bose-Einstein condensate*, Nature **419**, 51 (2002).

[61] C. Cohen-Tannoudji, J. Dupont-Roc, and G. Grynberg, *Atom-photon interactions* (John Wiley and Sons Inc., New York, 1992), ISBN 0-471-62556-6.

[62] C. S. Adams, M. Sigel, and J. Mlynek, *Atom optics*, Phys. Rep. **240**, 143 (1994).

[63] R. Grimm, M. Weidemller, and Y. B. Ovchinnikov, *Optical Dipole Traps for Neutral Atoms*, Adv. At., Mol., Opt. Phys. **42**, 95 (2000).

[64] A. J. Leggett, *Bose-Einstein condensation in the alkali gases: Some fundamental concepts*, Rev. Mod. Phys. **73**, 307 (2001).

[65] C. Pethick and H. Smith, *Bose-Einstein condensation in dilute gases* (Cambridge University Press, 2001), ISBN 0521665809.

[66] I. Bloch, J. Dalibard, and W. Zwerger, *Many-body physics with ultracold gases*, Rev. Mod. Phys. **80**, 885 (2008).

[67] F. Dalfovo, S. Giorgini, L. P. Pitaevskii, and S. Stringari, *Theory of Bose-Einstein condensation in trapped gases*, Rev. Mod. Phys. **71**, 463 (1999).

[68] K. Bongs and K. Sengstock, *Physics with coherent matter waves*, Rep. Prog. Phys. **67**, 907 (2004).

[69] D. S. Petrov, D. M. Gangardt, and G. V. Shlyapnikov, *Low-dimensional trapped gases*, J. Phys. IV **116**, 5 (2004).

[70] M. Lewenstein, A. Sanpera, V. Ahufinger, B. Damski, A. Sen, and U. Sen, *Ultracold atomic gases in optical lattices: mimicking condensed matter physics and beyond*, Adv. Phys. **56**, 243 (2007).

[71] S. Giorgini, L. P. Pitaevskii, and S. Stringari, *Theory of ultracold atomic Fermi gases*, Rev. Mod. Phys. **80**, 1215 (2008).

[72] P. S. Jessen and I. H. Deutsch, *Optical Lattices*, Adv. At., Mol., Opt. Phys. **37**, 95 (1996).

[73] G. Grynberg and C. Robilliard, *Cold atoms in dissipative optical lattices*, Phys. Rep. **355**, 335 (2001).

[74] W. Zwerger, *Mott-Hubbard transition of cold atoms in optical lattices*, J. Opt. B: Quantum Semiclass. Opt. **5**, S9 (2003).

[75] D. Jaksch and P. Zoller, *The cold atom Hubbard toolbox*, Ann. Phys. (N.Y.) **315**, 52 (2005).

[76] V. I. Yukalov, *Cold bosons in optical lattices*, Laser Phys. **19**, 1 (2009).

[77] S. Chu, *Nobel Lecture: The manipulation of neutral particles*, Rev. Mod. Phys. **70**, 685 (1998).

[78] C. N. Cohen-Tannoudji, *Nobel Lecture: Manipulating atoms with photons*, Rev. Mod. Phys. **70**, 707 (1998).

[79] W. D. Phillips, *Nobel Lecture: Laser cooling and trapping of neutral atoms*, Rev. Mod. Phys. **70**, 721 (1998).

[80] G. Ekspong (Nobel Foundation), ed., *Nobel Lectures in Physics 1996 - 2000* (World Scientific, 2002), ISBN 9812380035.

[81] D.-S. Lühmann, Diploma thesis, *Ultrakalte Atome in optischen Gittern*, Universität Hamburg, Hamburg, Germany (2006).

[82] H. Metcalf and P. van der Straten, *Cooling and trapping of neutral atoms*, Phys. Rep. **244**, 203 (1994).

[83] K. Sengstock and W. Ertmer, *Laser Manipulation of Atoms*, Adv. At., Mol., Opt. Phys. **35**, 1 (1995).

[84] W. Ketterle and N. V. Druten, *Evaporative Cooling of Trapped Atoms*, Adv. At., Mol., Opt. Phys. **37**, 181 (1996).

[85] C. S. Adams and E. Riis, *Laser cooling and trapping of neutral atoms*, Prog. Quantum Electron. **21**, 1 (1997).

[86] O. Mandel, M. Greiner, A. Widera, T. Rom, T. W. Hänsch, and I. Bloch, *Coherent Transport of Neutral Atoms in Spin-Dependent Optical Lattice Potentials*, Phys. Rev. Lett. **91**, 010407 (2003).

[87] J. Sebby-Strabley, B. L. Brown, M. Anderlini, P. J. Lee, W. D. Phillips, J. V. Porto, and P. R. Johnson, *Preparing and Probing Atomic Number States with an Atom Interferometer*, Phys. Rev. Lett. **98**, 200405 (2007).

[88] P. J. Lee, M. Anderlini, B. L. Brown, J. Sebby-Strabley, W. D. Phillips, and J. V. Porto, *Sublattice Addressing and Spin-Dependent Motion of Atoms in a Double-Well Lattice*, Phys. Rev. Lett. **99**, 020402 (2007).

[89] S. Peil, J. V. Porto, B. L. Tolra, J. M. Obrecht, B. E. King, M. Subbotin, S. L. Rolston, and W. D. Phillips, *Patterned loading of a Bose-Einstein condensate into an optical lattice*, Phys. Rev. A **67**, 051603 (2003).

[90] M. Baranov, L. Dobrek, K. Góral, L. Santos, and M. Lewenstein, *Ultracold Dipolar Gases - a Challenge for Experiments and Theory*, Phys. Scr. **T102**, 74 (2002).

[91] K. Góral, L. Santos, and M. Lewenstein, *Quantum Phases of Dipolar Bosons in Optical Lattices*, Phys. Rev. Lett. **88**, 170406 (2002).

[92] A. Griesmaier, J. Werner, S. Hensler, J. Stuhler, and T. Pfau, *Bose-Einstein Condensation of Chromium*, Phys. Rev. Lett. **94**, 160401 (2005).

[93] R. Barnett, D. Petrov, M. Lukin, and E. Demler, *Quantum Magnetism with Multicomponent Dipolar Molecules in an Optical Lattice*, Phys. Rev. Lett. **96**, 190401 (2006).

[94] C. Menotti, M. Lewenstein, T. Lahaye, and T. Pfau, *Dipolar interaction in ultra-cold atomic gases*, AIP Conf. Proc. **970**, 332 (2008).

[95] V. V. Flambaum, G. F. Gribakin, and C. Harabati, *Analytical calculation of cold-atom scattering*, Phys. Rev. A **59**, 1998 (1999).

[96] H. Feshbach, *Unified theory of nuclear reactions*, Ann. Phys. (N.Y.) **5**, 357 (1958).

[97] U. Fano, *Effects of Configuration Interaction on Intensities and Phase Shifts*, Phys. Rev. **124**, 1866 (1961).

[98] P. O. Fedichev, Y. Kagan, G. V. Shlyapnikov, and J. T. M. Walraven, *Influence of Nearly Resonant Light on the Scattering Length in Low-Temperature Atomic Gases*, Phys. Rev. Lett. **77**, 2913 (1996).

[99] J. L. Bohn and P. S. Julienne, *Semianalytic theory of laser-assisted resonant cold collisions*, Phys. Rev. A **60**, 414 (1999).

[100] M. Theis, G. Thalhammer, K. Winkler, M. Hellwig, G. Ruff, R. Grimm, and J. Hecker Denschlag, *Tuning the Scattering Length with an Optically Induced Feshbach Resonance*, Phys. Rev. Lett. **93**, 123001 (2004).

[101] E. Timmermans, P. Tommasini, M. Hussein, and A. Kerman, *Feshbach resonances in atomic Bose-Einstein condensates*, Phys. Rep. **315**, 199 (1999).

[102] R. A. Duine and H. T. C. Stoof, *Atom-molecule coherence in Bose gases*, Phys. Rep. **396**, 115 (2004).

[103] T. Köhler, K. Góral, and P. S. Julienne, *Production of cold molecules via magnetically tunable Feshbach resonances*, Rev. Mod. Phys. **78**, 1311 (2006).

[104] N. Nygaard, B. I. Schneider, and P. S. Julienne, *Two-channel R-matrix analysis of magnetic-field-induced Feshbach resonances*, Phys. Rev. A **73**, 042705 (2006).

[105] P. S. Julienne, E. Tiesinga, and T. Kler, *Making cold molecules by time-dependent Feshbach resonances*, J. Mod. Opt. **51**, 1787 (2004).

[106] E. G. M. van Kempen, S. J. J. M. F. Kokkelmans, D. J. Heinzen, and B. J. Verhaar, *Interisotope Determination of Ultracold Rubidium Interactions from Three High-Precision Experiments*, Phys. Rev. Lett. **88**, 093201 (2002).

[107] N. N. Klausen, J. L. Bohn, and C. H. Greene, *Nature of spinor Bose-Einstein condensates in rubidium*, Phys. Rev. A **64**, 053602 (2001).

[108] F. Deuretzbacher, Diploma thesis, *Spinor Bose-Einstein Kondensate*, Universität Hamburg, Hamburg, Germany (2005).

[109] F. Deuretzbacher, Ph.D. thesis, *Spinor Tonks-Girardeau gases and ultracold molecules*, Universität Hamburg, Hamburg, Germany (2008).

[110] R. Lehoucq, K. Maschhoff, D. Sorensen, and C. Yang, *Arnoldi Package (ARPACK)*, Rice University, Dept. of Computational & Applied Mathematics, Houston, Texas.

[111] E. W. Dijkstra, *A note on two problems in connexion with graphs*, Numerische Mathematik **1**, 269 (1959).

[112] F. Gerbier, A. Widera, S. Fölling, O. Mandel, T. Gericke, and I. Bloch, *Phase Coherence of an Atomic Mott Insulator*, Phys. Rev. Lett. **95**, 050404 (2005).

[113] V. A. Kashurnikov, N. V. Prokof'ev, and B. V. Svistunov, *Revealing the superfluid–Mott-insulator transition in an optical lattice*, Phys. Rev. A **66**, 031601 (2002).

[114] A. Hoffmann and A. Pelster, *Visibility of cold atomic gases in optical lattices for finite temperatures*, Phys. Rev. A **79**, 053623 (2009).

[115] M. Greiner, I. Bloch, O. Mandel, T. W. Hänsch, and T. Esslinger, *Exploring Phase Coherence in a 2D Lattice of Bose-Einstein Condensates*, Phys. Rev. Lett. **87**, 160405 (2001).

[116] M. Köhl, H. Moritz, T. Stöferle, K. Günter, and T. Esslinger, *Fermionic Atoms in a Three Dimensional Optical Lattice: Observing Fermi Surfaces, Dynamics, and Interactions*, Phys. Rev. Lett. **94**, 080403 (2005).

[117] S. Fölling, F. Gerbier, A. Widera, O. Mandel, T. Gericke, and I. Bloch, *Spatial quantum noise interferometry in expanding ultracold atom clouds*, Nature **434**, 481 (2005).

[118] I. B. Spielman, W. D. Phillips, and J. V. Porto, *Mott-Insulator Transition in a Two-Dimensional Atomic Bose Gas*, Phys. Rev. Lett. **98**, 080404 (2007).

[119] T. Rom, T. Best, D. van Oosten, U. Schneider, S. Fölling, B. Paredes, and I. Bloch, *Free fermion antibunching in a degenerate atomic Fermi gas released from an optical lattice*, Nature **444**, 733 (2006).

[120] T. Stöferle, H. Moritz, C. Schori, M. Köhl, and T. Esslinger, *Transition from a Strongly Interacting 1D Superfluid to a Mott Insulator*, Phys. Rev. Lett. **92**, 130403 (2004).

[121] I. B. Spielman, W. D. Phillips, and J. V. Porto, *Condensate Fraction in a 2D Bose Gas Measured across the Mott-Insulator Transition*, Phys. Rev. Lett. **100**, 120402 (2008).

[122] F. Gerbier, A. Widera, S. Fölling, O. Mandel, T. Gericke, and I. Bloch, *Interference pattern and visibility of a Mott insulator*, Phys. Rev. A **72**, 053606 (2005).

[123] F. Gerbier, S. Fölling, A. Widera, O. Mandel, and I. Bloch, *Probing Number Squeezing of Ultracold Atoms across the Superfluid-Mott Insulator Transition*, Phys. Rev. Lett. **96**, 090401 (2006).

[124] M. E. Fisher, M. N. Barber, and D. Jasnow, *Helicity Modulus, Superfluidity, and Scaling in Isotropic Systems*, Phys. Rev. A **8**, 1111 (1973).

[125] A. Leggett, *Topics in the theory of helium*, Phys. Fenn. **8**, 125 (1973).

[126] V. N. Popov and J. Niederle, *Functional Integrals in Quantum Field Theory and Statistical Physics* (Springer, 2001), ISBN 1402003072.

[127] N. F. Mott, *Metal-insulator Transitions* (Taylor & Francis, 1990), ISBN 0850667836.

[128] S. Lundqvist (Nobel Foundation), ed., *Nobel Lectures in Physics 1971 - 1980* (World Scientific, 1991), ISBN 9810207271.

[129] P. Sengupta, M. Rigol, G. G. Batrouni, P. J. H. Denteneer, and R. T. Scalettar, *Phase Coherence, Visibility, and the Superfluid–Mott-Insulator Transition on One-Dimensional Optical Lattices*, Phys. Rev. Lett. **95**, 220402 (2005).

[130] W. Krauth, M. Caffarel, and J.-P. Bouchaud, *Gutzwiller wave function for a model of strongly interacting bosons*, Phys. Rev. B **45**, 3137 (1992).

[131] B. Capogrosso-Sansone, N. V. Prokof'ev, and B. V. Svistunov, *Phase diagram and thermodynamics of the three-dimensional Bose-Hubbard model*, Phys. Rev. B **75**, 134302 (2007).

[132] N. Elstner and H. Monien, *Dynamics and thermodynamics of the Bose-Hubbard model*, Phys. Rev. B **59**, 12184 (1999).

[133] T. D. Kühner, S. R. White, and H. Monien, *One-dimensional Bose-Hubbard model with nearest-neighbor interaction*, Phys. Rev. B **61**, 12474 (2000).

[134] C. Kollath, U. Schollwöck, J. von Delft, and W. Zwerger, *Spatial correlations of trapped one-dimensional bosons in an optical lattice*, Phys. Rev. A **69**, 031601 (2004).

[135] R. V. Pai, R. Pandit, H. R. Krishnamurthy, and S. Ramasesha, *One-Dimensional Disordered Bosonic Hubbard Model: A Density-Matrix Renormalization Group Study*, Phys. Rev. Lett. **76**, 2937 (1996).

[136] T. D. Kühner and H. Monien, *Phases of the one-dimensional Bose-Hubbard model*, Phys. Rev. B **58**, R14741 (1998).

[137] V. F. Elesin, V. A. Kashurnikov, and L. A. Openov, *Mott-insulator–superfluid-liquid transition in a 1D boson Hubbard model*, JETP Lett. **60**, 177 (1994).

[138] V. A. Kashurnikov, A. V. Krasavin, and B. V. Svistunov, *Mott-insulator–superfluid-liquid transition in a one-dimensional bosonic Hubbard model: quantum Monte Carlo method*, JETP Lett. **64**, 99 (1996).

[139] W. Krauth, *Bethe ansatz for the one-dimensional boson Hubbard model*, Phys. Rev. B **44**, 9772 (1991).

[140] R. T. Scalettar, G. G. Batrouni, and G. T. Zimanyi, *Localization in interacting, disordered, Bose systems*, Phys. Rev. Lett. **66**, 3144 (1991).

[141] B. Damski, J. Zakrzewski, L. Santos, P. Zoller, and M. Lewenstein, *Atomic Bose and Anderson Glasses in Optical Lattices*, Phys. Rev. Lett. **91**, 080403 (2003).

[142] L. Fallani, J. E. Lye, V. Guarrera, C. Fort, and M. Inguscio, *Ultracold Atoms in a Disordered Crystal of Light: Towards a Bose Glass*, Phys. Rev. Lett. **98**, 130404 (2007).

[143] R. Pugatch, N. Bar-gill, N. Katz, E. Rowen, and N. Davidson, *Identifying the Bose glass phase*, arXiv:cond-mat/0603571 (2006).

[144] G. K. Campbell, J. Mun, M. Boyd, P. Medley, A. E. Leanhardt, L. G. Marcassa, D. E. Pritchard, and W. Ketterle, *Imaging the Mott Insulator Shells by Using Atomic Clock Shifts*, Science **313**, 649 (2006).

[145] R. Roth and K. Burnett, *Superfluidity and interference pattern of ultracold bosons in optical lattices*, Phys. Rev. A **67**, 031602(R) (2003).

[146] S. Fölling, A. Widera, T. Muller, F. Gerbier, and I. Bloch, *Formation of Spatial Shell Structure in the Superfluid to Mott Insulator Transition*, Phys. Rev. Lett. **97**, 060403 (2006).

[147] G. G. Batrouni, V. Rousseau, R. T. Scalettar, M. Rigol, A. Muramatsu, P. J. H. Denteneer, and M. Troyer, *Mott Domains of Bosons Confined on Optical Lattices*, Phys. Rev. Lett. **89**, 117203 (2002).

[148] S. Wessel, F. Alet, M. Troyer, and G. G. Batrouni, *Quantum Monte Carlo simulations of confined bosonic atoms in optical lattices*, Phys. Rev. A **70**, 053615 (2004).

[149] B. DeMarco, C. Lannert, S. Vishveshwara, and T.-C. Wei, *Structure and stability of Mott-insulator shells of bosons trapped in an optical lattice*, Phy. Rev. A **71**, 063601 (2005).

[150] T.-L. Ho and Q. Zhou, *Intrinsic Heating and Cooling in Adiabatic Processes for Bosons in Optical Lattices*, Phys. Rev. Lett. **99**, 120404 (2007).

[151] V. Ambegaokar, B. I. Halperin, and J. S. Langer, *Hopping Conductivity in Disordered Systems*, Phys. Rev. B **4**, 2612 (1971).

[152] M. A. Cazalilla and A. F. Ho, *Instabilities in Binary Mixtures of One-Dimensional Quantum Degenerate Gases*, Phys. Rev. Lett. **91**, 150403 (2003).

[153] M. Cramer, J. Eisert, and F. Illuminati, *Inhomogeneous Atomic Bose-Fermi Mixtures in Cubic Lattices*, Phys. Rev. Lett. **93**, 190405 (2004).

[154] L. Pollet, M. Troyer, K. Van Houcke, and S. M. A. Rombouts, *Phase Diagram of Bose-Fermi Mixtures in One-Dimensional Optical Lattices*, Phys. Rev. Lett. **96**, 190402 (2006).

[155] A. Imambekov and E. Demler, *Exactly solvable case of a one-dimensional Bose-Fermi mixture*, Phys. Rev. A **73**, 021602 (2006).

[156] L. Pollet, C. Kollath, U. Schollwock, and M. Troyer, *Mixture of bosonic and spin-polarized fermionic atoms in an optical lattice*, Phys. Rev. A **77**, 023608 (2008).

[157] M. Rizzi and A. Imambekov, *Pairing of one-dimensional Bose-Fermi mixtures with unequal masses*, Phys. Rev. A **77**, 023621 (2008).

[158] A. Mering and M. Fleischhauer, *One-dimensional Bose-Fermi-Hubbard model in the heavy-fermion limit*, Phys. Rev. A **77**, 023601 (2008).

[159] G. Refael and E. Demler, *Superfluid-insulator transition in Fermi-Bose mixtures and the orthogonality catastrophe*, Phys. Rev. B **77**, 144511 (2008).

[160] A. Zujev, A. Baldwin, R. T. Scalettar, V. G. Rousseau, P. J. H. Denteneer, and M. Rigol, *Superfluid and Mott-insulator phases of one-dimensional Bose-Fermi mixtures*, Phys. Rev. A **78**, 033619 (2008).

[161] M. Cramer, S. Ospelkaus, C. Ospelkaus, K. Bongs, K. Sengstock, and J. Eisert, *Do Mixtures of Bosonic and Fermionic Atoms Adiabatically Heat Up in Optical Lattices?*, Phys. Rev. Lett. **100**, 140409 (2008).

[162] R. M. Lutchyn, S. Tewari, and S. Das Sarma, *Boson Hubbard model with weakly coupled fermions*, Phys. Rev. B **78**, 220504 (2008).

[163] I. Titvinidze, M. Snoek, and W. Hofstetter, *Generalized dynamical mean-field theory for Bose-Fermi mixtures in optical lattices*, Phys. Rev. B **79**, 144506 (2009).

[164] R. M. Lutchyn, S. Tewari, and S. Das Sarma, *Loss of superfluidity by fermions in the boson Hubbard model on an optical lattice*, Phys. Rev. A **79**, 011606 (2009).

[165] K. Mitra, C. J. Williams, and C. A. R. Sá de Melo, *Superfluid and Fermi-liquid phases of Bose-Fermi mixtures in optical lattices*, Phys. Rev. A **79**, 055601 (2009).

[166] S. Sinha and K. Sengupta, *Phases and collective modes of a hardcore Bose-Fermi mixture in an optical lattice*, Phy. Rev. B **79**, 115124 (2009).

[167] S. Ospelkaus, Ph.D. thesis, *Quantum Degenerate Fermi-Bose Mixtures of ^{40}K and ^{87}Rb in 3D Optical Lattices*, Universität Hamburg, Hamburg, Germany (2006).

[168] F. Ferlaino, C. D'Errico, G. Roati, M. Zaccanti, M. Inguscio, G. Modugno, and A. Simoni, *Feshbach spectroscopy of a K-Rb atomic mixture*, Phys. Rev. A **73**, 040702 (2006).

[169] F. M. Cucchietti and E. Timmermans, *Strong-Coupling Polarons in Dilute Gas Bose-Einstein Condensates*, Phys. Rev. Lett. **96**, 210401 (2006).

[170] M. Bruderer, A. Klein, S. R. Clark, and D. Jaksch, *Polaron physics in optical lattices*, Phys. Rev. A **76**, 011605 (2007).

[171] G. D. Mahan, *Many-particle physics* (Springer, 2000), ISBN 0-306-46338-5.

[172] C. Klempt, T. Henninger, O. Topic, J. Will, W. Ertmer, E. Tiemann, and J. Arlt, ^{40}K-^{87}Rb *Feshbach resonances: Modeling the interatomic potential*, Phys. Rev. A **76**, 020701 (2007).

[173] E. A. Burt, R. W. Ghrist, C. J. Myatt, M. J. Holland, E. A. Cornell, and C. E. Wieman, *Coherence, Correlations, and Collisions: What One Learns about Bose-Einstein Condensates from Their Decay*, Phys. Rev. Lett. **79**, 337 (1997).

[174] J. T. Stewart, J. P. Gaebler, and D. S. Jin, *Using photoemission spectroscopy to probe a strongly interacting Fermi gas*, Nature **454**, 744 (2008).

[175] R. Ozeri, N. Katz, J. Steinhauer, and N. Davidson, *Colloquium: Bulk Bogoliubov excitations in a Bose-Einstein condensate*, Rev. Mod. Phys. **77**, 187 (2005).

[176] M. Kozuma, L. Deng, E. W. Hagley, J. Wen, R. Lutwak, K. Helmerson, S. L. Rolston, and W. D. Phillips, *Coherent Splitting of Bose-Einstein Condensed Atoms with Optically Induced Bragg Diffraction*, Phys. Rev. Lett. **82**, 871 (1999).

[177] J. Stenger, S. Inouye, A. P. Chikkatur, D. M. Stamper-Kurn, D. E. Pritchard, and W. Ketterle, *Bragg Spectroscopy of a Bose-Einstein Condensate*, Phys. Rev. Lett. **82**, 4569 (1999).

[178] D. M. Stamper-Kurn, A. P. Chikkatur, A. Görlitz, S. Inouye, S. Gupta, D. E. Pritchard, and W. Ketterle, *Excitation of Phonons in a Bose-Einstein Condensate by Light Scattering*, Phys. Rev. Lett. **83**, 2876 (1999).

[179] S. B. Papp, J. M. Pino, R. J. Wild, S. Ronen, C. E. Wieman, D. S. Jin, and E. A. Cornell, *Bragg Spectroscopy of a Strongly Interacting ^{85}Rb Bose-Einstein Condensate*, Phys. Rev. Lett. **101**, 135301 (2008).

[180] P. T. Ernst, Ph.D. thesis, *Bragg Spectroscopy in Optical Lattices and the Physics of Quantum Gas Mixtures*, Universität Hamburg, Hamburg, Germany (2009).

[181] J. Krauser, Diploma thesis, *Impulsaufgelöste Bragg-Spektroskopie an bosonischen Quantengasen in optischen Gittern*, Universität Hamburg, Hamburg, Germany (2009).

[182] A. M. Rey, P. B. Blakie, G. Pupillo, C. J. Williams, and C. W. Clark, *Bragg spectroscopy of ultracold atoms loaded in an optical lattice*, Phys. Rev. A **72**, 023407 (2005).

[183] G. Pupillo, A. M. Rey, and G. G. Batrouni, *Bragg spectroscopy of trapped one-dimensional strongly interacting bosons in optical lattices: Probing the cake structure*, Phys. Rev. A **74**, 013601 (2006).

[184] G. G. Batrouni, F. F. Assaad, R. T. Scalettar, and P. J. H. Denteneer, *Dynamic response of trapped ultracold bosons on optical lattices*, Phys. Rev. A **72**, 031601 (2005).

[185] E. Kim and M. H. W. Chan, *Probable observation of a supersolid helium phase*, Nature **427**, 225 (2004).

[186] N. Prokof'ev and B. Svistunov, *Supersolid State of Matter*, Phys. Rev. Lett. **94**, 155302 (2005).

[187] E. Burovski, E. Kozik, A. Kuklov, N. Prokof'ev, and B. Svistunov, *Superfluid Interfaces in Quantum Solids*, Phys. Rev. Lett. **94**, 165301 (2005).

[188] N. Prokof'ev, *What makes a crystal supersolid?*, Adv. Phys. **56**, 381 (2007).

[189] V. W. Scarola and S. D. Sarma, *Quantum Phases of the Extended Bose-Hubbard Hamiltonian: Possibility of a Supersolid State of Cold Atoms in Optical Lattices*, Phys. Rev. Lett. **95**, 033003 (2005).

[190] D. L. Kovrizhin, G. V. Pai, and S. Sinha, *Density wave and supersolid phases of correlated bosons in an optical lattice*, Europhys. Lett. **72**, 162 (2005).

[191] P. Sengupta, L. P. Pryadko, F. Alet, M. Troyer, and G. Schmid, *Supersolids versus Phase Separation in Two-Dimensional Lattice Bosons*, Phys. Rev. Lett. **94**, 207202 (2005).

[192] G. G. Batrouni, F. Hébert, and R. T. Scalettar, *Supersolid Phases in the One-Dimensional Extended Soft-Core Bosonic Hubbard Model*, Phys. Rev. Lett. **97**, 087209 (2006).

[193] S. Wessel and M. Troyer, *Supersolid Hard-Core Bosons on the Triangular Lattice*, Phys. Rev. Lett. **95**, 127205 (2005).

[194] D. Heidarian and K. Damle, *Persistent Supersolid Phase of Hard-Core Bosons on the Triangular Lattice*, Phys. Rev. Lett. **95**, 127206 (2005).

[195] R. G. Melko, A. Paramekanti, A. A. Burkov, A. Vishwanath, D. N. Sheng, and L. Balents, *Supersolid Order from Disorder: Hard-Core Bosons on the Triangular Lattice*, Phys. Rev. Lett. **95**, 127207 (2005).

[196] C. Orzel, A. K. Tuchman, M. L. Fenselau, M. Yasuda, and M. A. Kasevich, *Squeezed States in a Bose-Einstein Condensate*, Science **291**, 2386 (2001).

[197] D. S. Rokhsar and B. G. Kotliar, *Gutzwiller projection for bosons*, Phys. Rev. B **44**, 10328 (1991).

[198] M. Greiner, Ph.D. thesis, *Ultracold quantum gases in three-dimensional lattice potentials*, Ludwig Maximilians Universität München, München, Germany (2003).

[199] P. R. Johnson, E. Tiesinga, J. V. Porto, and C. J. Williams, *Effective three-body interactions of neutral bosons in optical lattices*, New J. Phys. **11**, 093022 (2009).

The author:
Dirk-Sören Lühmann

The thesis "Multiorbital Physics in Optical Lattices" covers ultracold bosonic gases and mixtures of bosons and fermions in optical lattices with special regard to finite-size and orbital effects. In preference for a Hubbard-type single-band Hamiltonian, the influence of higher bands in optical lattices has been widely neglected so far. In this thesis, it is shown that the inclusion of higher orbitals leads to novel physical effects such as a self-trapping behavior and the enhanced localization in attractively interacting mixtures as well as a complex quantum phase evolution in purely bosonic systems. The on-site interaction among the particles causes strongly correlated states, which are investigated using a multiorbital exact diagonalization technique.

Topics: introduction to ultracold atomic gases in optical lattices, bosonic atoms in finite optical lattices, excitation spectrum of Mott-insulator shells, self-trapping of bosonic and fermionic atoms, momentum-resolved Bragg spectroscopy, and multiorbital quantum phase evolution in optical lattices.